UPC

TECHNICAL UNIVERSITY OF CATALONIA. SCHOOL OF CIVIL ENGINEERING.

DEPARTMENT OF GEOTECHNICAL ENGINEERING AND GEOSCIENCES.

BARCELONA, SPAIN

-

UNIVERSITAT POLITÈCNICA DE CATALUNYA

ESCOLA TÈCNICA SUPERIOR D'ENGINYERS, CANALS I PORTS.

DEPARTAMENT D'ENGINYERIA DEL TERRENY I CARTOGRÀFICA

BARCELONA, ESPAÑA

MULTIPHASE GAS TRANSPORT IN A SHEAR ZONE

PHD THESIS SUBMITTED BY:

JORGE JÓDAR BERMÚDEZ

ADVISORS:

JESÚS CARRERA RAMÍREZ

AGUSTÍN MEDINA SIERRA

BARCELONA, APRIL 2007

HYDROGEOLOGY GROUP
TECHNICAL UNIVERSITY OF CATALONIA

"Each problem that I solved became a rule which
served afterwards to solve other problems."
Rene Descartes

To my family

ABSTRACT

In the post-operational phase of a Low/Intermediate-Low radioactive waste repository, gas will be generated in the caverns due to anaerobic corrosion of metals, and also chemical and microbial degradation of organic substances. Previous investigations on gas migration have indicated that discrete water-conducting features (e.g. shear zones) are mainly responsible for gas transport from the caverns through the geosphere. Two phase flow processes occur in these water conducting features; the continuity and spatial distribution of pore spaces, the pore size distribution and the interfacial forces of the three phases gas-water-rock have a significant influence on gas transport.

The main difficulties to be resolved when simulating two-phase flow processes in fractured rock are:

- The description of the internal heterogeneity of the individual water conducting features. The influence of channelling along preferential flow paths is even more important than for single phase fluid flow, because gas transport takes place more or less exclusively along the most transmissive channels.

- The determination of effective mass exchange coefficients of the relevant components of the system. Mass exchange may occur between three phases (gas-water-rock). It depends on the spatial distribution of water and gas along the water conducting features (i.e. specific surface of contact areas between phases), and on the solubility and diffusivity of the different components, but also on a couple of state variables of liquid phase (initial content of dissolve/free gas, initial pressure).

The work presented in this thesis aims to improve the understanding of the physics of single and multiphase transport phenomena, to be able to develop a quantitative description of gas transport in shear zones to overcome in a satisfactory way the problems described above.

RESUMEN

Durante la fase post-operacional de los depósitos de almacenamiento final de material radioactivo de baja y media actividad, es posible que se genere gas en el interior de las galerías del depósito. Este gas se genera como resultado de la corrosión anaeróbica de metales, así como de la degradación microbiológica de sustancias orgánicas presentes en el interior del depósito tras su clausura. Estudios previos sobre migración de gas indican que el gas se moverá básicamente por las fracturas existentes en el macizo rocoso que alberga al depósito de almacenamiento, pudiendo llegar a la superficie. El flujo y transporte del gas por el interior de esas fracturas se realizará en condiciones multifásicas; la conectividad hidráulica, la distribución espacial y de tamaño de poros y las tensiones superficiales entre las diferentes fases gas-agua-roca tendrán una influencia significante en el transporte de gas.

Las principales dificultades a resolver cuando se simulan procesos multifase en fracturas son:

- La descripción de la heterogeneidad interna de las fracturas. La existencia de canales o zonas de alta conectividad hidráulica es crucial para el caso de la migración de gases, ya que el transporte de gas se produce casi exclusivamente por las zonas más transmisivas.

- La determinación de los coeficientes de intercambio de masa entre los diferentes componentes del sistema multifásico. Este intercambio depende de la distribución espacial de agua y gas en el interior de la fractura (superficie de contacto específica entre las diversas fases), de la solubilidad y difusividad de los diferentes componentes gaseosos , así como del estado inicial de presiones de agua y concentración inicial de gas disuelto.

El trabajo presentado en esta tesis está dirigido a mejorar el conocimiento de la física relativa a los procesos del transporte en condiciones multifásicas. El objetivo es realizar una descripción cuantitativa satisfactoria del transporte de gas en fracturas.

RESUM

Durant la fase post-operacional dels dipòsits d'emmagatzematge final de material radioactiu de baixa i mitja activitat, és possible que es generi gas en l'interior de les galeries del dipòsit. Aquest gas es genera com resultat de la corrosió anaeròbia dels metalls, així com a de la degradació microbiològica de les substàncies orgàniques presents a l'interior del dipòsit després de la seva clausura. Els estudis previs sobre migració de gas indiquen que el gas es mourà bàsicament per les fractures existents en el massís rocós que alberga al dipòsit d'emmagatzematge, i pot arribar a la superfície. El flux i transport del gas per l'interior d'aquestes fractures es realitzarà en condicions multifàsiques; la connectivitat hidràulica, la distribució espacial i de grandària de porus i les tensions superficials entre les diferents fases gas-aigua-roca tindran una influència significant en el transport de gas

Les principals dificultats a resoldre quan se simulen processos multifàsics en fractures són:

La descripció de l'heterogeneïtat interna de les fractures. L'existència de canals o zones d'alta connectivitat hidràulica és crucial per al cas de la migració de gasos, ja que el transport de gas es dona gairebé exclusivament per les zones més transmissives.

La determinació dels coeficients de bescanvi de massa entre els diferents components del sistema multifàsic. Aquest bescanvi depèn de la distribució espacial d'aigua i gas a l'interior de la fractura (superfície de contacte específica entre les diverses fases), de la solubilitat i difusivitat dels diferents components gasosos , així com de l'estat inicial de pressions d'aigua i concentració inicial de gas dissolt.

El treball presentat en aquesta tesi està dirigit a millorar el coneixement de la física relativa als processos del transport en condicions multifàsiques. L'objectiu és realitzar una descripció quantitativa satisfactòria del transport de gas en fractures.

ACKNOWLEDGEMENTS

I would like to express my gratitude to all those who gave me the possibility to complete this thesis.

First and foremost I offer my sincerest gratitude to my advisor, Dr. Jesús Carrera, who has supported me though out my thesis with his patience and knowledge. His time is shared between many projects but still he has managed to guide my work at the right points with his many ideas, stimulating suggestions and encouragement helped me in all the time of research for and writing of this thesis.

Special thanks go to my co-advisor Agustín Medina and to Andrés Alcolea for their friendship, moral support and good times we have spent together. They helped me to handle the code TRANSIN-II and TRANSIN-IV, and also suffered with me during these long days when applying geostatistical inversion modeling to the field cases. They jointly with Ernest Mendoza looked closely at the final version of the thesis for English style and grammar, correcting both and offering suggestions for improvement.

My colleagues from the Hidrogeology Group of the Departament d'Enginyeria del Terreny, Cartogràfica i Geofísica (Department of Geotechnical Engineering & Geosciences) for their friendship. I want to thank them for all their help, support, interest and valuable hints. Especially I am obliged to Sebas Olivella, Peter Meier, Luis Vives, Alfredo Pérez, Lurdes Martinez, Javier Lambán, Xavier Sánchez-Vila, Marisol Manzano, Hipólita Ramajo (forever Poli), Felip Ortuño, Maarten Saaltink, Enric Vázquez, Elena Abarca, Juan Hidalgo, Matthias Willmann. Tobias Rötting, Paco Alcalá, Amaranta Marcuello and Adolfo Castro. Additional thanks to Silvia Aranda, Teresa Tolosana, Jordi Sánchez-Vila, Ester Yoldi and Bea Rodríguez for their valuable help during these years. Unfortunately there is not enough space to mention all my friends who indirectly contributed to this thesis, even if I had a complete record of their contributions.

My colleagues Luis Alberto Seguí and Luis Cabrera from TECNOMA and TYPSA respectively, for their constant encouragement and blind faith on my possibilities.

Thanks to Soledad Carreras and Montserrat Segura for their "logistic" support.

I acknowledge the Department of Geotechnical Engineering & Geosciences (Hydrogeology group) of the UPC who have supported my work on this thesis.

The GAM project was partially funded by the Spanish Nuclear Waste Management Agency (ENRESA) through grant number 703276. Thanks to all the people who have participated in the development of the project.

I cannot end without thanking my family, specially to my wife Itziar and our children Ana and Yago, for their support and tolerance during the writing of this thesis.

TABLE OF CONTENTS

Annex A8:
Tracer Test Simulation. Blind Prediction of PT5

Annex A9:
Gas Tracer Test Calibration

LIST OF FIGURES

LIST OF TABLES

Chapter 1

Introduction

Hydraulic characterization of single fractures has traditionally received scarce attention because they lack interest for water supply. However, a large effort has been devoted to these formations during the last 20 years because of the potential use of fractured media for radioactive waste isolation. Many projects were developed to understand the relevant processes that may occur in the whole repository system for a long term waste disposal, such as gas generation. In this sense, it is expected that gas can be produced during the post-operational phases of low and intermediate-level radioactive waste (L/ILW) repositories through anaerobic degradation, and accumulate in storage caverns. If the rate of gas production at the source is sufficiently large and the rock impervious, the resulting pressure build-up could have a negative effect on the barrier function of the rock and on the engineered barrier system (e.g. opening of existing fractures, generation of new fractures). In this situation, gas phase would migrate upwards through interconnected pores and fractures with the highest transmissivity. Shear zones might serve as primary conduits for gas migration away from the caverns through the geosphere. For those reasons, understanding gas flow and transport in fractured rocks is of primary importance for risk assessment of nuclear waste repositories.

The motivation of this thesis is to improve understanding of the heterogeneity and mass transfer mechanism in a single fracture. This is achieved by using different and complementary information from several tests to gain additional insight into the physics of single and multiphase transport phenomena. This work has been performed in the framework of GAM, a long-term project in which many institutions and research groups participated. Field scale experiments were performed at the Grimsel Test Site, integrated with laboratory experiments, theoretical investigations and numerical modelling. The main objective of GAM is precisely to provide a better understanding of gas transport mechanisms in shear zones.

The sequence of involved phenomena are summarised in Table 1.1. First, one needs to understand water flow in a single heterogeneous fracture. Then, one needs to understand how a solute migrating through the fracture behaves. Several transport mechanisms play different roles in terms of solute migration, such as the Darcy's flow and the ability of the solute to diffuse into the matrix zone. The third step is to understand two phase (air + water) flow in a single heterogeneous fracture. In this case not only Darcy flow but also capillarity forces control the size, shape, propagation and growing direction of the gas bubble through the fracture as free phase. Finally, it is necessary to understand how a gas tracer through the fracture in two phase flow conditions migrates. Gas transport is controlled by advection and dispersion in the gas phase and also by dissolution in the liquid phase. In a fractured medium, the rock matrix (and small aperture fractures) remains filled with virtually immobile water. Therefore, dissolved gases reach the interior of the matrix by diffusion. Hence, gas migration is very sensitive to gas solubility, diffusion coefficient and to the surface and volume available for dissolution/diffusion.

Table 1.1: Relevant processes in terms of the different problem scenarios

Problem	Processes
Water flow	Darcy flow
Solute transport	Advection Dispersion Matrix diffusion
Two phase (Air+ Water) flow	Darcy flow Capillarity
Gas tracer transport	Advection in the gas phase Dispersion in the gas phase Dissolution Matrix diffusion in liquid phase

The structure of this thesis follows the project program as a natural way to describe the different tasks performed during the project.

In chapter 2 a brief overview of the GAM project as well as site characterization is presented. Here are described the in situ testing activities and also the laboratory investigations performed in the framework of the GAM project.

The first step in the methodology for describing multiphase flow and transport is to characterize the heterogeneity of the fracture. In chapter 3, the fracture heterogeneity is examined in terms of the spatial correlation of transmissivity, and also in terms of the relationship between transmissivity and flow porosity. Matrix porosity has revealed as an important transport mechanism in order to explain the behaviour of the different solute tracers injected in the fracture. A general model selection criterion is presented to select the most suitable geostatistical hypothesis taking into account the obtained results from flow and transport in a jointly way.

Once the heterogeneity is properly characterized, the next step in the methodology is to simulate the multiphase flow in the fracture. Chapter 4 is devoted to a sensitivity study of the parameters controlling the gas flow into a multiphase system such as the GAM fracture during a gas threshold pressure test (GTPT), and then to find the best conceptual model in order to properly simulate the experimental data from the gas pressure tests.

The motivation of Chapter 5 is to shed light on processes affecting gas dissolution/diffusion processes in a partially saturated heterogeneous fracture. A formal analogy between gas transport in a two phase system equations and the solute tracer transport equation in water saturated system is presented. In addition, a numerical sensitivity analysis of the variables which govern the dissolution/diffusion processes in shear zones is performed. The model is potentially useful for predicting gas tracer migration, site characterisation, and also for experimental gas tracer tests design

The last step in the methodology is to reproduce the experimental gas breakthrough curves. In chapter 6 we present the results from the numerical modelling of gas injection tests performed in the framework of the GAM project. The simulated tracer

breakthrough curves of the different injections are rather similar, with small separation between tracers, and correctly match measured tracer breakthrough curves.

The chapters of this thesis, though self-consistent and addressing different problems, constitute part of a whole intended to improve understanding of multiphase flow and transport in a shear zone. The conceptualization of processes involved in gas migration through partially saturated shear zones has revealed as a very complex problem to undertake it in an individual way. For this reason it has been necessary to break it into several smaller parts. Although each part has its own goals and gets to specific conclusions, altogether allow to reproduce the whole problem.

Chapter 2: The GAM Project

2.1.Overview of the GAM Project

The GAM experiment **(Ga**s **M**igration in shear zones) is a long term project addressed to investigate the relevance of the gas migration through fractures. In this project agencies in charge of nuclear waste disposal (ENRESA, NAGRA, ANDRA, NAGRA and SNL from the US as Department of Energy) as well as research groups (UPC and ETH) have joined into a common interest point and have developed the so called GAM experimental programme (Marshall et al., 1998).

The general objectives of the GAM investigation programme were:

- To evaluate the applicability of common concepts of two-phase flow in fractured media, particularly emphasising the fact that water-conducting features are generally heterogeneous.

- To determine robust estimates for effective TPF parameters of single fractures on a local scale (metres to decametres)

- To determine realistic mass exchange coefficients for multi-component gas transport in a two-phase flow system.

- To evaluate the consistency between the numerical simulations of gas threshold pressure tests and gas tracer tests.

The main purpose of our contribution to GAM is to acquire fundamental knowledge of fracture flow and transport processes in order to interpret multi-tracer tests, which can help us to characterize the fracture internal heterogeneity. The main idea is to develop conceptual models of a fracture that are hydraulically equivalent, and to assess whether they exhibit differences from the point of view of the multiphase flow and

The project investigation programme consisted of complemented field and laboratory experiments which provides experimental data to develop consistent conceptual models to gain additional insight into the physics of single and multiphase transport phenomena.

The design of the experimental activities to be performed in the framework of the GAM project is very complete and ambitious. Field and laboratory experiments as well as the previous results obtained from them are briefly presented in the following sections. For more detailed questions about the field experiments it is recommended the reading of the next chapters.

2.2.Characterization of the GAM fracture

The fracture characterization consist basically of detailed mapping of the structural information (core logging and, optionally, BIPS-TV), hydraulic tests (pulse, and constant rate injection), tracer tests (single phase liquid solute and particle tracers), gas threshold pressure tests (single hole and crosshole) and gas tracer (He, Xe, SF_6, Ar, H_2S) injection tests. The objective of injecting so many tracers is to obtain the flow and transport parameters (single phase) and also the description of heterogeneity in terms of: average flow porosity (solute tracers) and aperture distribution (particle tracers). The general objective of the gas tracer testing is to provide a better understanding of gas transport mechanisms and properties in shear zones in order to determine realistic mass exchange coefficients (advection/ diffusion/ dissolution/ sorption) in a two phase flow (gas and water) system.

2.2.1 Site description

The GAM shear zone is located in the southern part of the Grimsel Test Site (GTS). The Grimsel Test Site (GTS) is located (Fig. 2.1) at an altitude of 1730 metres in the granitic rock of the Aar Massif in central Switzerland. It lies at a depth of around 450 metres beneath the surface and is reached by an access tunnel belonging to the Kraftwerke Oberhasli AG (KWO), the local hydro-power company.

The GTS tunnel system is around one kilometre long and was excavated in 1983 using a full-face tunnelling machine (diameter 3.5m). The Test Site offers ideal conditions for carrying out a wide range of test investigation programmes such as the GAM project

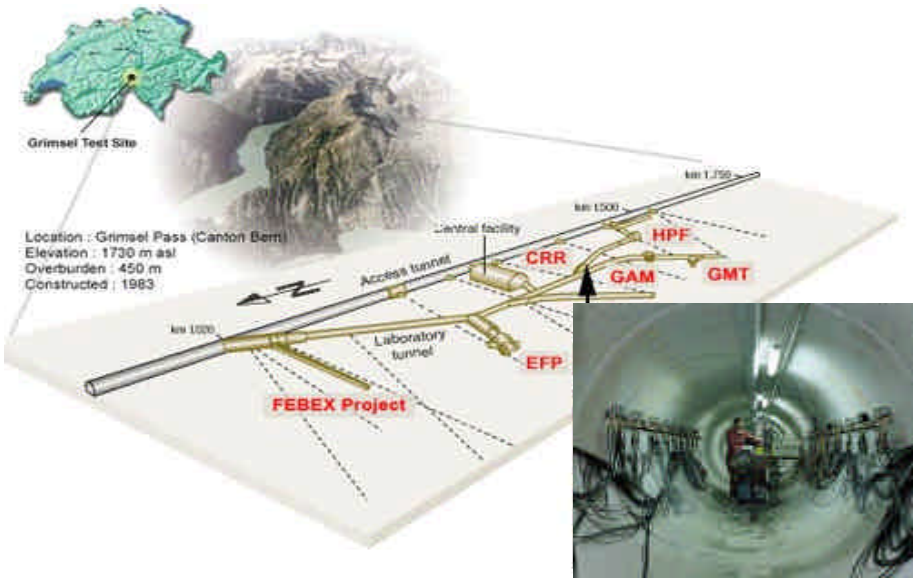

Figure 2.1: General situation of the GTS and tunnel layout.

The Aare Massif consists of a metasedimentary envelope that was intruded by Hercynian granitoids (320-280 My) such as the Central Aare granite (in the North of the GTS) and the Grimsel granodiorite (in the South of the GTS); the latter is the host rock

of the site investigated. The age of solidification of the granites is approximately 290-300 My; subsequently the rocks were intruded by sets of lamprophyres and aplites (250 My ago).

The whole Aar Massif was subjected to strong alpine deformation and metamorphism. The dominant overprinting of the rocks are associated with ductile deformation, that is indicated by a cleavage of variable intensity (orientated NE-SW), and also by ductile shear zones and mylonites.

During the subsequent uplift (which is still ongoing) and cooling, the deformation changed from ductile to brittle behaviour, resulting in fractures and fault breccias. Brittle deformation concentrated along the old cleavage planes, NE-SW-striking shear zones and along the lamprophyre/granite contacts. At present, these brittle structures represent the main groundwater flowpaths at the site.

Based upon an investigation carried out by Keusen et al. (1989) and in direct observations (Pardillo et al., 1997), four main categories of discontinuities are found:

- S-zones, which are fracture bearing, shear zones that generally dip steeply SE, parallel to the foliation in the rock.
- K-zones striking WNW and intersecting the rock fabric at a high angle.
- Steeply dipping lamprophyres, which are highly discontinous and are widely distributed at the GTS.
- Finally, subhorizontal, poorly connected tension joints.

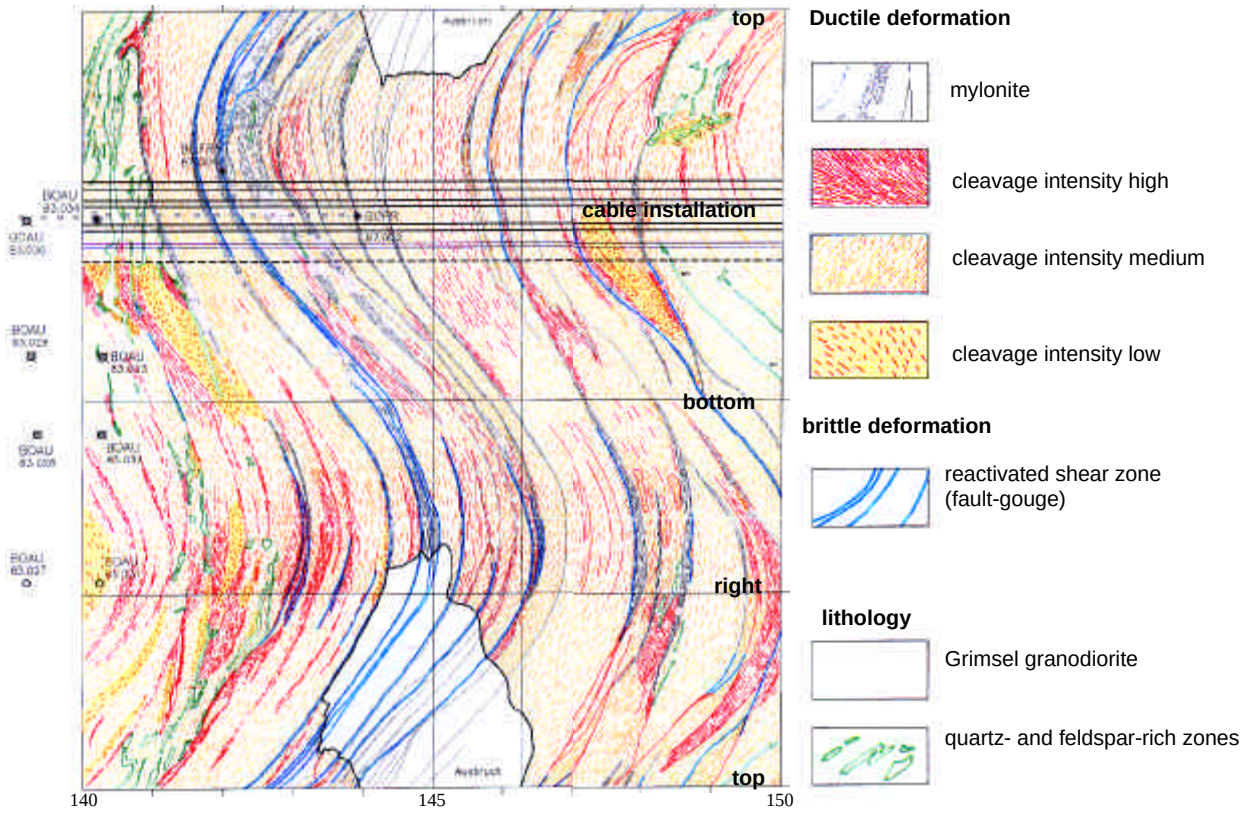

Figure 2.2: Structural tunnel mapping of the GAM shear

In our area of interest in GTS (the GAM fracture) all the detected shear zones exhibit similar structure. The fractures steeply dipping and the dominant strike is EN-SW. Macroscopically, the shear zones are characterised by zones of ductile deformation with high damage intensity with mica-rich mylonite bands, and brittle fault breccia horizons with a thickness ranging from a few millimetres to one centimetre, located at the zones of the highest ductile deformation. These zones contain fine-grained, non-cohesive gauge material (Fig. 2.2).

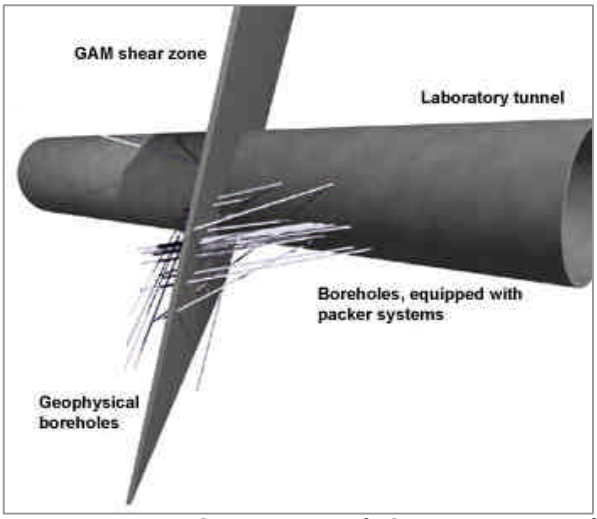

Figure 2.3: Visualization 3D of the intersection of suitable boreholes at the GAM site with the shear zone plane

2.2.2 Site preparation

The preparation of the shear zone includes drilling and instrumentation of boreholes (Gemperle 1999b) which are of two types: On the one hand boreholes that intersect the fracture shear zone (22 boreholes) used to perform the hydraulic, tracer and gas injection tests as well as observation boreholes, and on the other hand geophysical boreholes, drilled parallel to the shear zone with a "fan-like" distribution, at a distance of one meter (4 boreholes in each side of the shear zone). These boreholes are used to have a geophysical imaging of the shear zone by radar reflection methods. These boreholes do not affect the hydraulic conditions in the shear zone while they are “observing“ what is going on in the fracture. The locations of the borehole intersections with the shear-zone are depicted in Fig 3. The intersection of the tunnel and the shear zone was sealed with a special exposy resin in order to prevent a dominating constant pressure boundary during testing, so water does not flow to the tunnel

2.2.3 Site characterization. Testing activities in the GAM fracture

2.2.3.1 Hydraulic testing

Several hydraulic tests have been performed in the GAM fracture during the former TPF project (Wyss 1996) and the GAM project itself (Gemperle 1999a, Gemperle 1999b, Fierz and Piedevache 2000, Trick 2000 and Trick 2001). These measurements extend over a period of five years from January 1995 to December 2000 and include single borehole tests as well as cross-hole hydraulic tests (see Table 2.1). Their specific objective was to obtain information about the hydraulic coefficients (transmissivity, storativity) and the static pressure distribution in the shear zone, which will be used as a priori information for the solute tracer test program.

Table 2.1: Summary of the hydraulic tests performed in the GAM shear zone. For each test the measurement campaign and the corresponding bibliographic reference is indicated (1 Wyss 1996; 2 Gemperle 1999b; 3 Fierz and Piedevache 2000; 4 Trick 2000; 5 Trick 2001.). For cross-hole tests, which can consist in either constant-rate injection test (RI) or constant-head injection test (HI), 🡻 means injection borehole whereas the symbol ☒ denotes the observation boreholes

Borehole	Pulse tests	Cross-hole hydraulic tests							
		Jun 1995 [1]	Jul 1995 [1]	Nov 1998 [2]	Nov 1998 [2]	Jan 2000 [3]	Aug 2000 [4]	Dec 2000 [5]	Dec 2000 [5]
		RI/HI	RI/HI	RI/HI	RI/HI	RI	RI/HI	RI	RI
AU83.034		☒	☒	☒	☒	☒	☒	☒	☒
FR87.001		☒	☒	☒	☒	☒	☒	☒	☒
FR87.003		☒	☒	☒	☒	☒	☒	☒	☒
FR89.001		☒	☒	☒	☒	☒	☒	☒	🡻
TPF95.001	Jun 1995 [1]	🡻	☒	☒	☒	☒	☒	☒	☒
TPF95.002	Jun 1995 [1]	☒	🡻	☒	☒	☒	☒	☒	☒
TPF95.003	Jun 1995 [1]	☒	☒						
TPF95.004	Jun 1995 [1]	☒	☒	☒	☒	☒	☒	☒	☒
TPF95.005	Jun 1995 [1]	☒	☒	☒	☒	☒	☒	☒	
TPF95.006	Jun 1995 [1]	☒	☒	☒	☒	☒	☒	☒	☒
TPF95.007	Jun 1995 [1]	☒	☒	☒	☒	☒	☒	🡻	☒
GAM98.001	Dec 2000 [5]			☒	☒				
GAM98.002	Nov 1998 [2] Jan 2000 [3]			🡻	☒	🡻	☒	☒	☒
GAM98.003	Dec 2000 [5]			☒	☒		☒	☒	☒
GAM98.004	Nov 1998 [2] Dec 2000 [5]			☒	🡻	☒	🡻	☒	
GAM98.005	Dec 2000 [5]			☒	☒	☒	☒	☒	☒
GAM98.006	Dec 2000 [5]			☒	☒	☒	☒	☒	☒
GAM98.007	Dec 2000 [5]			☒	☒	☒	☒	☒	☒
GAM98.008	Dec 2000 [5]			☒	☒	☒	☒	☒	☒

As it is shown in Table 2.1, during these hydraulic tests campaigns pulse injection tests (PI), constant rate injection tests (RI), and constant head injection tests (HI) have been performed.

A pulse injection test consists of producing a sudden pressure increase within a borehole by quick injection of water and monitoring the response of the system to the perturbation of the pressure field. The pressure recovery curve is mainly controlled by the hydraulic properties in the vicinity of the well.

The PI campaign of June 1995, was preliminary interpreted by Wyss (1996). The pressure-recovery data from pulse-injection tests were manually calibrated using Cooper's type curves (Cooper and Papadopulos 1967). Successively, the same data were automatically calibrated (Appendix 4) with an algorithm based on Barker's solution (Barker, 1988). In chapter 3 the obtained results are presented and discussed. In general, the parameters resulting from calibration present a strong local variability on transmissivity, which varies over three orders of magnitudes (10^{-11} to 10^{-8} m^2/s). The different methods present a good agreement with regards to transmissivity identification. In contrast, striking differences can be observed in the storativity values calibrated using different methods, which suggest that these estimates are unreliable (Meier et al., 1998).

Constant rate/head injection consists of a water injection, either at constant flow rate or at constant pressure, into a borehole over a period variable from fractions of an hour (short-term experiment) to several days (long-term experiment). During injection, the area of influence of the well extends to larger and larger portions of the fracture whose hydraulic pressure is perturbed. The pressure response to the forcing water injection is monitored at the injection well as well as at other additional boreholes (observation boreholes). Then injection stops and pressure recovery is observed for a time that is typically 2 to 4 times longer than the injection period.

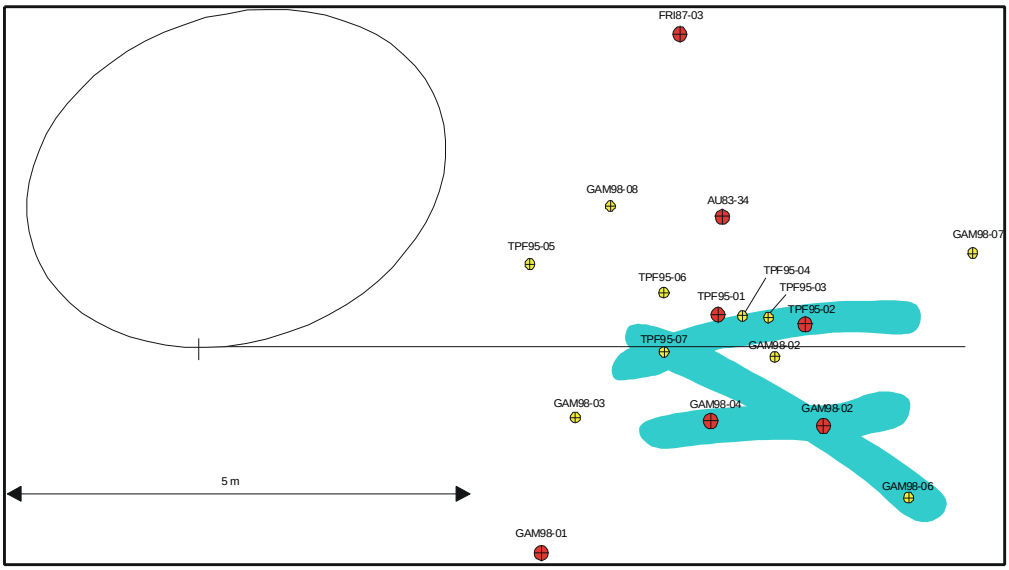

Figure 2.4: Intersection of boreholes at the GAM site with the shear zone, and hydraulic connection resulting from the storativities analysis (Meier et al 1998)

Constant rate injection tests were previously interpreted (Appendix 5) by means of Jacob's semi-logarithmic approximation (Cooper and Jacob 1946), obtaining a previous estimate of both transmissivity and storativity of the fracture. The relative abundance of observation wells has allowed identifying preferential connections (Fig. 2.4) between boreholes using the methodology presented by Meier et al (1998). As in the case of the pulse tests the obtained results are presented and discussed in chapter 3.

A further analysis of the crosshole hydraulic tests shows many effects which can be interpreted as strong spatial variability of transmissivities. The representation of (s/q) vs. (t/r^2), where s[L] is the measured drawdown, q[L^3T^{-1}] is the injection flow rate, r[L] is the distance between the injection and the observation boreholes and t[T] is the time, shows a line for each one of the observation boreholes (Figure 5). That means that the fracture is rather heterogeneous, because if the fracture was homogeneous the same line must be obtained for all the observation boreholes. The complex structure of the fracture creates the need for a more complex interpretation model of the hydraulic test that might account for the space variability of the parameters.

In chapter 3 more detailed data regarding hydraulic testing activities is provided, as well as the joint interpretation of the RI tests by means of geostatistical inversion, taking into account different hypothesis about the correlation structure of transmissivity.

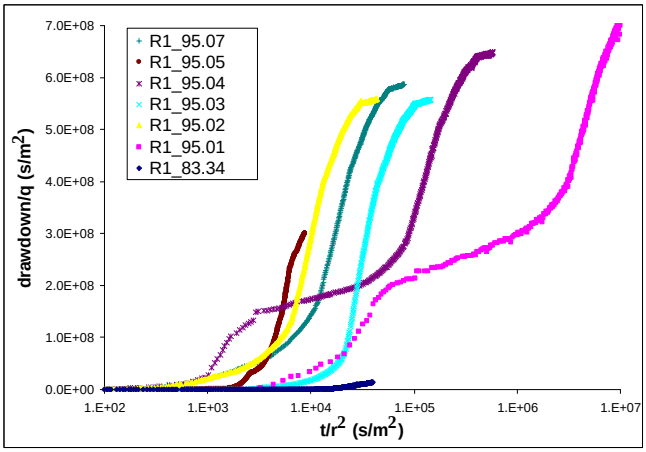

Figure 2.5: Normalized drawdown vs. normalized time observed in every one of the observation boreholes used during the first constant rate injection test (RI1) performed in the GAM fracture. The drawdown is normalized by the flow rate, and the time by the square of the distance between the injection and the observation borehole.

2.2.3.2 Solute tracer test campaigns

As a part of the hydraulic characterisation of the GAM shearzone, five tracer test have been performed using a dipole configuration (Kennedy 1999a, Kennedy 1999b, Kennedy 1999c, Kennedy & Kleiner 2000), changing dipole configuration (i.e. injection and extraction boreholes), injection and extraction flow rates, and also changing the injected tracers from one tracer test to the next one.

The spatial variability of the fracture properties is investigated by considering different dipole locations within the GAM fracture and by using particle tracers in combination with solute tracers in the same test. The purpose of using particle and solute is to obtain complementary information on the pore space and investigate the medium in term of a multi-porosity structure. Due to their finite size, colloids are excluded from the smallest porosity and are mainly transported in the main flow channels, showing no diffusion into matrix or stagnant pores. In contrast, solute tracers are transported by advection-dispersion processes, exploring the entire system of connected porosity. The following tracers were used in the different tests:

- Non-sorbing solute tracers (Uranine, Napthionate, Sulphurhodamine)
- Fluorescent latex microsperes (diameter 1 μm)
- Nanospheres (diameter 1 nm)
- Biocolloids consisting in different bacteriophages (H40, MS2, H6) with a size ranging from 20 to 350 nm.

A brief summary of the successful test configurations is give in Table 2.2. In chapter 3 more detailed data regarding tracer test is provided as well as different tracer transport models, which included a-priori information on the transmissivity field inferred from geostatistical inversion of hydraulic tests.

Table 2.2: Summary of test configurations

		PT1	PT2	PT3	PT4	PT5
Tracers	Solutes	Uranine	Napthionate	Sulphur-hodamine	Uranine	Uranine
	Colloids	microsphere, nanosphere.	-	-	-	-
	Bacteriophages	H40	MS2	H6	-	-
Injection Borehole		GAM98.002	TPF95.001	TPF95.001	TPF95.004	TPF95.007
Extraction Borehole		GAM98.004	GAM98.002	GAM98.004	GAM98.004	GAM98.002
Inter-well distance [m]		1.2	1.7	1.2	1.1	1.9
Injection rate [ml/min]		1	1.5	1.6	1.5	1.5
Extraction rate [ml/min]		1	1.6	1.6	1.6	1.6
Injection time [h]		20	30	17.5	4	4
Date		09/04/1999 to 05/05/1999	04/05/1999 to 27/05/1999	05/08/1999 to 19/08/1999	19/08/1999 to 26/08/1999	03/09/1999 to 09/09/1999

2.2.3.3 Radar measurements.

Within the framework of the GAM experiment, two high resolution measurements with borehole radar have been performed to visualize gas and brine flow in the GAM shear zone: The first one was conducted in the period between November 16th and 19th , 2000, and the second one between February 1st and 4th, 2001. Brine and gas respectively were injected in the fracture in a radially diverging flow field (Alber,W., 2000a,b,c). Radar measurements were carried out in the geophysical boreholes and also along the tunnel wall (Fig. 2.6)

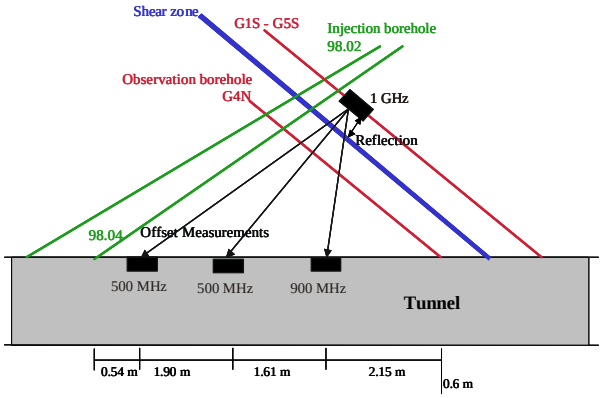

Figure 2.6: Sketch of measurement area

The obtained results present a complex diffraction image which is stable whit time (upper left square in Fig. 2.7). The diffraction is generated by metal objects (packers, tubing, etc) in the boreholes. In both cases (brine and gas injection tests) the shear zone itself is barely visible in the radiograms. In Figure 6 the difference in the reflectograms is shown after 1hour, 5 hours and 22 hours of gas injection (lower left square, upper right square and lower right square respectively in Fig. 2.7). After 5 hours significant changes in the reflectograms could be seen, and after 22 hours the flow field seemed to stabilise. The gas distribution agreed with the results of the hydraulic tests which suggested these were the most likely flow paths in the shear zone. This technique allows the visualisation of the gas flow path.

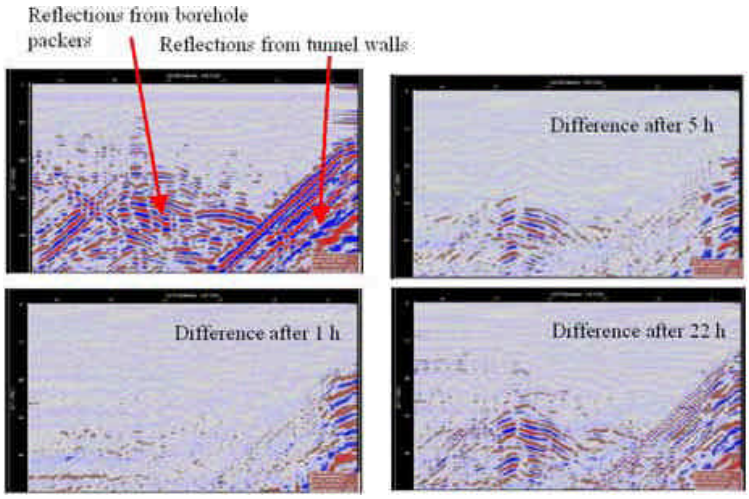

Figure 2.7: Reflection radargrams obtained after 1, 5 and 22 hours of gas injection

The execution of this test should not suppose any variation in the internal structure of the fracture. Nevertheless, the execution of the hydraulic test (gas or brine injection test, necessary to establish the radially diverging flow which are interested in visualize) have changed the internal fracture structure.

Some anomalies have been detected in the hydraulic response of several boreholes from the hydraulic tests performed after the first brine injection test. These anomalies persist and became grater after the second radar measurement campaign, where gas was the injected fluid to generate the diverging flow field. Looking at the Figure 8 we find the representation of s/q vs. t/r^2, where s[L] is the measured drawdown, q[L^3T^{-1}] is the injection flow rate, r[L] is the distance between the injection and the observation boreholes and t[T] is the time at every well for two different hydraulic tests: The first performed in November 1998 and the second one in August 2000. Both injection tests were performed at the some pumping well (borehole GAM98.004). It can be shown that the response at the same well is different when it should be exactly the same (the same could be said for the hydraulic tests performed in November 1998 and January 2000 in pumping borehole GAM98.004). Those differences are due to some heterogeneity changes in the medium, and depending on the selected hydraulic test the hydraulic connectivity structure changes. Maybe the fracture structure changes are due to pressure release, washing-out caused by an increasing water flow during brine injection, or the existence of a high hydraulic gradient during testing.

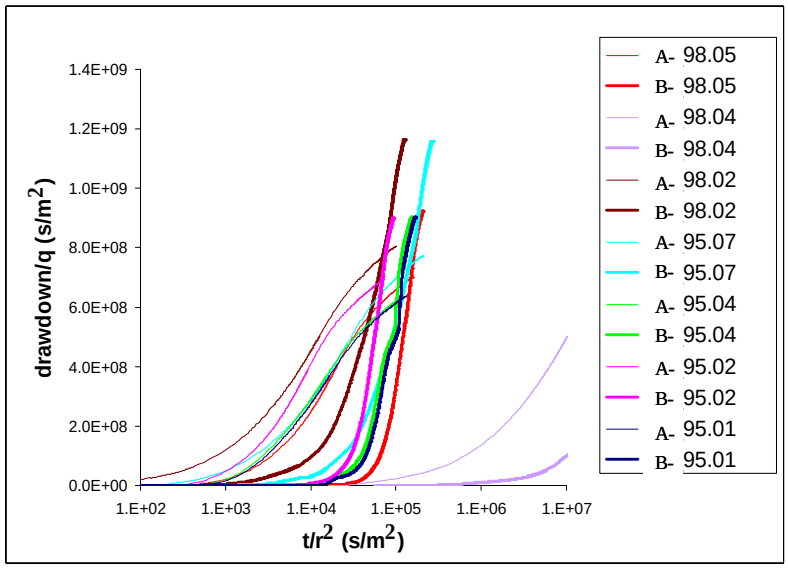

Figure 2.8: Normalised drawdown vs. normalised time observed at every well simultaneously for the two hydraulic tests performed in borehole GAM98.004 during Nov.1998 (A Series, thin lines) and Aug.2000 (B series, bold lines). The drawdown is normalised by the flow rate, and the time by the square of the distance between the injection and the observation borehole. The hydraulic response in each well should be the same for the two hydraulic tests. The increase in the slope of the hydraulic responses in the observation wells in during Aug.2000 shows a decrease in the effective transmissivity of the fracture.

2.2.3.4 Gas threshold injection testing

The objective of these tests is twofold: to determine the pressure that the gas requires to enter the formation and start displacing water and to obtain a better characterisation of the multiphase flow problem in terms of the constitutive laws.

The gas threshold pressure tests (GTPT) was designed as a constant rate gas injection test. Before the gas injection, the test interval water is replaced by nitrogen gas. This is accomplished by injecting gas through the pressure line and extracting the water through the flow line located in he innermost point in the interval. Then N_2 is injected at a constant rate, and the gas pressure in the injection interval increases until the gas threshold pressure is achieved, and gas begins to flow through the fracture.

Three GTPT have been conducted preceding every one of the three gas tracer tests campaigns performed in the GAM fracture (Fierz et al. 2000, Trick et al. 2000, Trick et al. 2001). Actually the GTPT correspond to the first step to achieve in the gas tracer test methodology, that is, once the N_2 has penetrated in the fracture, the gas injection into the injection borehole continues until a stable gas flow field is established.

In general, while the gas is being injected in the fracture, boreholes which intersect the fracture present clearly 3 behaviours (Fig. 2.8):

- Wells with an instantaneous gas injection response what implies a perfect connection between wells (98.002, 98.004 and 95.007).

- Wells that respond slightly later, which are, therefore, not that well connected as the previous ones (95.001, 95.004, 98.005, 95.002, 98.008)

- Wells that have very little connection or that are not connected at all because the response is negligible (83.034, 87.003, 95.005, 98.003, 98.006, 98.007).

Looking at figure 9 and taking account the geometric borehole distribution (Fig. 2.4) one question arises regarding observation borehole instantaneous responses: how can two wells that are separated 1m from the injection well react at the same time? The only explanation is that there is a highly transmissivity zone with a very small gas entry pressure, so that when there is the exchange of N_2 in the injection well the gas also reaches these boreholes. This confirms the existence of channels where the entry pressure in them must be very close to zero.

There are other effects that need to be considered, such as the degassing phenomenon: Groundwater degassing may contribute to the development of a local, unsaturated zone around the borehole, which may affect the outcome of hydrotests. Water pressure around the observation wells was in some of the cases considerably above atmospheric pressure preventing degassing. The interpretation of these tests is highly complex. For a better understanding of the multiphase flow tests, a sensitivity analysis has been done in chapter 4.

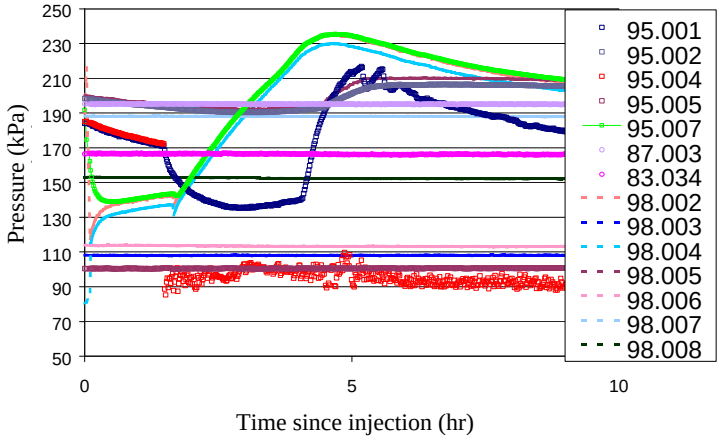

Figure 2.9: Pressures recorded in all the boreholes during the GTPT-2 conducted in of Aug. 2000.

2.2.3.5 Gas tracer testing

The objective of these tests is two-fold. On one hand, to shed light on transport processes in the gas phase. On the other hand, they should help on understanding gas-liquid interaction. Specifically, these gas tracers dissolve in the water and diffuse away from the liquid-gas interface. Hopefully, because of differences in solubility and diffusivity, each gas tracer behaves differently, leading to chromatographic effects (different breakthrough for each tracer).

The information we can capture from GTT is the water available along the trajectory of the gas tracer. Retardation factor give you an idea about the volume of water available for the gas to be diffused in it.

Three gas tracer testing campaigns have been carried out in the GAM shear zone (Fierz et al. 2000, Trick et al. 2000, Trick et al. 2001), performing several gas tracer injection tests (dipole configuration), using different gas tracers and different flow fields.

From the experimental viewpoint the gas tracer tests set-up was a success except for the short tracer gas detection. Almost all the tracers used (He, Ne, Xe…) showed very similar breakthrough curves. No clear effect regarding retardation effects caused by different solubility of the tracer gases could be observed. In chapter 5 a sensitivity analysis is presented, in terms of the phenomenological coefficients that come into play on processes affecting gas dissolution/diffusion in shear zones.

In chapter 6 more detailed data regarding gas tracer test is provided as well as the results obtained by the gas transport fracture model, developed to simulate the gas migration through a partially saturated heterogeneous fracture.

2.3.Laboratory investigations

The laboratory experiments were performed to determine two-phase flow properties of shear zone materials from the same zone in which the gas tracer test were been run in the field. The objectives of these experiments were to determine two-phase flow properties as well as quantitative characterization of pore geometry of the same shear zone materials. For those reasons two cores, both cored parallel to the shear zone were recovered. In these cores were conducted the laboratory investigations (Brodsky et al., 2000).

Two measurement systems were used to conduct the flow measurements. The Overburden Permeameter-Porosimeter (OPP), used to measure gas permeability and porosity, and the Automated Two-Phase Flow device (ATPF) designed to perform steady state liquid and gas permeability measurements, transient relative permeability measurements and capillary pressure-saturation tests in cores.

The obtained results are presented in terms of porosity, gas permeabilities, liquid permeabilities, relative permeability and capillary pressure

2.3.1 Porosity

Porosity is determined using the gas expansion technique. After the specimen is placed in the OPP, the confining pressure is applied, and a pore pressure is established in the specimen and the associated test system (the volume of tubing and valves adjacent to the core). Once equilibrium of the pore pressure is achieved, the core is exposed to a reservoir of a known volume. The system pressure adjusts (decreases) as gas moves into the additional volume of the reservoir. The test is terminated once the pressure stabilizes at its final value. Knowing the volume of the reservoir and the test system, the pore volume can be calculated from the measured pressure change. The volume of the test system is determined by means of a calibration test that utilizes a solid machined steel cylinder in place of a specimen. The calibration is then verified over the operating range by testing steel cylinders with central holes of known dimensions in place of a rock core.

The porosity is determined from the measured pore volume and core volume as:

$$f = \frac{V_p}{V_i} \tag{2.1}$$

where f[-] id the porosity, and V_p[L^3] and V_i[L^3] are the pore volume and initial total specimen volume, respectively. The OPP has the capability to measure porosities in the range of 0.1% to 30%

The measured or bulk porosity of the core consist of the porosity of the shear zone and the porosity of matrix material. The measured porosity can be corrected to yield the the shear zone porosity by subtracting the matrix material contribution, that is:

$$f_s=(f_s-(1-c)f_s)/c \tag{2.2}$$

Where f[-] is the porosity, and the subscripts s, m and b refer to the shear zone, matrix and bulk material respectively. c[-] is the fraction of the core that consists of shear zone material.

The shear zone porosity calculated from Equation 2.2 is given in Fig. 2.10 as a function of effective confining pressure. The shear zone fraction was estimated from visual observations as 20%. The matrix porosity was adjusted for confining pressure using the straight line fit to the matrix porosity data. All but one of the calculated shear zone porosity values is in the range of 2 to 3%. The single exception was a value of about 1% obtained at a ~14 MPa confining pressure.

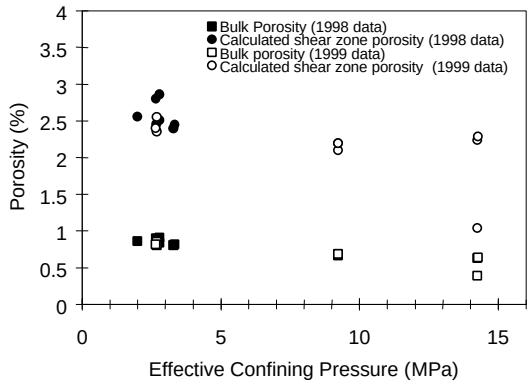

Figure 2.10: Measured bulk porosity and calculated shear zone porosity as a function of effective confining pressure

2.3.2 Gas permeability

Gas permeability measurements were made in the OPP device using the pressure decay technique. For these measurements, the OPP is configured such that there is an upstream and a downstream reservoir. The upstream reservoir is relatively large compared to the pore volume and test system volume, and is referred to as an infinite volume reservoir. The downstream volume is much smaller, and can be switched between different known volumes to adjust the resolution of the OPP from about 10^{-15} m^2 to 10^{-21} m^2

A confining pressure is first applied to the core, followed by the establishment of the desired pore pressure in the core and the test system. The infinite reservoir is then isolated from the core, and its pressure is increased by a specified amount to produce a pressure pulse. Once the increased pressure equilibrates in the infinite reservoir, the pulse is exposed to the core. Gas flows through the core and into the downstream reservoir. The pressure difference across the core is monitored as it decays with time. The rate of decay is dependent on the rock permeability as well as test system parameters such as the downstream reservoir volume. The permeabilities given below were interpreted using the method of Bourbie and Walis (1982). This technique is more applicable to rocks with low permeabilities than the exponential solution of Brace et al. (1968).

Gas permeability measurements in low permeability media can be affected, by the Klinkenberg or molecular slip phenomenon, due to interaction between. the gas molecules and the flow path wall. Because of this effect, the measured gas permeability is greater than the intrinsic permeability by an amount inversely proportional to the pore pressure. By conducting tests at different pore pressures, a correction for this effect can be developed If the measured permeabilities are plotted as a function of inverse pore pressure then the intercept of the straight line fit through the data at infinite pressure corresponds to the intrinsic gas permeability

The gas permeabilities were obtained from a number of tests conducted at constant effective stress but variable pore pressure in order to derive the Klinkenberg-corrected permeability. These data were also corrected for the effective area of the shear zone in a manner similar to that used to calculate the shear zone porosity. Because the matrix permeability is more than two orders of magnitude lower than that measured, the effective shear zone permeability $k_s[L^2]$ can be calculated from the interpreted Klinkenberg permeability $k[L^2]$ as

$$k_s = k/c \tag{2.3}$$

Results from these tests are summarized in Fig. 2.11. The measurements conducted at the same effective confining pressure indicate that the gas permeability ranged from $2 \cdot 10^{-15}$ to $3 \cdot 10^{-15}$ m^2 during the August, 1998 tests, but was only $5 \cdot 10^{-16}$ m^2 during the July, 1999 tests. The data obtained during July, 1999 indicates a decrease from about $5 \cdot 10^{-16}$ to $2 \cdot 10^{-16}$ m^2 as the effective confining pressure was increased from about 2 to 14 MPa.

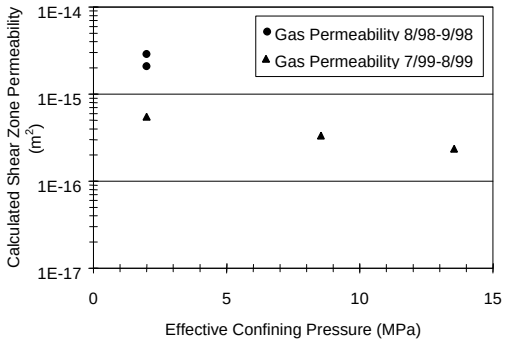

Figure 2.11: Shear zone gas permeability as a function of effective confining pressure.

2.3.3 Liquid Permeability

After the core is placed in the ATPF and a confining pressure applied, the test system and the core are both vacuum-saturated with the liquid of choice (the liquid used was produced by dissolving ground Grimsel core in distilled water. Ground rock was recovered during specimen coring and placed in a large flask of distilled water at room temperature. The flask was placed on an automatic stirring device for several days. The liquid was then poured through a 0.45 μm filter so that only clear liquid remained. This

clear liquid was used as the permeant). The desired pore pressure is then established by means of a pair of precision pumps. These pumps are used to increase the pressure on the top of the core, while the downstream pressure is maintained with a regulator. At least one pore volume of liquid is forced through the core prior to initiating the permeability test to promote full saturation of the core. The flow rate of liquid is measured with the pumps, and is used to interpret permeability once it achieves a constant rate. The ATPF is designed to measure steady-state liquid permeability in the range of 10^{-15} m^2 to 10^{-21} m^2.

The measured liquid permeabilities were corrected to yield an estimate of the shear zone permeability. Results are summarized in Fig. 2.12. Tests conducted at the same effective confining pressure indicate that the liquid permeabilities decreased almost an order of magnitude from nearly 10^{-15} to 10^{-16} m^2 from September to November. It is possible that the liquid permeant caused swelling of any clay minerals and thereby decreased permeability, or that fine particles of rock in the permeant (<0.45 μm) blocked flow through the finer pore structures. The data suggest a possible moderate decrease in permeability with an increase in effective confining pressure.

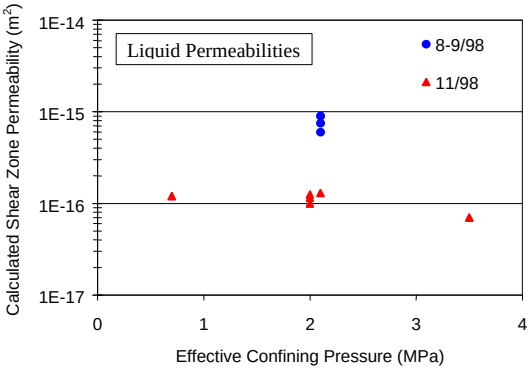

Figure 2.12: Calculated shear zone liquid permeability as a function of effective confining pressure (Brodsky et al, 2000).

2.3.4 Relative permeability.

Relative permeability measurements were conducted in the ATPF device using an unsteady-state technique. The test begins with the core subjected to a confining pressure and saturated with liquid at the desired pore pressure. Gas is then introduced to the top of the core at a pressure greater than the pore pressure. The gas displaces liquid from the core, eventually leading to breakthrough of gas through the core (that is, continuous gas flow through the core). The displaced fluid from the bottom of the core is separated into its liquid and gas fraction by means of a gravimetric separator. The liquid displaced from the core is weighed, and the amount of gas produced is measured by venting it into reservoirs and monitoring the pressure build-up. For relative permeability tests, the ATPF is configured so that the pressure in the line downstream of the core will increase as fluid moves through the core and into this line until the gas breaks through the core and activates a pressure relief regulator. Thus, the pressure difference across the core can decrease during the conduct of the test until gas production is observed. The test is terminated after the ratio of gas flow to liquid flow reaches a pre-determined level.

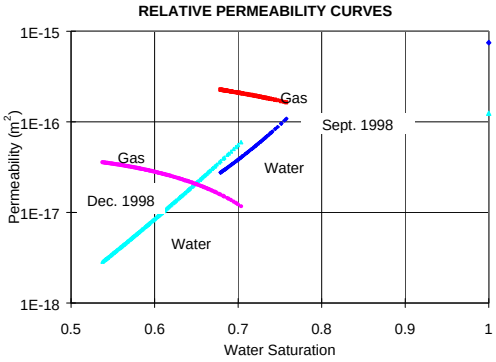

Figure 2.13: Unsaturated Permeability as a function of water saturation (Brodsky et al, 2000).

Test data are interpreted in terms of relative permeability using the method of Jones and Roszelle (1978). It was assumed that the gas movement was principally through the shear zone; consequently, the intrinsic permeability assumed for the data reduction method was that calculated for the shear zone. Consistent with the observed changes in permeability over time (see Fig. 2.13), the intrinsic permeability was assumed to be 7.5×10^{-16} m^2 and 1.3×10^{-16} m^2 for the first and second data sets, respectively.

2.3.5 Capillary pressure-saturation

Capillary pressure-saturation tests are conducted in the ATPF. A confining pressure is applied to the core, and liquid is circulated through the core to ensure that it is saturated. Gas is introduced at the top of the core under a pressure greater than the pore pressure. The difference in gas and liquid pressures is the capillary pressure. Under a sufficient capillary pressure, the gas will displace water. A porous ceramic membrane, saturated with liquid, is located at the base of the core. The membrane will remain saturated with liquid (in this case water containing dissolved solids as described in 3.3) until a characteristic threshold capillary pressure is reached. Liquid that is displaced from the core is collected and weighed, permitting the saturation to be calculated. The capillary pressure-saturation tests are conducted by progressively increasing the capillary pressure and de-saturating the specimen. The maximum capillary pressure that can be imposed is equivalent to the threshold pressure of the membrane, which was specified as 1.5 MPa for these tests.

The data from the two tests, shown in Fig. 2.14, are comparable until a saturation of about 0.8 is reached. The data from the first test (CP3) indicate that the water saturation does not decrease much below 0.8, whereas for the second test (CP4), the saturations are much lower at comparable capillary pressures.

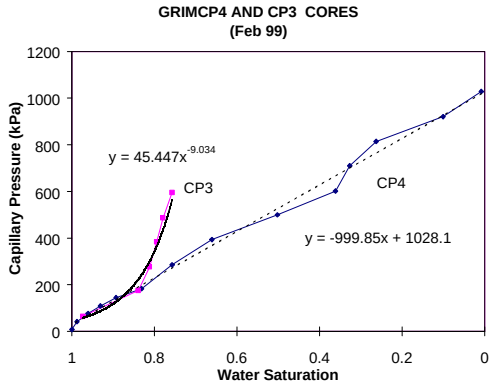

Figure 2.14: Capillary pressure-saturation test results

2.3.6 Core Imaging

Two types of core imaging techniques were applied to these cores. (1) Laser confocal microscopy provided high resolution images of the pore structure within the shear zone and also within the matrix material.(2) X-ray imaging provided lower resolution information and was primarily implemented to assess the viability of application of technique to the GAM shear zone.

2.3.6.1 Laser Scanning Confocal Microscopy

Laser scanning confocal microscopy (LSCM) is illustrated schematically in Fig. 2.15. As noted by Fredrich et al. (1995), the technique has been used extensively in the biological sciences and has had more limited applications to nonbiological (solid) materials (Kobayashi and Shockey, 1991.) The distinguishing feature of LSCM is that both illumination and detection are confined to a single location on the specimen at anyone time. Resolutions in the x-y plane of 200 nm and in the z direction of <0.1 μm can be obtained. 3D imaging is obtained by scanning at successively increasing focal depths and U using commercially available image analysis software to reconstruct the image.

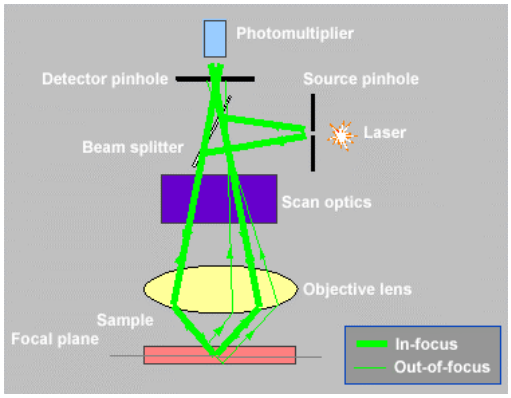

Figure 2.15: Schematic representation of Laser Scanning Confocal Microscopy setup

Fig. 2.16 is an image of the pore structure within the macroscopic shear zone. Bright areas indicate fluorescence and therefore represent pore spaces filled with doped epoxy. Dark areas represent the absence of fluorescence and therefore represent the intact rock mass. Sharp transitions between the rock and pore space are noted as is a preferred microcrack orientation. Fig. 2.17 is a 3-dimensional reconstruction of the void volume within a section of the macroscopic shear zone viewed from below. The heterogeneous pore size distribution is evident. The shear zone is highly complex, and much of the porosity is contained in an extremely fine microcrack structure at the micron to sub-micron scale, with preferred orientation. The heterogeneity of the shear zone is localized in regions of intense microcracking and interconnected porosity existing outside of the shear zone with sporadic distribution.

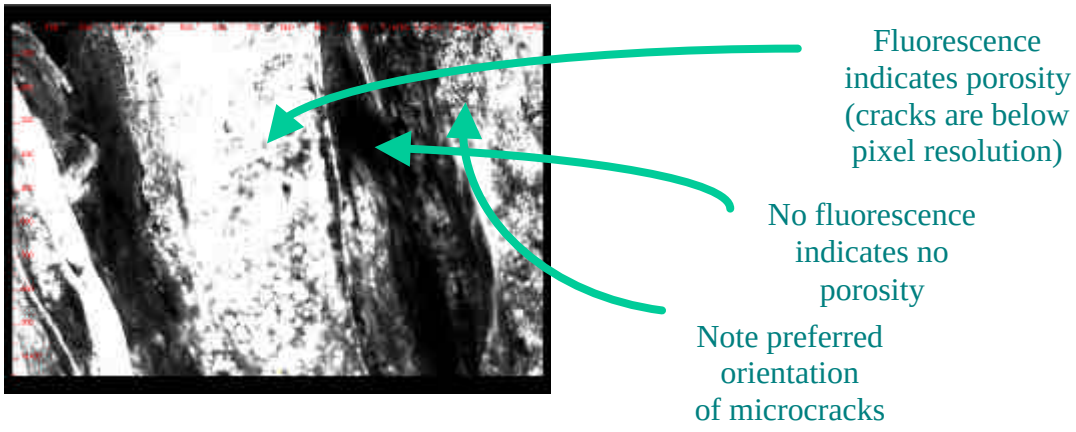

Figure 2.16: Low magnification view of region within several mm-wide macroscopic shear zone. 768 x 512 pixels with 2.055 micron pixel size; 1.578 x 1.052 mm.

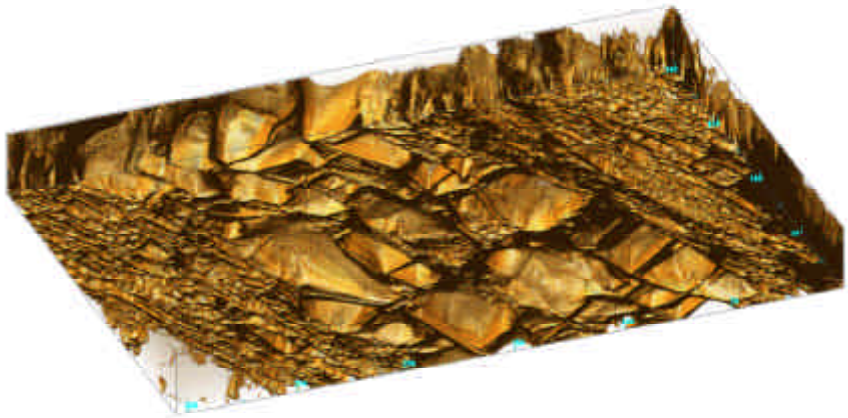

Figure 2.17: Three-dimensional rendering of void space in the shear zone Higher magnification view of region within macroscopic shear zone illustrating bimodal porosity distribution within shear zone. 76 optical sections; 768 x 512 x 76 with 0.40 micron cubic voxels; 305 x 204 x 30 micron.

2.3.6.2 X-Ray Imaging

A 9-mm diameter subcore that intersected the shear zone was taken from Core #1. The subcore was fragile and fell apart during coring. It was taped together and imaged using X-ray techniques at Argonne National Laboratories. A resulting photograph is shown in Fig. 2.18. The dark areas are the larger voids within the shear zone. This technique was used to create a sequence of images parallel to the plane.

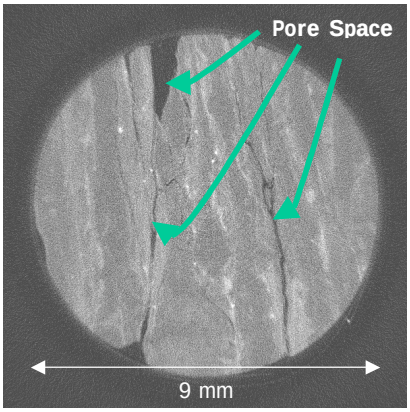

Figure 2.18: X-ray image of shear zone, looking down axis of 9 mm

2.4.Conclusions

The overall aim of the GAM project was to understand and analyse the transport of water and gas in a complex shear zone.

The design of the experimental activities to be performed in the framework of the GAM project was very complete and ambitious. The experimental research was split between in-situ field tests carried out at the GTS and tests carried out in a laboratory environment:

- The insitu field phase included a series of hydraulic crosshole tests to characterise the water flow through the shear zone. Also a series of dipole tracer tests were carried out using different tracers: Solute tracers (non-reactive tracers e.g. fluorescent dyes), Particle tracers (microspheres / nanospheres and pharges) and Gas tracers (helium, xenon, argon and SF6).

  A series of Radar Reflection surveys were also carried out during gas injection tests.

- The laboratory tests were focused on three main issues: Development of new coring techniques to recover undisturbed shear zone samples as a previous step to obtain shear zone cores where perform the laboratory experiments. Porosity, permeability (gas/liquid and relative) and capillary pressure measurements, and finally the visualisation and structural analysis of pore spaces in a shear zone sample

Through a preliminary analysis of all the collected data from the field and laboratory experiments a previous conclusion about the GAM fracture is obtained: The shear zone is rather heterogeneous. In terms of transmissivity it seems there are preferential connections between boreholes. In terms of pore structure the shear zone is highly complex, and much of the porosity is contained in an extremely fine microcrack structure.

The complex structure of the fracture create the need for a more complex interpretation model of the hydraulic and tracer (solutes, particle and gas) tests that might account for the space variability of the parameters.

The integration of all the obtained experimental data forms the basis of the modelling studies presented in the following chapters.

2.5.References

Alber, W. (2000a): Radar measurements at the GAM experiment site. NAGRA Internal Report 99-283, Wettingen, Switzerland.

Alber, W. (2000b): Radar measurements at the GAM experiment site during a brine injection test. NAGRA Internal Report 00-92, Wettingen, Switzerland.

Alber, W. (2000c): Radar measurements at the GAM experiment site during a gas injection experiment (GT1). NAGRA Internal Report 00-93, Wettingen, Switzerland.

Brodsky, N., Stormont, J., Fredrich, J. (2000): Laboratory measurements of porosity, gas threshold pressures, and gas, liquid, and relative permeabilities for shear zone material from the Grimsel Test Site, Switzerland. NAGRA Internal Report 00-15, Wettingen, Switzerland.

Bourbie, T., and J.D.Walls, (1982): Pulse Decay Permeability: Analytical Solution and Experimental Test, Society of Petroleum Engineers of AIME Journal, October, pp 719-721.

Brace, W.F., J.B. Walsh, and W.T. Frangos, (1968): Permeability of Granite under High Pressure. Journal of Geophysical Research, Vol. 73, Number. 6, pp. 2225-2236.

Cooper, H., Jacob, C., (1946): A generalized graphical method for evaluating formation constants and summarizing well-field history. AGU, 27(4), 526-534.

Cooper, H.H. J.D. & Papadopulos, S. (1967): Response of a finite diameter Well to an Instantaneous Charge of Water. Water Resources Research, Vol. 27, Number 4, pp. 526-534.

Fierz, T., E. Proust., M. Combarieu and P. Meier, (2000): Gas tracer test series GT1 in the GAM shear zone (February 2000). Dipole flow field GAM98-002/TPF95-007. NAGRA Internal Report 99-30, Wettingen, Switzerland.

Fredrich, J.T., B. Menendez, and T.F. Wong, (1995): Imaging the pore structure of geomaterials, Science, Vol. 268, pp. 276-279.

Gemperle, R., & SOLEXPERTS AG, (1999a). Hydraulic testing in GAM 98.002 and GAM 98.004. NAGRA Internal Report 99-03, Wettingen, Switzerland.

Gemperle, R., & SOLEXPERTS AG, (1999b): Final Borehole completion report. NAGRA Internal Report 99-02, Wettingen, Switzerland.

Jones, S.C. and W.O. Roszelle, (1978), Graphical Techniques for Determining Relative Permeability from Displacement Experiments. Journal of Petroleum Technology, Vol. 30, Number 5, pp. 807-817.

Kennedy, K., (2000a): Solute and particle tracer tests PILOT and PT1 in the GAM shear zone (Dec, 1998 to April, 1999). NAGRA Internal Report NTB 99-49, Wettingen, Switzerland.

Kennedy, K., (2000b): Solute and particle tracer test PT2 in the GAM shear zone (May 1999). NAGRA Internal Report NTB 00-07, Wettingen, Switzerland.

Kennedy, K., (2000c): Solute and particle tracer test PT3 in the GAM shear zone (August 1999). NAGRA Internal Report NTB 00-08, Wettingen, Switzerland.

Kennedy, K., Keiner, A.,(2000): Tracer tests PT4 and PT5 in the GAM shear zone (August, September 1999). NAGRA Internal Report NTB 00-41, Wettingen, Switzerland.

Keusen, H.R., Ganguin; J., Schuler, P., Buletti, M., (1989): Grimsel Test Site Geology. Technical Report 87-14E.February 1989. NAGRA, CEDRA, CISRA. GEOTEST, Zollikofen/Bern.

Kobayashi, T. and D.A. SHOCKEY. (1991): Adv. Mater. Proc. Vol. 140, 28 (November, 1991) and 24 (December 1991): Trans. Soc. Prof. Well Log Anal., Thirty-third Annual Logging Symp. Paper Number. 9926, Oklahoma City, OK, 14 to 17 June 1992 (Soc. Prof. Well Log. Anal., Houston, TX, 1992.)

Marschall, P., Albert, W., Carbonell, R., Carrera, J., Davies, P.B., Kinzelbach, W., Mayor, J.C., Nieheren, S., (1998): Investigation programme for the GYS PhaseV experiment “gas migration in shear zones”(1998-2000). NAGRA Internal Report NTB 98-12, Wettingen, Switzerland.

MEIER, P. M., CARRERA, J., SANCHEZ-VILA, X., (1998): An evaluation of Jacob's method for the interpretation of pumping tests in heterogeneous formations. Water Resources Research, Vol. 34, Number 5, pp 1011-1025.

Pardillo, J., Campos,R., and J.GUIMERÀ (1997):” Geological characterisation of the Febex experiment”, Febex project, Work Package 2 report.

PERSOFF AND PRUESS, K., (1995): Two-phase flow visualization and relative permeability measurement in natural rough-walled fractures. Water Resources Research, Vol. 31, Number 5, pp 1175-1186.

Trick, T., T. Fierz, E. Proust, P. Meier and M. Combarieu, (2001): Gas tracer test series GT2 in the GAM shear zone (August 2000). Dipole flow field GAM98-004/TPF95-004. NAGRA Internal Report 00-49, Wettingen, Switzerland, 2000.

Trick, T., M. Piedevache, E. Proust, P. Meier and M. Combarieu, (2001): Gas tracer test series GT3 in the GAM shear zone (December 2000). Dipole flow field GAM98-002/TPF95-007. NAGRA Internal Report 01-02, Wettingen, Switzerland.

WYSS, E., (1996): Site preparation, borehole installation, hydraulic characterization and gas threshold pressure test at the Grimsel Test Site. NAGRA Internal Report 96-34, Wettingen, Switzerland.

Chapter 3: Flow and solute tracer transport modelling in a heterogeneous fracture.

3.1. Introduction

A hydraulic characterisation of the fracture is needed before any attempt to quantitative description of gas transport through single fractures. In order to characterise fracture heterogeneities, several tests campaigns have been performed in a granite fracture, at the Grimsel rock laboratory in Switzerland, in the framework of the GAM project, including hydraulic (pulse and cross-hole) and tracer (dipole configuration) tests (Wyss 1996, Gemperle 1999a, Fierz and Piedevache 2000, Fierz et al. 2000, Trick 2000, Trick et al. 2000, Trick et al. 2001). One of the objectives of this chapter is to present the hydraulic and tracer tests activities performed in the framework of the GAM project as a first step in the fracture characterisation.

Heterogeneity is a fundamental characteristic of nature, present in most of the variables characteristics of natural phenomena. It is known that heterogeneity of hydraulic conductivity and porosity have a large impact on solute or gas transport. Meier et al. (1998) demonstrated that transmissivity estimates, obtained through the interpretation of cross-hole pressure test responses, using Jacob's method (Cooper and Jacob, 1946) are very close to the effective value of the transmissivity of heterogeneous formations for parallel flow conditions, whereas the storativity estimates are strongly influenced by the heterogeneity. However conventional interpretation of cross-hole tests do not provide quantitative information of the spatial distribution of the transmissivity (i.e. heterogeneity), which is required for the interpretation of tracer tests, because solute transport is more influenced by heterogeneity than flow.

Heterogeneity of the transmissivity field has a large impact when modelling flow and transport. Heterogeneity has led naturally to geostatistical inversion methods, in which some parameters (usually the log-transmissivity) are viewed as regionalized variables. A number of approaches to this estimation problem have been developed. A critical review and assessment of various techniques from the perspective of functional analysis is given by McLaughlin and Townley (1996). However, the major attempt to compare different geostatistically based inverse estimation approaches is given by Zimmerman et al. (1998). These two papers as well as other review articles (Carrera et al, 2005), provide general background and highlight the strengths and weaknesses of different inverse approaches to the problem of estimating spatially variable property fields.

Geostatistical inversion methods can be classified in two groups, which are commonly named as estimation and simulation inversions. The first group seeks an optimum identification of the regionalized variables (i.e. conditional expectation, minimum estimation error or similar) given all available information. In this case the estimated transmissivity field is a smooth function of space (as a result of being an expected value) that coincides with point transmissivity measurements where available, and leads to accurate simulation of available head measurements (Carrera and Neuman 1986c, RamaRao et al., 1995, Zimmerman et al., 1995 and Yeh et al., 1996 among others).

Simulation inversion is much more recent. The standard approach is the one described by Gómez-Hernández et al. (1997) and by Capilla et al. (1997). The outcome of the method is a set of equally likely simulations of Log-Transmissivity fields conditioned

on direct measurements of Log-Transmissivity and heads. Despite simulation and estimation inversions are very similar, both are computationally demanding and both require a proper estimation of the statistical properties of the input fields. The main differences rely on the ability to accommodate unusual statistical assumptions (Medina and Carrera, 2003).

There we use a geostatistical inversion procedure that is based on the expected value of the likelihood (Medina and Carrera, 2003), to estimate the most suitable transmissivity field at the scale of the tracer tests performed in the framework of the GAM project. This method allows us to use the full-time length of pumping tests drawdown data (at several observation boreholes) to estimate the transmissivity at a large number of zones.

Conventional tracer tests analysis methods do not account for the heterogeneity of transmissivity and flow porosity. This can result in anomalies of transport parameters derived from breakthrough curve analysis and can lead to inconsistencies between field observations and model predictions (Carrera, 1993). In this work the estimated transmissivity field is the basis for the analysis of the five tracer tests conducted in the so called GAM fracture. Three conceptual models for the variability of porosity and their relevance for the estimation of matrix diffusion parameters are studied. The other objective of this work is to take into account the heterogeneity of transmissivity in the analysis of tracer tests performed in the framework of the GAM project, reproducing the measured solute breakthrough curves and obtaining a representative transport parameter set for the fracture at the experiment scale.

3.2. Description of the experiment

3.2.1 Site characterisation

The GTS (Grimsel Test Site) is a rock laboratory which consists of a series of galleries lying 450m below surface within granitic rock. The GAM shear zone is located in the southern part of the GTS. In this area, all the detected shear zones exhibit similar structure. The fractures dip steeply and the dominant strike is EN-SW. Macroscopically, the shear zones are characterised by zones of ductile deformation with high damage intensity and mica-rich mylonite bands, and brittle fault breccia horizons with a thickness ranging from a few millimetres to several centimetres, located at the zones of the highest ductile deformation. These zones contain fine-grained, non-cohesive gauge material.

The heterogeneous pore size distribution is evident. The shear zone pore size distribution is highly complex, and much of the porosity is contained in an extremely fine microcrack structure at the micron to sub-micron scale, with preferred orientation.

Porosity of the fault gauge horizons is estimated in the range from 0.1 to 0.3, although it has never been measured at the laboratory. Bossart & Mazureck (1991) identified four types of pore spaces on a micro-scaling:

- Grain boundary porosity (connected web-like pore space system along the grain boundaries of the minerals).
- Mica porosity (pore space parallel to the orientation of the cleavage plane of sheet silicates).
- Transgranular pores (microfractures and fissures).

- Solution pores (pores with a finely branching cavities extending from both sides of the pore channel into the mineral grain).

Recent studies (Marshall and Croisé, 1999) showed that the aperture distribution across the brittle structures is typically described by a log-normal distribution with mean values of about 0.2-0.5 mm and a cumulative thickness in the cm range.

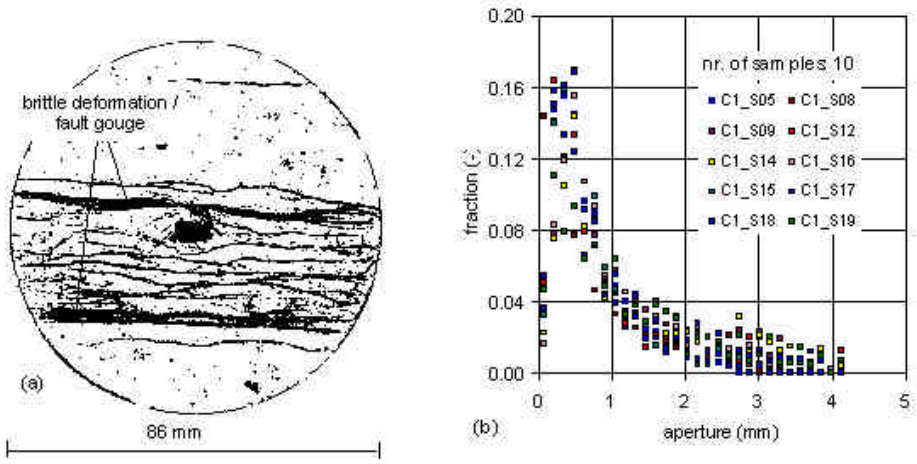

Figure 3.1: Structural characterisation of core samples of shear zones material (from Marschall et al. 1999). (a) bitmap of a core section drilled from the GAM fracture and (b) aperture distributions of 10 core samples.

Furthermore, results arising from quantitative porosimetry (Brodsky et al., 2000) showed that an average porosity for the shear zone could be found in the range 2% to 7%, and that, the average porosity for the matrix could range from 0.25% to 0.5%. The measured matrix porosities are lower than the previously reported accessible porosity of Grimsel granodiorite of about 1% (Schneebeli et al., 1995).

Intrinsic permeability measured by Gimmi et al. (1997) is about 3×10^{-18} m^2. This value is somewhat smaller than the value measured by Brodsky et al. (2000), which ranges between 10^{-16} m^2 to 10^{-15} m^2.

3.2.2 *Instrumentation at the site*

Field investigations were being carried out in a 4*6 meter section of the GAM shear zone, which was explored with a total of 26 boreholes. Most of the boreholes are oriented sub-horizontally with a diameter which ranges from 86 mm to 35 mm, intersecting the GAM shear zone at some distance along hole. Figure 3.2 shows the intersection points of these boreholes with the plane of the shear zone. Also, a fan like array of boreholes was drilled parallel to the shear zone in a distance of about 1 m from the target structure (see Chapter 2). These boreholes where used in the course of the radar surveys for logging the site with a especial borehole radar antenna.

After drilling, all boreholes except the geophysical boreholes were equipped with single or multipacker systems, aiming at a hydraulic separation of the GAM shear zone. Orientations, diameters, and lengths of investigation//geophysical boreholes as well as borehole specifications and instrumentation layout are documented in Gemperle (1999b).

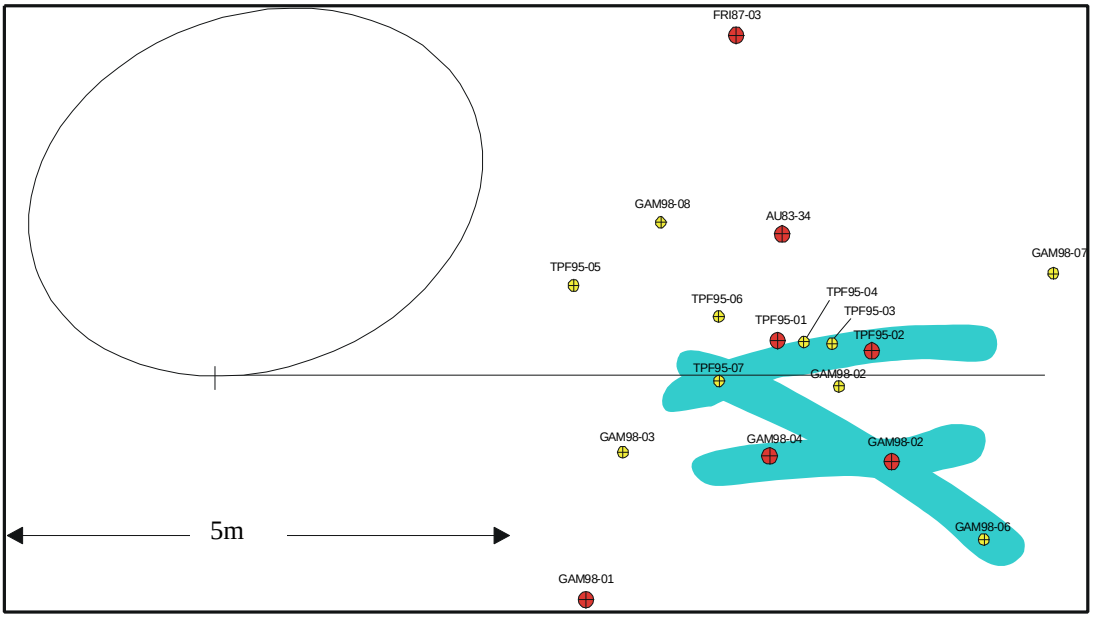

Figure 3.2: Intersection of boreholes at the GAM site with the shear zone, and hydraulic connection (overshadowed zone connecting boreholes) resulting from the storativities analysis (Meier et al 1998) obtained from the constant rate injection tests.

3.2.3 *Hydraulic-test campaigns and previous interpretation*

In order to characterise flow and transport properties of the GAM fracture several hydraulic tests were performed. during the previous TPF project (Wyss 1996) and the GAM project itself (Gemperle 1999a, Gemperle 1999b, Fierz and Piedevache 2000, Trick 2000). These measurements extend over a period of five years from January 1995 to December 2000 and include single borehole tests (pulse tests) as well as cross-hole hydraulic tests.

Pulse and cross-hole tests performed in the GAM fracture are summarised in Tables 1 and 2, respectively.

Table 3.1: Summary of the pulse injection tests

Test	Injection Borehole	Date	Volume Injection (ml)	Duration (min)
P1	TPF95.01	28/06/1995	13.200	0.96
P2	TPF95.02	28/06/1995	15.800	0.96
P3	TPF95.03	28/06/1995	7.100	0.96
P4	TPF95.04	28/06/1995	10.000	0.96
P5	TPF95.05	28/06/1995	13.500	0.96
P6	TPF95.07	28/06/1995	14.000	0.96
P7	GAM98.01	05/15/2000	354.1407	5.82
P8	GAM98.03	05/15/2000	381.024	0.84
P9	GAM98.04	01/15/2000	157.201	2.34
P10	GAM98.05	06/15/2000	156.655	1.56
P11	GAM98.06	05/15/2000	2.943	0.90
P12	GAM98.07	01/15/2000	5.040	0.42
P13	GAM98.08	05/15/2000	1709.470	5.46

Table 3.2: Summary of the constant rate injection tests

Test	Injection Borehole	Date	Flow rate (ml/min)	Duration (hr)
RI1	TPF95.01	05/06/1995	8.5	9.0
RI2	TPF95.02	11/07/1995	3.6	28.0
RI3	GAM98.02	10/11/1998	10.0	10.8
RI4	GAM98.04	27/11/1998	4.0	27.6
RI5	GAM98.02	20/01/2000	2.5	140.4
RI6	GAM98.04	15/08/2000	2.5	92.4

A pulse injection test consists of producing a sudden pressure increase within a borehole by quick injection of water and monitoring the response of the system to the perturbation of the pressure field. The pressure recovery curve is mainly controlled by the hydraulic properties in the vicinity of the well.

The pulse test campaign of June 1995, was preliminary interpreted by Wyss (1996) to obtain estimates of the interval transmissivities: the pressure-recovery data from pulse-injection tests were manually calibrated using Cooper's type curves (Cooper and Papadopulos 1967). Successively, the same data were automatically calibrated with an algorithm based on Barker's solution (Barker, 1988). Two different types of automatic calibrations were considered: first the well-bore storage coefficient S_w was fixed and assumed to be equal to the manually-calibrated value, then this constraint was released and S_w was also calibrated. The parameters resulting from these different calibrations are compared in Table 3.3. We observe a strong local variability of the transmissivity field, which varies over three orders of magnitudes (10^{-11} to 10^{-8} m^2/s), and a general good agreement among the three methods with regards to transmissivity identification. In contrast, large differences can be observed in the storativity values calibrated using different methods, which suggests that these estimates are unreliable. This might reflect

the uncertainty in estimating storativity from single well tests or it might be the product of local heterogeneities of the field around the well that makes the applied interpretation model inaccurate (Meier et al., 1998).

Table 3.3: Summary of results of Pulse tests, comparing *T*, *S* and S_w obtained by three different ways: manual calibration reported by Wyss; automatic calibration of *T* and *S*, fixing S_w to the value reported by Wyss; automatic calibration of *T*, *S* and S_w.

	Manual curve type			Automatic interpretation					
	Wyss (1996)			Fixing S_w			Estimating S_w		
	$T(m^2/s)$	S	$S_w(m^2)$	$T(m^2/s)$	S	$S_w(m^2)$	$T(m^2/s)$	S	$S_w(m^2)$
TP95.001	4.40E-09	1.18E-06	1.37E-07	8.11E-09	2.64E-08	1.37E-07	1.82E-09	1.46E-05	4.87E-08
TP95.002	2.70E-09	1.51E-06	1.76E-07	4.33E-09	1.21E-06	1.76E-07	1.68E-09	7.26E-06	1.15E-07
TP95.003	8.10E-11	3.75E-06	7.64E-08	9.45E-11	3.57E-06	7.64E-08	7.73E-09	7.69E-06	7.27E-08
TP95.004	2.30E-09	5.29E-06	1.07E-07	1.67E-09	1.37E-05	1 .07E-07	3.97E-10	2.89E-04	6.07E-08
TP95.005	1.10E-11	1.34E-04	1.37E-07	1.25E-11	1.37E-04	1.37E-07	1.10E-11	1.80E-04	1.32E-07
TP95.006	1.10E-10	5.39E-05	2.74E-07	5.13E-08	1.03E-04	2.74E-07	7.66E-11	1.72E-04	2.60E-07
TP95.007	2.60E-08	1.54E-06	1.56E-07	6.17E-08	9.36E-13	1.56E-07	3.26E-08	2.09E-08	1.05E-07

Constant rate/head injection consists of a water injection, either at constant flow rate or at constant pressure, into a borehole over a period that can vary from fractions of an hour to several days. During injection, the area of influence of the well extends to larger and larger portions of the fracture whose hydraulic pressure is perturbed. The pressure response to the forcing water injection is monitored at the injection well as well as at other additional boreholes (observation boreholes). Then injection stops and pressure recovery is observed for a time that is typically 2 to 4 times longer than the injection period.

Constant rate injection tests were previously interpreted by means of Jacob's semi-logarithmic approximation (Cooper and Jacob 1946), obtaining a preliminary estimate of both transmissivity and storativity of the fracture (Table 3.4). Meier et al (1998) studied the effects of using Jacob interpolation in a large-scale homogeneous medium. They showed that Jacob interpretation still provides a robust estimate for the effective transmissivity, whereas storativity estimates are unreliable. The large spatial variability of the estimated storativity is unrealistic, and it rather reflects the connectivity between the observation boreholes and the injection well: better-connected boreholes show a faster response to the injection signal, which yields a smaller storativity. The relative abundance of observation wells has allowed identifying preferential connections between boreholes (overshadowed zone connecting boreholes in Figure 3.2).

Table 3.4: Hydraulic parameters obtained by means of automatic calibration based on Jacob approximation., and using the drawdown curves registered in the observation boreholes during the constant rate injection tests performed in the framework of the GAM project. (🡻injection borehole.)

Borehole	Constant rate Injection tests							
	Jun 1995 (RI1)		Jul1995 (RI2)		Nov 1998 (RI3)		Nov 1998 (RI4)	
	T $*10^{-10}$ m^2/s	S $*10^{-6}$	T $*10^{-10}$ m^2/s	S $*10^{-6}$	T $*10^{-10}$ m^2/s	S $*10^{-6}$	T $*10^{-10}$ m^2/s	S $*10^{-6}$
TPF95.01	🡻	🡻	4.06	1.35	3.85	2.05	6.27	2.75
TPF95.02	2.72	3.27	🡻	🡻	3.36	4.70	5.35	1.68
TPF95.03	2.40	12.3	4.66	7.13				
TPF95.04	3.85	18.1	4.27	4.25	3.93	2.56	6.29	2.50
TPF95.05	0.86	2.24	0.88	1.41	2.24	2.34	1.98	4.17
TPF95.07	2.84	5.20	5.06	0.70	3.66	1.05	5.82	2.44
GAM98.01					1.83	4.40	1.67	8.26
GAM98.02					🡻	🡻	5.81	0.98
GAM98.03					2.27	397	2.85	9.33
GAM98.04					3.63	2.19	🡻	🡻
GAM98.05					3.40	6.60	5.48	3.33
GAM98.06					11.00	20.6	10.90	2.01
GAM98.07					9.19	66.7	16.10	28.3
GAM98.08					5.68	10.0	10.10	11.2

3.2.4 Solute tracer test campaign

The GAM experiment was thought as an integrated research project on solute, particle and gas transport in a single fracture, which is characterised by heterogeneous internal structure (shear zone). In terms of tracer tests, the investigation program consisted of a set of complementary tracers. Non-sorbing solute tracers in combination with particle tracers (micro and nano spheres, and bacteriophages) and gas tracers (He, Xe, Ar, SF_6) have been used because their different migration behaviours permit investigation of different domains within the multi-porosity shear zone structure (Fig. 3.3). Particle tracers are focused on the main flow channels, showing no diffusion into matrix or stagnant pores. A gas phase predominantly migrates along those flow channels with large pore radii. Finally, non-sorbing solute tracers are governed by advection-dispersion processes as well as matrix diffusion, and respond to the entire system of connected porosity.

Five tracer tests have been performed in the framework of the GAM project (Kennedy, 1999, Kennedy, 2000(a,b), Kennedy and Kleiner, 2000). All of them were base on a dipole configuration, changing injection and extraction boreholes, injection and extraction flow rates, and also the injected tracers from one tracer test to the next one.

As pointed before, several types of tracers (“tracer cocktail”) have been injected in each tracer test. On one hand three different solute tracers have been injected: uranine, Napthionate, and Sulphurodamine-B. On the other hand several types of colloids have been injected (Table 3.5).

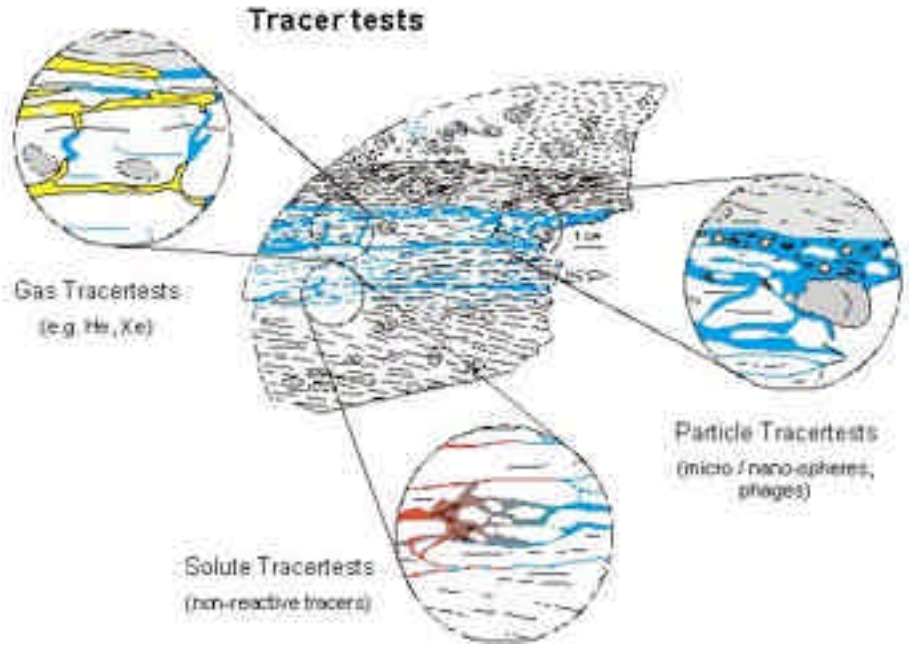

Figure 3.3: Characterisation of the multi-porosity shear zone structure with complementary tracers: (i) non-sorbing solute tracers respond to the entire system of connected porosity (advection and dispersion), (ii) particle tracers are focused on the main flow channels (particle exclusion, no diffusion) and (iii) gas tracers are sensitive to the specific gas/water interface (surface tension, gas solubility).

Table 3.5: Tracer test configurations

Tracer test	Tracers		Injection borehole	Extraction borehole	Length (m)	Q_{inj} (ml/min)	Q_{ext} (ml/min)
	Solutes	Bacteriophages					
PT1	Uranine	H40	98.02	98.04	1.23	1.00	1.00
PT2	Naphtionate	M62	95.01	98.02	1.58	1.50	1.64
PT3	Sulphurodamine B	H6	95.01	98.04	1.06	1.50	1.60
PT4	Uranine	(-)	95.04	98.04	1.09	1.52	1.59
PT5	Uranine	(-)	95.07	98.02	1.94	1.52	1.59

Tracer test	Injection tracer concentrations		Maximum extraction tracer concentrations	
	Solutes (ppb)	Bacteriophages (pfu/ml)	Solutes (ppb)	Bacteriophages (pfu/ml)
PT1	1650	4.60e+06	558	8.55e+05
PT2	28100	1.90e+05	10190	696
PT3	1100	1.57e+06	163	515
PT4	76	(-)	6	(-)
PT5	150	(-)	11	(-)

Tracer test	Tracer Recovery (%)		Peak time (hr)	
	Solutes	Bacteriophages	Solutes	Bacteriophages
PT1	100	41.0	36.10	33.90
PT2	24	0.2	34.70	14.30
PT3	23	0.1	27.20	19.70
PT4	42	(-)	27.00	(-)
PT5	18	(-)	23.00	(-)

As shown in Table 3.5, tracer recovery for solute tracers ranges between 100% to 18%. This is a very good result taking into account the difficulties that arise when working in low permeability formations. The very low tracer recovery obtained with bacteriophages can be explained in terms of the porosity distribution of the fractured medium. Bacteriophages use the highly permeable zones, that means larger and empty

fracture aperture zones (no fault gauge filling material), whereas solute tracers diffuses into less permeable zones.

3.3.Hydraulic and tracer tests interpretation.

3.3.1 Mathematical framework

3.3.1.1 Direct problem equations

We will now briefly describe the flow equation and the solute transport equation. We assume that these equations are well known and thus skip a complete development. These equations have to be solved in order to simulate the solute transport tests performed in the framework of the GAM project. The flow equation can be written as (Bear, 1972):

$$\nabla(T\nabla h) + q_A = S\frac{\partial h}{\partial t} \tag{1}$$

where h[L] is piezometric head, q_A[LT^{-1}] is areal recharge, S[-] is the storage coefficient, T[L^{2}T^{-1}] is the formation transmissivity. Transmissivity can show a spatial correlation structure. If the transmissivity field had clear anisotropic structure it would appear after the calibration, so the general trend of the transmissivity field structure should be reproduced. When we talk about anisotropy, it must be understood as the interpretation of the spatial transmissivity distribution

The transport equations including advection and dispersion/diffusion in the mobile zone, and also matrix diffusion in the immobile zone are:

$$\frac{\partial}{\partial t}(Rfc) = \nabla\left(a_L|\mathbf{q}| + fD_f\right)\nabla c - \mathbf{q}\nabla c + F_i \tag{2}$$

$$\frac{\partial}{\partial t}\left(\frac{R_i f_i}{L_i}c_i\right) = \frac{\partial}{\partial h}\left(\frac{D_i f_i}{L_i}\frac{\partial}{\partial h}c_i\right) \tag{3}$$

where f [-] is porosity, c [ML^{-3}] solute concentration at the mobile zone, a_L [L] is longitudinal dispersivity, D_f [L^{2}T^{-1}] is molecular diffusion at the mobile zone, **q** is Darcy's flow [LT^{-1}], c_i [ML^{-3}] is solute concentration at immobile zones, f_i [-] is immobile zone porosity, D_i [L^{2}T^{-1}] is molecular diffusion of the solute at the immobile zone, R [-] is retardation coefficient due to adsorption phenomena at the mobile zone, R_i [-] is the retardation coefficient at the immobile zone, h [L] is the coordinate axis perpendicular to the flow direction, and t[T] is time. The last term in the right-hand side of Equation (3.2), F_i is a sink/source term related to matrix diffusion.

Note that in two dimensions, q=-$T\tilde{N}h$ is not Darcy's flux, but flow rate per unit width [L^{2}T^{-1}], and f is redefined as thickness-porosity, being the product of fracture thickness and porosity, that is (bϕ) [L].

If the matrix zone is viewed as a sequence of plates of thickness $2L_i$ then matrix diffusion is governed by Equation (3.4).

$$F_i = \frac{D_i f_i}{L_i} \frac{\partial c_i}{\partial h}\bigg|_{h=0} \tag{4}$$

Continuity conditions have to be imposed at the interface between the matrix and flowing water, that is:

$$c(x,x,t=0) = 0 \quad \forall x \in \Omega \quad 0 < x < 1 \tag{5}$$

$$c(x,x=0,t) = c(x,t) \quad \forall t > 0 \quad \forall x \in \Omega \tag{6}$$

$$\frac{\partial}{\partial x} c\bigg|_{x=1} = 0 \quad \forall x \in \Omega \; \forall t > 0 \tag{7}$$

Where Equation (3.5) expresses the concentration initial condition inside the matrix; Equation (3.6) expresses continuity of concentrations at the interface between the flowing and matrix zones (ξ=0); and Equation (3.7) is the boundary condition at the innermost portion of the matrix (ξ=1).

3.3.1.2 Inverse problem equations. Overview of the Maximum Likelihood Method and expected value of the Likelihood.

The ideal statement for any kind of inversion procedure would be to find the set of parameters that make the solution of the model equal to the true heads and/or concentrations. The Maximum Likelihood Method (ML) can account prior information of the parameters to be estimated in a natural way, making possible the estimation of ground water flow and transport parameters from steady-state and transient data (head and concentration) and prior information on these parameters (Carrera and Neuman 1986a,b).

The usual way to obtain a good agreement between measured (z*) and computed values (z) consists in defining an appropriate distance between these vectors. There are many ways to do it, including least squares, generalized least squares, etc. However, this is not possible as we don't know the true values. For this reason we have selected the maximum likelihood method, as it can account prior information of the parameters to be estimated in a natural way.

With the hypothesis that residuals (z-z*) and prior estimates (p*) have a multigaussian distribution, and assuming the independence of errors of heads, concentrations and model parameters, the likelihood function of a hypothesis p on the parameters to be estimated can be written as (Medina and Carrera, 2003):

$$L = (2p)^{-\frac{n}{2}} \left(|\mathbf{C}_h| |\mathbf{C}_c| \prod_j |\mathbf{C}_j| \right)^{-\frac{1}{2}} \cdot \exp\left[-\frac{1}{2} \left[(\mathbf{h} - \mathbf{h}^*) \mathbf{C}_h^{-1} (\mathbf{h} - \mathbf{h}^*) \right] \right] \cdot$$
$$\cdot \exp\left[-\frac{1}{2} \left[(\mathbf{c} - \mathbf{c}^*) \mathbf{C}_c^{-1} (\mathbf{c} - \mathbf{c}^*) + \sum_j (\mathbf{p}_j - \mathbf{p}_j^*) \mathbf{C}_j^{-1} (\mathbf{p}_j - \mathbf{p}_j^*) \right] \right] \tag{8}$$

where **h*** is the vector of n_h head measurements, **c*** is the vector of n_c concentration measurements, $\mathbf{p}^*$ is the vector of n_j prior information data of the j-th type parameters

(j=1 for transmissivity, 2 for storativity, etc.), **h** and **c** are the vectors of computed head and concentration respectively, $\mathbf{p}_j$ is the vector of computed values of the j-th type parameters, $\mathbf{C_h}$, $\mathbf{C_c}$ and $\mathbf{C_j}$ are the covariance matrices of errors in heads, concentrations and type j parameters respectively.

Maximizing Equation (3.8) is equivalent to minimizing the support function defined as:

$$S = -2Ln(L) \tag{9}$$

It is also assumed that there exist some unknown scalars t_h, t_c, t_j (subscript j ranges from 1 to n_p, number of parameters to be estimated), that multiply matrices $\mathbf{V_h}$, $\mathbf{V_c}$ and $\mathbf{V_j}$ to obtain the true but unknown covariance matrices $\mathbf{C_h}$, $\mathbf{C_c}$ and $\mathbf{C_j}$, that is,

$$\mathbf{C_h} = t_h \mathbf{V_h} \; ; \; \mathbf{C}_c = t_c \mathbf{V}_c ; \; \mathbf{C}_j = t_j \mathbf{V}_j \tag{10}$$

Operating in Equation (3.9) taking into account equations (8) and (10), neglecting the terms in the resulting equation that only depend on the statistical parameters $t_h,, t_c,, t_j$ and multiplying by t_h, the objective function to be minimized becomes:

$$F = F_h + l_c F_c + \sum_j l_j F_j \tag{11}$$

Where F_h, F_c and F_p are defined as:

$$F_h = \left(\mathbf{h} - \mathbf{h}^*\right)^t \mathbf{V}_h^{-1} \left(\mathbf{h} - \mathbf{h}^*\right) \tag{12}$$

$$F_c = \left(\mathbf{c} - \mathbf{c}^*\right)^t \mathbf{V}_c^{-1} \left(\mathbf{c} - \mathbf{c}^*\right) \tag{13}$$

$$F_p = \left(\mathbf{p_j} - \mathbf{p_j}^*\right)^t \mathbf{V}_p^{-1} \left(\mathbf{p_j} - \mathbf{p_j}^*\right) \tag{14}$$

The parameters l_c and l_j are weights between the different pieces of information (heads, concentrations and prior information), more precisely:

$$l_c = \frac{t_h}{t_c} \; ; \quad l_i = \frac{t_h}{t_i} \tag{15}$$

These weights control the relative importance assigned to the different types of information taken into account during the minimization process. Giving too much importance to some data may bias the estimation. For this reason it is important to find the so called optimal weights in order to obtain the parameter data set that maximize Equation (3.8).

The statistical parameters (t_h, t_i etc) have been traditionally estimated by ML, however ML presents some problems: On the one hand no minimum exists for S (Eq. 3.9) in terms of l for many geostatistical inversion problems. On the other hand, likelihood estimation is often ambiguous, that is, the optimum weight between head and transmissivity data may occur not at the maximum of the likelihood function, but at an inflexion point (Carrera and Medina, 1994). To overcome these problems several

authors point out the use of the expected value of the likelihood, rather than the likelihood itself (Akaike 1978, Honjo et al. 1994, Kitanidis 1995, Medina and Carrera 2003).

The expected likelihood function is given by:

$$\overline{L} = \int (2p)^{-\frac{n}{2}} \left(|t_h \mathbf{V}_h| |t_c \mathbf{V}_c| \prod_j |t_j \mathbf{V}_j| \right)^{-\frac{1}{2}} \exp\left[-\frac{1}{2} \left[t_h^{-1} F_h + t_c^{-1} F_c + \sum_j t_j^{-1} F_j \right] \right] dp \qquad (16)$$

One can define a support function $\overline{S_2}$, and then, as in the case of the likelihood function (Eq. 3.8 and 3.9) minimize this support function with respect to the weighting coefficients rather than maximize the expected likelihood. We skip the complete development of the equations and address the reader to Medina and Carrera (2003) for further information. The support function $\overline{S_2}$,is defined as:

$$\overline{S_2} = N + \ln|\mathbf{H}| + N \ln\left(\frac{F}{N}\right) - \sum_i n_i \ln l_i - \sum_j k_j \ln m_j \qquad (17)$$

Where N is the total number of data, n_i and k_j are the number of measurements of state variable 'i' and the number of the prior information data of the j-th parameter type respectively, l_i and m_j are the relative weights of state variables, and **H** is an approximation of the Hessian matrix at the end of the optimization process.

3.3.2 Geostatistical inversion

During the inversion process geostatistics comes into play when transmissivity is assumed to be a random function: that is, when point values of transmissivity (T) are taken to be random variables with a predefined correlation structure (Carrera et al., 1992). The result of the geostatistical inversion is the conditional expectation of T (actually, log T) conditioned by measurements of T and head. This means that the estimated T field is a smooth function of space (as a result of being an expected value) that coincides with point T measurements where available, and leads to accurate simulation of available head measurements.

Briefly the practical steps of the methodology for stochastic inversion of flow parameters consists of:

- Definition of the conceptual flow model.
- Definition of the geostatistical model.
- Non linear estimation of the model parameters by means of the maximization of the likelihood.

3.3.2.1 Conceptual model

The fracture is modelled as a rectangular (2D) domain of 52*52 m^2, centred on the access gallery. Transmissivity is treated as a regionalized variable. Its heterogeneity was established by the previous hydraulic test interpretation (see chapter 2). Therefore, the model domain is divided into 2086 transmissivity zones, which are more finely discretized in the region where the observation points are located (intersection between drilled boreholes and the fracture plane). The storativity was assumed to be

homogeneous within the model domain because of the difficulty of obtaining storativity from conventional hydrotest analysis (Meier et al., 1998).

Two different hydraulic conditions were considered for defining the boundary conditions: Steady-state (SS) conditions without testing activities and transient conditions during the pumping tests. Constant head boundaries at the outer model domain and also a leakage condition at the gallery were applied for SS, whereas for transient conditions zero drawdown was imposed on the boundaries at the outer model domain, no flow condition at the gallery, and prescribed flow rate at the pumping well were applied. Heads at the outer boundary were estimated during model calibration at the four corners of the domain because no head measurements were available at the boundaries. Heads between these points were interpolated linearly.

3.3.2.2 Geostatistical model

Prior information on the *T* zones estimates and their covariance, which are both necessary for the no linear ML estimation of the model parameters were obtained by block kriging, using the code KRINET (Olivella and Carrera, 1987). The input parameters for block kriging are the point transmissivity estimates obtained from the pulse tests analysis, the geometry of the transmissivity zones, and a correlation structure in terms of a variogram model. The scarcity of the point transmissivity data did not allow us to estimate a variogram, so several assumptions about the correlation structure on transmissivity have been made, based on the qualitative information on the preferred orientation of connected high transmissivity zones. In all cases an exponential variogram was considered, with a sill (σ^2_{lnT}) of 100. The different *T* correlation lengths in X and Y directions ($\mathbf{R_{X/Y}}$ hereinafter) considered are [0.4m/0.4m], [0.8m/0.4m], [0.8m/0.8m], [1.6m/0.4m], [1.6m/0.8m], [1.6m/1.6m], [3.2m/0.4m], [3.2m/0.8m], [3.2m/1.6m] and [3.2m/3.2m], which give four different T anisotropy ratios ($\mathbf{R_{XY}}$ hereinafter), that explicitly are R_{XY}=1, 2 4 and 8 (Table 3.6).

3.3.2.3 Results obtained from the geostatistical inversion

The nonlinear estimation of the model parameters (i.e. transmissivities values and strorativity) was performed with the finite element code TRANSIN-II (Medina et al., 1996). The transmissivity fields obtained through the stochastic inversion are presented in Figure 3.4. Four drawdown data sets (RI1, RI2, R3, RI4), and the steady-state heads were used simultaneously to do the geostatistical inversion. All the inverted transmissivity fields display the same transmissivity structure, but due to the different anisotropy ratio of the variogram, they present slight differences, changing the direction of some high-T channels. The transmissivity fields derived from the inversion show strong heterogeneity and suggest the existence of channels. All of them represent the spatial distribution of expected transmissivity (actually, Log-transmissivity) conditioned on steady–state, transient heads and point transmissivity measurements. All fields are equally well conditioned. Examples of the good agreement between computed and measured heads are shown in Figure 3.5, where RI2 measured drawdowns are jointly depicted with the computed responses for all the assumed $R_{x/y}$. In all cases the calculated drawdown fits pretty well for every inverted transmissivity field.

All *T* fields indicate a strong heterogeneity and the existence of channels between the observation boreholes. Despite the different assumed correlation structures, the pattern is very similar in all *T* fields. In fact, the estimated transmissivity fields which have the same anisotropy ratio R_{XY} (Table 3.6) show a spatial transmissivity structure practically

identical. Attending to this, the transmissivity fields can be grouped in four different classes taking into account the *T* anisotropy ratio, that is, R_{XY}.

Table 3.6: Transmissivity fields associated to the different anisotropy ratios considered

R_{XY} = 1	[0.4m / 0.4m] [0.8m / 0.8m] [1.6m / 1.6m] [3.2m / 3.2m]
R_{XY} = 2	[0.8m / 0.4m] [1.6m / 0.8m] [3.2m / 1.6m]
R_{XY} = 4	[1.6m / 0.4m] [3.2m / 0.8m]
R_{XY} = 8	[3.2m / 0.4m]

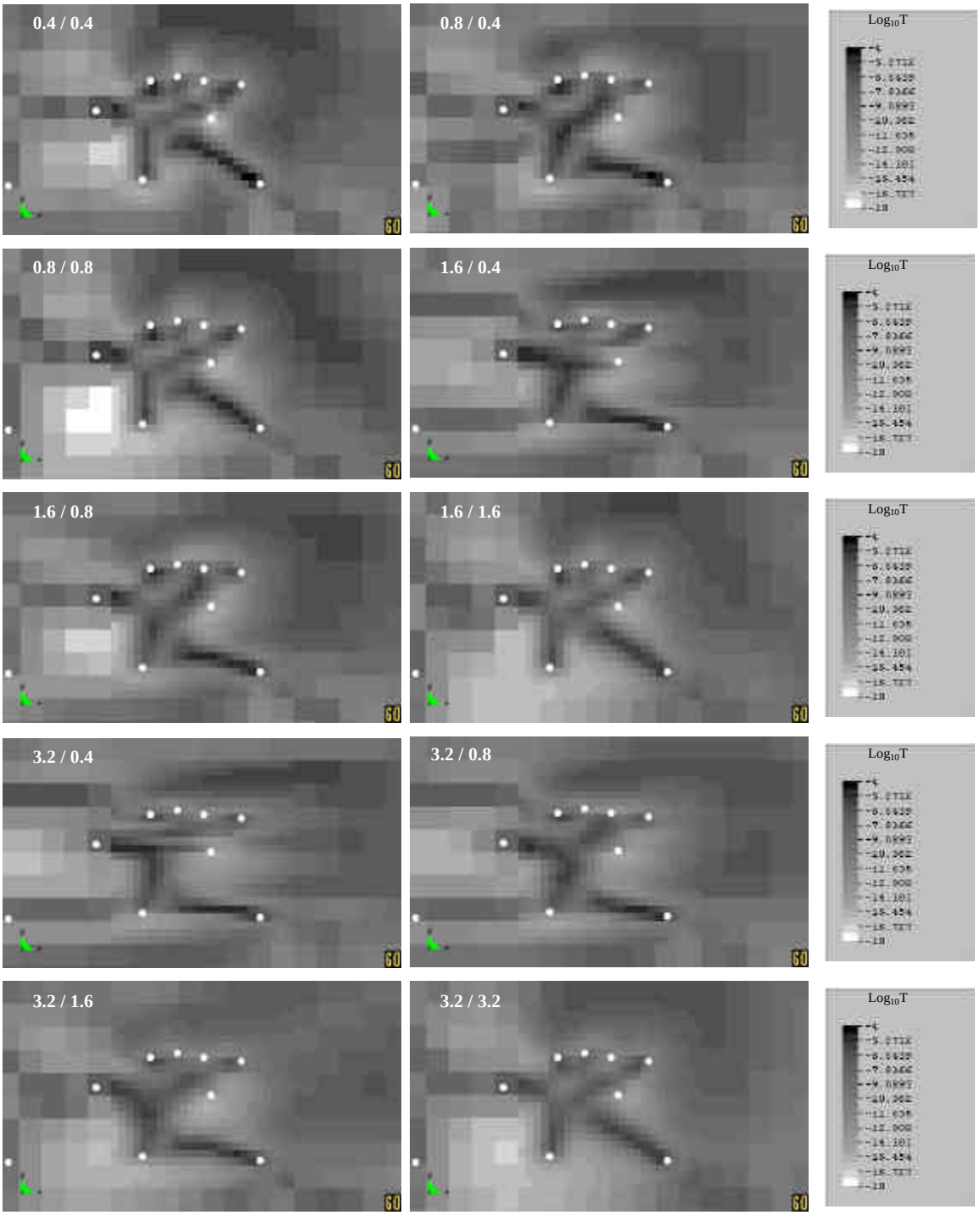

Figure 3.4: Log_{10}-Transmissivity Fields obtained from the joint interpretation (RI1, RI2, RI3, RI4 and steady state heads) by means of geostatistical inversion. The assumed $R_{X/}Y$ which indicates the correlation lengths in X and Y directions of the variogram is showed on the upper left corner of each transmissivity field. White points are observation boreholes.

These results suggest that the coarse structure of the heterogeneous transmissivity field has been revealed by the geostatistical inversion, independently of the assumed correlation structure.

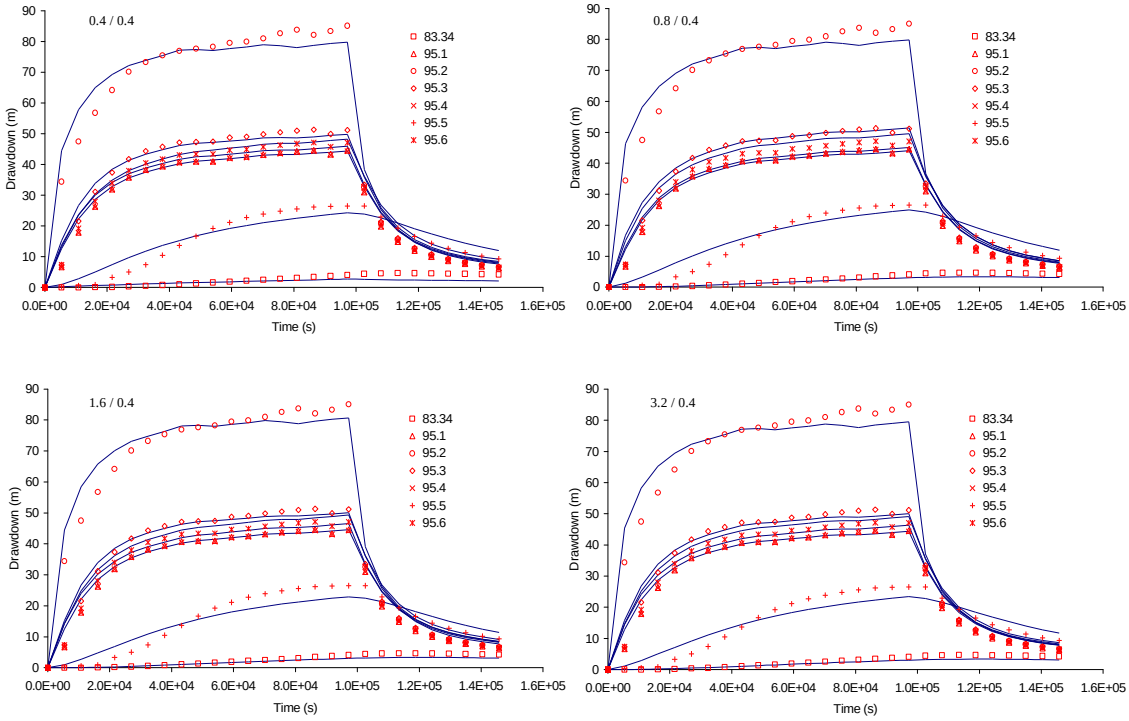

Figure 3.5: Measured (dots) and calculated (lines) cross-hole drawdown data for the pumping test RI2, regarding the four different anisotropy ratios R_{XY} of 1 ($R_{X/Y}$ = 0.4m / 0.4m), 2 ($R_{X/Y}$ = 0.8m / 0.4m), 4 ($R_{X/Y}$ = 1.6m / 0.4m) and 8 ($R_{X/Y}$ = (3.2m / 0.4m).

Due to the fact that more than one geostatistical assumption is similar in terms of agreement between measured and computed heads (i.e. in terms of the objective function) the arising question would be how to choose the best geostatistical hypothesis. There are several model selection criteria available in the literature such as Akaike (1977, 1994), Hannan (1980) and Kashyap (1982). All these criteria respect the parsimony principle. However, several comparisons done by Carrera (1984), by Carrera and Neuman (1986c), and by Medina and Carrera (1992) with synthetic examples show that the Kashyap criterion seems to be the best.

The Kashyap criterion is obtained by minimizing the average probability of selecting the wrong model among a set of alternatives. This criterion can be written as:

$$d_M = S + M \ln\left(\frac{N}{2p}\right) + \ln|\mathbf{F}| \tag{18}$$

$$N = n_h + n_c \tag{19}$$

Where S is the support function (Eq. 3.9), M is the number of estimated parameters, and being n_h and n_c the total number of head (drawdown) and concentration measurements

respectively. **F** is the Fisher information matrix, which is the minimum variance bound of the covariance matrix (Bury, 1975). Given a number of alternative models, one can select the one leading to maximum information content, or equivalently to minimum parameter uncertainty. In order to select one model among several alternatives, the largest value of d_M gives the worse model.

The Kashyap criterion is computed for all the models. Three interesting results can be obtained from the analysis of Fig. 3.6 where d_M is depicted as a function of the different geostatistical models:

- The Kashyap criterion penalizes the geostatistical models with large range in the X direction R_X.
- For models with the same the same R_X the Kashyap criterion penalizes those models which have the largest R_Y. In other words, the Kashyap criterion penalizes the isotropy.

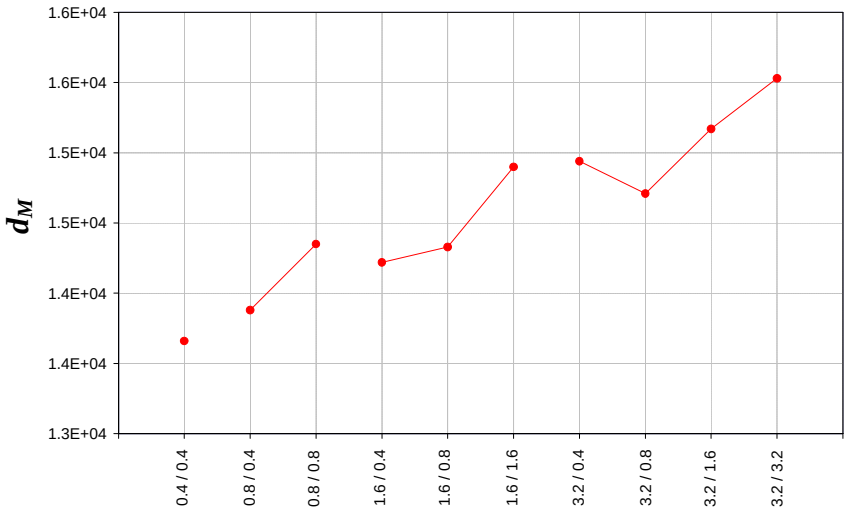

Figure 3.6: Kashyap criterion as a function of the different geostatistical models

Taking into account the latter results, in terms of $R_{X/Y}$ one may conclude that the best geostatistical hypothesis is [0.8/0.4], closely followed by [1.6/0.4]. Nevertheless, in terms of either, objective function and transmissivity field structures, is difficult to select one as the best model since all the accounted models are very similar, in these terms.

3.3.3 Interpretation of the solute tracer tests.

3.3.3.1 Conceptual model

As in the case of the hydraulic characterization, the fracture is modelled as a rectangular domain of 52*52 m^2, centred on the access gallery. The transmissivity fields are those obtained by means of the geostatistical inversion presented in the previous section. Storativity is assumed to be constant within the fracture.

The depth-averaged pore velocity v[LT^{-1}] which controls the solute migration through the fracture is given by

$$v = -\frac{T}{bf}\nabla h \tag{20}$$

Equation (3.20) makes it clear that correlation between transmissivity (T) and thickness-porosity (the product bf is named thickness porosity, which indicates the fracture pore volume per unit of fracture horizontal area) plays an important role in the spatial variability of pore velocity, thus in solute propagation.

In the solute migration conceptual models that we use, all transport parameters are assumed to be homogeneous, except the thickness porosity that depends on the accounted model (Fig. 3.7). Three different fracture models are examined:

- Fault gauge filled fracture model, with constant thickness (FFC)
- Fault gauge filled fracture model, whit variable thickness porosity (FFNC)
- Open Fracture model (OF)

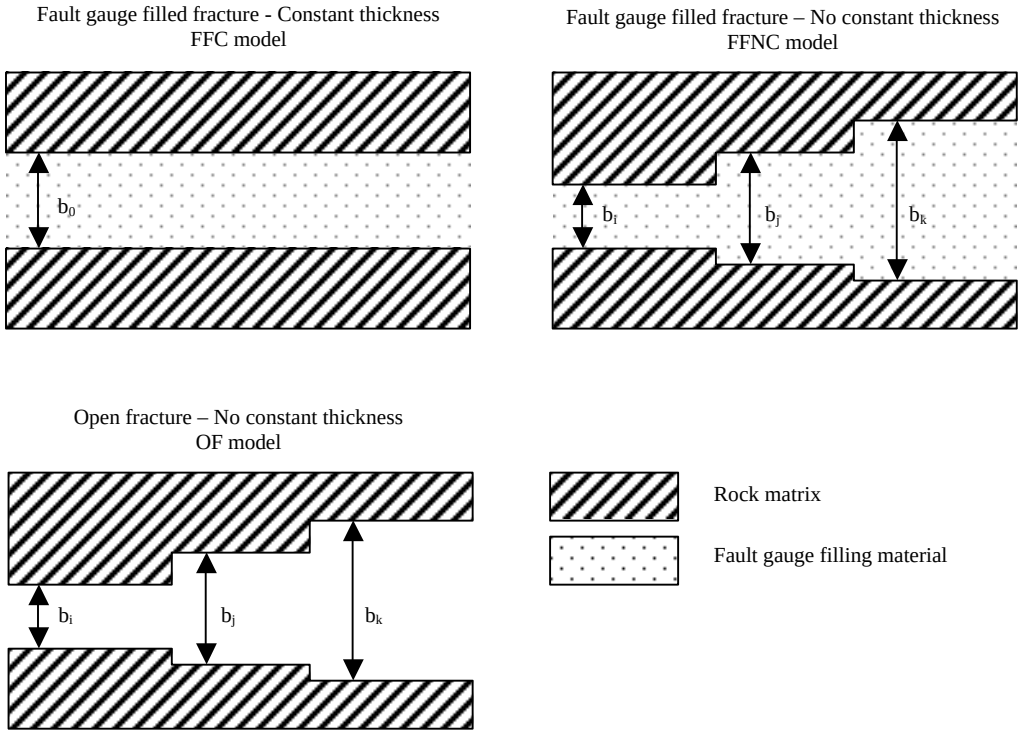

Figure 3.7: Fracture conceptual models

As can be seen in Table 3.7, the fracture aperture value comes directly from field measurements for the FFC model. For advection dominated transport systems, the mean arrival time t [T] is simply given by the flow accessible volume of the system V_p [L^3] divided by the pumping flow rate Q [L^3T^{-1}] (Nauman and Buffham, 1983), that is:

$$t = \frac{V_p}{Q} \tag{21}$$

The flow accessible pore volume in the fracture is given by Equation (3.22)

$$V_p = b_0 f_0 p R^2 \tag{22}$$

Where b_0[L] is the mean fracture thickness, f_0[-] is the fracture porosity and R[L] is the dipole length. Taking into account equations (21) and (22), the mean fracture thickness can be obtained directly in terms of the mean arrival time obtained from the breakthrough curve analysis, the fracture porosity obtained from field measurements, the pumping flow rate and the dipole length, that is:

$$b_0 = \frac{Qt}{f_0 p R^2} \tag{23}$$

In the case of FFNC, the thickness b[L] of the fracture is calculated as considering the fracture as an equivalent porous media, that is, dividing the transmissivity T[L^2T^{-1}] by the fracture permeability K[LT^{-1}]:

$$b = \frac{T}{K} \tag{24}$$

When the medium is assumed to be an open fracture, the transmissivity follows the cubic law with the aperture, that is:

$$b = \left(\frac{12m}{rg} T \right)^{\frac{1}{3}} \tag{25}$$

Where m[$ML^{-1}T^{-1}$] is the dynamic viscosity, r[ML^{-3}] is water density and g[LT^{-2}] is the gravity acceleration.

In this case, an effective aperture b_{eff} is derived (Meier 1999, 2001) assuming n parallel fractures, with transmissivity T/n and aperture b_{eff}/n. Rewriting the Equation (3.25) leads to:

$$b_{eff} = n^{\frac{2}{3}} \left(\frac{12m}{rg} T \right)^{\frac{1}{3}} = fb \tag{26}$$

$$f = n^{\frac{2}{3}} \tag{27}$$

Each of the three previous models are subdivided in two depending whether matrix diffusion is considered or not (MD and NMD models respectively). Thus, all the solute transport models are: FFC-NMD, FFC-MD, FFNC-NMD, FFNC-MD, OF-NMD, and OF-MD.

Table 3.7: Transmissivity and fracture thickness relationships depending on the fracture model. The subscript *j* stands for every element of the grid.

Fracture model	Thickness [L]	Porosity [-]	Thickness- Porosity [L]
Fault gauge filled fracture with constant thickness	$b_j = b_0 \quad \forall j$	$f_j = f_0 \quad \forall j$	$b_0 f_0$
Fault gauge filled fracture with variable thickness	$b_j = \frac{T_j}{K_0}$	$f_j = f_0 \quad \forall j$	$b_j f_0$
Open fracture	$b_j = \left(\frac{12m}{r\,g} T_j \right)^{\frac{1}{3}}$	$f_j = 1$	$b_j f$

Transport calibrated parameters are dependent on the model (see Table 3.8).
In the FFC models the fracture thickness porosity is directly the calibrated parameter. In the cases of FFNC and OF fractures the theoretical fracture thickness porosity field remains constant and the parameter f (multiplier parameter of thickness-porosity to correct the mean advection time) is calibrated. In all cases longitudinal dispersivity is calibrated, and in those cases where matrix diffusion is taken into account, matrix porosity and matrix diffusion parameters are also calibrated.

Table 3.8: Calibrated parameter for the different fracture models depending if the matrix diffusion is accounted or not.

No matrix diffusion	Fracture Parameters	
FFC-NMD	bf	a_L
FFNC-NMD	f	a_L
OF-NMD	f	a_L

Matrix diffusion	Fracture Parameters		Matrix Parameters			
FFNC-MD	bf	a_L	f_i	$D_{i1}{}^{*}$	$D_{i2}{}^{**}$	$D_{i3}{}^{***}$
FFNC-MD	f	a_L	f_i	$D_{i1}{}^{*}$	$D_{i2}{}^{**}$	$D_{i3}{}^{***}$
OF-MD	f	a_L	f_i	$D_{i1}{}^{*}$	$D_{i2}{}^{**}$	$D_{i3}{}^{***}$

* Matrix diffusion coefficient for Uranine
** Matrix diffusion coefficient for Naphtionate
*** Matrix diffusion coefficient for Sulfurodamine

Three different tracers were injected during the different tracer tests performed in the GAM experiment (see Table 3.5). These tracers show different molecular weight (Table 3.9). Usually, the larger the molecular weight, the bigger the molecular size. The bigger the molecular size, the shorter the penetration length and exploration in the matrix pore volume. So it is expected to have different matrix diffusion coefficient for the three different tracers.

Constant head boundary condition was considered at the outer model domain, no flow condition at the gallery, prescribed injection flow rate and mass flux at the injection borehole, and prescribed extraction flow rate at the extraction borehole. In order to

solve the flow and transport equations, initial conditions have to be imposed. In the case of the flow problem steady state measured heads at the injection, extraction and observation boreholes are used as initial conditions, as well as the steady state heads at the four corners of the outer boundary of the domain, computed through the previous T field geostatistical inversion. Initial heads at the rest of the fracture domain is obtained by linear interpolation. Initial condition for the transport problem is zero concentration at every point of the fracture domain.

Table 3.9: Molecular weight and assumed matrix diffusion length for the three injected solute tracers.

Solute Tracers	Molecular weight ($g \cdot mol^{-1}$)	L_i(m)
Uranine	376	$4 \cdot 10^{-3}$
Naphtionate	254	$5 \cdot 10^{-3}$
Sulphurodamine-B	607	$1 \cdot 10^{-3}$

3.3.3.2 Results obtained from the solute tracer tests inversion

The calibration of the transport parameters was performed with the finite element code TRANSIN-IV (Medina et al., 2000). The numerical results obtained from the tracer test inversion are summarized in Table 3.10 and 3.11, and are presented in terms of longitudinal dispersivity (a_L), thickness-porosity (bf or f), matrix porosity (f_i). matrix diffusion coefficients (D_i) and concentration objective function for all the fracture models (i.e. FFC-NMD, FFC-MD, FFNC-NMD, FFNC-MD, OF-NMD, and OF-MD) and all the transmissivity fields (i.e. [0.4/0.4], [0.8/0.4], [0.8/0.8], [1.6/0.4], [1.6/0.8], [1.6/1.6], [3.2/0.4], [3.2/0.8], [3.2/1.6] and [3.2/3.2])

Table 3.10: Calibrated transport parameters resulting from the joint inversion of the four tracer test performed in the framework of the GAM project, considering FFC, FFNC and OF transport models and no matrix diffusion for all the calibrated transmissivity fields

FFC-NMD	**0.4/0.4**	**0.8/0.4**	**0.8/0.8**	**1.6/0.4**	**1.6/0.8**	**1.6/1.6**	**3.2/0.4**	**3.2/0.8**	**3.2/1.6**	**3.2/3.2**
α_L	0.328	0.273	0.353	0.285	0.287	0.336	0.3	0.294	0.269	0.32
$b\phi$	0.0131	0.0109	0.0141	0.0114	0.0115	0.0134	0.0120	0.0118	0.0108	0.0128
Conc. Obj. Funct	1.35E+04	1.35E+04	1.35E+04	1.36E+04	1.35E+04	1.36E+04	1.36E+04	1.36E+04	1.36E+04	1.35E+04
FFNC-NMD	**0.4/0.4**	**0.8/0.4**	**0.8/0.8**	**1.6/0.4**	**1.6/0.8**	**1.6/1.6**	**3.2/0.4**	**3.2/0.8**	**3.2/1.6**	**3.2/3.2**
α_L	0.542	0.4	0.503	0.371	0.405	0.447	0.241	0.346	0.335	0.431
f	64.804	65.766	76.584	80.402	79.016	87.08	87.743	86.644	95.84	90.56
Conc. Obj. Funct	1.35E+04	1.35E+04	1.36E+04	1.37E+04	1.36E+04	1.38E+04	1.34E+04	1.38E+04	1.34E+04	1.40E+04
OF-NMD	**0.4/0.4**	**0.8/0.4**	**0.8/0.8**	**1.6/0.4**	**1.6/0.8**	**1.6/1.6**	**3.2/0.4**	**3.2/0.8**	**3.2/1.6**	**3.2/3.2**
α_L	0.47	0.47	0.434	0.374	0.45	0.362	0.338	0.322	0.341	0.301
f	6.195	6.614	14.569	9.732	11.65	21.849	12.645	15.246	21.999	32.723
Conc. Obj. Funct	1.36E+04	1.35E+04	1.38E+04	1.35E+04	1.36E+04	1.57E+04	1.37E+04	1.40E+04	1.58E+04	1.71E+04

Table 3.11: Calibrated transport parameters resulting from the joint inversion of the four tracer test performed in the framework of the GAM project, considering FFC, FFNC and OF transport models and matrix diffusion for all the calibrated transmissivity fields

FFC-MD	**0.4/0.4**	**0.8/0.4**	**0.8/0.8**	**1.6/0.4**	**1.6/0.8**	**1.6/1.6**	**3.2/0.4**	**3.2/0.8**	**3.2/1.6**	**3.2/3.2**
α_L	0.0198	0.0196	0.0198	0.0197	0.0197	0.0199	0.0196	0.0195	0.0196	0.0200
$b\phi$	0.0019	0.0022	0.0020	0.0025	0.0022	0.0021	0.0025	0.0025	0.0026	0.0020
ϕ_i	0.0046	0.0053	0.0046	0.0064	0.0058	0.0048	0.0066	0.0060	0.0063	0.0046
$D_{i\text{-Uranine}}$	7.34E-11	7.49E-11	7.36E-11	7.14E-11	7.40E-11	7.60E-11	7.34E-11	7.46E-11	7.47E-11	7.47E-11
$D_{i\text{-Naphtionate}}$	1.12E-10	9.79E-11	1.10E-10	1.05E-10	9.67E-11	1.08E-10	1.00E-10	1.00E-10	1.01E-10	1.09E-10
$D_{i\text{-Sulphurodamine}}$	7.12E-12	2.02E-11	7.12E-12	7.10E-12	7.06E-12	7.10E-12	7.04E-12	7.04E-12	7.03E-12	7.10E-12
Conc. Obj. Funct	1.33E+04	1.33E+04	1.32E+04	1.32E+04	1.33E+04	1.32E+04	1.33E+04	1.33E+04	1.33E+04	1.33E+04
FFNC-MD	**0.4/0.4**	**0.8/0.4**	**0.8/0.8**	**1.6/0.4**	**1.6/0.8**	**1.6/1.6**	**3.2/0.4**	**3.2/0.8**	**3.2/1.6**	**3.2/3.2**
α_L	0.0414	0.0398	0.0503	0.0497	0.0500	0.0493	0.0489	0.0491	0.0483	0.0490
f	29.790	29.250	33.990	36.150	35.530	39.440	39.790	39.530	42.150	40.940
ϕ_i	0.0043	0.0050	0.0044	0.0060	0.0054	0.0047	0.0063	0.0058	0.0062	0.0046
$D_{i\text{-Uranine}}$	6.10E-11	6.76E-11	6.84E-11	6.90E-11	6.98E-11	7.50E-11	7.54E-11	7.49E-11	8.35E-11	7.85E-11
$D_{i\text{-Naphtionate}}$	1.12E-10	1.00E-10	1.12E-10	1.04E-10	1.00E-10	1.14E-10	9.99E-11	1.02E-10	1.03E-10	1.15E-10
$D_{i\text{-Sulphurodamine}}$	1.12E-10	1.00E-10	1.12E-10	1.04E-10	1.00E-10	1.14E-10	9.99E-11	1.02E-10	1.03E-10	1.15E-10
Conc. Obj. Funct	1.34E+04	1.34E+04	1.33E+04	1.32E+04	1.33E+04	1.33E+04	1.33E+04	1.33E+04	1.33E+04	1.33E+04
OF-MD	**0.4/0.4**	**0.8/0.4**	**0.8/0.8**	**1.6/0.4**	**1.6/0.8**	**1.6/1.6**	**3.2/0.4**	**3.2/0.8**	**3.2/1.6**	**3.2/3.2**
	0.0197	0.0196	0.0198	0.0198	0.0199	0.0196	0.0197	0.0196	0.0194	0.0192
f	1.740	1.940	4.490	2.690	3.290	8.990	3.770	5.240	9.710	14.100
ϕ_i	0.0050	0.0057	0.0050	0.0069	0.0062	0.0053	0.0070	0.0065	0.0069	0.0051
$D_{i\text{-Uranine}}$	7.14E-11	7.29E-11	7.26E-11	7.04E-11	7.19E-11	7.48E-11	7.20E-11	7.23E-11	7.45E-11	7.84E-11
$D_{i\text{-Naphtionate}}$	1.17E-10	1.06E-10	1.15E-10	1.10E-10	1.05E-10	1.16E-10	1.03E-10	1.07E-10	1.06E-10	1.19E-10
$D_{i\text{-Sulphurodamine}}$	7.31E-12	7.24E-12	7.30E-12	7.25E-12	7.19E-12	7.29E-12	7.12E-12	7.18E-12	7.16E-12	7.28E-12
Conc. Obj. Funct	1.34E+04	1.34E+04	1.33E+04	1.32E+04	1.33E+04	1.33E+04	1.33E+04	1.33E+04	1.33E+04	1.33E+04

a_L values are larger for the models without matrix diffusion (Fig. 3.8-right), because a_L has also to account for the spreading of tracer due to matrix diffusion. In general a_L diminish for the models with large range, and it is counterbalanced by an increase in the model porosity (Fig. 3.9).

In general, the obtained values of a_L for OF-MD and FFNC- MD fracture models are larger than the values obtained for FFC-MD. These results are in agreement with the theoretical work of Hassan el al. (1998), who found that a positive correlation between transmissivity and flow porosity decreases longitudinal dispersion and vice versa. Consequently, in order to fit the same breakthrough curve from a tracer test in a heterogeneous media, model parameters controlling longitudinal dispersion have to be larger for models with a positive correlation between flow porosity and transmissivity than for models assuming a constant flow porosity.

The a_L values for the models with matrix diffusion are slightly smaller than the average side length of 0.08m for the T blocks within the tracer test area. This suggests that the dispersive flux due to the heterogeneity of transmissivity is effectively taken into account by the estimated T field, despite the fact that this T field can be assumed to be a conditional expectation, hence less variable than reality. In general the values of a_L are smaller for the FFC than for the FFNC models.

In general thickness-porosity becomes larger as the integral distance on transmissivity increases. There are two different behaviours depending on the correlation between

thickness porosity and transmissivity (Figs.9-left and 10-left). FFNC and OF fracture models show an increase on the estimated value of bf as the anisotropy ratio R_{XY} becomes shorter. On the other hand, bf for the FFC fracture model decreases while the anisotropy ratio R_{XY} becomes larger.

The value of bf is slightly larger for FFC-NMD model than FFC-MD model, because the retardation of the tracer due to matrix diffusion has to be compensated by a larger bf in the FFC-NMD model. The fracture porosity obtained for the MD models correlates linearly with the NMD fracture porosity (Fig. 3.8-left).

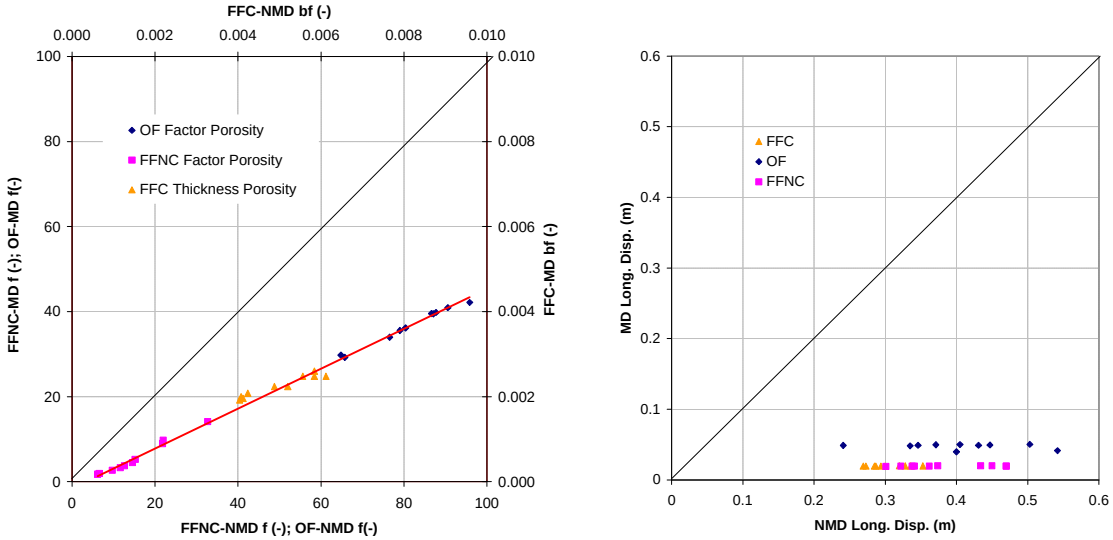

Figure 3.8: Correlation between (left) bϕ, f and (right) α_L taking into account matrix diffusion and their homologue parameters without matrix diffusion.

For every considered transmissivity field a lower and upper bounds estimates for transport parameters have been obtained by varying the correlation between flow porosity and transmissivity. As it can be seen in Table 3.10 the variation range of the estimated matrix diffusion parameters is small for all of them. This confirms the coherence in the value of these parameters for the different correlation structures considered of transmissivity.

Matrix porosity becomes larger when the correlation range in the X direction (R_X) increases, maintaining constant the anisotropy ratio $R_{X/Y}$. When R_X grows up the small structure on T disappears, and the answer of the system is to enlarge the matrix porosity, in order to delay the arrival of the tracer.

The matrix diffusion coefficients obtained for the three different tracers agree with what was discussed before, where the bigger molecular size presents the shorter penetration length, and also the shorter matrix diffusion coefficient.

The obtained fits when matrix diffusion is not taken account are not good enough (see annex 7). The rest of the fracture models which account for matrix diffusion (i.e. FFC-MD, FFNC-MD and OF-MD) fit pretty well the concentration measurements (Fig.

3.11). The adjustments are very similar among them as well as expected with the obtained concentration objective functions.

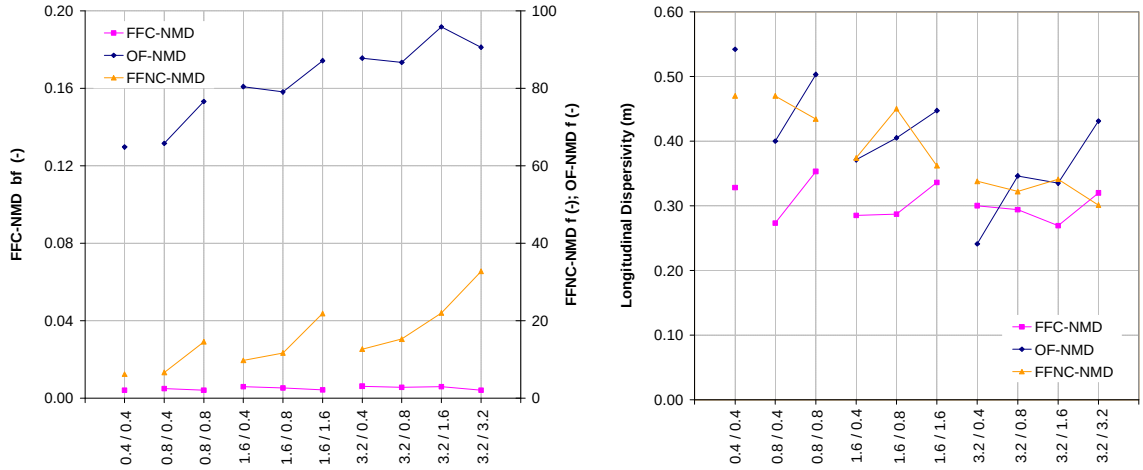

Figure 3.9: Transport parameters variation in terms of the geostatistical assumption:
Left: FFC-NMD bϕ, FFNC-NMD bϕ and OF-NMD f vs. $R_{X/Y}$
Right: FFC-NMD α_L, FFNC-NMD α_L and OF- NMD α_L vs $R_{X/Y}$

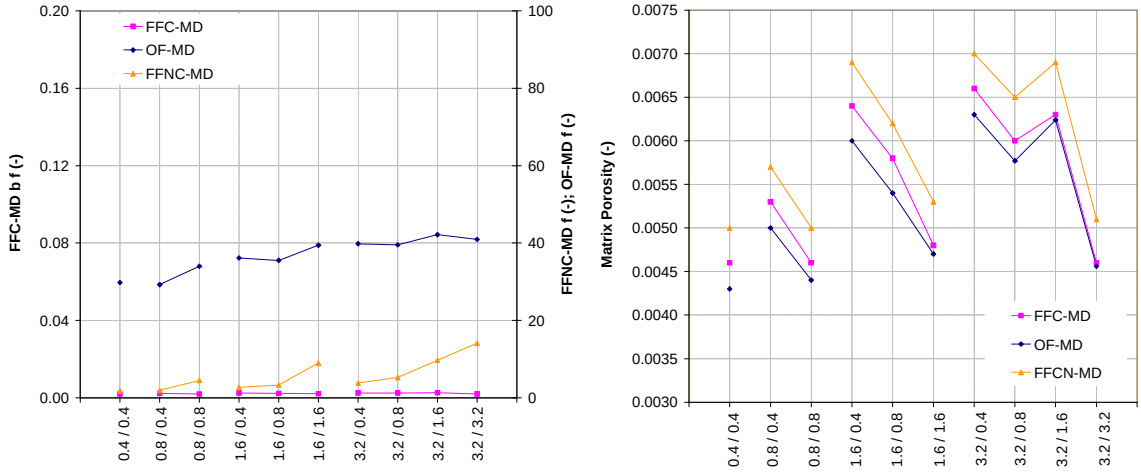

Figure 3.10: Transport parameters variation in terms of the geostatistical assumption:
Left: FFC-MD bϕ, FFNC-MD bϕ and OF-MD f vs. R_x/R_y.
Right: FFC-MD ϕ_i, FFNC-MD ϕ_i and OF-MD ϕ_i vs. R_x/R_y

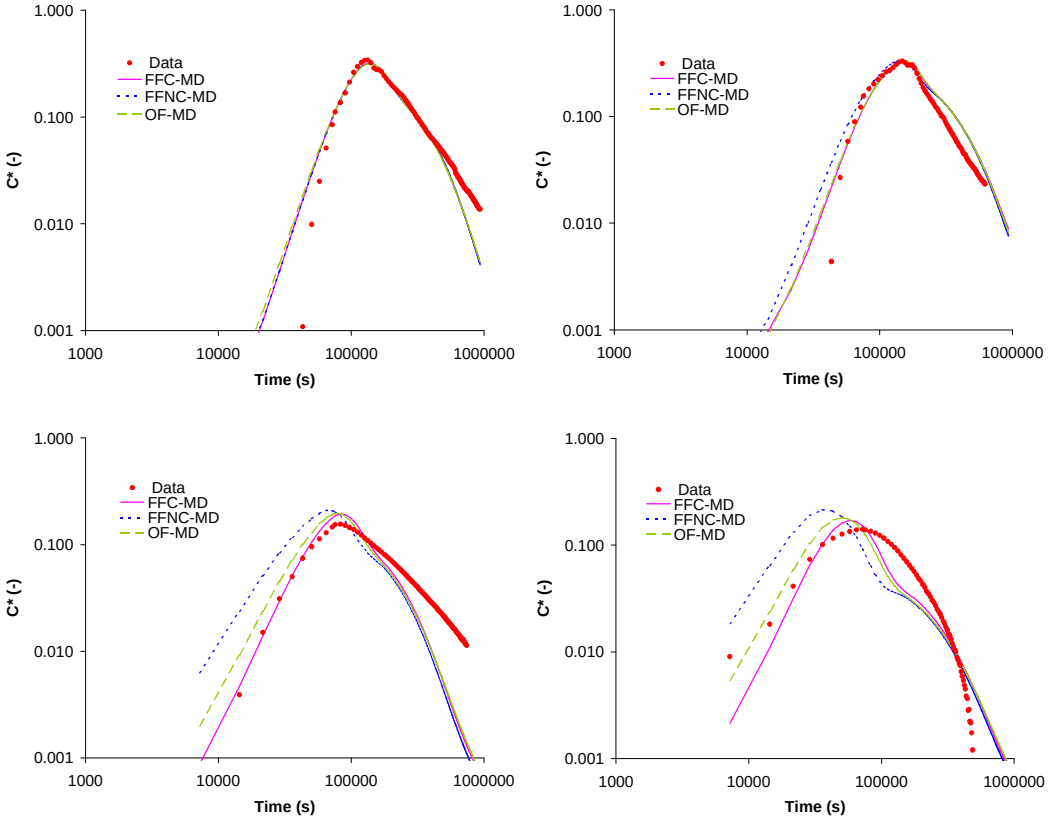

Figure 3.11: Observed and calculated breakthrough curves for PT1, PT2, PT3 and PT4, using the transmissivity field with anisotropy ratio of [1.6/0.4], and taking into account FFC-MD, FFNC-MD and OF-MD fracture models.

Selecting one geostatistical model as the most suitable one using the concentration objective function value as the only one selection criteria is very difficult. The function shape of the Kashyap's criterion in terms of the transmissivity field is not repeated with the objective function of concentrations.

For this reason, we define a new variable, that take into account jointly the Kashyap criterion for the flow and the concentration objective function. This variable, *G*, is defined as the global praising variable:

$$G = \langle G_i \rangle = \frac{G_i - G_{\min}}{G_{\max} - G_{\min}} \tag{28}$$

Where G_i, is defined as the sum of the "praised" kashyap's criterion $<dM_i>$ plus the "praised" concentration objective function $<FC_i>$ for each transport model, that is:

$$G_i = \langle dM_i \rangle + \langle FC_i \rangle \tag{29}$$

As can be seen in (Eq. 3.28), once the G_i values are calculated for each transport model, the global praising function is directly obtained by prising everyone of the Gi values.

In Figure 3.12 the *G* function is depicted. It can be seen that the minimum of *G* is obtained for the FCC-MD fracture model and the $R_{X/Y}$ = [0.4/0.4]. Nevertheless, taking into account the same transmissivity field, FFNC-MD and OF-MD fracture models are "very far" from the minimum of *G*. On the other hand, all values of *G* for $R_{X/Y}$=[1.6/0.4] are very close to the minimum and exhibit very similar *G* values.

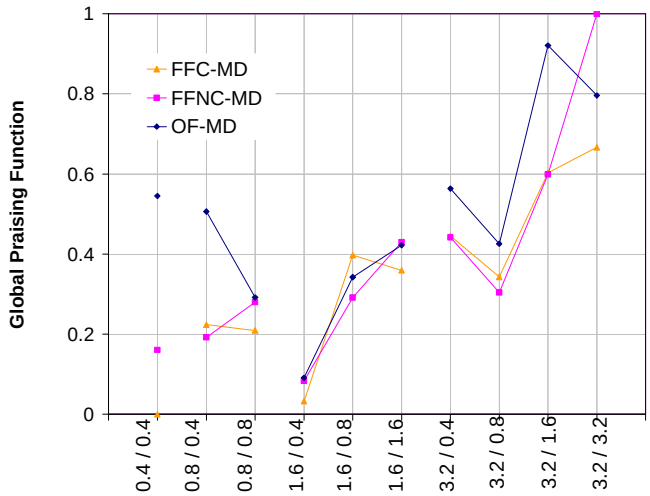

Figure 3.12: Global Praising Function obtained for all transport models

In order to use the G function as a selection we impose a new condition to G: the most suitable transport model is the one which minimize G, and also minimizes the dispersion values of G for the different fracture models and the same T field. In this sense $R_{X/Y}$ = [1.6/0.4] reveals as the most suitable T field obtained for flow and transport modelling.

Using the calibrated solute transport models, predictions were made for the PT5 tracer test. The transport parameters (Table 3.10) estimated from the joint inversion of the four previous tracer tests (PT1, PT2, , PT2 and PT4) were used for the predictions with all the transmissivity fields and all the fracture models. In Figure 3.13 the predicted breakthrough curves for [0.4/0.4] y [1.6/0.4] T fields and all MD fracture models are displayed. In both cases calculated breakthrough curves fit pretty well the observed data. Nevertheless, the transport prediction using the [1.6/0.4] T field is slightly better than the prediction obtained using the [0.4/0.4] T field. This result support the idea presented before in order to select the most suitable transmissivity field for flow and transport.

The selected transport model (in fact the correlation structure in transmissivity) by means of the *G* function is in agreement with the theoretical work of Lunati (2003), who found that at integral distance comparable with the dipole size it is impossible to discriminate among different fracture models, because the effects of local variability in transmissivity dominate those of thickness-porosity-transmissivity correlation. This prevents the identification of any qualitative difference between the breakthrough curves of different fracture models. In this sense all the fracture models fit equally well the observed breakthrough curve using the transmissivity field selected by the *G* selection criterion. In terms of fit, it is not possible to discern any of the three fracture

models as the best fracture spatial variability model of flow porosity for the selected [1.6/0.4] transmissivity field.

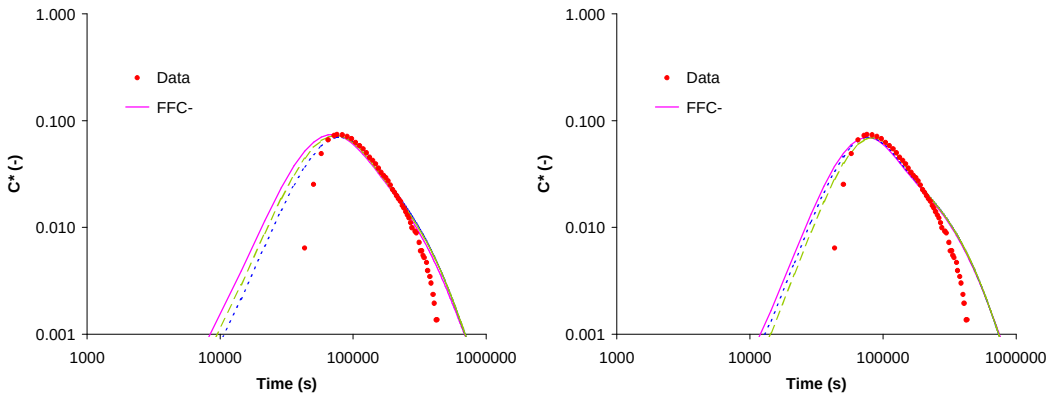

Figure 3.13: Observed and calculated breakthrough curves for PT5 using the transmissivity fields (left) [0.4/0.4] and (right) [1.6/0.4] for FFC-MD, FFNC-MD and OF-MD fracture models.

3.4.Conclusions.

A total of 10 transmissivity fields conditioned on cross-hole pumping test were obtained for different assumed spatial correlation structures of transmissivity, using the geostatistical inverse modelling approach based on the maximum likelihood method.

All the inverted transmissivity fields show the same transmissivity structure, but due to the different anisotropy ratio they display slight differences. The transmissivity fields derived from the inversion reveal a strong heterogeneity and suggest the existence of channels. The main differences between the calibrated T fields stands on these channels.

Despite the different assumed correlation structures, the pattern is very similar in all T fields. In fact, the estimated transmissivity fields with the same anisotropy ratio $R_{X/Y}$ show a practically identical spatial transmissivity structure.

The tracer test model results show that the breakthrough curves can be jointly fitted by using different fracture models on spatial variability of flow porosity.

In general, the obtained values of α_L for OF-MD and FFNC- MD fracture models are larger than the values obtained for FFC-MD. These results are in agreement with the theoretical work of Hassan el al. (1998), who found that a positive correlation between transmissivity and flow porosity decreases longitudinal dispersion and vice versa. Consequently, in order to fit the same breakthrough curve from a tracer test in a heterogeneous media, model parameters controlling longitudinal dispersion have to be larger for models with a positive correlation between flow porosity and transmissivity than for models assuming a constant flow porosity.

In practice, is difficult to establish an adequate model for the spatial variability of flow porosity and its correlation with transmissivity. The lack of a common selection criterion for flow and transport makes it difficult to select the most suitable jointly flow

and transport. The selection criterion in terms of the concentration objective function does not coincide with the Kashyap's criterion.

In order to establish a common selection criterion for flow and transport, a new function named Global Praising Function "*G*" has been defined. The out come of transport predictions for PT5 vouches for the Global Praising Function selected model; $R_{X/Y}$=[1.6/0.4] has revealed as the most suitable T field obtained for flow and transport modelling.

The simulated breakthrough curves for PT5, obtained using the transmissivity field selected by the *G* selection criterion are very similar. In this sense all the fracture models fit equally well the observed PT5 concentration data. In terms of fit, it is not possible to discern any of the three fracture models as the best fracture spatial variability model of flow porosity for the selected $R_{X/Y}$=[[1.6/0.4] transmissivity field.

3.5.References.

Akaike, H., (1974): A new look at statistical model identification. IEEE Trans. Automat. Contr. AC-19:716-722.

Akaike, H., (1977): On entropy maximization principle. In: Krishaiah PR (ed) Applications of statistics. North Holland, Amsterdam, pp27-41.

Akaike, H., (1978): A new look at the Bayes procedure. Biometrika, 65(1), 53-59

Barker, J., (1988): A generalized radial-flow model for pumping tests in fractured rocks. British Geological Survey. Wallinford, Oxfordshire, ox10 8BB, UK55 pp.

Bear, J., (1972): Dynamics of fluids in porous media. Elsevier, 1972.

Bossart, P. and M. Mazurek, (1991): Structural geology and water flow-paths in the migrati0on shear-zone. NAGRA Technical Report 91-12. Wettingen, Switzerland.

Brodsky N., Stormont J., Fredrich J. (2000): Laboratory measurements of porosity, gas threshold pressures, and gas, liquid, and relative permeabilities for shear zone material from the Grimsel Test Site, Switzerland. NAGRA Internal Report 00-15, Wettingen, Switzerland

Bury, K.V.,(1975): Statistical models in applied science. John Wiley. New York.

Capilla JE, Gómez-Hernández JJ, Sahuquillo A, (1997): Stochastic Simulation of Transmissivity Fields Conditional to Both Transmissivity and Piezometric data, 2.Demonstration on a Synthetic Aquifer, J Hydrol 1997; 203:175-88.

Carrera, J., (1984). Estimation of aquifer parameters under transient and steadystate conditions Ph. D. Dissertation. Departemento de Hidrología y Recursos Hidráulicos. Universidad de Arizona. Tucson, Arizona, 258 p.

Carrera J, Neuman SP.,(1986): Estimation of aquifer parameters under transient and steady-state conditions, 1. Maximum likelihood method incorporating prior information, Water Resour Res 1986a; 22(2): 199-210.

Carrera J, Neuman SP., (1986): Estimation of aquifer parameters under transient and steadystate conditions, 2. Uniqueness, Stability and Solution Algorithms, Water Resour Res 1986b; 22(2):211-27.

Carrera J, Neuman SP., (1986): Estimation of aquifer parameters under transient and steady-stateconditions, 3. Application to synthetic and field data. Water Resources Research 1986c; 22(2), 228-242.

Carrera J., Medina A., Sanchez-Vila X., (1992): Geostatistical Formulation of Groundwater Coupled Inverse Problems.TROIA'92. Fourth Int. Geostatistics Congress. Vol. 2, pp. 779-793.

Carrera J.,(1993): An overview of uncertainties in modelling groundwater solute transport. J. Contam Hydrol 1993, 13: 23-48.

Carrera J. and A. Medina, (1994). An improved form of adjoint-state equations for transient problems. X International Conference on Methods in Water Resources, (A. Peters, G. Wittum, B. Herrling, W. Meissner, C. A. Brebbia, W. Grau, G. Pinder) Heidelberg, Alemania, Julio 19-22.pp. 199-206.

Cooper H. and C. Jacob., (1946): A generalised graphical method for evaluating formation constants and summarising well-field history. AGU, 27(4), 526-534.

Cooper, H., Papadopulos, I.S., (1967): Response of a finite diameter well to an instantaneous charge of water. Water Resources Research(27), 4: 526-534.

Fierz T., and M. Piedevache, (2000): GTS/GAM: Results of hydraulic tests and gas threshold pressure tests in GAM 98-002 (January/February 2000). NAGRA Internal Report 00-14, Wettingen, Switzerland.

Fierz T., Proust E., Combarieu M.and P. Meier, (2000): GTS/GAM: Gas tracer test series GT1 in the GAM shear zone (February 2000). Dipole flow field GAM98-002/TPF95-007. NAGRA Internal Report 99-30, Wettingen, Switzerland.

Gemperle, R., & SOLEXPERTS AG, (1999a). Hydraulic testing in GAM 98.002 and GAM 98.004. NAGRA Internal Report 99-03, Wettingen, Switzerland.

Gemperle, R., & SOLEXPERTS AG, (1999b): Final Borehole completion report. NAGRA Internal Report 99-02, Wettingen, Switzerland.

Gimmi T., Schneebeli M., Flühler H., Wydler H., Baer T., (1997): Field-Scale Watrer Transport in Unsaturated Crystalline Rock. Water Resources Research, Vol. 33, Number 4, pp 589-598.

Gómez-Hernández JJ, Sahuquillo A, Capilla JE., (1997): Stochastic simulation of transmissivity fields conditional to both transmissivity and piezometric data. 1. Theory, J Hydrol 1997; 204(1-4):162-74.

Hannan, E.S., (1980): The estimation of the order of the ARMA process. Ann. Stat. (8):1071-1081.

Hassan A.E., Cushman J.H. and Delleur J.W., (1998): The significance of porosity variability to transport in heterogeneous porous media. Water Resources Research, Vol. 34(9), pg 2249.

Honjo Y., Wen-Tsung L. and Sakajo S. (1994): Aplication of Akaike information criterion statistics to geotechnical inverse analysis: the extended Bayesian method. Structural Safety, 14. 5-29.

Kashyap R.L.,(1982): Optimal choice of AR and MA parts in autoregressive moving average models. IEEE Trans. Pattern. Anal. Mach. Intel. PAMI 4(2):99-104.

Kennedy, K., (1999): Solute and particle tracer tests PILOT and PT1 in the GAM shear zone (Dec, 1998 to April, 1999). NAGRA Internal Report IB 99-49, Wettingen, Switzerland.

Kennedy, K., (2000a): Solute and particle tracer test PT2 in the GAM shear zone (May, 1999). NAGRA Internal Report IB 00-07, Wettingen, Switzerland.

Kennedy, K., (2000b): Solute and particle tracer test PT3 in the GAM shear zone (August, 1999). NAGRA Internal Report IB 00-08, Wettingen, Switzerland.

Kennedy, K. and Kleiner, A., (2000): Tracer tests PT4 and PT5 in the GAM shear zone (August, September 1999). NAGRA Internal Report IB 00-41, Wettingen, Switzerland.

Kitanidis P.K, (1995). Quasi-linear geostatistical theory for inversing.Water Resources Research, 31(10), 2411-2419.

Lunati I. (2003): Conceptuals models of single and multiphase transport in a fracture. Ph.D. dissertation, Eidgenössische Technische Hochschule Zürich (ETH) Switzerland.

Marschall P., Croisé J., (1999): Grimsel Test Site - Determination of two-phase flow properties in shear zones. NAGRA (Nationale Genossenschaft für die Lagerung radioaktiver Abfälle) Internal Report NTB 97-06, Wettingen, Switzerland

McLaughlin D, Townley LLR., (1996): A reassessment of the groundwater inverse problem, Water Resour Res 1996; 32(5):1131-61.

Medina A, Carrera J., (1992): Estimación de parámetros e identificación de modelos en problemas de flujo y transporte transitorios. V-Simposio de Hidrogeología. Alicante, pp 77-91.

Medina A, Galarza G., Carrera J.,(1996): Transin-II,Fortran code for solving the coupled flow and transport inverse problem in saturated conditions. In El Berrocal Project. ENRESA Topical Report 4(16).

Medina A, Carrera J., (2003): Geostatistical inversion of coupled problems: dealing with computational burden and different types of data, J Hydrol 2003; 281:251–64.

Medina A, Alcolea A, Carrera J, Castro LF., (2000) Modelos de flujo y transporte en la geosfera: Código Transin IV. [Flow and transport modelling in the geosphere: the code TRANSIN IV], in: IV Jornadas de Investigación y Desarrollo Tecnológico de Gestión de Residuos Radiactivo de ENRESA. Technical publication 9/2000: 195-200

Meier P., Carrera J., Sanchez-Vila X., (1998): An evaluation of Jacob's method for the interpretation of pumping tests in heterogeneous formations. Water Resources Research(34), 5: 1011-1025.

Meier P., (1999): Estimation of representative groundwater flow and solute transport parameters in heterogeneous formations. Ph.D. dissertation, School of Civil Engineering, Barcelona.

Meier P., Medina A., Carrera J., (2001): Geostatistical inversion of cross-hole pumping test for identifying preferential flow channels within a shear zone. Ground Water, 39(1), 10-17.

Nauman E.B., Buffham B.A. (1983): Mixing in continuous flow systems. John Wiley & sons.

Olivella S., Carrera J., (1987): KRINET (kriging Network). Computer code for optimal design of observation networks through geostatistics. User's guide (draft) E.T.S.I. Caminos Canales y puertos. Universitat Politècnica de Catalunya, Barcelona, Spain.

RamaRao BS, Lavenue M, de Marsily GH, Marietta MG., (1995): Pilot point methodology for automated calibration of an ensemble of conditionally simulated transmissivity fields. 1. Theory and computational experiments, Water Resour Res 1995; 31 (3):475-93.

Schneebeli M., Flühler H., Gimmi T., Wydler H., Läser H., (1995): Measurements of Water Potential and Water Content in Unsaturated Crystalline Rock. Water Resources Research, Vol. 31, Number. 8, pp. 1837-1843.

Trick, T., (2000): GTS V/GAM: Results of hydraulic tests in GAM 98-004 (August 2000). NAGRA Internal Report 00-50, Wettingen, Switzerland.

Trick T., Fierz T., Proust E., Meier P., and Combarieu M., (2000):.GTS/GAM: Gas tracer test series GT2 in the GAM shear zone (August 2000). Dipole flow field GAM98-004/TPF95-004. NAGRA Internal Report 00-49, Wettingen, Switzerland.

Trick T., Piedevache M., Proust E., Meier P. and Combarieu M., (2000):. GTS/GAM: Gas tracer test series GT3 in the GAM shear zone (December 2000). Dipole flow field GAM98-002/TPF95-007. NAGRA Internal Report 01-02, Wettingen, Switzerland.

Wyss, E. (1996): GTS/TPF: Site preparation, borehole installation, hydraulic characterisation and gas threshold-pressure tests at the Grimsel Test Site. (July, 1996). NAGRA Internal Report 96-34, Wettingen, Switzerland.

Yeh, T.C.J., M. Jin, S. Hanna (1996): An iterative stochastic inverse method: Conditional effective transmissivity and hydraulic head fields. Water Resour Res 1996; 32(1): 85-92 .

Zimmerman DA, de Marsily GH, Gotway CA, Marietta MG, Axness CL, Beauheim RL, Bras RL, Carrera J, Dagan G, Davies PB, Gallegos DP, Galli A, Gómez-Hernández J, Grindrod P, Gutjahr AL, Kitanidis PK, Lavenue AM, McLaughlin D, Neuman SP, RamaRao BS, Ravenne C, Rubin Y. (1998): A comparison of seven geostatiscally based inverse approaches to estimate transmissivities for modelling advective transport by groundwater flow, Water Resour Res 1998; 34(6): 1373-1413.

Chapter 4: Multiphase flow in a heterogeneous fracture. Sensitivity to Injection and Observation wells

4.1. Introduction

Quantitative description of multiphase flow in fracture media is still an area under development. One of the main difficulties to overcome is the description of internal heterogeneity in the most conductive hydraulic structures. This is due to the fact that gas flux concentrates in open channels. The physical problem becomes difficult to simulate because trajectories followed by the gas are extremely sensitive not only hydraulic conductivity, but also retention properties and variations in pressure.

Fracture conceptualisations available in the literature include channel models, two-dimension heterogeneous porous medium and one-dimensional variable aperture fracture models.

The channel model was proposed by Tsang and Tsang (1987) and Neretnieks (1993), on the basis of both theoretical and experimental observations. They used a system of statistically equivalent one-dimensional flow paths as channels to simulate the flow and convection processes in a fracture. The characteristic parameters for channel models are the effective channel length and width and the aperture density distribution and spatial correlation length. The aperture channels were generated by geostatistical methods, providing both variable channel density and apertures along individual flow channels.

Channelling may occur even if channels are not modelled explicitely. Moreno and co-workers (1988) modelled the fracture as a strongly heterogeneous porous medium. The fracture was discretised into a squared mesh to which variable apertures were assigned. These were generated using geostatistical methods based on the probability density distribution and a spatial correlation length. This model has been used to study the channelling behaviour. They showed that flow concentrates on a few channels.

The one-dimensional variable aperture fracture model was initially developed by Neuzil and Tracy (1981). In this model, a fracture is conceptualised as having a constant aperture in the direction of flow but variable apertures in the normal direction. Neretnieks and others (1982) used this fracture model to describe a series of solute migration experiments in a single fracture in granite. They showed that the model reproduced experimentally measured breakthrough curves and solutes were only transported in a limited number of channels.

Even though for any problem involving single-phase flow it is possible to conceptualise a single fracture as a set of interconnected channels, these channel models are not suitable for two-phase flow modelling. This is caused by the presence of one phase in a fracture that can block the other, forcing each phase to use different flow channels. Definition of these channels would be impossible, since the connected region for each phase would vary with changes in saturation and potential gradient (Murphy and Thomson, 1993).

Mendoza (1992) improved the theory of Pruess and Tsang (1990) by incorporating the inlet accessibility and fluid trapping criteria. In all these cases, the theory followed is the

percolation theory which should be only applied when the displacement is dominated by capillary pressure and the driving forces can be neglected.

Simulations of multiphase flow through a single fracture using a conventional multiphase flow approach will encounter serious difficulties in modelling gas migration. The pressures registered in field experiments (Fierz et al. 2000, Trick et al. 2000, Trick et al. 2001) demonstrate that the gas injected does not migrate uniformly from the injection point in the fracture. It moves following preferential paths. Due to the sensitivity of gas to the heterogeneity of the medium, the physical problem becomes difficult to solve. For this reason, a sensitivity analysis of the gas injection tests to various parameters is carried out.

4.2. Model development

4.2.1 Governing equations

The equations governing multiphase flow are derived from momentum conservation (Darcy's law) and mass conservation. The latter is expressed for each component, which reads:

$$\frac{\partial}{\partial t}\left(q_l^w S_l f + q_g^w S_g f\right) + \nabla \cdot \left(\mathbf{j}_l^w + \mathbf{j}_g^w\right) = f^w \tag{4.1}$$

$$\frac{\partial}{\partial t}\left(q_l^a S_l f + q_g^a S_g f\right) + \nabla \cdot \left(\mathbf{j}_l^a + \mathbf{j}_g^a\right) = f^a \tag{4.2}$$

Where the superscripts *w* and *a* represents species water and air respectively, and the subscripts *l* and *g* refer to liquid and gas phase respectively, *f*[-]is porosity, *?*[ML^{-3}] is the mass content per unit volume of phase (i.e., *?=? r* being *?* [-] the mass fraction and *r*[ML^{-3}] the density*)*, *S* [-] is the phase saturation degree, *f*[$ML^{-3}T^{-1}$] is a sink/source term (i.e. an external supply of water or air depending on the superscript), and **j**[$ML^{-2}T^{-1}$] is a total mass flux respect a fixed reference system.

The total mass flux of a species in a phase is the sum of three terms:

- The nonadvective flux (diffusive/dispersive)
- The advective flux caused by species motion
- The advective flux caused by solid (which contains the species) motion

The relative contribution of each flux term to the total flux is not always the same. For instance, diffusion will become more important if advection is small.

The constraints associated with equations 1 and 2 are:

$$P_c = P_g - P_l \tag{3}$$

$$S_l + S_g = 1 \tag{4}$$

Where P_c [$ML^{-1}T^{-2}$] is capillary pressure.

These equations are subjected to the definition of the boundary conditions and complemented by the constitutive laws for the fluids and the medium.

The interaction between the fluids is described by the relative permeability curves. The multiphase studies have considered the relative permeability of individual fractures as two phases flowing simultaneously. It was found that interference between phases is strong Persoff et al. (1991). This causes the sum of wetting and nonwetting phase-relative permeabilities to be small ($k_{rw}+k_{rg}<1$) at the intermediate saturations (Pruess and Tsang, 1990). This was confirmed with laboratory experiments (Persoff and Pruess, 1995), being consistent with insights gained from percolation theory for the connectivity of 2-D lattices.

In Figure 4.1 relative permeability data obtained from the laboratory investigations performed in cores samples containing GAM shear zone material (Brodsky et al. 2000), and also relative permeability data for flow through rough-walled empty fractures obtained by Persoff et al. (1991) and Persoff and Pruess (1995). are showed. These data are compared against commonly used relative permeability relations for porous media, the X-curve (Romm, 1996) and Corey curve (Corey, 1954). As can be sown the experimental relative permeability data from the GAM fracture resembles more the X-curve model. In this sense, taking into account the X-curve model, a linear relationship is assumed between the relative permeability of every phase α and the phase saturation degree, that is:

$$K_{ra} = S_a \tag{5}$$

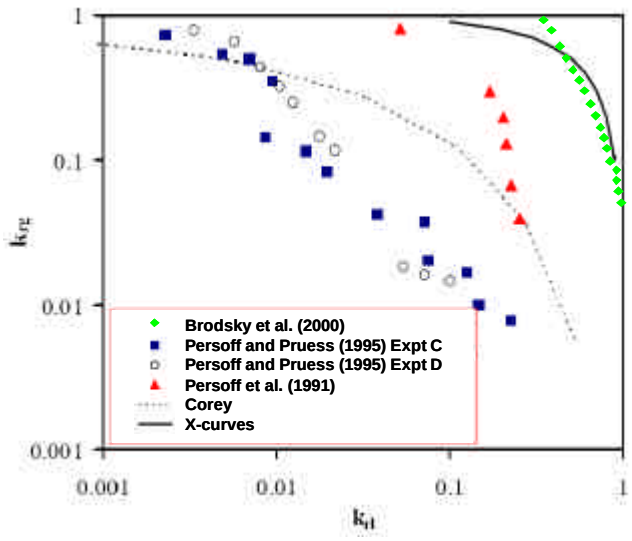

Figure 4.1: Measurement of air-water relative permeabilities in rough-walled empty fractures (Modified original from Horne et al. 2000).

Two different scenarios for modelling two phase flow were considered: Fault gauge filled fracture and Open Fracture (Fig. 4.2).

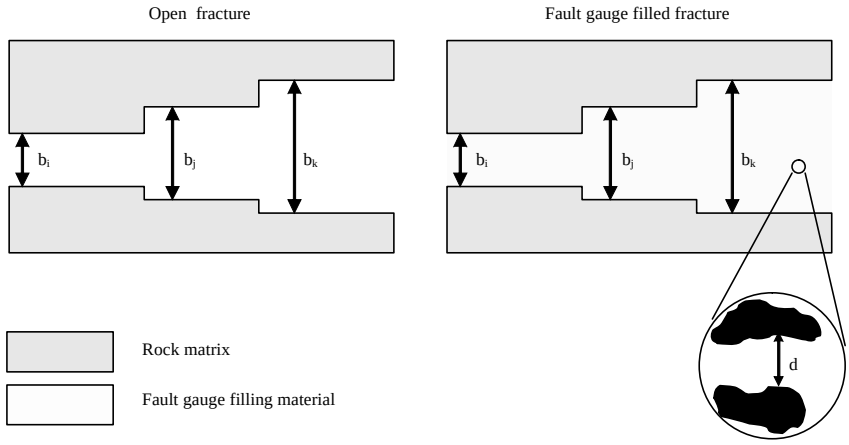

Figure 4.2: Fracture conceptual models

The constitutive laws to compute fracture aperture, capillary pressure and gas entry pressure are different depending on the considered fracture model.

4.2.1.1 Fault gouge filled fracture constitutive laws

In this case, the thickness of the fracture b[L] is calculated as considering the fracture as an equivalent porous media, that is, dividing the transmissivity T[L^2T^{-1}] by the fracture permeability K[LT^{-1}]:

$$b = \frac{T}{K} \tag{6}$$

In order to calculate the capillary pressure P_c[$ML^{-1}T^{-2}$] as a function of the liquid saturation degree S_l[-] we use the Van-Genuchten (1980) equation that is:

$$P_c = P_b \left(S_l^{-\frac{1}{l}} - 1 \right)^{1-l} \tag{7}$$

Where l[-] is the Van-Genuchten parameter, P_b[$ML^{-1}T^{-2}$] is the gas entry pressure .

The Van-Genuchten parameter l has been fitted by means of several laboratory experiments (Marshall et al., 1998) performed in representative fault gouge filling material from the GAM fracture.

Entry pressure P_b [$ML^{-1}T^{-2}$] is the microscopically definition of capillarity derived from the Young-Laplace equation, and is computed as:

$$P_b = C_{pb} \left(\frac{2s}{d} \right) \tag{8}$$

where: C_{pb}[-] is a proportionality coefficient, s [$ML^{-1}T^{-2}$] is the surface tension and d[L] is the pore aperture.
To compute the pore aperture we use Hazen's approximation (Hazen 1911), which is an empirical equation which estimates hydraulic conductivity K[LT^{-1}] as being linearly proportional to the square of the effective grain size (d_{10}), that is:

$$K = C_H d_{10}^2 \tag{9}$$

where C_H[$L^{-1}T^{-1}$] is a material coefficient. Mbonimpa et al. (2002) present a summary about the estimation values of C_H in terms of K and d_{10}.

4.2.1.2 Open fracture constitutive laws
In this case fracture thickness b[L] is computed in terms of fracture transmissivity T[L^2T^{-1}] by means of the cubic law, that is:

$$b = \left(\frac{12m}{rg} T \right)^{\frac{1}{3}} \tag{10}$$

Where m[$ML^{-1}T^{-1}$] is the dynamic viscosity, r[ML^{-3}] is water density and g[LT^{-2}] is the gravity acceleration.

The interaction between phases is represented by means of a step retention curve (Equ.11) based upon the idea that parallel plates that represent the domain are in practice either full or empty of water (similar to the concept of two states in percolation theory). In this sense the P_c is computed as a linear function of the product between the factor b[$ML^{-1}T^{-2}$] and the liquid saturation degree S_l.

$$P_c = -bS_l + \left(b + P_b \right) \tag{11}$$

The factor b is related with the fracture aperture distribution (Ramajo et al, 2002), and is computed as:

$$b = 2s \left(\frac{1}{b_{\min}} - \frac{1}{b_{\max}} \right) \tag{11}$$

where s [$ML^{-1}T^{-2}$] is the surface tension and b_{min}[L] and b_{max}[L] are the minimum and maximum values respectively of the fracture aperture field obtained applying (Eq. 4.10) to the fracture T field. In order to obtain a sharp retention curve is necessary to set a sufficiently small value of b.

Entry pressure P_b is computed as in the fault gouge fracture filled case (Eq. 4.8). In this case the pore aperture d becomes equals to the fracture thickness b (Eq. 4.10).

In this case, the interaction between phases is represented by means of a step retention curve based upon the idea that parallel plates that represent the domain are in practice either full or empty of water (similar to the concept of two states in percolation theory.

Due to the complexity of the above equations they cannot be solved analytically, for this reason we need to apply numerical methods. The numerical simulations for these gas injection tests were performed using the multiphase flow code CODE-BRIGHT (Olivella et al., 1996). It is a finite-element code to analyse thermo-hydraulic-mechanics problems (THM).This code has not implemented the automatic inversion approach. Indeed, it is a trial-and-error code to simultaneously match the pressure data for all the gas-injection tests. This approach is an alternative to quantitative optimisation schemes. These rely on automatic adjustments of parameter values to reduce the sum of weighted variance of physical states to a given criterion. It relies on the subjective judgement of the researcher and is more flexible than the automatic optimisation scheme. It also allows incorporation of soft information. Soft data such as geological and radar information can help to shed light on the flow connectivity and permeability characteristics of the medium when coupled with crosshole pressure data. Such soft information is useful for the problem: although we conceptualise the fracture as a continuum, flow is in fact channelled through preferred paths of lower fluid resistance.

4.2.2 Conceptual model

This work focuses mainly on modelling multiphase flow in a fracture. The problem consider 3 phases: solid phase, liquid phase (water and dissolved gas), and gas phase.

The physics of two-phase flow in fractures is well understood. Nevertheless, modelling presents some problems due to the difficulty in obtaining consistent hydrogeological parameters and constitutive relationships at the appropriate scale.

Many studies have shown that the idealised parallel-plate model is inadequate for understanding flow and transport behaviour of fractures on a field scale. There are a number of methods to calculate fracture aperture that control contaminant transport. The hydraulic aperture of a fracture is defined by its hydraulic properties that produces a given discharge. The transport aperture of a fracture can be defined by average aperture that matches the velocity calculated by solute transport. The mechanical aperture which can be defined two ways: 1) the arithmetic mean of all the aperture values in flow path and 2) a generic measure of physical separation of two walls of a fracture. The differences in methods to calculate aperture can create discrepancies in contaminant transport calculations. For instance, the transport fracture aperture can exceed the "'hydraulic" fracture aperture by as much as 2 or 3 orders of magnitude (Neretnieks, 1993). The large deviation from the cubic law arises from the spatial variability of apertures in real rough-walled fractures. Generally speaking, smallest apertures (bottlenecks) control permeability, while the larger apertures contribute most to the void volume to be swept by solute tracer. Thus, fracture permeability and fracture aperture, in the sense of void volume per unit fracture wall area, are essentially independent parameters for real rough-walled fractures. The contaminant model predictions differences arise when determining whether to use hydraulic, transport or mechanical fracture apertures.

In some circumstances it is necessary to distinguish between the rock matrix porosity and the fracture porosity. In spite of the fact that fluid may flow mainly through the fracture, it is recognised that the interaction with the matrix could be important when it provides a significant addition to the storage capacity of the system. In this sense, several investigations were carried out in our interest area, where the GAM project was

performed. On one hand, there is an investigation performed by Bossart & Mazureck (1991) that aimed estimating the porosity of the gouge material. On the other hand, there are also recent studies done by Marschall and Croisé (1999) whose objectives were to study the aperture distributions across the brittle structures. Finally, there is another investigation carried out by Sandia laboratories (Brodsky et al, 2000), to obtain relationships between permeability and porosity at the field scale. The experimental data and the geological composition suggests that the interaction between the matrix and the fracture is negligible during multiphase flow. Then the fracture zones filled with fault gauge are assumed to behaves as a porous medium. Nevertheless, the empty fracture zones (containing no material) which are the preferential paths followed by the gas are assumed to follow a parallel-plate model.

The fracture is considered as a 2D domain initially fully saturated of water (S_l=1). Gas is injected in the fracture displacing the liquid phase (liquid phase is considered incompressible) and assuming laminar flow for gas and water.

The considered forces are: viscosity, capillarity and gravitational (in our case heterogeneity and viscous terms are much more important than gravity since aperture is small), and isothermal conditions (T= 15ºC) are supposed.

We analyse sensitivity to those parameters which are unknown or highly uncertain. These parameters are:

- The injection well: gas /water exchange: Prior to beginning of the gas injection test, the water within the injection test interval is replaced by gas. This is accomplished by injecting gas through the injection (pressure) line and extracting water through the extraction (flow) line (Fig 3). Gas pressure at injection interval increase until the gas formation entry pressure is reached, and then gas begins to flow inside the fracture. During the gas/water exchange, since there is no gas flux inside the fracture, pressure evolution inside the injection interval basically depends on the interval volume. This volume depends on the amount of water remaining in the interval after the gas/water exchange. This volume is relevant for two reasons: On one hand the smaller injection interval the faster pressure increasing, and on the other hand the water volume in the injection interval behaves as a reservoir for dissolved gas, been the gas solubility in water a function of the partial gas pressure inside the gas injection interval.

- The observation wells: They might be a possible storage of dissolved gas because the volume of water between packers (interval) is large compared to the volume in the fracture.

- The relationship between transmissivity and thickness porosity: To this end we consider two fracture hypotheses. First, we have described the fracture as an open fracture, assuming a cubic relation (Equ.10) between the aperture and the *T*. Second, an homogenous fault gouge filled fracture whit variable aperture, calculated as considering the fracture as an equivalent porous media, that is, dividing the transmissivity by the fracture permeability (Equ.6)

- T fields: The correlation length of the T in the field is a hazy parameter since it is obtained from geological soft data. Consequently, we need to observe for

various correlations so as to get several T fields where multiphase flow must be carried out. The T fields taken into account for this purpose are different from those obtained in chapter 3, because the internal structure of the fracture have changed as was pointed in chapter 2. These structural changes were due to pressure release, washing-out caused by an increasing water flow or the existence of a high hydraulic gradient during brine injection. For this reason, a new geostatistical inversion of the two last constant rate injection test was performed. In this case the T anisotropy ratios considered for the variogram were [0.4m /0.4m], [0.8m /0.4m], [1.6m /0.4m] and [1.6m /0.8m] (i.e. Range-X / Range-Y).

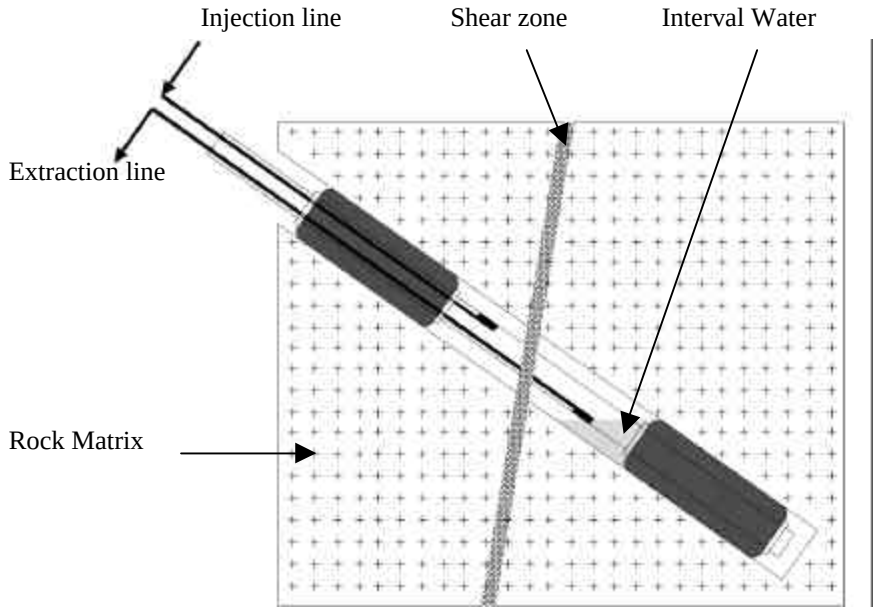

Figure 4.3: Schematic representation of the isolated borehole interval which penetrates a shear zone. The interval is isolated by means of a packer system. In order to replace water by gas in the interval, gas is injected through the injection line, and water is extracted through the extraction line. Depending on the position of the extraction line inside the interval, a volume of water will remain inside the interval inside the interval.

4.2.3 Model structure

During the GAM project the field investigations were being carried out in a 4x6 m^2 section of the GAM shear zone. The investigations involved the exploration of the fracture with 26 boreholes. Figure 4.4 shows the intersection points of the boreholes with the plane of the shear zone. The modelled region has been represented as a rectangular 2D domain of 18.6x18.6 m^2 centred on the wells, in order to simulate the gas pressure injection tests performed in the shear zone in the framework of the GAM project.

As explained in Chapter 3 the transmissivity field values are obtained following the same methodology presented by Meier et al. (2001). This methodology consist in the geostatistical inversion of the two last hydraulic tests performed in the fracture at the Grimel test site (Alber,W., 2000a,b,c) in the framework of the GAM project. The effective transmissivity is of the order of 10^{-9} m^2/s and the storage coefficient falls around 10^{-6}.

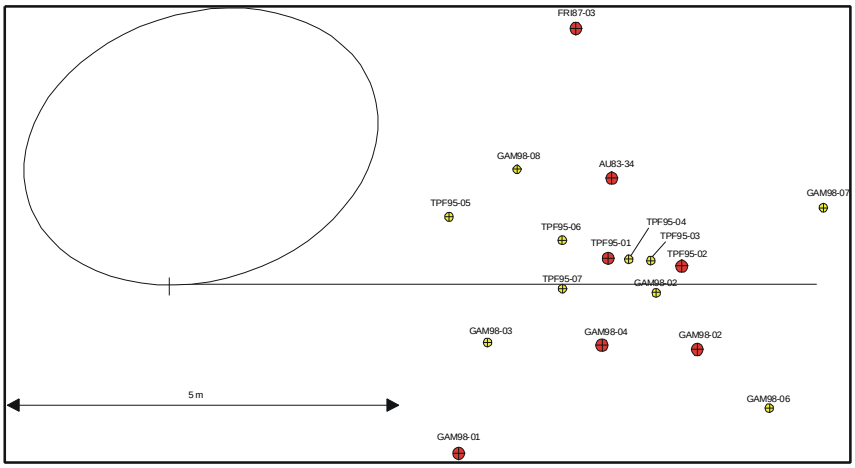

Figure 4.4: Intersection of boreholes at the GAM site with the shear zone plane. Small (yellow) circles are the boreholes with diameters of 36mm and big (red) circles are boreholes with diameters of 86mm or more.

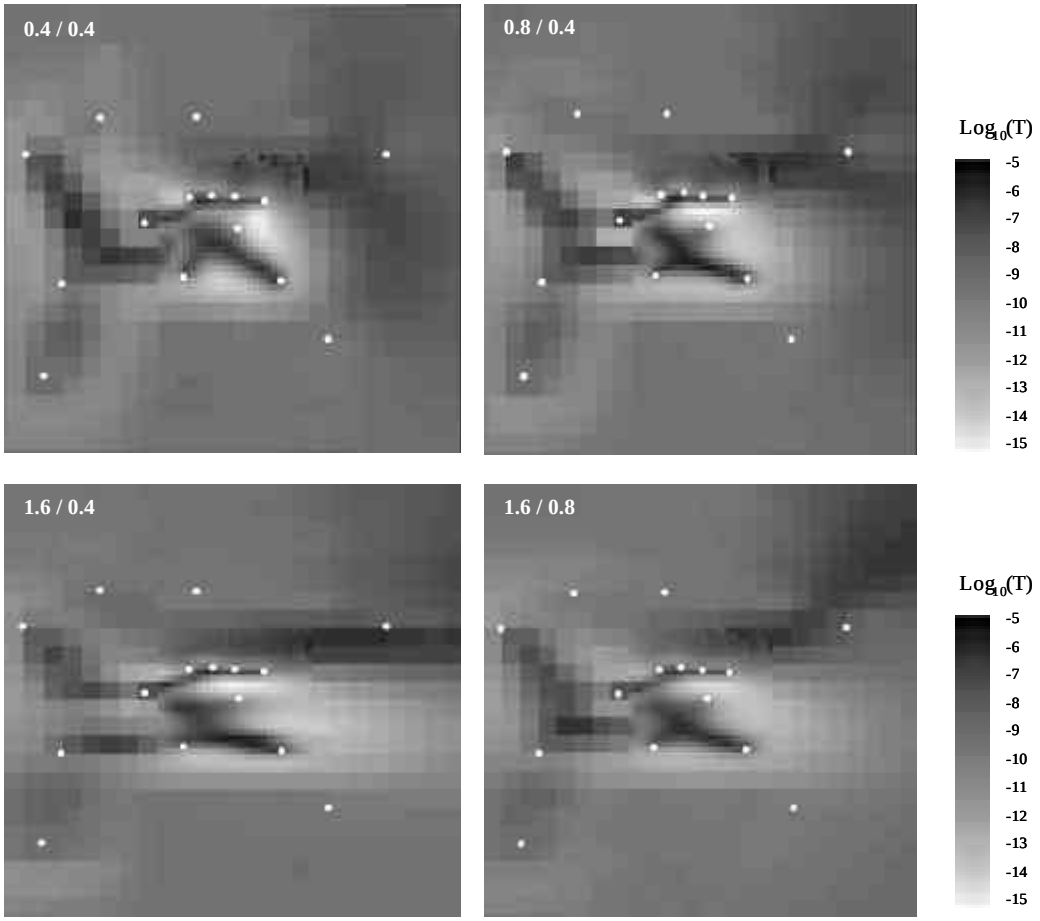

Figure 4.5: Log_{10}-Transmissivity Fields obtained from the joint interpretation of the last two hydraulic tests performed in the framework of the GAM project by means of stochastic inversion. The transmissivity anisotropy ratio (I_x/I_y) is showed on the upper left corner of each transmissivity field. White points are observation boreholes

Once the transmissivity field is defined we must establish the relationship between T and the thickness porosity. To this purpose, we must select between a fault gouge filled fracture or an empty fracture model.

We have represented the injection, the extraction and the observation wells using 1D elements that incorporate the interval properties. These properties are: the known volume between packers, the high transmissivity assigned to the interval between packers, the capillary pressure near zero in order to define a plane interface between the liquid and the gas phases. A maximum degree of water saturation of 0.01 to represent an injection well interval initially filled with gas, and finally a linear relative permeability curve K_{rl} for the liquid and a K_{rg} equal to 1 to represent a fully mobile phase.

Another necessary information is the initial and the boundary conditions used for the model. We have a gas injection at the injection well to represent the known inflow rate, and a mixed condition at the extraction well. Here the liquid pressure is prescribed to the atmospheric pressure to represent the fact that the hole is open at the tunnel. Hydrostatic conditions were applied at the external boundaries. To simulate this state we have defined 1-D elements at the external boundaries with the following properties: small porosity to avoid the storage of water in these elements, high transmissivity, high gas entry pressure so as to consider just water. Prior to simulating the gas-injection experiments, the initial equilibrium pressure distribution of the medium under gravity was obtained until the system reached steady state for the assumed hydrostatic initial conditions.

The criterion followed to choose the spatial discretisation is the one used by the hydraulic and tracer tests (Jodar et al., 2003). Due to CPU limitation, when interpreting the hydraulic and tracer tests by means of the geostatistical inversion approach we cannot afford a fine discretisation. This is a misfortune for the multiphase flow simulation where discretisation should be finer. This complicates the method because if we want to discretise more, we also need to find equivalent parameters in a smaller Representative Elemental Volume (REV) referring to the downscaling problem. In this work, we have assumed that the variability is small in the central part where the majority of the wells are located. If the heterogeneity is relatively small, it was proved in a previous investigation (Ramajo et al., 2002) that the solution practically was the same for coarser and finer grids, which simplifies calculations.

4.3. Results

In order to find the model that best reproduces the features of the field data a large number of simulations were. The simulation that best fits the experimental measurements in terms of pressures and volume of gas recovered is defined as the base case. In order to study the relative importance of the different parameters pointed out in the last section, we have carried out a sensitivity study respect to the selected parameters, modifying the base case and comparing the obtained results.

The base case main features are: anisotropic transmissivity field, with an anisotropy ratio of [1.6m /0.8m], an open fracture model, with field apertures related by the cubic law with the transmissivity field values and the hydrostatic pressure as external boundary condition. The observation boreholes are included as possible gas storage and finally an injection well interval initially filled with gas. Thus, so no gas /water

exchange is taken into account. In Table 4.1, we present the characteristics of the different cases accounted in the sensitivity analysis.

Table 4.1 Characteristics of the different models accounted in the sensitivity analysis

	Anisotropy Ratio*	Fracture Model	Observation Wells	Gas/Water Exchange
Base Case	1.6 / 0.8	Open Fracture	Yes	No
Case-I	1.6 / 0.8	Open Fracture	Yes	Yes
Case-II	1.6 / 0.8	Open Fracture	No	No
Case-III	1.6 / 0.8	Porous Media	Yes	No
Case-IV	0.8 / 0.4	Open Fracture	Yes	No
Case-V	0.4 / 0.4	Open Fracture	Yes	No
Case-VI	1.6 / 0.4	Open Fracture	Yes	No

* See Fig. 4.5

The sensitivity analysis has been performed respect to the parameters highlighted in Section 4.2.2. These are gas/water exchange in the injection well, the role play by the observation wells, the relationship between transmissivity and thickness porosity, and finally the transmissivity fields. Results are presented in terms of gas pressure at the injection well, the gas flow rate recovered, and also the gas pressure at the observation wells (Figs. 6 to 9).

Regarding the effect of gas/water exchange (Case-I) at the injection well study: In terms of calculated gas pressure (P_g), the main difference between the base case and the case that simulates the exchange of gas and water at the injection well, is detected at the very beginning of the response (Fig. 4.6A). Field data fits a linear function that describes the increase of the gas pressure that holds at the injection well. When the exchange is simulated, the initial pressure achieved depends on the characteristics of the field around the well, whereas, in the base case, the initial pressure is equal to the measured data. This originates the shift of the latter from the base case. This deviation becomes negligible when the response goes further than the so-called radius of influence. They converge once the injection interferes with the boundary of the model, i.e., when the response begins to stabilise. The same faster response are found exactly for the rest of the wells represented (Fig. 4.6C). In terms of gas flow rate recovered (Fig. 4.6B), gas arrives at the extraction well earlier when simulating the exchange. This is because the gas pressure at injection point is higher; consequently the gas enters the medium and starts displacing water before. For longer times, both reach the same steady state.

Regarding the effect of neglecting gas storage at the observation wells (Case-II), the results obtained show the opposite behaviour. For short times, the gas pressure at the injection well (Fig. 4.7A) presents a increase for both the base case and for the case with no observation wells. Nevertheless, when the gas starts moving through the medium the patterns described by the gas are different. In the case where the observation wells are physically represented (Fig. 4.7C), there are some wells, which do not respond. Consequently, the number of paths available for the gas to reach the production well decrease. This effect together with fact that the wells might be considered as a barrier for the gas displacement (i.e. gas might get dissolved in the volume of water presents in the observation wells), causes the gas pressure at the injection well to be slightly higher than the case where the wells are not simulated. In terms of the gas outflow (Fig. 4.7B), this plot supports the earlier explanation. When the observation wells are represented, gas takes longer to reach the extraction well. At the end, the same steady situation is obtained in both cases. The use of monitoring wells can provide additional information

for determining areal distribution.

Regarding the relationship between fracture transmissivity and porosity we can see that the main difference between the Base Case and the Case-III is the faster build up of gas pressure in the injection well in the latter case. This is due to the fact that entry pressure P_b (Ecu 8) in the Case-III (fault gauge filled fracture considered as porous media) is larger than P_b for the base Case (open fracture model). Consequently, the gas enters the medium and starts displacing water, and the gas arrives before to the well of extraction. As a result, the gas pressure inside the fracture (reported by the gas evolution in the observation wells) does not grow as much as in the Base Case, and becomes more stable.

Regarding the transmissivity correlation structure, this analysis shows that for small times the system behaves as an isotropic medium (Fig. 4.8A). However examining the complete response, the case that provides the best pattern when comparing with the measurements is[1.6m /0.8m]. This demonstrates that in the area where the wells are concentrated there is a clear anisotropy in the x-direction. With regard to the gas recovered (Fig. 4.8B), the best results are obtained for the model with [1.6m /0.8m], even though the arrival time is not exactly gained. In reference to the field with the correlation length of [1.6m /0.4m] is not definitely a good field to describe the heterogeneity of this medium because the calculated responses are negligible and show different behaviour than those calculated for the other study cases.

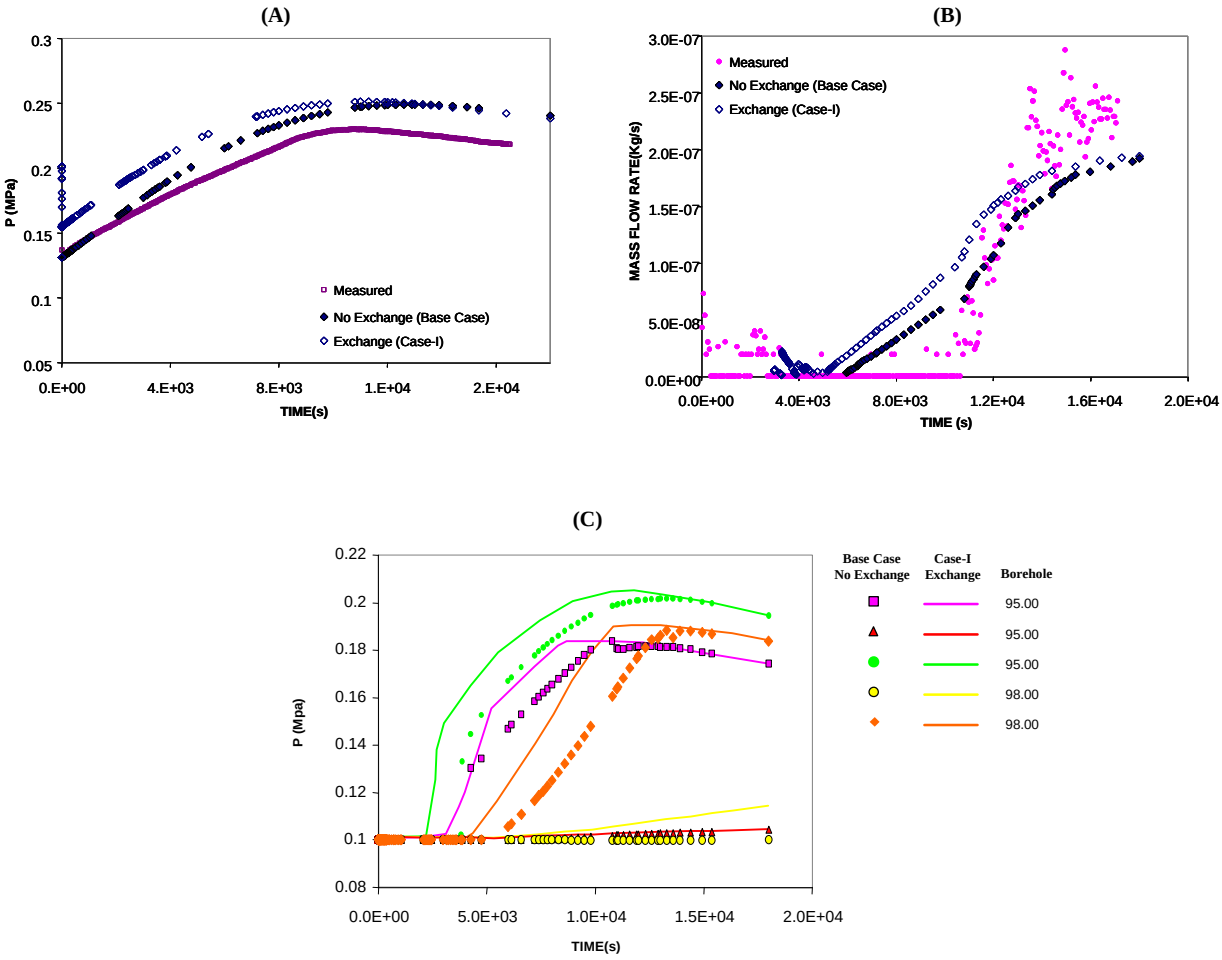

Figure 4.6: Comparison of Base Case and Case-I (simulating gas/water exchange at the injection well); (A) Time evolution of the gas injection pressure at the injection well, (B) Time evolution of the mass flow rate of gas that is recovered from the extraction well, (C) Time evolution of the crosshole pressures at the observation boreholes for both cases.

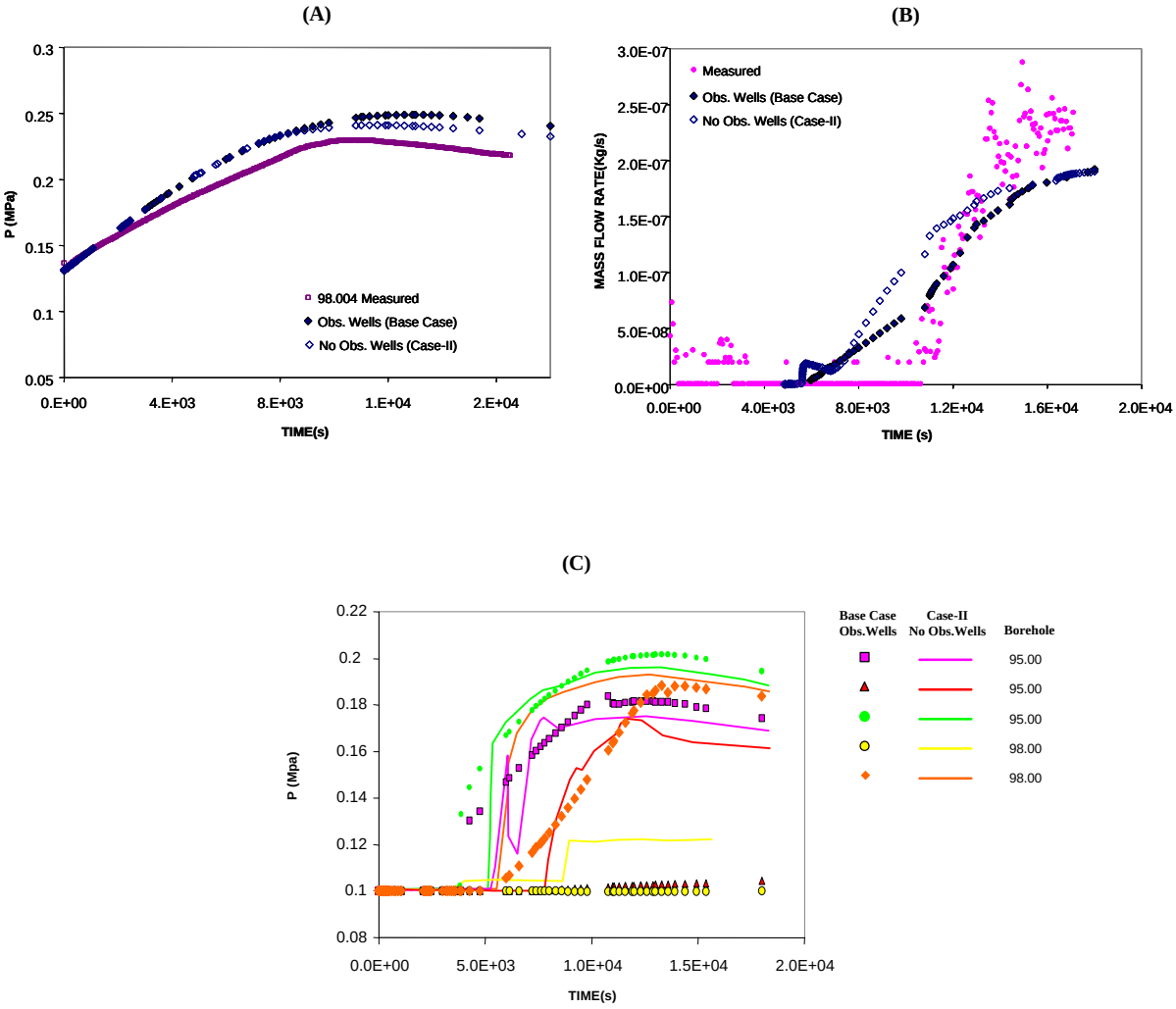

Figure 4.7: Comparison of Base Case and Case-II (where the observation wells are not explicitly simulated); (A) Time evolution of the gas injection pressure at the injection well, (B) Time evolution of the mass flow rate of gas that is recovered from the extraction well, (C and D) Time evolution of the crosshole pressures at the observation boreholes for both cases.

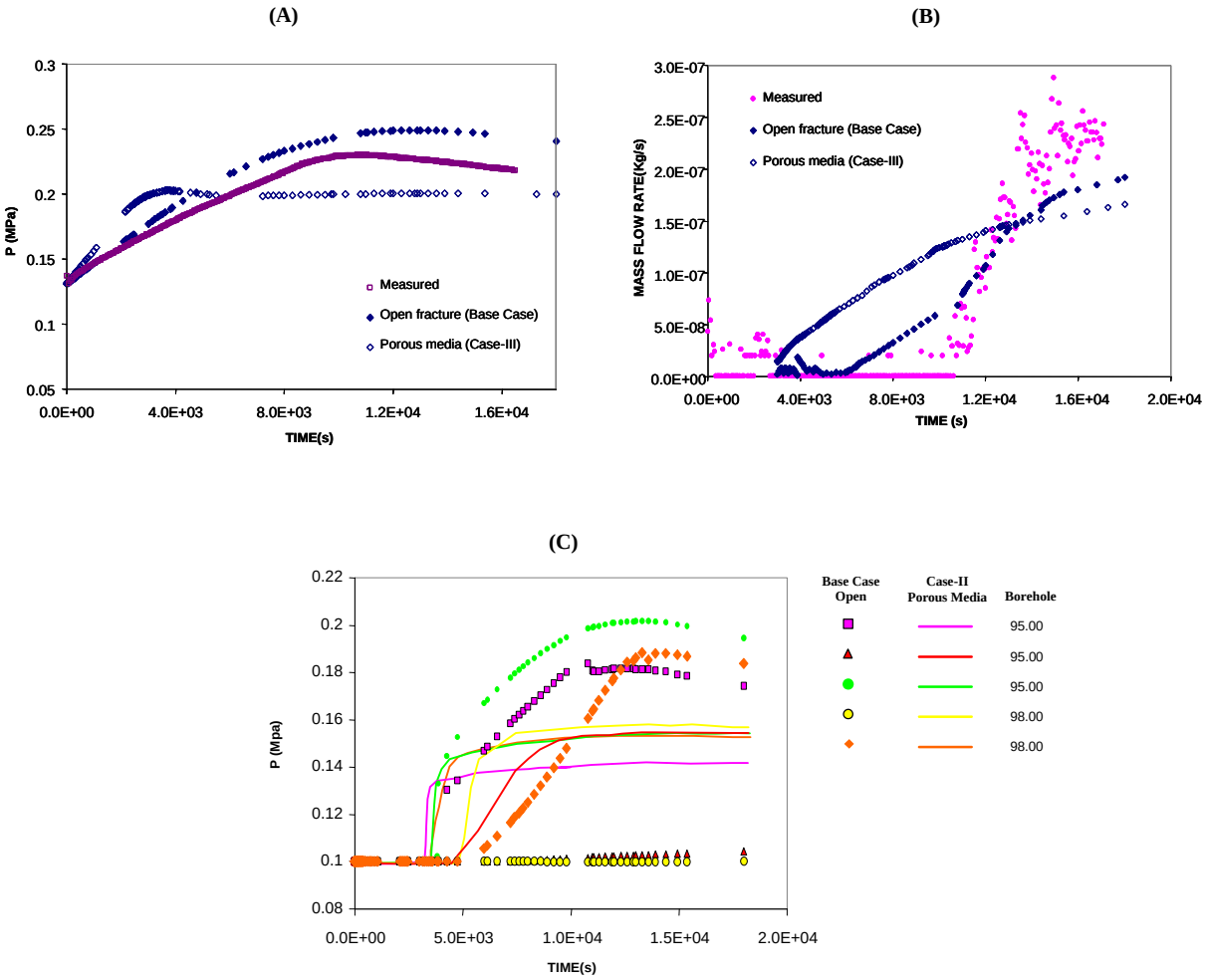

Figure 4.8: Comparison of Base Case and Case-III (where the fracture is considered as an homogenous fault gouge filled fracture whit variable aperture); (A) Time evolution of the gas injection pressure at the injection well, (B) Time evolution of the mass flow rate of gas that is recovered from the extraction well, (C) Time evolution of the crosshole pressures at the observation boreholes for both cases.

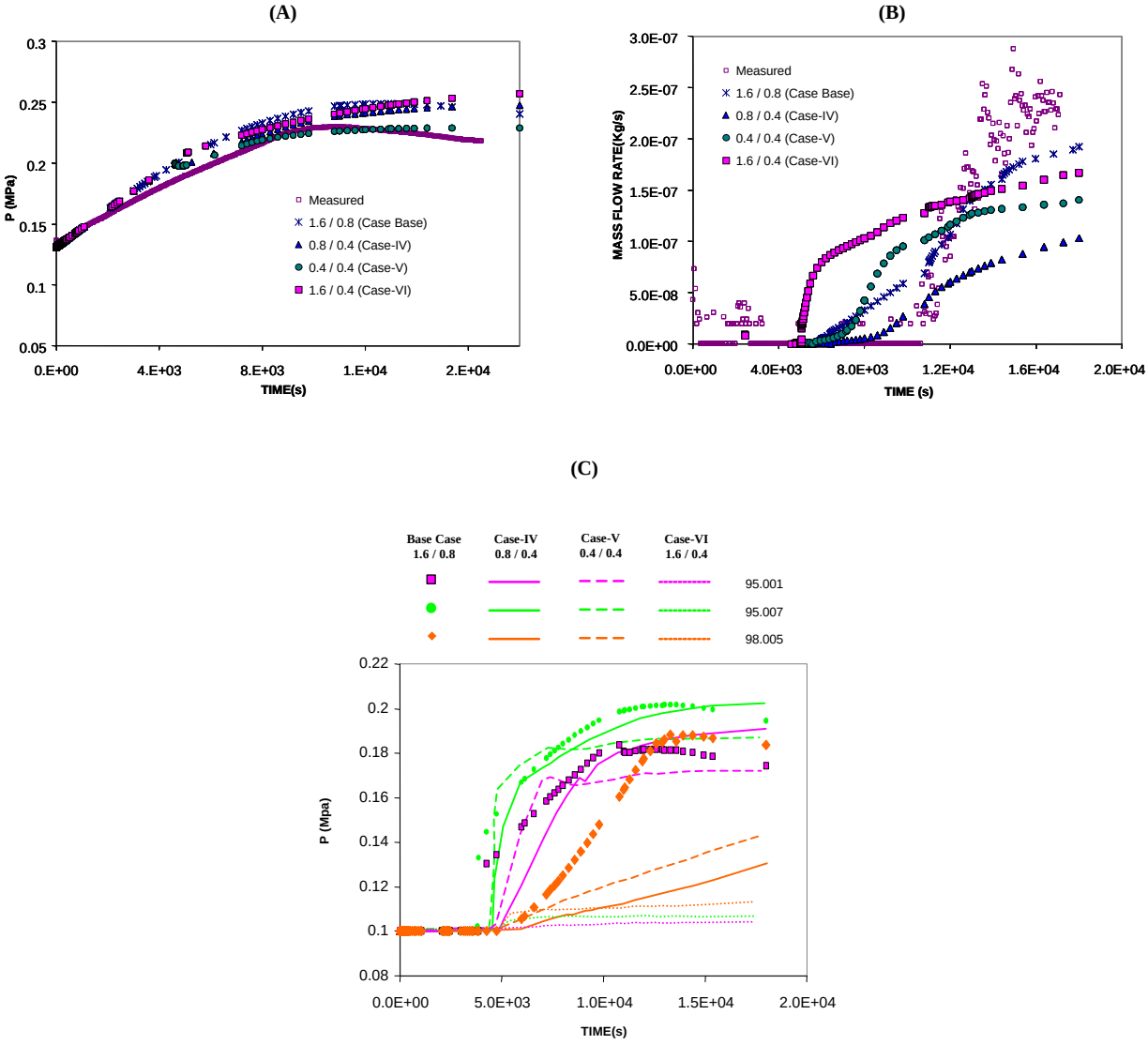

Figure 4.9: Comparison of Base Case and Cases IV, V and VI (considering several transmissivity fields accounting for different geostatistical assumptions); (A) Time evolution of the gas injection pressure at the injection well, (B) Time evolution of the mass flow rate of gas that is recovered from the extraction well, (C) Time evolution of the crosshole pressures at the observation boreholes for the Base Case, Case IV, V and VI.

4.4. Conclusions

On the basis of this sensitivity study, the following conclusions can been made:

Injection well study: When the exchange is simulated, the initial pressure achieved depends on the characteristics of the field around the well. For the Base Case the initial pressure is prescribed at the formation pressure. This originates differences between simulating the exchange or not, and consequently the shift of the former pressure. The deviation becomes negligible when the response goes further than the so-called radius of influence. In terms of gas flow rate recovered, gas arrives first to the extraction well when simulating the exchange. This is because the gas pressure at injection is higher. For longer times, both cases reach the same steady state.

Observation well study: In the case where the observation boreholes are physically represented the observed answer is different, because the observation boreholes might considered as a barrier for the gas displacement. Due to this, the spatial distribution of paths available for gas flow varies, and gas takes longer to reach the extraction well. However, in terms of mass flow rate the same steady situation is obtained in both cases. The use of monitoring wells can provide additional information to determine areal gas distribution.

Porosity field study: when the fracture is assumed to be as a porous medium the gas pressure in the injection well grows faster, but it is stabilized before. Consequently, the gas enters the medium and starts displacing water before, and the gas arrives before to the well of extraction. As a result, the gas pressure inside the fracture becomes smaller and more stable.

Transmissivity field study: this analysis shows that in the area where the wells are concentrated there is a clear anisotropy in the x-direction. The results can provide a new tool to minimize the number of transmissivity fields obtained by means of geostatistical inversion of hydraulic and tracer test, which are equally equiprobables.

4.5. References

Alber, W. (2000a): Radar measurements at the GAM experiment site. NAGRA Internal Report 99-283, Wettingen, Switzerland.

Alber, W. (2000b): Radar measurements at the GAM experiment site during a brine injection test. NAGRA Internal Report 00-92, Wettingen, Switzerland.

Alber, W. (2000c): Radar measurements at the GAM experiment site during a gas injection experiment (GT1). NAGRA Internal Report 00-93, Wettingen, Switzerland.

Bossart, P. and M. Mazurek, (1991): Structural geology and water flow-paths in the migration shear-zone. NAGRA Technical Report 91-12. Wettingen, Switzerland.

Brodsky, N., Stormont, J., Fredrich, J. (2000): Laboratory measurements of porosity, gas threshold pressures, and gas, liquid, and relative permeabilities for shear zone material from the Grimsel Test Site, Switzerland. NAGRA (Nationale Genossenschaft für die Lagerung radioaktiver Abfälle) Internal Report 00-15, Wettingen, Switzerland.

Corey, A.T.,(1954): The Interrelations Between Gas and Oil Relative Permeabilities, *Producers Monthly* Vol. 19, p. 38-41.

Fierz, T., E. Proust., M. Combarieu and P. Meier, (2000): GTS/GAM: Gas tracer test series GT1 in the GAM shear zone (February 2000). Dipole flow field GAM98-002/TPF95-007. NAGRA Internal Report 99-30, Wettingen, Switzerland.

Hazen, A. (1911) Discussion of dams on sand foundations, Transactions, American Society of Civil Engineers 73, 199–203.

Jodar, J., Ramajo, H., Olivella, S., Carrera,J., (2003) Multiphase flow and transport in a shear zone in granite. UPC contribution to the GAM (Gas Migration) project. ETSICCP (UPC),Spain.

Marschall, P., Croisé, J., (1999): Grimsel Test Site - Determination of two-phase flow properties in shear zones. NAGRA Internal Report NTB 97-06, Wettingen, Switzerland.

Meier, P., Medina, A., Carrera, J., (2001): Geostatistical inversion of cross-hole pumping tests for identifying preferential flow channels within a shear zone. Ground Water, Vol. 39, Number 1, pp 10-17.

Mendoza, C. A., (1992): Capillary pressure and relative permeability relationships describing two-phase flow through rough-walled fractures in geologic materials. Ph.D. dissertation, Dep. Of Earth Science., Univ. of Waterloo, Waterloo, Ontario, Canada.

Moreno, L.W., Tsang, C.F., Tsang, .F.v.,.and Neretnieks,I., (1988): Flow and tracer transport in a single fracture. Water Resources Research, Vol. 24, Number 12, pp 2033-2048.

Mbonimpa, M., Aubertin, M., Chapuis, R.P, and Bussière , B., (2002): Practical pedotransfer functions for estimating the saturated hydraulic conductivity. Geotechnical and Geological Engineering 20: 235–259.

Murphy, J.R. and Thomson, N. R., (1993): Two-phase flow in a variable aperture fracture. Water Resources Research, Vol. 29, Number 10, pp 3453-3476.

Neretnieks, I., Eriksen, T., and Tähtinen, P., (1982): Tracer movement in a single fissure in granitic rock: Some experimental results and their interpretation. Water Resources Research, Vol. 18, pp 849.

Neretnieks, I., (1993): Solute transport in fractured rock. Applications to radionuclide waste repositories. Flow and Contaminant Transport in Fractured Rock. Edited by J. Bear, C. F. Tsang, and G. de Marsily, pp 39-127. Academic Press, San Diego, California.

Neuzil, C. E., and Tracy, J. V (1981): Fow through fractures. Water Resources Research, Vol. 17, Number 1, pp 191-199.

Olivella, S., Carrera, J.,Gens, and Alonso., (1994), Nonisothermal multiphase flow of brine and gas through saline media, Transport in porous media, Vol.15, pp. 271-293.

Olivella, S., Gens A., Carrera J., and Alonso. (1996), Numerical formulation for a simulator (CODE-BRIGHT) for the coupled analysis of saline media . Engineering computations, Vol.13, Number 7, pp. 87-112.

Persoff, P. K., Pruess, K. and Myer, L., (1991): Two-Phase Flow Visualization and Relative Permeability Measurement in Transparent Replicas of Rough-Walled Rock Fractures". Proceedings 16th Workshop on Geothermal Reservoir Engineering, Stanford University, Stanford, California, January 23-25.

Persoff and Pruess, K., (1995): Two-phase flow visualization and relative permeability measurement in natural rough-walled fractures. Water Resources Research, Vol. 31, Number 5, pp 1175-1186.

Pruess, K., and Tsang, W.(1990): On two-phase relative permeability and capillary pressure of rough-walled fracture. Water Resources Research, Vol. 26, Number 9, pp 1915-1926.

Ramajo, H, Olivella, S, Carrera J. and. Sánchez-Vila, X. (2002): Simulation of gas dipole tests in fractures at the intermediate scale using a new upscaling method. Transport in porous media, Vol. 46, Number. 2-3, pp. 269-284.

Romm, E. S. (1996): On two-phase relative permeability and capillary pressure of rough-walled fracture. Water Resour. Res., VOL. 26, Number 9, pp 1915-1926.

Trick, T., T. Fierz, E. Proust, P. Meier and M. Combarieu, (2000): GTS/GAM: Gas tracer test series GT2 in the GAM shear zone (August 2000). Dipole flow field GAM98-004/TPF95-004. NAGRA Internal Report 00-49, Wettingen, Switzerland.

Trick, T., M. Piedevache, E. Proust, P. Meier and M. Combarieu, (2001): GTS/GAM: Gas tracer test series GT3 in the GAM shear zone (December 2000). Dipole flow field GAM98-002/TPF95-007. NAGRA Internal Report 01-02, Wettingen, Switzerland.

Tsang, Y. W., and Tsang, C. F. (1987): Channel model of flow through fractured media.. Water Resources Research, Vol. 23, Number 3, pp 467-479.

Van Genuchten, R., (1980): A closed-form equation for predicting the Hydraulic conductivity of unsaturated soils. Soil Science. Soc. Am. J. Vol. 44, pp 892-898.

Chapter 5: Gas tracer transport modelling in a heterogeneous fracture at two phase flow conditions. Model development and parameter sensitivity.

5.1. Introduction

The gas phase and its behaviour has become an important part of the performance assessment of radioactive waste repositories (Nuclear Energy Agency, 2000). Most investigations into gas migration through engineered and geological barriers of deep radioactive waste repositories have only taken place over the past 15 years. Nevertheless, a substantial body of work has been carried out in numerous national and international programmes, such as the experiment "**Ga**s **M**igration in shear zones" (GAM), an international research project carried out at the Grimsel Test Site, addressed to investigate gas transport processes in heterogeneous shear zones. This work is a result of our participation in the GAM project.

Once the caverns in a repository for low and intermediate-level waste (l/ILW) have been sealed, gas (e.g. H_2, CH_4, CO_2) may be generated by corrosion of metals and by degradation of organic substances. In addition, small quantities of toxic and radioactive gases may be produced. Gas will migrate from emplacement caverns mainly via geological discontinuities (e.g. shear zones). Depending on the gas production rate, gas migration may occur by different transport mechanisms. If gas generation is small, then the gas can be dissolved in the pore water and migrate by diffusion in the liquid phase under saturated conditions. If the production rate is high, gas will displace water from the fracture zone until an almost complete gas phase pathway is formed. In this situation the migration of gases inside the gas bubble is likely controlled by advection, dispersion/diffusion in the gas phase, and also dissolution in the liquid phase through the gas-water interface area.

On the other hand there are other many areas where the generation and the possible development and migration of a gas phase though the porous media have received considerable attention, such as landfills and disposal sites for hazardous wastes. Several toxic substances such as volatile organic compounds (VOCs) and gases, are released in the environment from existing landfills. Numerical models of varying complexity have been presented to simulate gas migration. From the point of view of gas transport mechanisms a first group of models simulated gas migration in soils, where advection and diffusion of gas species in the gas phase are the only gas transport mechanisms taken into account (Fadel et al. 1996, Giogia et al. 1997), neglecting the interaction between the gas and the liquid phases. A second group of numerical models simulated gas migration through the unsaturated zone (Popovicová and Brusseau 1998, Fang and Montcrieff 1999, Nastev et al. 2001), through saturated zones (Fry et al. 1995, Donaldson et al. 1998) and both (Thomson et al. 1997). Depending on the model gas species transport occurs by mean of advective and diffusive transport in the gas phase, and advective and dispersive transport in the aqueous phase. Gas diffusion in the liquid phase normally is not taken into account. The contribution of liquid phase diffusion to the total effective diffusion maybe equal to or higher than that of gas phase diffusion when the soil is close to saturation (Simunek and Suarez 1993), and ignoring liquid phase diffusion can cause an error in the estimate of the gas species fluxes.

Common concepts in gas migration through porous media are applied to a low permeability fracture, where intrinsic properties are not constant in space but randomly distributed along water conducting features. In a gas filled fracture, small aperture fracture zone, fault gouge fracture filling material, and also the rock matrix remain filled with virtually immobile water. Therefore, dissolved gasses reach the interior of such structures by molecular diffusion. The overall process is similar to solute matrix diffusion. Hence is very sensitive to gas solubility, gas diffusion coefficient, gas-water interface area and also to the bubble size or volume available for dissolution/diffusion.

In order to solve the gas transport problem mainly two approaches have been used. Analytical models developed describing the transport of gas into a fracture (Gascoyne and Wuschke 1991, 1997, Lineham et al. 1996) focus their interest in the gas-water interface velocity, being the advection the only transport mechanism taken into account to model gas migration. Numerical models developed to simulate gas transport in fractures at two-phase flow conditions are relatively scarce (Senger 1997, Lunati 2000, Garcia and Caussade 2001), and addressed to characterise the two phase flow parameters of the fracture on a local scale (meter to decametres). Quantitative description of gas transport in fractured formations has not yet been accomplished in a satisfactory way. One of the main difficulties to be resolved when simulating two phase flow processes in fractured rock is the determination of effective mass exchange coefficients of the relevant components of the system. Mass exchange depends on the spatial distribution of water and gas along the water-conducting features, and also on the solubilities and diffusivities of the different components

The objective of this work is to shed light on processes affecting gas dissolution/diffusion processes in shear zones, and to assess the relative importance of various phenomenological coefficients that come into play. In order to reach this objective numerical simulations of multiphase flow and gas transport are performed together with sensitivity analysis of the variables which govern the dissolution/diffusion processes is shear zones. The model, developed to simulate the gas migration through a partially saturated heterogeneous fracture, takes advantage of the formal analogy between gas transport in a two phase system equations and the solute tracer transport equation in water saturated systems.

5.2. Model development

It is expected that gas can be produced during the post-operational phases of low and intermediate-level radioactive waste repositories through anaerobic degradation. Gas will migrate from emplacement caverns mainly via geological discontinuities (e.g. shear zones). If the production rate is high or the gas quantity is large, gas will displace water from the fracture zone until an almost complete gas phase pathway is formed. Once the gas bubble is inside the fracture it migrates displacing the water from zones where the entry pressure is small (i.e. zones of empty fracture with high apertures, or macropores). In those fracture zones where the capillary pressure is very high to allow the gas to penetrate, water is not displaced, so that the water saturation remains constant.

The fracture conceptualisation for gas migration requires the consideration of these two different scenarios (Fig.5.1), open fracture zones fully saturated with gas (mobile zone), and fault gauge filled zones partially or fully saturated with water (immobile zone).

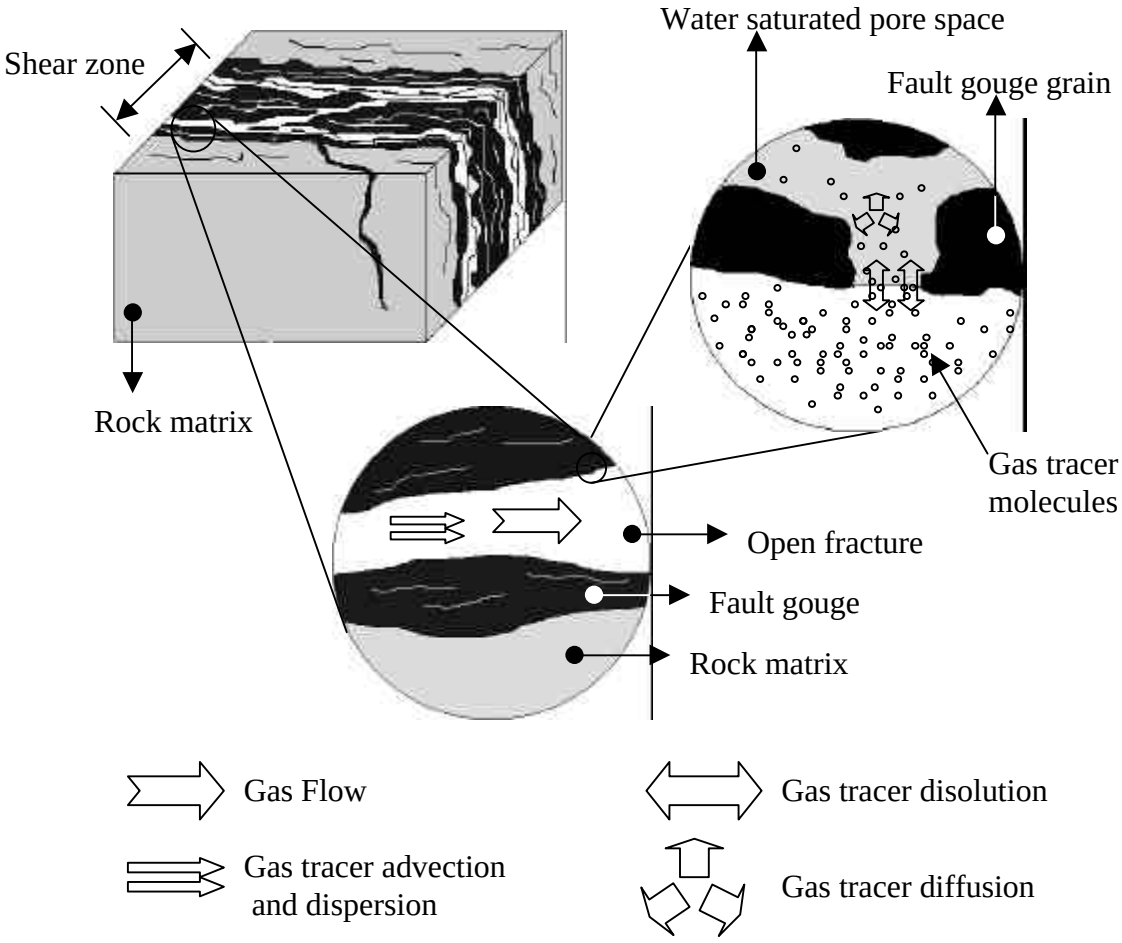

Figure 5.1: Scheme of gas transport in a shear zone. Gas transport in the open fracture gas filled is governed by advection and dispersion, while in the fine grained water saturated porous medium, the main transport mechanism is diffusion in water.

In order to simulate the gas bubble conditions, several gas tracer injection tests (dipole configuration) have been carried out in a granite fracture, at the Grimsel Test Site (Fierz et al. 2000, Trick et al. 2000, Trick et al. 2001). First a steady state gas flow-field is

established by injecting nitrogen at a constant rate into the injection borehole. After stationary conditions are achieved, gas tracers are injected simultaneously.

In the mobile zone several open paths partially filled with gas will conduct the major quantity of gas from the injection borehole to the extraction borehole. We make the hypothesis that inside those open paths water is just wetting the wall paths as a water film and it does not move, so only gas flows through the open paths (gas advective fracture zone). Advection, diffusion and dispersion of gas tracer in the gas phase are the transport mechanisms taken into account in the open fracture zones.

On the other hand, it is assumed that entry pressure in the immobile zones is too high to allow the gas to enter. In this situation, water which is saturating the fault gouge fracture filling material is not displaced, so water saturation degree remains more or less constant and equal to one. As water is still occupying the small pores of the fault gauge and tight fractures, gas phase does not flow through these structures. In the development of the model, gas tracer mass transfer between gas phase (mobile zone) and liquid phase (immobile zone) will be assumed to be essentially instantaneous and governed by Henry's law. Experiments have shown that the assumption of local equilibrium for gas-liquid mass transfer is usually good (Brusseau (1991), Gierke et al. 1992). Dissolved gas tracer transport in the immobile water zone takes place by molecular diffusion.

5.2.1 Multiphase flow and transport of gaseous species

The main objective of this work is the characterisation of the transport processes at two phase flow conditions in heterogeneous media (fractures). We have modelled the fracture as an empty fracture, where the aperture is a regionalized variable, varying from point to point. Nevertheless to solve the gas transport problem, it is necessary to know what are the two phase flow conditions that were existing during the gas transport. For this reason we have to solve the multiphase flow equations in heterogeneous media. The equations governing multiphase flow as well as the assumed assumptions to perform the multiphase flow simulations are described in the Chapter 4.

On the other hand a general definition of gas mass balance for gas transport at two phase flow conditions is presented here. The species *k* (injected gas tracer) is present in the gas and liquid phases, so the total mass balance of the species *k* is expressed as:

$$\frac{\partial}{\partial t}\left(f S_l r_l c_l^k + f S_g r_g c_g^k\right) + \nabla \cdot \left(\mathbf{j}_l^k + \mathbf{j}_g^k\right) = G^k \tag{5.1}$$

where $\mathbf{j}^k_l$ and $\mathbf{j}^k_g$ [$ML^{-2}\ T^{-1}$] are the total mass flux of the species k in the liquid and in the gas phase, and c^k_l and c^k_g are the mass fractions of the species *k* in the liquid and the gas phase respectively. G^k [$ML^{-3}T^{-1}$] includes sinks or sources due to the presence of wells or mass transfer from other phases.

The total mass flux of species *k* in phase α ($\mathbf{j}^k_\alpha$) is composed of a advective term ($\mathbf{I}^k_\alpha$) and a non-advective term ($\mathbf{i}^k_\alpha$):

$$\mathbf{j}_a^k = \mathbf{I}_a^k + \mathbf{i}_a^k \tag{5.2}$$

In general form, the advective flux is expressed as:

$$\mathbf{I}_a^k = r_a \mathbf{q}_a c_a^k \tag{5.3}$$

where $\mathbf{q}_\alpha$ [LT^{-1}] is the Darcy's flux of phase a.

For the fluid phases the convective flux arising from the phase velocity will be written using a generalised Darcy's law (Bear, 1972). Darcy's law can be used for gas flow assuming that gas compressibility effects are negligible and the "slip flow" or Klinkenberg effect is minimum. The Klinkenberg effect is generally negligible for sands, silts and gravels (Thorstenson and Pollock 1989, Abu-El-Sha'r and Abriola 1997, Wu et al. 1998, Skjetne and Auriault 1999). The assumption of incompressibility which is used for water flow is typically not valid for gas flow, but when the pressure difference inducing flow is small, compressibility may be ignored (Johnson et al 1990).

The non-advective mass fluxes are computed as the sum of two components: the diffusive component, which depends on the species, and the mechanical dispersion. The latter only depends on the phase considered as a result of the macroscale evaluation. In aqueous phase mechanical dispersion is usually much more important than diffusion. For the gas phase, diffusion is of greater significance because diffusion coefficients are much larger than aqueous phase diffusion coefficients. Diffusion dominates over mechanical dispersion for gas transport except when velocities are very high (Gierke et al. 1992).

In extremely fine porous media and capillaries having small diameters compared with the mean free path of gas molecules (about 0.1 μm at standard temperature and pressure), gas diffusion rate is dominated by the so called Knudsen diffusion, that is, by collision of molecules whit the capillary walls (Thorstenson and Pollock 1989), and Fick's law is not adequate for representing diffusion in systems where contributions of Knudsen is signifficant. In our case Knudsen diffusion is negligible, hence the non-convective mass fluxes are computed through Fick's law which expresses them in terms of gradients of mass fraction of species (Bird et al. 1960).

$$\mathbf{i}_a^k = -r_a \left(\mathbf{D}_a + f S_a D_{m_a}^k \mathbf{I} \right) \nabla c_a^k \tag{5.4}$$

As outlined before the non-advective mass fluxes are computed as the sum of the mechanical dispersion and diffusive fluxes. The mechanical dispersion $\mathbf{D}_a$ [L^2T^{-1}] only depends on the phase considered, and the diffusive component $D_{m_a}^k$ [L^2T^{-1}] depends also on the species. **I** is the identity matrix.

Equations (5.3) and (5.4) are the general forms of the advective and non-advective mass fluxes of the species *k* in the phase a. Including them in equation (5.1) for $a=l$ and $a=g$ (liquid and gas phase, respectively) a general mass balance equation for the species k at two phase flow conditions is obtained:

$$\frac{\partial}{\partial t}\left(fS_l r_l c_l^k + fS_g r_g c_g^k\right) = \nabla\cdot\left(r_l\left(\mathbf{D}_l + fS_l\mathbf{D}_{m_l}^k\right)\nabla c_l^k + r_g\left(\mathbf{D}_g + fS_g\mathbf{D}_{m_g}^k\right)\nabla c_g^k - \left(r_l\mathbf{q}_l c_l^k + r_g\mathbf{q}_g c_g^k\right)\right) + G^k \quad (5.5)$$

Gases are soluble in water (sometimes their solubility is large) and it is possible that, once the gas bubble has been developed, a large amount of water still remains in the fracture. In the model, mass transfer between gas and liquid phases will be assumed to be instantaneous, and governed by Henry's Law, which is generally assumed as valid for low pressures. Solubility is characterised by Henry's constant K_H [$ML^{-1}T^{-2}$], that relates concentration of gas (low mole fraction) in the liquid and gas phases:

$$c_l^k = \frac{c_g^k P_g}{K_H} \quad (5.6)$$

Taking into account the relationship between gas density and gas pressure at a certain temperature (perfect gases law) and Equation (5.6), Equation (5.5) can be written as:

$$\frac{\partial}{\partial t}\left(\left(fS_l r_l \frac{P_g}{K_H} + fS_g r_g\right)c_g^k\right) = \nabla\cdot\left(\left(r_l\frac{P_g}{K_H}\left(\mathbf{D_l} + fS_l\mathbf{D}_{\mathbf{m_l}}^{\mathbf{k}}\right) + r_g\left(\mathbf{D_g} + fS_g\mathbf{D}_{\mathbf{m_g}}^{\mathbf{k}}\right)\right)\nabla c_g^k - \left(\frac{P_g}{K_H}r_l\mathbf{q}_l + r_g\mathbf{q_g}\right)c_g^k\right) + G^k \quad (5.7)$$

where R is the perfect gases constant, and T is absolute temperature. Equation (5.7) is the total mass balance of species k, expressed in terms of the gas species, taking into account the solubility of species k in the liquid phase. The transport processes which affect the tracer while it is moving inside the fracture, such as diffusion and advection processes, both in liquid and gas phases, are included.

5.2.2 Initial and Boundary conditions

The initial condition at in the injection and extraction boreholes must be taken into account in order to simulate the gas injection test. Before the gas injection and generation of a stationary gas flow field inside the fracture, the test interval water of the injection borehole is replaced by gas (Fig.5.2). This is accomplished by injecting gas through the injection (pressure) line and extracting water through the extraction (flow) line. Depending on the position of the extraction line inside the interval, it is possible to find a big volume of remaining water in the innermost part of the injection interval. This volume is relevant because it behaves as a reservoir for dissolved gas, and dilutes the gas species concentration injected in the interval. The volume of water remaining in the interval can be much bigger than the volume of water accessible by the gas by diffusion processes, and it can play a signifficant role in the transport of the gas tracers. This effect can be minimised by installing the gas injection line in the innermost part of the interval. On the other hand, in the extraction borehole, where water is displaced by the gas which is leaving the fracture, and it is very difficult to determine the amount of

water that is still in the interval once the stationary gas flow-field of the dipole is established.

To evaluate the influence of water remaining in the interval in the concentration of the injected gas tracer, the mass balance of the species k is written as:

$$\frac{\partial}{\partial t}\int_{\Omega} r_g c_g^k dv + \frac{\partial}{\partial t}\int_{\Omega} r_l c_l^k dv = Q_g r_g c_{g_{INY}}^k + \int_{\Gamma} \mathbf{q}_g r_g c_g^k \mathbf{n} ds + \int_{\Gamma} (-r_g D_{m_g}^k \nabla c_g^k)\mathbf{n} ds + \int_{\Gamma} (-r_l D_{m_l}^k \nabla c_l^k)\mathbf{n} ds \quad (5.8)$$

Where Q_g [L^3T^{-1}] is the injection gas flow rate, and $c_{g_{INY}}^k$ is the prescribed mass fraction of the species *k*. Taking into account Equation (5.6) and simplifying, Equation (5.8) can be written as:

$$\frac{\partial}{\partial t}\left(V_g r_g + V_l r_l \frac{P_g}{K_H}\right) c_g^k = Q_g r_g \left(c_{g_{INY}}^k - c_g^k\right) - (r_g D_{m_g}^k + r_l D_{m_l}^k \frac{P_g}{K_H}) A_\Gamma \nabla c_g^k \mathbf{n} \quad (5.9)$$

Where V_g [L^3] and V_l [L^3] are the volumes in the interval occupied by gas and water respectively, and A_Γ [L^2] is the surface where the gas leaves through the interval.

Depending on the value of V_l and K_H the effect of the water in the interval can be negligible or dominant.

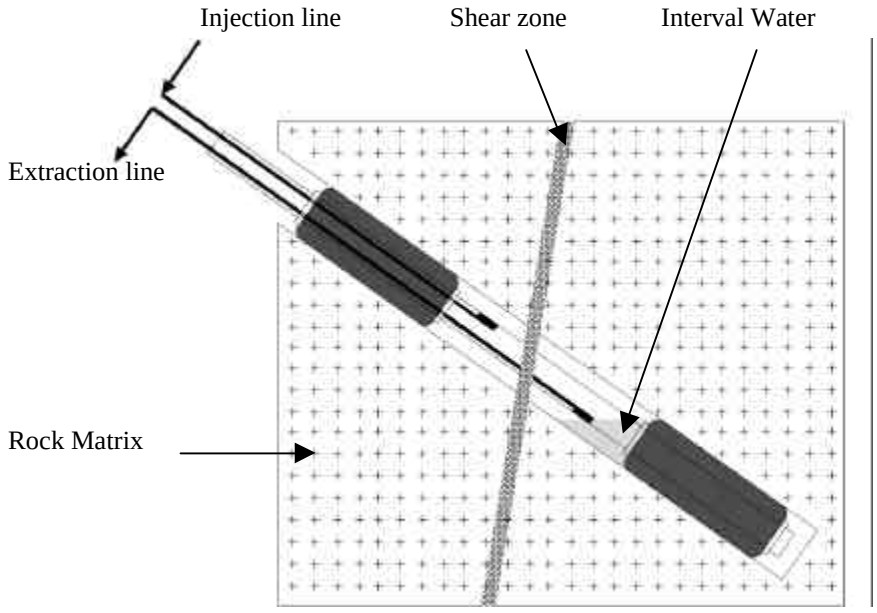

Figure 5.2: Schematic representation of the isolated borehole interval which penetrates a shear zone. The interval is isolated by means of a packer system. In order to replace water by gas in the interval, gas is injected through the injection line, and water is extracted through the extraction line. Depending on the position of the extraction line inside the interval, a volume of water will remain inside the interval.

Initial conditions for Equation (5.9) consist of specification of initial gas tracer concentration in the fracture:

$$c_g^k\left(x,y,t=0\right)=c_{g_0}^k\left(x,y\right) \tag{5.10}$$

Where $c_{g_0}^k$ is the initial gas tracer mass fraction in the fracture.

In general, boundary conditions are considered by adding a flux or flow rate. The mass flux or flow rate of species k as a component of the phase α is:

$$j_a^k=\left(c_a^k\right)^0 q_a^0+\left(c_a^k\right)^0 g_a\left(P_a^0-P_a\right)+b_a\left(\left(r_a c_a^k\right)^0-\left(r_a c_a^k\right)\right) \tag{5.11}$$

Where the subscript ()° stands for the prescribed values, c_a^k is the mass fraction of the species *k* in the gas phase, r is the mole density of the species k in the phase a , P_a is the pressure of the phase a , q_a^o is a prescribed flow of the phase a , and g_a and b_a are two parameters of the boundary condition. In other words, a Dirichlet type boundary condition term, plus a Newman type term plus a Cauchy type term.

5.2.3 Transport through mobile and immobile zones

Taking into account the two different scenarios in which we have divided the fracture system in terms of gas transport properties (see Figure 5.1), we will apply the mass balance equation:

In the gas advective fracture zone (mobile zone) gas flows through the open paths, and the gas tracer is transported mainly by advection, but also dispersion and diffusion in the gas phase take place. There is no water flowing through the open paths because water is only wetting the wall paths as a water film. That means $\mathbf{q}_l=0$. If there is not water advection then mechanical dispersion is null ($\mathbf{D}_l=0$). On the other hand, due to the small amount of water the diffusive component ($\mathbf{D}_{m_l}^k=0$) is neglected. Including all this information in Equation (5.7), expanding the term of mechanical dispersion, and rearranging terms, gives the new mass balance equation for the species *k* on the open fissure fracture:

$$\begin{aligned}&\frac{\partial}{\partial t}\left(\left(f_M S_l r_l\frac{P_g}{K_H}+f_M S_g r_g\right)c_{g_M}^k\right)=\nabla\cdot\left(\left(a_{L_M} r_g\mathbf{q_g}+f_M S_g r_g\mathbf{D}_{\mathbf{m_g}}^{\mathbf{k}}\right)\nabla c_{g_M}^k\right)-\\&-\nabla\cdot\left(r_g\mathbf{q_g}c_{g_M}^k\right)+G_I^k\end{aligned} \tag{5.12}$$

The last term G_I^k in the right hand of Equation (5.12) is a sink/source term related to the gas mass transfer by diffusion between the gas advective fracture zone and the

immobile water fracture zone (the subscripts *M* and *I* stands for mobile and immobile zones respectively), and is given by:

$$G_I^K = \frac{f_I S_l r_l}{L_I} \frac{P_g}{K_H} \mathbf{D}_{m_l}^k \frac{\partial}{\partial h} c_{g_I}^k \Big|_{h=0} \tag{5.13}$$

Where f_I, L_I, and $c_{g_I}^k$ are porosity, diffusion length and mass fraction in the immobile fracture zone respectively.

On the other hand, in the fault gauge filled fracture zone (immobile zone) it is assumed that water is not displaced by the gas due to the high gas entry pressure ($\mathbf{q}_l = 0$ and $\mathbf{q}_g = 0$). If no gas phase is present in the fault gauge filled fracture, then transport is null in the gas phase. Molecular diffusion of dissolved gas is the only transport mechanism that takes place in this water non-advective domain. Including all this information in Equation (5.7) and taking into account Equation (5.13), it is obtained a new mass balance of the species *k* inside the fine grained water saturated porous media.

$$\frac{\partial}{\partial t}\left(\left(\frac{f_I S_l r_l}{L_I} \frac{P_g}{K_H} \right) c_{g_I}^k \right) = \frac{\partial}{\partial h}\left(\frac{f_I S_l r_l}{L_I} \frac{P_g}{K_H} \mathbf{D}_{m_l}^k \frac{\partial}{\partial h} c_{g_I}^k \right) \tag{5.14}$$

Continuity conditions have to be imposed at the interface between the gas advective fracture zone and the immobile water fracture zone the open fracture gas filled zones (*h*=0), that is, both mass fractions must be equal.

$$c_{g_I}^k \left(x, y, h = 0, t\right) = c_{g_M}^k \left(x, y, t\right) \tag{5.15}$$

5.2.4 Analogy between gas transport and solute transport equations

The transport equation in a single phase system, including advection and dispersion/diffusion in the mobile zone, and also diffusion in immobile zone is given by:

$$\frac{\partial}{\partial t}\left(R_m f_m c_m\right) = \nabla \cdot \left(\left(a_{L_m} |\mathbf{q}| + f_m D_f \right) \nabla c_m - \mathbf{q} c_m \right) + F_i \tag{5.16}$$

$$\frac{\partial}{\partial t}\left(\frac{R_i f_i}{L_i} c_i \right) = \frac{\partial}{\partial h}\left(\frac{D_i f_i}{L_i} \frac{\partial}{\partial h} c_i \right) \tag{5.17}$$

where f_m [-] is porosity (sub-index m stands for mobile porosity in the case of solute transport, to avoid confusions with the porosity in the case of gas transport at two phase flow conditions), c_m [ML^{-3}] solute concentration, a_{L_m} [L] is longitudinal dispersivity, D_f [L^2T^{-1}] is molecular diffusion at the mobile zone, **q** is Darcy's flux [LT^{-1}], c_i [ML^{-3}] is solute concentration at immobile zones, f_i [-] is immobile zone porosity, D_i [L^2T^{-1}] is molecular diffusion of solute at the immobile zone, R_m [-] is retardation coefficient due

to adsorption phenomena at the mobile zone, R_i [-] is the retardation coefficient at the immobile zone, h [L] is the coordinate axis perpendicular to the flow direction, and t[T] is time. The last term F_i in the right-hand side of Equation (5.16) is a sink/source term related to immobile zone diffusion.

Note that in two dimensions, in Equation (5.16) $\mathbf{q}=-\mathbf{T}\nabla h$, q is not Darcy's flux, but flow rate per unit width [L^2T^{-1}], **T** is transmissivity [L^2T^{-1}], and f_m [L] is redefined as thickness-porosity, being the product of fracture thickness and porosity.

If the immobile zone is viewed as a sequence of plates of thickness $2L_i$ then immobile zone diffusion is governed by Equation (5.18).

$$F_i = \frac{D_i f_i}{L_i} \frac{\partial c_i}{\partial h}\bigg|_{h=0} \tag{5.18}$$

Equations (12) and (14) can be transformed into equations (16) and (17) respectively by defining the following analogy:

Table 5.1. Analogy between solute and gas transport variables

Variable in the solute transport equations	Variable in the gas transport equations	
c_m	$c^k_{g_M}$	(5.19)
c_i	$c^k_{g_I}$	(5.20)
f_m	$f_M S_g r_g$	(5.21)
f_i	$f_I S_l r_l \frac{P_g}{K_H}$	(5.22)
R_m	$1+\frac{S_l r_l}{S_g r_g}\frac{P_g}{K_H}$	(5.23)
R_i	1.0	(5.24)
D_f	$D^k_{m_g}$	(5.25)
D_i	$D^k_{m_l}$	(5.26)
$\mathbf{q}$	$r_g \mathbf{q_g}$	(5.27)
a_{L_m}	a_{L_M}	(5.28)
L_i	L_I	(5.29)
V_{bh}	$V_g r_g + V_l r_l \frac{P_g}{K_H}$	(5.30)
$D_{f,bh}$	$r_g D^k_{m_g} + r_l D^k_{m_l}\frac{P_g}{K_H}$	(5.31)

In order to apply the analogy to the whole gas tracer migration problem, we have to extend it to the injection and extraction boreholes, to take into account the dilution effect in concentration due to the volume of water remaining in the interval. Applying the presented analogy to Equation (5.9), it can be written as:

$$V_{bh}\frac{\partial c_m}{\partial t} = Q_{bh}\left(c_0 - c_m\right) - (D_{f,bh}\nabla c_m)A_\Gamma \mathbf{n} \tag{5.32}$$

Where $D_{f,bh}$ [L^2T^{-1}]is the molecular diffusion coefficient of the tracer in the injection interval, V_{bh} [L^3] is the analogous volume in the interval occupied by solute, A_Γ [L^2] is the surface where the solute leaves through the injection borehole interval.

5.3. Methodology

The methodology used to simulate the gas tracer transport in a heterogeneous fracture at two phase flow conditions consist of two main steps: simulate the two phase flow conditions inside the fracture, and then, simulate the gas tracer migration through the fracture at the two phase flow conditions achieved.

In order to carry out the first step it is necessary to compute all the parameters needed to solve the multiphase flow equations, such as transmissivities, porosities or retention curve coefficients. We consider a two dimensional system, representing an isolated and empty fracture (no filling solid material is considered), where transmissivity is treated as a regionalized variable varying from point to point. The transmissivity field values are obtained following the same methodology presented by Meier et al. (2001). This methodology consist in the geostatistical inversion of several hydraulic tests performed in the fracture at the Grimel test site (Wyss 1996, Gemperle(2) 1999, Fierz and Piedevache 2000, Trick 2000) in the framework of the GAM project (Marschall et al. 1998) (Figure 5.3-A).

Porosity varies spatially as a function of transmissivity according the cubic law (laminar flow between parallel plates) since we are assuming an empty fracture.

Diffusion coefficients are obtained from the literature for gas tracer diffusion in pure water and gas. In our case $D_{m_l}^k$ and $D_{m_g}^k$ (equations 12 and 14) are effective diffusion coefficients, that is, they include the effects of porosity and tortuosity of the medium in the diffusion coefficient. Since we are considering an empty fracture $D_{m_g}^k$ coincides with the gas tracer diffusion coefficient in pure gas In the case of gas tracer diffusion in the water which is bounding the gas bubble or is still saturating fracture zones where the gas entry pressure is very high, the effective diffusion coefficient is different from its value in pure water. In order to obtain the effective value from the diffusion coefficients obtained in the literature we have used the relationship included in Boving and Grathwohl (2001):

$$\frac{D_{m_l}^k}{D_{aq}^k} = f^{2.2} \tag{5.33}$$

where D_{aq}^k [L^2T^{-1}] is the aqueous diffusion coefficient in pure water, and f [-] is the overall fracture porosity.

The interaction between phases is represented by means of a linear-step retention curve. As in the case of porosity the slope of the retention curve b varies spatially, in this case b varies as a function of the fracture aperture (desaturation begins in the widest zones and ends in the narrowest zones). Following the methodology proposed by Ramajo et al. (2002) one can assume that every value of the transmissivity field is the result of an upscaling process inside each transmissivity zone, so, at the end, one can think in terms of a field of geometric mean transmissivities. In the other hand the entry pressure P_b is a function of the maximum aperture (desaturation begins in the widest zones). Taking into account that the fracture aperture is a log-normal variable (defined by its mean and

variance) the relationships included in Ramajo et al. (2002) can be transformed into Equation (5.34) and (5.35) for b and P_b respectively.

$$b = \frac{4s\ \sinh(a)}{b_g} \tag{5.34}$$

$$P_b = \frac{2s}{b_g\left(\sinh(a)+\cosh(a)\right)} \tag{5.35}$$

where following the upscaling hypothesis, b_g [L] is the geometric mean aperture calculated before by means of the cubic law, a is a parameter related to the aperture standard deviation, and s [MT^{-2}] is the water surface tension.

To simulate the two phase flow conditions inside the fracture prior to the gas tracer injection test we have simulated a gas injection test (dipole configuration), in the initially water saturated fracture. We inject gas (nitrogen) through the injection borehole at a constant mass rate, until the steady state is achieved, that is, until the extraction gas flow rate through the extraction borehole is constant, and also the gas and liquid pressures inside the fracture become stationary (Figure 5.3-B,C). The multiphase flow finite element simulator CODE-BRIGHT (Olivella et al. 1996) is used to simulate the gas dipole injection test.

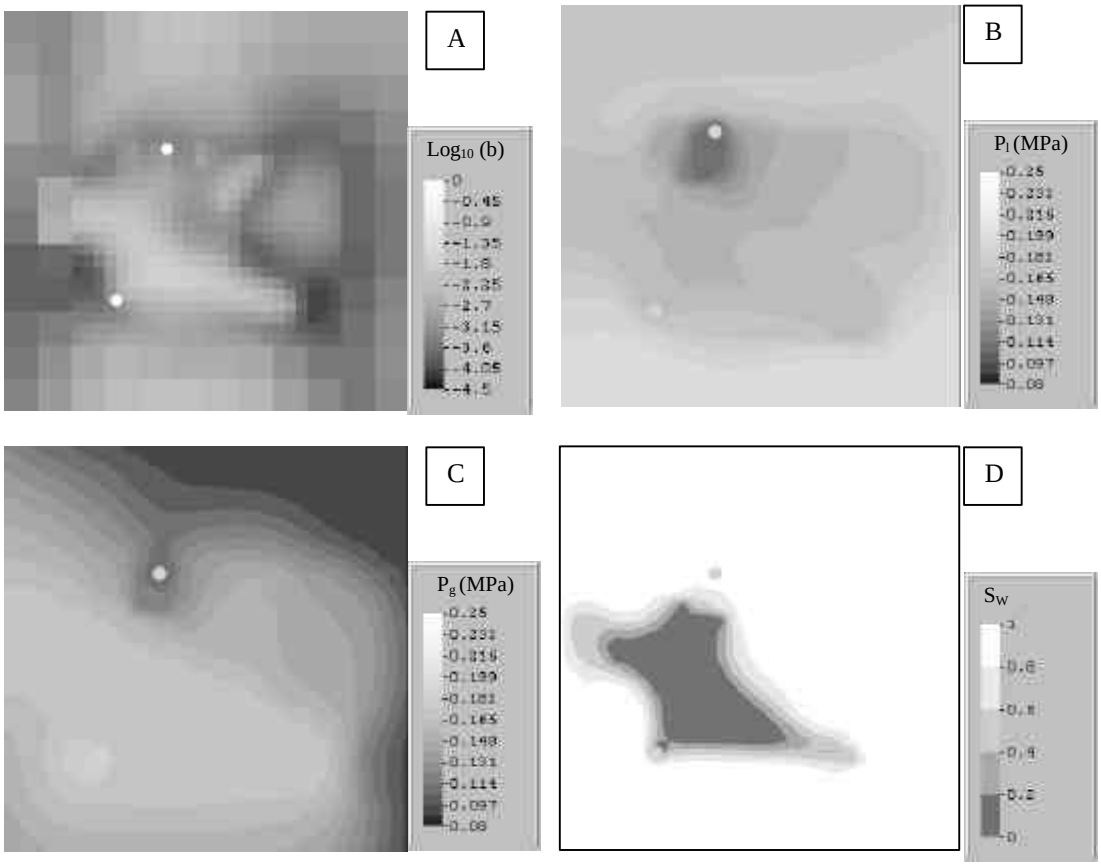

Figure 5.3: A) Log_{10} aperture field inside the fracture, around the injection borehole (lower white point) and extraction borehole (upper white point). B, C and D) Liquid pressure, gas pressure and water saturation degree respectively, obtained trough a simulation of a gas injection test (dipole configuration) once the steady state is reached. (The distance between injection and extraction boreholes is 1.14m).

Once the generation of the gas bubble is simulated, and the steady state is achieved, we know the two conditions previous to the gas tracers injection test. After this, the gas tracer injection test simulation is conducted. This consist of injecting gas tracer at a constant mass rate, and obtaining different breakthrough curves in the extraction borehole depending on the injected gas tracer. Input parameters needed to solve the transport equation, are directly obtained through Equation (5.19) to (5.31) using the developed analogy. To simulate the solute tracer transport through the heterogeneous fracture, is used the finite element code TRANSIN IV (Medina et al., 2000).

5.4. Sensitivity analysis

We have carried out a sensitivity analysis to study the relative importance of the phenomena that take part in the transport of gaseous tracers in heterogeneous media, the role played by the different parameters from the analogy which reproduce these phenomena, as well as the different scenarios in which they can take place. This sensitivity analysis has been divided into various basic sections:

- Gas tracer transport in the mobile zone
- Gas tracer transport in the immobile zone
- Effect of the gas bubble size
- Effect of the heterogeneity
- Effect of the injection borehole

Several gas transport simulations have been carried out. A base case has been defined, injecting helium as gas tracer at a constant concentration, and obtaining the gas tracer breakthrough curves. We have varied the values of the different transport parameters with respect to this base case, according to the different hypotheses about the transport problem to be studied.

Table 5.2. Base case parameters

Base case parameter description	Value
Thickness of the fractured zone (cm)	10.0
Diffusion specific surface of the non-advective gas zone (1/m)	33.3
Volume of the injection borehole (ml)	400
Volume of the extraction borehole (ml)	400
Volume fraction of water at the injection borehole (%)	25.0
Volume fraction of water at the extraction borehole (%)	25.0
Extraction pressure at the extraction borehole (MPa)	0.1
Temperature (K)	288.15
Average porosity	0.1

Table 5.3. Solubility and molecular diffusion coefficients of some gases

Gas	Solubility* $g = K_H^{-1}$ $\left(moles_w moles_g^{-1} bar^{-1}\right)$	Molecular diffusion coefficient	
		In water** D_{aq}($m^2 s^{-1}$)	In gas (N_2) D_{mg}($m^2 s^{-1}$)
N_2	1.35e-5	1.88e-9	--
He	7.12e-6	6.28e-9	7.05e-5
H_2S	2.33e-3	1.26e-9	3.26e-5

Note: (*) Inverse of Henry's constant expressed as a molar fraction as in $K_H^{-1} = f/p$ at 288 K (**) Gas tracer diffusion coefficient in pure water D^k_{aq}, it does not take into account the effects of porosity and tortuosity of the medium.

In order to be able to generalise the results provided by the solution of equations (16) and (17), one can define dimensionless time and space for advection and dispersion/diffusion processes in the mobile zone, and also for molecular diffusion in the immobile zone. Dimensionless space x_D and time t_D definition require a reference value x_0 [L] and t_0 [T]. The former x_0 can be taken as a characteristic length of the medium. The later t_0 is a characteristic time depending on the dominant process that takes place in a given problem.

Table 5.4. Characteristic times for transport processes

	Solute tracer	Gas tracer using the analogy	
Advection at the mobile zone	$t_0 = \frac{R_m f_m x_0}{\lvert\mathbf{q}\rvert}$	$t_0 = \frac{S_l r_l}{S_g r_g}\frac{P_g}{K_H}\frac{f_M S_g x_0}{\lvert\mathbf{q}\rvert}$	(5.36)
Diffusion/dispersion at the mobile zone	$t_0 = \frac{R_m f_m x_0^2}{a_{L_m}\lvert\mathbf{q}\rvert + f_m D_f}$	$t_0 = \frac{\frac{S_l r_l}{S_g r_g}\frac{P_g}{K_H} f_M S_g x_0^2}{a_{L_M}\lvert\mathbf{q_g}\rvert + f_M S_g D^k_{m_g}}$	(5.37)
Diffusion at immobile zone	$t_0 = \frac{R_m x_0^2}{D_i}$	$t_0 = \frac{S_l r_l}{S_g r_g}\frac{P_g}{K_H}\frac{x_0^2}{D^k_{m_i}}$	(5.38)

A further step in this analysis is the introduction of the Peclet's number (*Pe*). It is a dimensionless number, defined as the ratio between the diffusion/dispersion (Eq. 6.39) and advective characteristic times (i.e. equations 5.36 and 5.37 respectively):

$$Pe = \frac{\lvert\mathbf{q}_g\rvert x_0}{a_{L_M}\lvert\mathbf{q}_g\rvert + f_M S_g D^k_{m_g}} \tag{5.39}$$

If *Pe*>1 then advective flux is the most important transport mechanism and conversely, if *Pe*<1 then diffusive fluxes should be expected to be more important than advective

fluxes. For advection dominated situations t_0 is proportional to x_0. If diffusion dominates over advection then t_0 is proportional to the square of the characteristic length (x^2_0).

Using x_0 =1.14m (dipole length), being the mean S_l= 40 % and S_g= 60 %, the $|\mathbf{q_g}|$= 3.6E-07 m/s, a_{LM}= 0.08 m, f_M= 0.002 m, and D^k_{mg}= 6.98e-05 m^2/s gives Pe= 0.511. In this case the diffusive/dispersive flux component is more important than the advective component, so we will have to define a characteristic time t_o proportional to x^2_0 (Table 5.4, characteristic time of diffusion/dispersion at the mobile zone).

5.4.1 Mobile gas zone

Several transport simulations have been conducted to see which is the role played by the gas tracer solubility. Changing only the gas tracer solubility value K_H^{-1}, and leaving without any change the other transport parameters. Different breakthrough curves are obtained (Figure 5.4). The solubility values selected to conduct the simulations range from 2.33e-03 bar^{-1} to 7.12e-6 bar^{-1}. These values correspond to H_2S and helium respectively. As can be seen the larger the solubility is the most delayed the gas tracer breakthrough in the extraction borehole. The large dimensionless times required to reach steady state conditions are due to several factors, among them, the large volumes of injection and extraction boreholes.

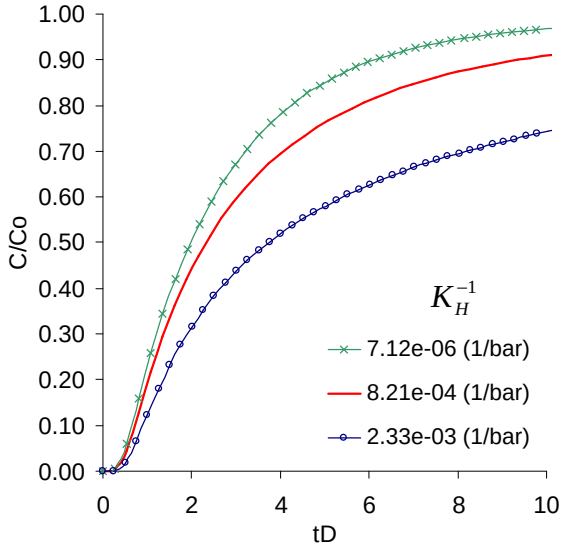

Figure 5.4: Breakthrough curves obtained changing the solubilities value respect to the base case. Transport parameters are for He except solubility $\left(K_H^{-1}\right)$ which is indicated in the picture.

Figure 5.5 displays the breakthrough curves obtained if we change only the gas tracer diffusion coefficient value D^k_{mg}. In this case the breakthrough curves show two different behaviours: For early times (t_D<0.3) the lager the diffusion coefficient is the faster the breakthrough takes place. This result is due to the quick first arrival of the tracer to the extraction borehole. After this initial period, the larger diffusion coefficient becomes the most delayed because a gas with larger value of gas diffusion coefficient diffuses in a

bigger bubble volume. This different behaviour in gas migration depending on the gas molecular diffusion coefficient D^k_{mg} for early and late dimensionless times can be also sawn in figures 6 and 7, where are depicted the spatial distribution of gas tracer for D^k_{mg}. = 10^{-4} and 10^{-6} m^2/s for t_D=0.3 and 5 respectively.

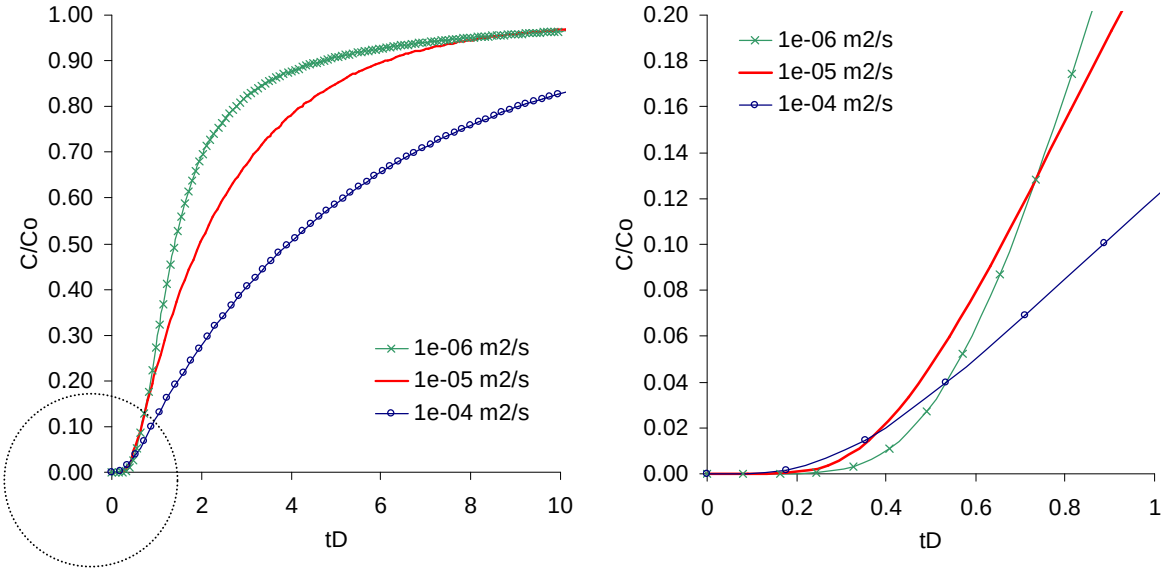

Figure 5.5: Breakthrough curves obtained changing the gas tracer diffusion coefficients respect to the base case. On the right figure is presented the circled area on the left figure, in order to show the different behaviour of the breakthrough curves for early and late times. Transport parameters are for He except gas diffusion coefficient in gas which is indicated in the picture.

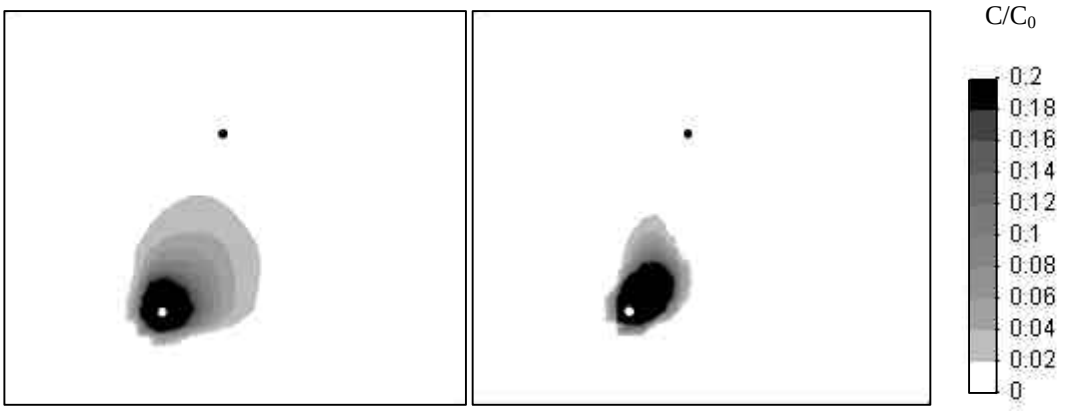

Figure 5.6: Spatial distribution of gas tracer at dimensionless time t_D = 0.3, for two different gas diffusion coefficient values D^k_{mg} , (Left) 10^{-04} m^2/s and (right) 10^{-06} m^2/s. (White and black points are the gas injection and extraction boreholes respectively)

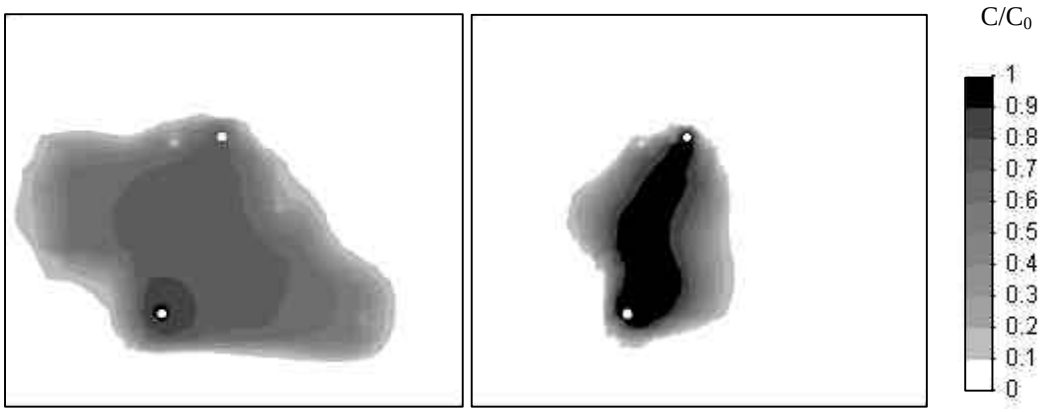

Figure 5.7: Spatial distribution of gas tracer at dimensionless time $t_D = 5$, for two different gas diffusion coefficient values D^k_{mg}, (Left) 10^{-04} m^2/s and (right) 10^{-06} m^2/s. (Lower and upper white points are the gas injection and extraction boreholes respectively)

5.4.2 Immobile gas zone

We have defined the immobile zone as the gouge fill, where the gas entry pressure is too high for the gas to enter as a free phase. So the geometrical structure of the fracture filling material can be an important limiting factor for the gas tracer migration.

Gas diffusion coefficient in water, together with the specific surface (diffusion surface per formation volume unit of formation), and thickness of the fractured zone are the parameters used to perform the sensitivity analysis respect to the gas migration through the immobile gas zone. Helium and H_2S are used as gas tracers.

Figure 5.8(a) displays the breakthrough curves obtained for He and H_2S (left and right, respectively) changing the value of $D^k_{m_i}$ and maintaining the rest of their transport parameter set fixed.

Figures 8(b) and 8(c) display the breakthrough curves obtained for both dissolved gas tracers when changing, first, the specific surface available for diffusion while keeping constant the total pore volume accessible by diffusion, and second, the thickness of the fractured zone or in other words, the total pore volume accessible by diffusion is changed (remaining the specific surface for diffusion constant in all cases, 33.3 m^{-1}).

Two different behaviours can be seen in figures 8(a) to 8(c) in terms of the selected gas tracer. This different response is due to the big difference between the solubilities of He and H_2S (Table 5.3). In the case of helium, no sensitivity is seen for any of the three cases presented. In the case of the H_2S, the resulting breakthrough curves show that the case with the larger specific surface for diffusion is the most delayed. The case with larger specific surface available for diffusion is also the most delayed, and finally, in the case of sensitivity respect to the total fracture thickness volume accessible by diffusion, although the small sensitivity of helium with respect to this parameter, the larger the fracture thickness is the most delayed breakthrough takes place.

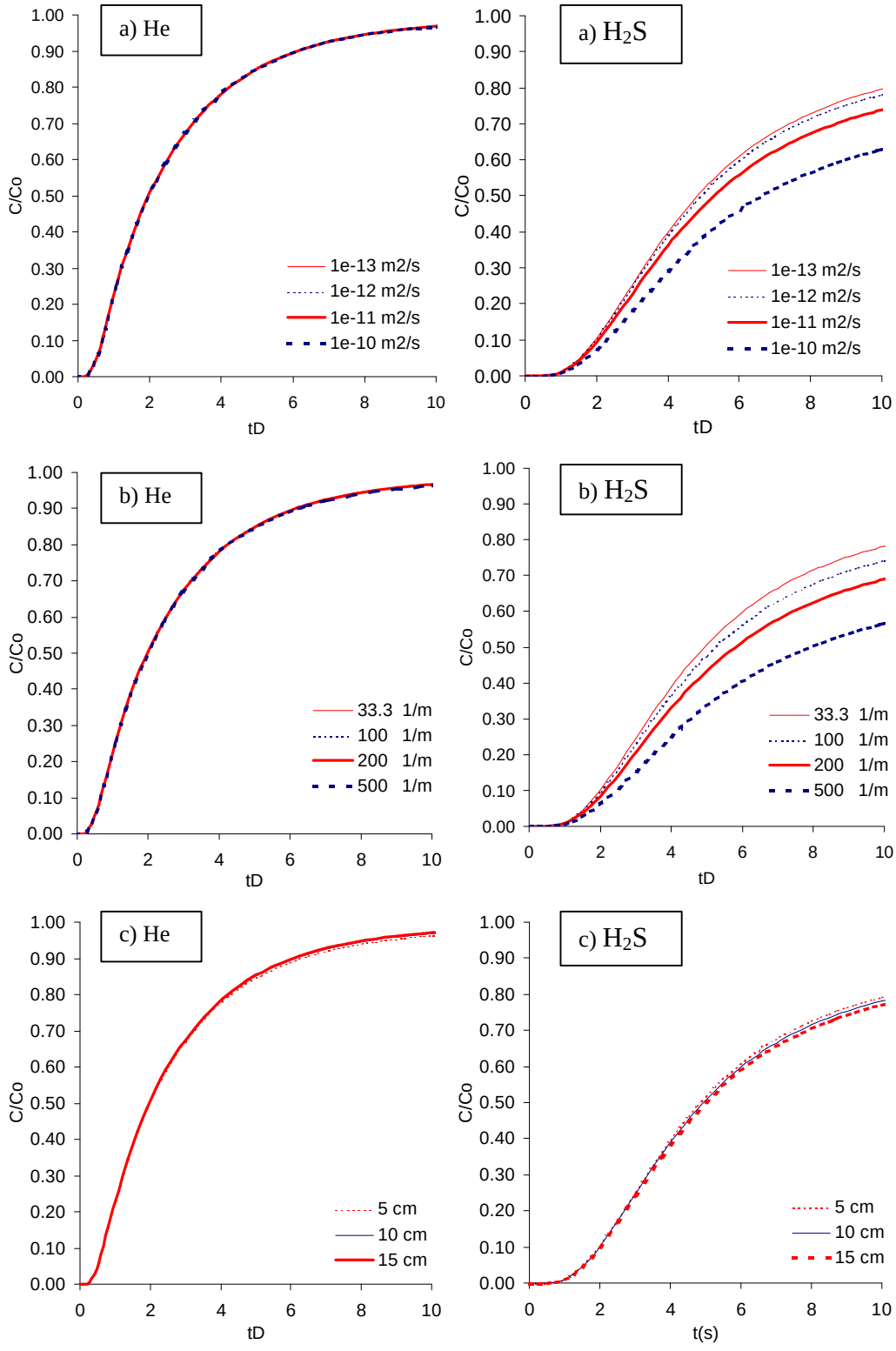

Figure 5.8: Breakthrough curves obtained for helium (left side) and sulphur hexafluoride (right side) changing: a) gas tracer diffusion coefficient in water, transport parameters are for He and H_2S respectively except the value of the gas diffusion coefficient in water, which is indicated in the picture b) diffusion specific surface of the water saturated fracture filling material, c) thickness of the fracture zone

5.4.3 Size of the gas bubble

Since the size of the gas bubble is controlled by the extraction pressure, different gas tracer simulations have been conducted considering different gas extraction pressures. An increase in the extraction pressure leads to an increase in the gas pressure throughout the flow domain and a corresponding increase in the capillary pressure, and also an increase in the portion of the domain that can be dewatered (Figure 5.7). As a result,

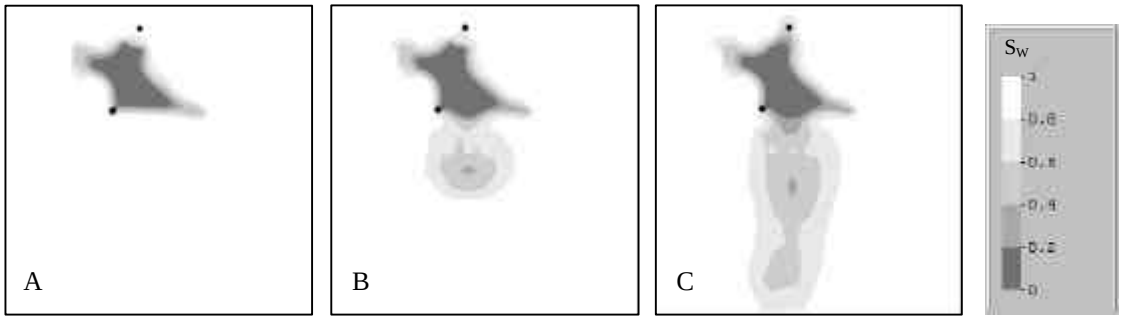

Figure 5.9: Steady state water saturation fields, obtained through the simulation of the gas injection tests, and imposing different gas extraction pressure: A) 0.1 Mpa, B) 0.2 Mpa, C) 0.3 Mpa. (The injection borehole is the lower black point, and the extraction borehole is the upper black point, being the distance between injection and extraction boreholes 1.14m)

both mean residence time in the gas filled zone, and also surface available for dissolution/diffusion increase in response to increases in the gas pressure. As can be seen in Figure 5.10, increasing the extraction pressure leads to increasing the breakthrough curves delay. This reflects both the decrease in the fracture water content and the increase of the gas bubble size.

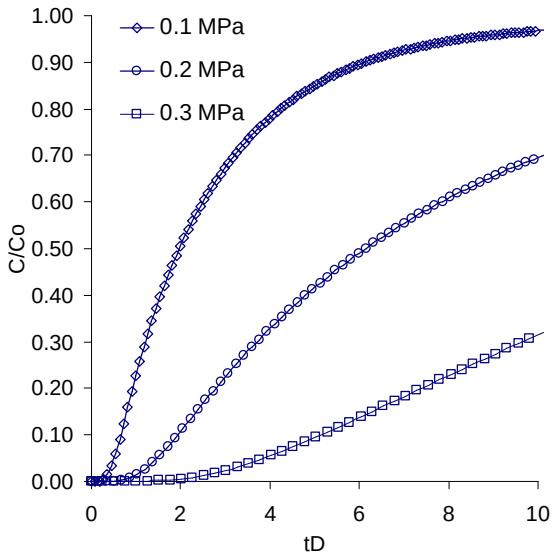

Figure 5.10: Breakthrough curves obtained changing the gas extraction pressure, and helium as gas tracer.

5.4.4 Effect of heterogeneity

The initial transmissivity field used to conduct the sensitivity analysis (Fig.5.11-A) comes from the geostatistical inversion of several hydraulic test performed in a fracture in the framework of the GAM project. In this case (geostatistical fracture model), the result of the geostatistical inversion is the conditional expectation of transmissivity conditioned by measurements of transmissivity and heads. This means that the estimated transmissivity field is a smooth function of space (as a result of being an expected value) that coincides with point transmissivity values where available, and that leads to accurate simulation of available head measurements. In order to represent the spatial variability patterns of the "actual" transmissivity field we have conducted three conditional simulations (Fig.5.11-B,C,D) (simulation-1, simulation-2 and simulation-3 fracture models respectively), which are generated using the computed code GCOSIM3D (Gómez-Hernández and Journel, 1993). Spatial variability of the transmissivity is defined by the same geostatistical model used in the geostatistical inversion, that is, a multigaussian model, with a $Log_{10}T$ variance of 9.4 and mean equal to -9.6. The variogram is exponential and isotropic, with a range of 0.4 m.

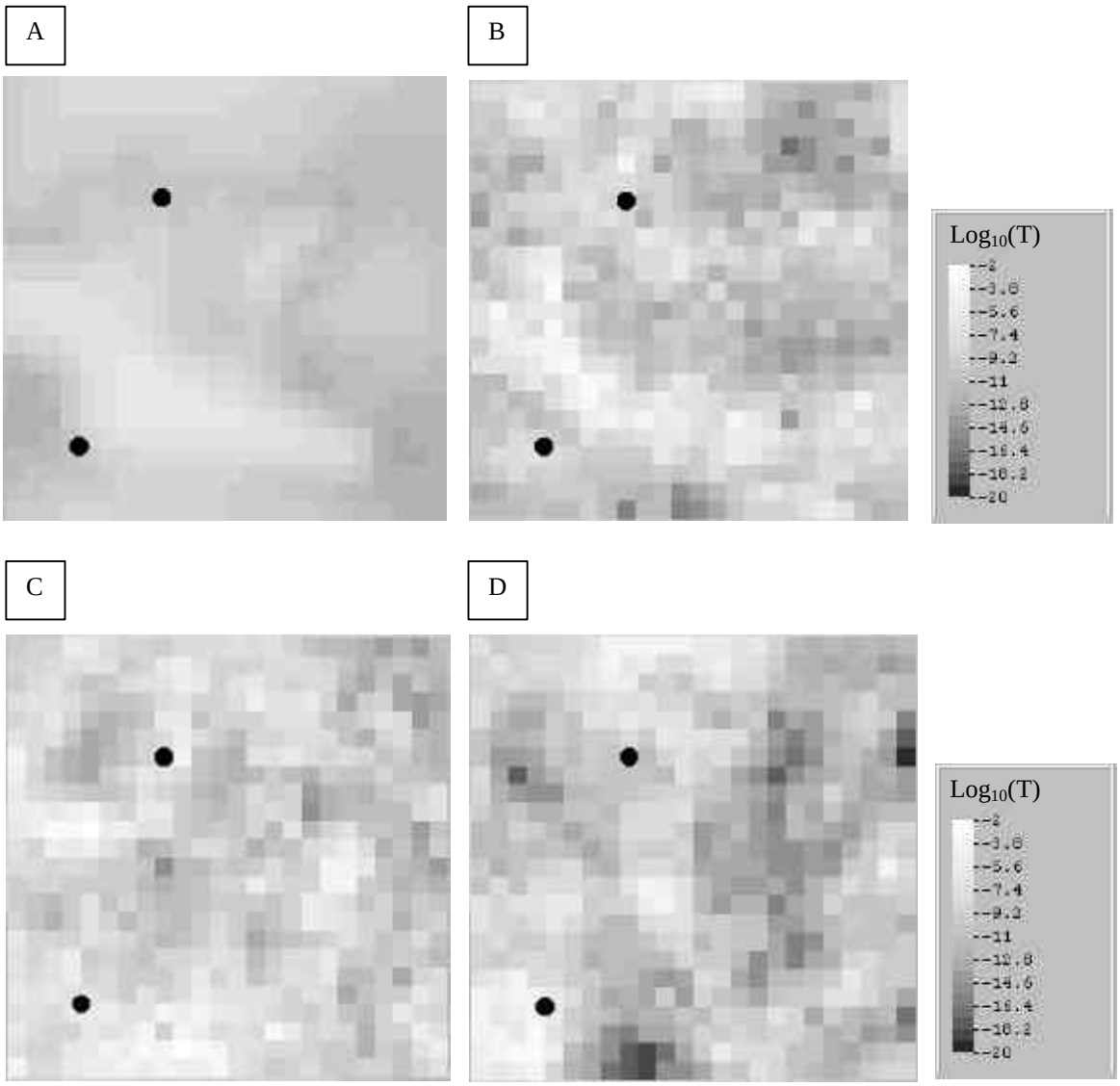

Figure 5.11: Transmissivity fields used to conduct the sensitivity analysis respect to the heterogeneity (the injection borehole is the lower black point, and the extraction borehole is the upper black point, being the distance between injection and extraction boreholes 1.14m). A) T field from the geostatistical inversion, B) C) D) T field conditional simulation 1, 2 and 3 respectively.

On the other hand, in order to compare the results obtained using the heterogeneous transmissivity fields with a simple fracture model, an homogeneous T field was used to represent an empty fracture, taking a constant fracture transmissivity value of 2.55e-10 m^2/s (the geometric transmissivity mean of the calibrated field).
Following the same methodology presented in point 3, first we simulate the two phase flow conditions inside the fracture previous to the gas tracer injection tests for each fracture transmissivity field, and then we conduct the gas tracer transport simulations.

During steady state conditions of gas flow, before the gas tracer injection, and depending on the selected fracture model, gas pressure ranges from 0.196 to 0.8 MPa (Table 5.5) at the injection borehole. This leads to a variation in the gas pressure throughout the flow domain, and as we showed in point 4.3, it has a direct effect on the breakthrough curves. On the other hand capillary pressure field, and water saturation field are different for each fracture model (Figure 5.12). That means different volume of water remaining in the fracture for each fracture model, and also different shape of the gas bubble. Consequently, the gas tracer has different volume of water for dissolution/diffusion and also different mean residence time in the gas filled zone.

Table 5.5. Steady state pressures before conducting the gas tracer injection tests

	Fracture model				
	Geostatistical Inversion	Simulation 1	Simulation 2	Simulation 3	Homogeneous
$P_g^{IB}(MPa)$ (1)	0.196	0.293	0.206	0.338	0.82
$P_g^{EB}(MPa)$ (2)	0.100	0.100	0.100	0.100	0.100
$S_g(\%)$ (3)	60	64	59	37	12

Note: (1) IB stands for injection borehole. (2) EB stands for extraction borehole. (3) mean gas saturation in the zone of interest.

Figure 5.13 shows the breakthrough curves obtained for the different fracture models. Gas solubility plays an important role in the breakthrough of the gas tracer. Homogeneous fracture model is delayed with respect to the others because the large water saturation degree between the injection and the extraction boreholes (Table 5.5). In the other cases, due to the different gas bubble size, and also different water saturated degree, different delays are obtained between the three T field realisations and the calibrated T field. The bigger volume occupied by the gas bubble makes smaller the water volume accessible for gas dissolution and diffusion into the immobile zone, and reduce the effect of the non mobile gas zone on the delay of the breakthrough curves.

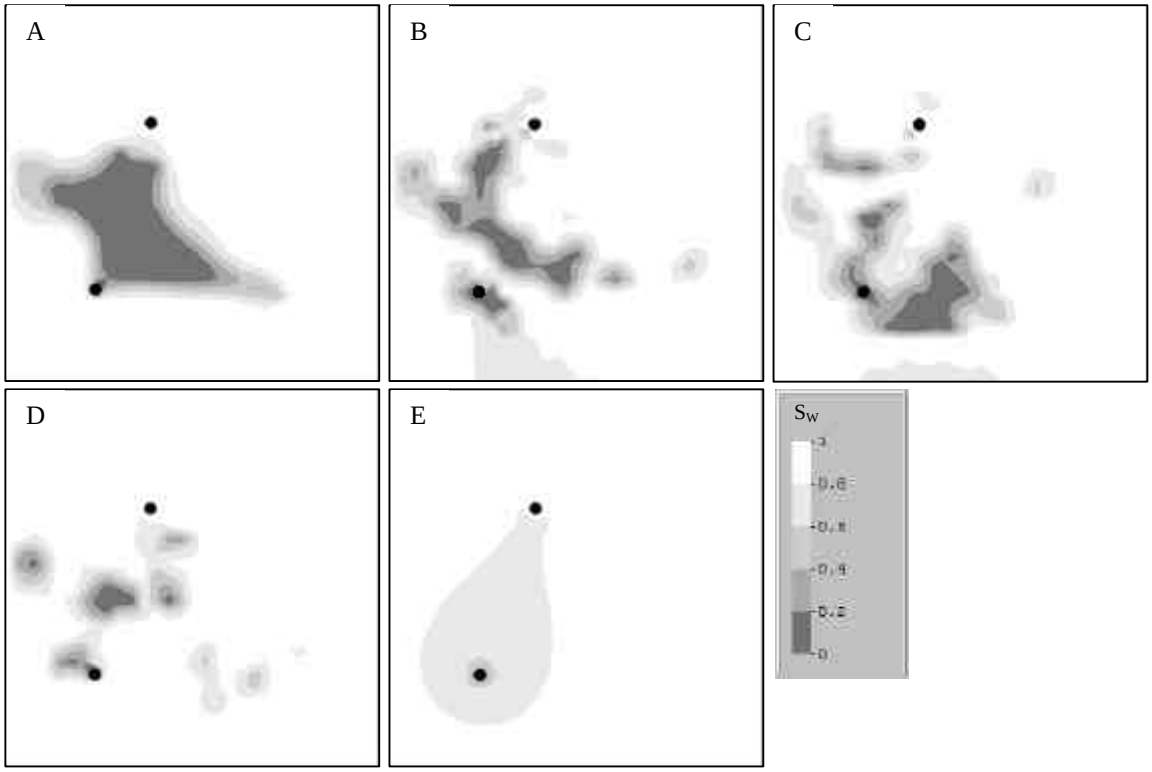

Figure 5.12: Steady state water saturation fields, obtained through the simulation of gas injection tests in the different fracture models: A) T field from the geostatistical inversion, B) C) D) T field conditional simulation 1, 2 and 3 respectively, E) Homogeneous T fracture model. (The injection borehole is the lower black point, and the extraction borehole is the upper black point, being the distance between injection and extraction boreholes 1.14m)

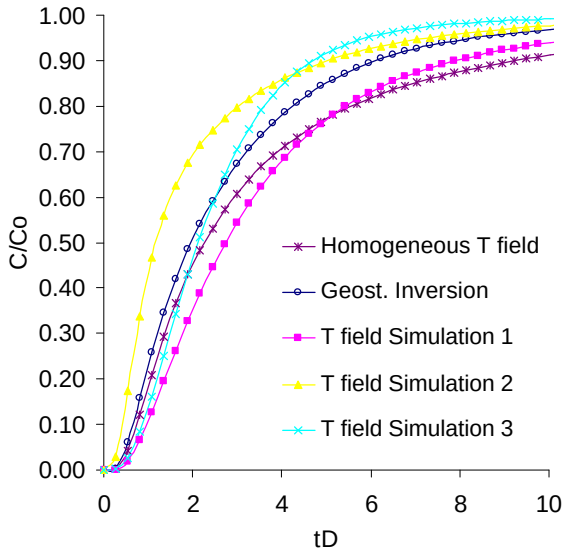

Figure 5.13: Breakthrough curves obtained changing the T field fracture model, and helium as gas tracer.

5.4.5 Effect of injection and extraction boreholes

In order to study what is the effect of the injection and extraction boreholes in the gas tracer breakthrough curves we have conducted several gas tracer simulations, changing injection borehole properties, such as borehole volume or the volume fraction of water

which is present at the injection interval between packers, while the gas tracer is being injected. The volume of he injection and extraction boreholes is relevant because it behaves as a gas storage for dissolved gas, and dilutes the gas tracer concentration injected in the injection interval. The volume of water remaining in the interval can be much bigger than the volume of water accessible by the gas by diffusion processes, and can play a significant role in the transport of the gas tracers.

Figure 5.14 shows the breakthrough curves obtained changing the volume of the injection interval respect to the base case. Several injection interval volumes are considered ranging from 0 up to 1.1 times the volume of water (3000 ml) remaining in the interest fracture area around the injection and extraction boreholes, and considering in all cases the same borehole volume fraction occupied by water (25%). The bigger injection interval volume presents the most delayed breakthrough curve. This behaviour is reproduced by both gas tracers, showing the breakthrough curves an interesting chromatographic effect respect to the injection interval volume, being the delay more important in the case of the H_2S.

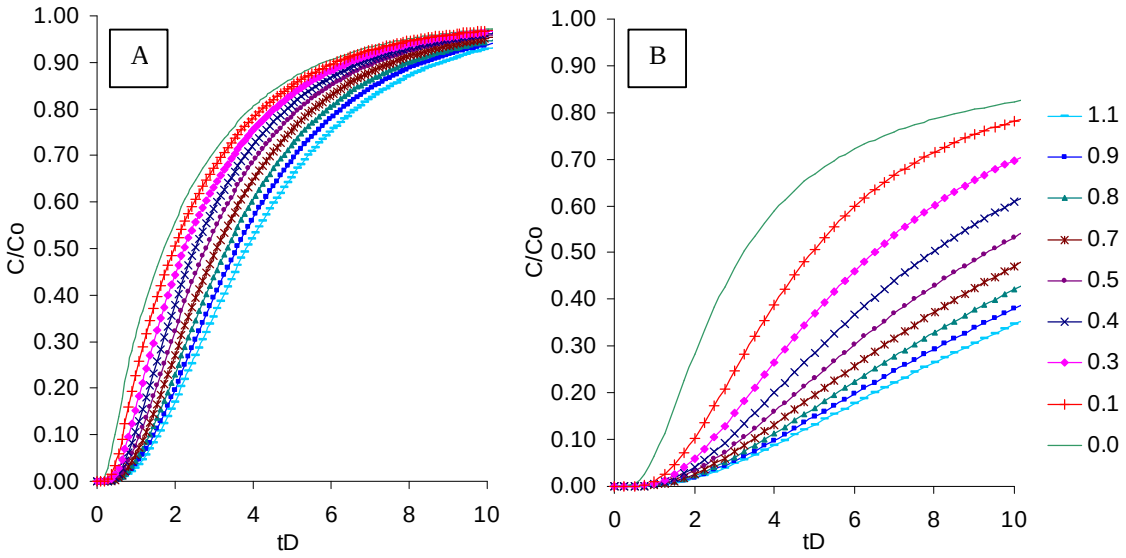

Figure 5.14: Breakthrough curves obtained changing the volume of the injection interval borehole, refereed to the total water volume remaining in the interest area, around the injection and the extraction boreholes, for different gas tracers: A) and helium as gas tracer, B) H_2S.

Figure 5.15 shows the breakthrough curves obtained for helium and H_2S changing the fraction of the injection interval volume occupied by water, and remaining the injection interval volume constant (400 ml). In the case of the helium (fig 13-A) no sensitivity is barely seen respect to the water saturation of the injection interval. The behaviour of H_2S is totally different. This big difference between the two tracers is due to the large differences in their solubilities (7.12e-6 bar^{-1} for He and 4.93e-3 bar^{-1} for H_2S). This is an important point to take into account when gas injection tests are performed, because

not only the injection interval volume induces a delay. Depending on the solubility of the selected gas tracer, water saturation of the injection interval can play an important role in the observed breakthrough curves.

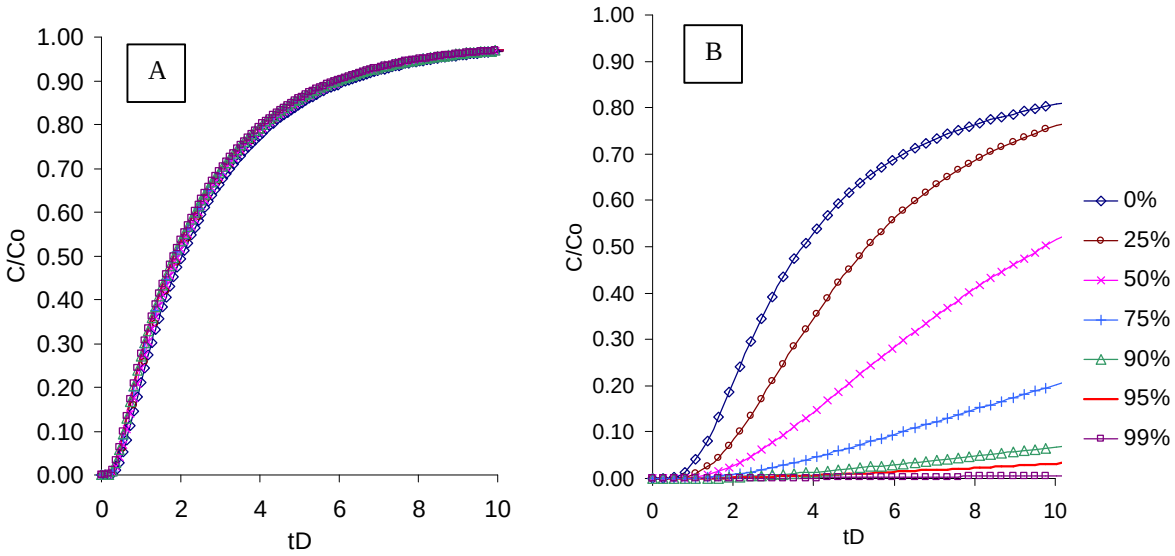

Figure 5.15: Breakthrough curves obtained changing the fraction of the injection interval volume occupied by water, remaining the injection interval volume constant (400 ml) A)Helium B) H_2S

5.5. Conclusions

The objective of this study was to gain further understanding of processes affecting gas tracer migration in shear zones under two phase flow conditions. A numerical model developed to take into account several hypothesis about gas transport through partially saturated heterogeneous fractures. The model takes advantage of the formal analogy between gas transport in a two phase system equations and the solute tracer transport equation in water saturated systems, uncoupling the solution of the multiphase flow and gas tracer transport equations. A sensitivity analysis have been carried out, paying special attention to those variables which govern the dissolution/diffusion processes is shear zones. The model is potentially useful for predicting gas tracer migration, site characterisation, and also for experimental gas tracer tests design.

In general, gas tracer migration is very sensitive to the solubility, affecting to the gas tracer transport in both, mobile and immobile zones. As can be seen in the breakthrough curves, the larger the gas solubility value the most delayed the breakthrough takes place. That means that depending on the solubility value gas tracer partitioning from the gas phase into an aqueous phase may be an important factor in the transport of gases through fractures by diffusion processes. This is a reason to take into account in order to determine the solubility for toxic gases under different conditions.

Effective gas diffusion coefficients depend on porosity, tortuosity and also temperature. In the transport simulations a isothermal condition is assumed. The model can account with non-isothermal scenarios, being the effective diffusion coefficient a space function depending on the spatial temperature distribution.

In order to investigate the effect of the heterogeneity on the breakthrough curves, different equally probably transmissivity realisations have been considered. The results show that different breakthrough curves are obtained depending on the water content of the fracture. A bigger surface of water in contact with the gas tracer implies a larger delay in the breakthrough.

Gas migration shows a great sensitivity respect to the formation pressure. In a hypothetical scenario where gas is generated at enough production rate, gas will displace water from the fracture zone. During this early times where transient two phase flow conditions exist, a high gas pressure inside the initial gas bubble is expected to be found, increasing the gas mass transfer between the mobile and immobile zones through the gas-water interface. As we have shown in the sensitivity analysis respect to the gas pressure, the higher the gas pressure larger the mean residence time and also the surface available for dissolution/diffusion.

On the other hand, the effect of the injection/extraction boreholes (injection interval volume and water saturation) is very important to take into account in the design and performance of future gas tracer injection tests in fractures, due to the fact that the injection interval behaves as a storage for dissolved gas. This effect must be taken into account during the interpretation of the experimental breakthrough curves.

5.6. References

Abu-El-Sha'r, W. and L.M. Abriola, (1997): Experimental assessment of gas transport mechanisms in natural porous media: Parameter evaluation. Water Resour. Res., 33(4), 505-516.

Baeher, A.L. and C.J. Brruell, (1990): Application of the Stefan-Maxwell equations to determine limitations of Fick's law when modelling organic vapour transport in sand columns. Water Resour. Res., 26(6), 1155-1163.

Bear, J., (1972): Dynamics of fluids in porous media. Elsevier.

Bird R.B., W.E. Stewart and E.N. Lightfoot, (1960): Transport phenomena. New York: John Winley.

Brusseau, M. L., (1991): Transport of organic chemicals by gas advection in structured or heterogeneous porous media: Development of a model and application to a column experiments. Water Resour. Res., 27(12), 3189-3199.

Fierz, T., and M. Piedevache, (2000): GTS/GAM: Results of hydraulic tests and gas threshold pressure tests in GAM 98-002 (January/February 2000). NAGRA Internal Report 00-14, Wettingen, Switzerland.

Fierz, T., E. Proust., M. Combarieu and P. Meier, (2000): GTS/GAM: Gas tracer test series GT1 in the GAM shear zone (February 2000). Dipole flow field GAM98-002/TPF95-007. NAGRA Internal Report 99-30, Wettingen, Switzerland.

García, M. and S. Caussade, (2001): Modelisation et calage d'essais de tracage dans le gaz dans le cadre du projet GAM pour la Phase V du laboratoire Grimsel, Suisse. Rapport Final. Internal Report. (In English).

Gascoyne, M. and D.M. Wuschke, (1997): Gas migration through water-saturated, fractured rock: results of a gas injection test. J. Hydrol.,196, 76-98.

Gemperle,R.,(1999): GTS/GAM: Hydraulic testing in GAM 98.002 and GAM 98.004. NAGRA (Nationale Genossenschaft für die Lagerung radioaktiver Abfälle) Internal Report 99-02, Wettingen, Switzerland.

Gierke, J. S., N. J. Hutzler, and J. C. Crittenden, (1990): Modelling the movement of volatile chemicals in columns of unsaturated soil. Water Resour. Res., 26(7), 1529-1547.

Gierke, J. S., N. J. Hutzler, and D. B. McKenzie, (1992): Vapour transport in unsaturated soil columns: Implications for vapour extraction. Water Resour. Res., 28(2), 323-335.

Gómez-Hernández, J. J.and A. G. Journel, (1993): Joint sequential simulation of multigaussian fields. In A. Soares (Editor), Geostatistics Trója '92, Vol. 1. Kluwer, Dordrecht, pp. 85-94.

Lineham, T.R., P.J. Nash, W.R. Rodwell, J. Bolt, V.M.B. Watkins, P. Grainger, M.J. Heath and J.R. Merefield, (1996): Gas migration in fractured rock: results and modelling of a helium gas injection experiment at the Reskajeage Farm Test Site, SW England, United Kingdom. J. Contam Hydrol, 21, pp. 101-113.

Lunati, I., (2000): GTS/GAM: Simulation of dipole experiments: Solute transport and gas migration in a two dimensional fault gouge filled fracture. NAGRA Internal Report 00-24, Wettingen, Switzerland.

Johnson, P.C., M.W. Kemblowski and J.D. Colthart, (1990): Quantitative analysis for the clean up of hydrocarbon-contaminated soils by insitu venting. Ground Water, 28(3), 413-429.

Marshall, P., W. Albert, R. Carbonell, J. Carrera, P.B. Davies, W. Kinzelbach, J.C. Mayor and S. Niehren, (1998): GTS/GAM: Investigation programme fot thr GTS Phase V experiment "Gas migration in shear zones" (1998-2000). NAGRA Internal Report 98-12. Wettingen, Switzerland.

Medina A, Alcolea A, Carrera J, Castro LF., (2000) Modelos de flujo y transporte en la geosfera: Código Transin IV. [Flow and transport modelling in the geosphere: the code TRANSIN IV], in: IV Jornadas de Investigación y Desarrollo Tecnológico de Gestión de Residuos Radiactivo de ENRESA. Technical publication 9/2000: 195-200

Olivella, S., J. Carrera, J. Gens, and E. Alonso, (1996): Numerical formulation for a simulator (CODE-BRIGHT) for the coupled analysis of saline media, Engineering Computations, Vol 13, Number 7, pp 87-112.

Popovicová, J. and M. L. Brusseau, (1998): Contaminant mass transfer during gas-phase transport in unsaturated porous media. Water Resour. Res., 34(1), 83-92.

Pruess, K., (1991): A general purpose simulator for multiphase fluid and heat flow. Lawrence Berkeley Laboratory, University of California, Berkeley.

Ramajo, H., S. Olivella and J. Carrera, (2002): Simulation of gas dipole tests in fractures at the intermediate scale using a new upscaling method. Transport in porous media 46: 269-284.

Skjetne, E. and J.L. Auriault, (1999): Homogenisation of wall-slip gas flow through porous media. Transport in porous media 36: 293-306.

Thorstenson, D.C. and D.W Pollock (1989): Gas transport in unsaturated zones: Multicomponent systems and the adequacy of Fick's laws. Water Resour. Res., 25(3), 477-507.

Trick, T., T. Fierz, E. Proust, P. Meier and M. Combarieu, (2000): GTS/GAM: Gas tracer test series GT2 in the GAM shear zone (August 2000). Dipole flow field GAM98-004/TPF95-004. NAGRA Internal Report 00-49, Wettingen, Switzerland.

Trick, T., M. Piedevache, E. Proust, P. Meier and M. Combarieu, (2001): GTS/GAM: Gas tracer test series GT3 in the GAM shear zone (December 2000). Dipole flow field GAM98-002/TPF95-007. NAGRA Internal Report 01-02, Wettingen, Switzerland.

Boving, T.B., Grathwohl, P., (2001): Tracer Diffusion Coefficients in Sedimentary Rocks: Correlation to Porosity and Hydraulic Conductivity. J. Contaminant Hydrology, 53, 85-100

Wu, Y.S., K. Pruess and P. Persoff, (1998): Gas flow in porous media with Klinkenberg effects. Transport in porous media 32: 117-137.

Wyss, E., (1996): GTS/TPF: Site preparation, borehole installation, hydraulic characterisation and gas threshold-pressure tests at the Grimsel Test Site. (July, 1996). NAGRA Internal Report 96-34, Wettingen, Switzerland.

Chapter 6: Gas tracer transport modelling in a heterogeneous fracture in two phase flow conditions. Experimental results.

6.1 Introduction

The behaviour of the gas phase has become an important part of the performance assessment of radioactive waste repositories. It is expected that gas will be produced during the post-operational phases of radioactive waste repositories through anaerobic degradation and accumulated in storage caverns. If the rate of gas production at the source is sufficiently large and the rock impervious, pressure will build-up, which could have a negative effect on the barrier function of the rock and engineered barrier system (opening of existing fractures, generation of new fractures). This would allow gas to migrate upwards through interconnected pores and fractures with the highest transmissivity. Shear zones might serve as primary conduits for gas migration away from the caverns through the geosphere. To assess the effect of gas migration on waste storage safety, one needs to understand, first, how gas flows through the rock and, second, how specific components of the gaseous phases are transported.

A number of studies and experimental programs have been carried out to assess whether gas can indeed escape from the repositories into the fractured host rock and migrate away. Field investigations of gas migration through initially water saturated fractured rock have been performed using different approaches: injection into an isolated zone in a borehole to establish gas entry pressures (Wyss 1996, Croise el al. 1999); monitoring the appearance of gas injected into fractured rock from an isolated zone of a borehole (Thunvik and Braester 1987, Lineham et al. 1996, Gascoyne and Wuschke 1997); investigation of gas migration along fractures connecting a pair of boreholes (Marshall et al. 1998). To investigate the gas transport mechanisms in real shear zones, Fierz et al. (2000) and Trick et al. (2000 and 2001) carried out three gas tracer test campaigns in a granite fracture at the GTS, in the framework of the GAM project. These field campaigns were aimed at determining realistic mass exchange coefficients in two phase flow through fractures, and to investigate the role played by the different gas tracers solubility and diffusion coefficients in gas migration through rock fractures.

The objective of this chapter is twofold. On one hand we present experimental results obtained from gas tracer testing activities. On the other, we analyse the two phase flow conditions inside the fracture in terms of the observed breakthrough curves and the gas flow field. The objective is to reproduce the experimental gas tracer breakthrough curves in order to simulate the behaviour of the gas tracers by means of valid gas transport models.

6.2 Gas tracer tests

6.2.1 Site characterisation

The GTS (Grimsel Test Site) is a rock laboratory that consists of a series of galleries lying about 450m below surface within granitic rock. The GAM shear zone is located in the southern part of the GTS. In this part all shear zones exhibit similar structure. The fractures dip steeply and the dominant strike is EN-SW. Macroscopically, shear zones are characterised by zones of ductile deformation with high damage intensity with mica-rich mylonite bands, and brittle fault breccia horizons with a thickness ranging from a few millimetres to several centimetres, located at the zones of the highest ductile deformation. These zones contain fine-grained, non-cohesive gauge material. Bossart and Mazureck (1991) investigated the macroscopic arrangement of these flow paths. Porosity of the gouge material ranges from 0.1 to 0.3. On the other hand, recent studies of Marschall et al. (1999) showed that the aperture distributions across the brittle structures is typically described by a log-normal distribution, with mean values of 0.2-0.5 mm and cumulative thickness in the centimetre range. Field investigations were carried out in a 4x6 m^2 section of the GAM shear zone, which was explored with a total of 20 boreholes (Fig.6.1). Gemperle (1999) summarises the borehole specifications and instrumentation layout.

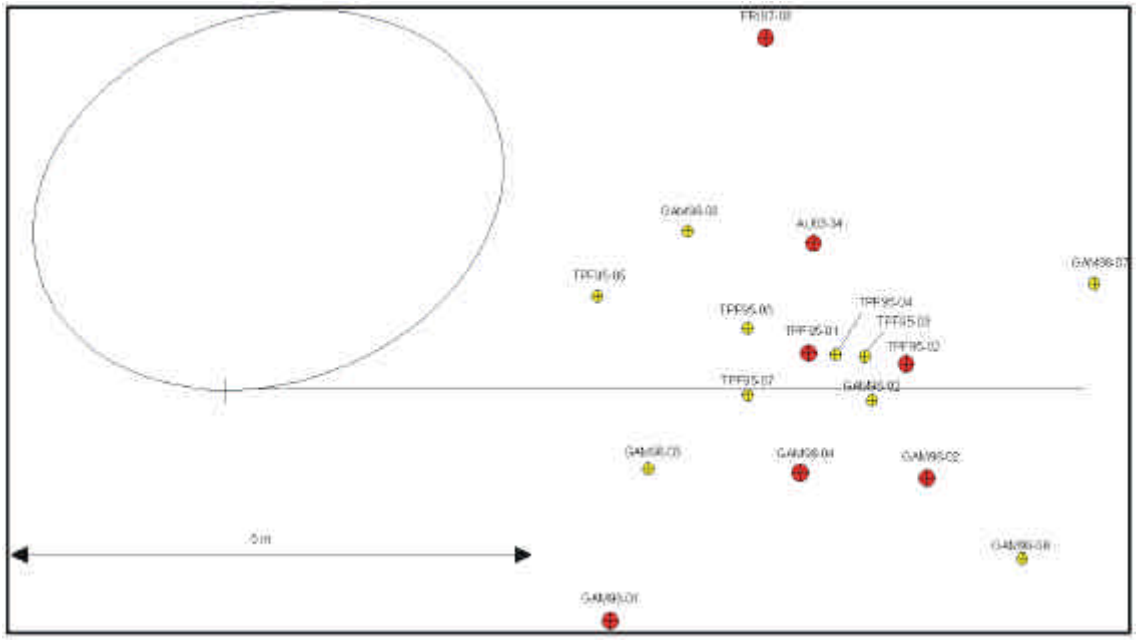

Figure 6.1: Intersection of the access tunnel and drilled boreholes at the GAM site with the shear zone

The transmissivity field values are obtained following the same methodology presented by Meier et al. (2001). This methodology consists of the geostatistical inversion of several hydraulic tests (Wyss 1996, Gemperle 1999, Fierz and Piedevache 2000) in the framework of the GAM project (Marschall et al. 1998) (Fig.6.2). The method allows us to use all pumping tests drawdown data (at several observation boreholes) to estimate the spatial distribution of the expected value of the transmissivity. Geostatistical inversion confirms the large heterogeneity of the domain and the existence of well connected high transmissivity regions that can be viewed as preferential flow zones (Ramajo et al., 1999). Effective transmissivity is of the order of $2 \cdot 10^{-10}$ m^2/s and storage coefficient falls around $2 \cdot 10^{-6}$. The procedure was described in chapter 3.

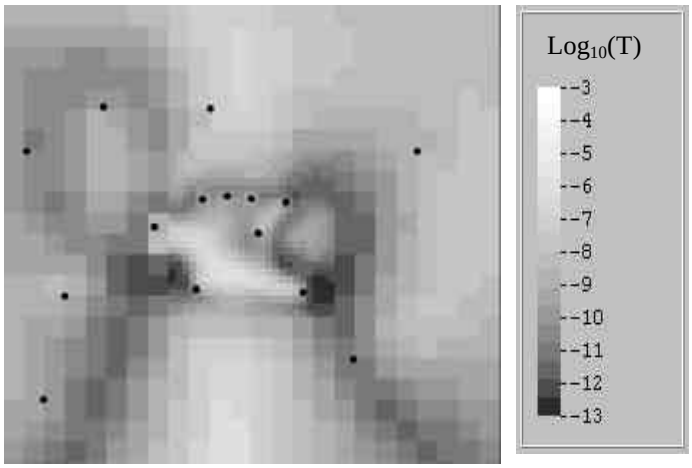

Figure 6.2: Most discretized zone of the transmissivity ($Log_{10}T$) field calibrated in the framework of the GAM project (the black points are the intersection of the boreholes with the GAM shear zone)

We are assuming an empty fracture, ant that aperture varies spatially as a function of transmissivity according the cubic law (laminar flow between parallel plates).

Five dipole tracer tests were performed in the fully water saturated fracture project (Kennedy, 1999, Kennedy, 2000(a,b), Kennedy and Kleiner, 2000), using a number of solute tracers with the objective of characterising transport within the fracture zone. Both dissolved tracers and particles have been used. In general terms, results of the tracer tests are consistent with hydraulic tests. Effective transport apertures derived from the tests are of the order of 2 mm.

6.2.2 Methods and Materials

During a dipole gas injection test, as gas is injected, water is displaced laterally in the fracture along permeable pathways, until an almost full gas phase pathway is formed between the injection and the extraction boreholes. Once the gas bubble has been created (steady state conditions) a gas tracer "cocktail" is injected.

The set up of gas tracer tests is presented in Figure.3. A stable gas flow field is established by injecting nitrogen into the injection borehole. The injection (and extraction) gas flow is measured with Brooks gas flow controllers type 5850S. Pressures at the extraction side were controlled by a pressure regulation valve which can be readjusted manually during the tracer injection if necessary. The gas/water separator is used to extract water during the prior gas injection, which is performed to generate a stable gas flow field inside the fracture. The extracted water is measured with a meter scale, which is connected to the data acquisition system. After stable conditions have been achieved, a gas tracer cocktail is injected (Tables 1 to 3), and the different breakthrough curves corresponding to the different gas tracers are measured at the extraction borehole. When the saturation of the breakthrough curves has been achieved (plateau in breakthrough), tracer injection is stopped, and the recovery of the tracers is measured. A Balzers Mass Spectrometer data acquisition system (type Omnistar) is used for monitoring the different tracers concentrations. The mass spectrometer is

calibrated before starting each tracer test and at the end of its recovery phase. Nitrogen is injected during the entire test at a constant rate to maintain the direct gas phase connection (gas bubble) between injection and extraction boreholes. A more extensive description about experiment design and testing activities can be found in Fierz et al. (2000) and Trick et al.(2000, 2001). In Table 4 the different properties of gas tracers injected during the gas testing activities are presented.

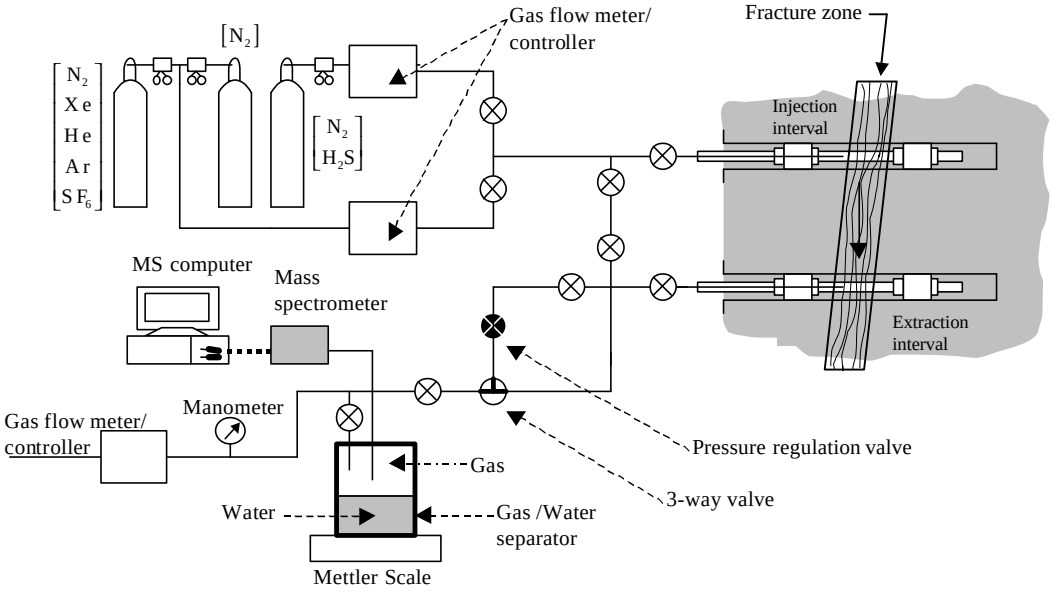

Figure 6.3: Gas tracer set-up (Trick et al. 2000)

Table 6.1: Tracer gas mixtures

	Tracer gas mixture 1 Concentration (volume %)				Tracer gas mixture 2 Concentration (volume %)			Uncertainty (volume %)
	He	Xe	Ar	SF_6	N_2	H_2S	N_2	
GT1	0.530	0.500	--	--	98.970	--	--	$\pm 1^{o}/_{oo}$
GT2	0.502	0.500	0.500	0.501	97.970	--	--	$\pm 4^{o}/_{o}$
GT3	0.502	0.500	0.500	0.501	98.000	0.100	99.900	$\pm 1^{o}/_{oo}$

Table 6.2: Total input gas volume cm^3 (STP)

		Injection flow rate ml(STP)/min			Input gas volume cm^3 (STP)				
		Mixture 1	Mixture 2	Total	He	Xe	Ar	SF_6	H_2S
GT1	Run1	--	--	--	74.730	70.750	--	--	--
	Run2	50	--	50	96.990	91.280	--	--	--
	Run3	10	--	10	18.073	17.050	--	--	--
GT2	Run4	10	--	10	24.740	24.650	24.650	24.690	--
	Run5	100	--	100	48.690	48.500	48.500	48.600	--
	Run6	100	--	100	151.100	150.500	150.500	150.800	--
GT3	Run7	10	5	15	57.300	57.300	57.300	57.300	5.730
	Run8	25	50	75	26.710	26.710	26.710	26.710	10.710
	Run9	100	200	300	51.510	51.510	51.510	51.510	20.610
	Run10	100	200	300	210.040	210.040	210.040	210.040	84.040
	Run11	100	500	600	141.000	141.000	141.000	141.000	141.000

Table 6.3: Recovery mass (%)

		Total injection flow rate ml(STP)/min	He	Xe	Ar	SF_6	H_2S
GT1	Run1	--	--	--	--	--	--
	Run2	50	97.5	99	--	--	--
	Run3	10	96	91	--	--	--
GT2	Run4	10	92	96	96	99	--
	Run5	100	41	46	48	46	--
	Run6	100	97	99	99	99	--
GT3	Run7	15	98	97	100	99	1
	Run8	75	100	100	100	100	6
	Run9	300	100	100	100	100	52
	Run10	300	99	97	99	98	78
	Run11	600	98	96	98	97	83

Table 4: Properties of gas tracers

	He	Xe	Ar	SF_6	H_2S
Molecular weight (g/mol)	4.003	131.97	39.91	146.05	34.08
Solubility* $g = K_H^{-1}$ $\left(moles_w moles_g^{-1} bar^{-1}\right)$	7.12e-6	1.05e-4	3.02e-5	4.93e-3	2.33e-3
Molecular Diffusion Coefficient in water (m^2/s)	6.28e-9	2.20e-9	2.00e-9	1.20e-9	1.26e-9
Molecular Diffusion Coefficient in N_2 (m^2/s)	7.05e-5	1.30e-5	2.00e-5	1.04e-5	3.26e-5

* Inverse of Henry's constant expressed as a molar fraction as in $K_H^{-1} = f/p$ at 288 K (Sander, 1999)

6.2.3 Gas tracer testing GT1, GT2 and GT3

Three gas tracer tests campaigns were performed in the GAM shear zone: February 2000 (Fierz et al. 2000), August 2000 (Trick et al. 2000) and December 2000 (Trick et al. 2001).

The first gas tracer test campaign GT1 (Fierz et al. 2000) was performed by injecting at borehole GAM98.02 and extracting at borehole TPF95.07. During GT1 three gas tracer tests were performed (Run1, Run2, and Run3 respectively). The purposes of the first campaign were to see the feasibility of the test set-up, the feasibility of the mass spectrometer used to measure gases, and finally to compare the breakthrough curves of the injected gas tracers.

During Run1, the gas extraction flow rate was 10 times lower than the gas injection rate, that is 100ml(STP)/min (**S**tandard **T**emperature and **P**ressure). Based on this low gas extraction flow rate low tracer recovery was expected. Therefore tracer gas injection was limited to a short time to minimise the contamination of the site. From the experimental point of view, Run1 was not a success, except for the different control devices which worked perfectly.

In Run2, the injection and extraction rates were reduced to 50ml(STP)/min. During the first two hours after tracer injection gas outflow was regulated by a gas flow controller. The gas controller caused a back pressure in the extraction line and biased the function of the gas water separator, so the gas outflow was measured using the unregulated mode of the gas controller. The gas outflow showed large fluctuations (Fig.6.4), the average gas outflow was 47.5ml(STP)/min after the reinstallation of the controller. Both injection interval and extraction interval pressure were stable during the entire test period.

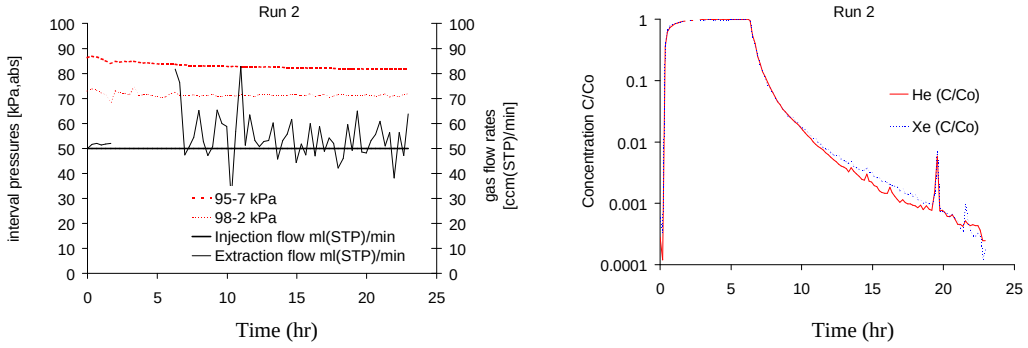

Figure 6.4: Run 2. Left: Injection and extraction interval pressures (bold and thin dashed lines respectively), and injection and extraction dipole gas flow rates (bold and thin continuous lines respectively). Right: Tracer gas breakthrough curves, semi log scale.

In Run3, the injection and extraction rates were 10ml(STP)/min. The flow field was perfectly stable during the entire test period (Fig.6.5).

From the experimental point of view, Run2 and Run3 were a success. Both tracers (He, Xe) showed a very similar breakthrough curves (Fig.6.4 and 6.5, right side), and no clear effect regarding different solubility of the tracer gases can be observed (Table 4).

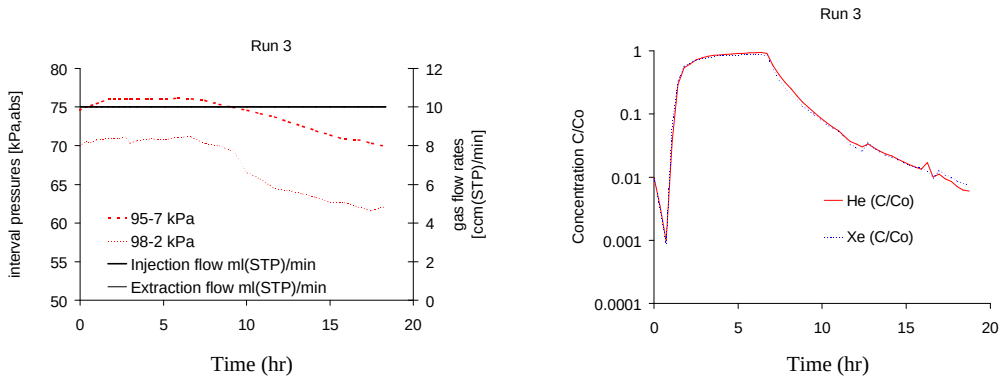

Figure 6.5: Run 3. Left: Injection and extraction interval pressures (bold and thin dashed lines respectively), and injection and extraction dipole gas flow rates (bold and thin continuous lines respectively). Right: Tracer gas breakthrough curves, semi log scale.

During the second gas tracer testing campaign GT2 (Trick et al. 2000), the dipole flow field was from GAM98.04 to TPF95.04. Three gas tracer tests were performed (Run4, Run5 and Run6) changing the injection flow rate, and two different gas tracers (Ar and SF_6) were added to the previous (GT1) tracer cocktail.

The flow field in Run4 started with an injection rate of 10ml(STP)/min (Fig.6.6). The injection gas flow was controlled by the flow controller, while the valve at the extraction flow controller was open. The gas outflow varied between 8 and 13ml(STP)/min.

During the test Run5, the injection flow rate was a factor of ten larger than during Run4 (Fig.6.7). The injection gas flow was controlled by the flow controller, while the valve at the extraction flow controller was open. Pressures at the extraction side were controlled by a pressure regulation valve, which was readjusted manually during tracer injection.

In Run6 a gas injection flow rate of 100ml(STP)/min was applied during gas tracer injection (the same as Run5). The injection/extraction gas flow ratio of 1:1 was regulated by the flow controllers. Therefore the pressure at the extraction side was controlled by the flow controller during gas tracer injection, being the extraction pressure regulation valve by-passed (Fig.6.3). After finishing gas tracer injection (5 hour since the beginning of Run6) the flow field was continued injecting N2 with 10ml(STP)/min, and the extraction flow controller was set as a flow meter, so the gas extraction flow rate was free.

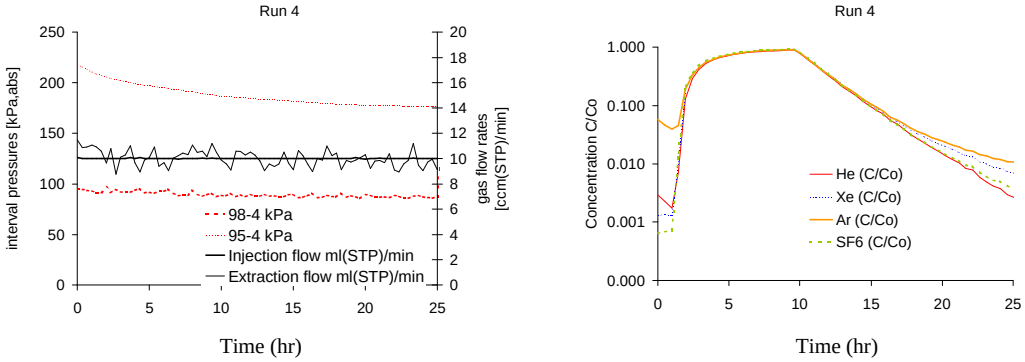

Figure 6.6: Run 4. Left: Injection and extraction interval pressures (bold and thin dashed lines respectively), and injection and extraction dipole gas flow rates (bold and thin continuous lines respectively). Right: Tracer gas breakthrough curves, semi log scale.

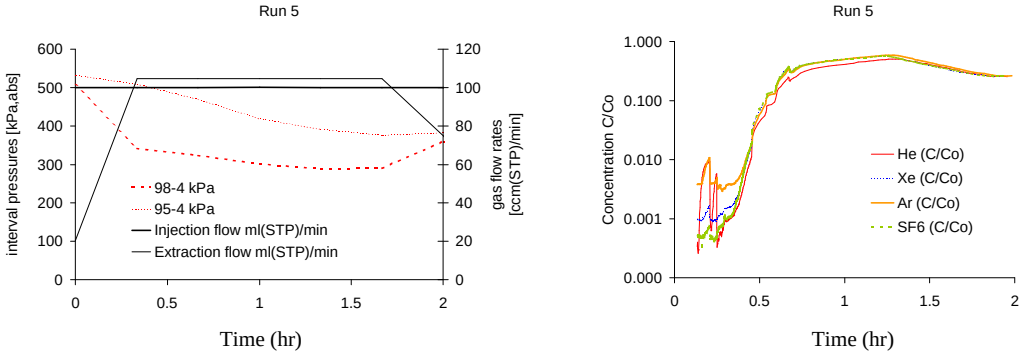

Figure 6.7: Run 5. Left: Injection and extraction interval pressures (bold and thin dashed lines respectively), and injection and extraction dipole gas flow rates (bold and thin continuous lines respectively). Right: Tracer gas breakthrough curves, semi log scale.

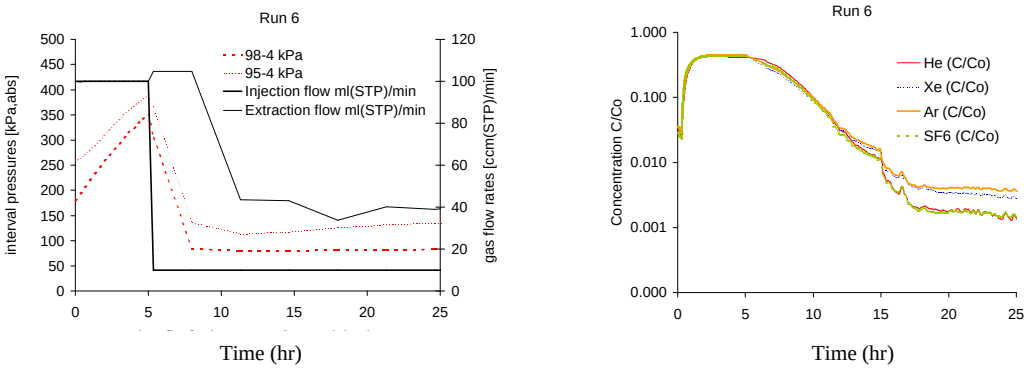

Figure 6.8. Run 6. Left: Injection and extraction interval pressures (bold and thin dashed lines respectively), and injection and extraction dipole gas flow rates (bold and thin continuous lines respectively). Right: Tracer gas breakthrough curves, semi log scale.

From the experimental point of view Run4, Run5, and Run6 were also a success. All breakthrough curves are very similar, with the same breakthrough time, peak time and almost no separation between the different gas tracers. Intuitively, different breakthrough curves would be expected because differences in solubility and diffusivity. If any detectable retardation effect due to dissolution/diffusion takes place, it happens in regions where gas saturation is small, and the gas flow is slow. The slowest streamlines are in regions where gas relative permeability is small, thus gas saturation is small. Even if the dissolution rate depends strongly on the contact surface between the

two phases, the amount of gas dissolved is determined by the volume of water in the formation, so in order to observe a separation of the peak times of different tracers with very different water dissolution coefficients are needed (see chapter 5). Unfortunately, the solubility of the selected gases was so low that the dissolution/diffusion effects appeared to be negligible. This is the reason why no chromatographic effect was observed (Fig.6.6 to 6.8, right side).

During the third testing campaign GT3 (Trick et al. 2001) five gas tracer tests were performed (Run7, Run8, Run9, Run10, Run11) with different gas velocities within the same flow field, from borehole GAM98.02 to borehole TPF95.07. Two gas bottles containing two different gas mixtures were used. Gas bottle-1 is the same used during GT2 which contains a gas mixture of Xe, He, Ar, SF_6 and N_2. Gas bottle-2 contains a new gas mixture of H_2S and N_2. This new added tracer (H_2S) has one order of magnitude higher solubility in water compared to the gas tracers used during the previous gas testing campaigns, but it is also reactive. The objective is to observe different H_2S retardation with respect to various flow rates within the same flow field.

From Run7 to Run 11 the flow field was established by gas injection controlled by gas flow controllers. During the tracer dosage, the sum of the tracer gas mixture rates (H_2S mixture and noble gas mixture) was equal to the nitrogen injection flow rate before and after tracer dosage (Table 6.2). The valve at the extraction interval flow line was opened (withdrawal against atmospheric pressure). The free gas outflow out of the extraction borehole was measured by a third gas flow meter (Fig.6.3)

In Run7, the flow field was started with an injection rate of 15ml(STP)/min, being the tracer gas mixture rates of 10ml(STP)/min for gas mixture-1 [Xe, He, Ar,SF_6, N_2], and 5ml(STP)/min for gas mixture-2 [H_2S, N_2]. At the beginning of the test the pressures were not completely stabilised (Fig.6.9). The test was started so early in order to run the tracer test in a gas flow field where the ground water still was present (the earlier the more water for tracer gas dissolution/diffusion).

The flow field in Run8 started with an injection rate of 75ml(STP)/min, being the tracer gas mixture rates of 25ml(STP)/min for gas mixture-1, and 50ml(STP)/min for gas mixture-2. The gas injection flow rate of the dipole was stable during the experiment, and the extraction gas flow was about equal to the gas injection rate (Fig.6.10).

During the test Run9 the injection flow rate was 300ml(STP)/min, being the tracer gas mixture rates of 100ml(STP)/min for the gas mixture-1, and 200ml(STP)/min for the gas mixture-2. The gas injection flow rate of the dipole was stable during the experiment (Fig.6.11). The extraction gas flow rate during the first two hours of the test was strongly fluctuating and higher than the injection rate. After two hours the extraction gas rate stabilised at 300ml(STP)/min. Pressures within the shear zone were not stable during the test.

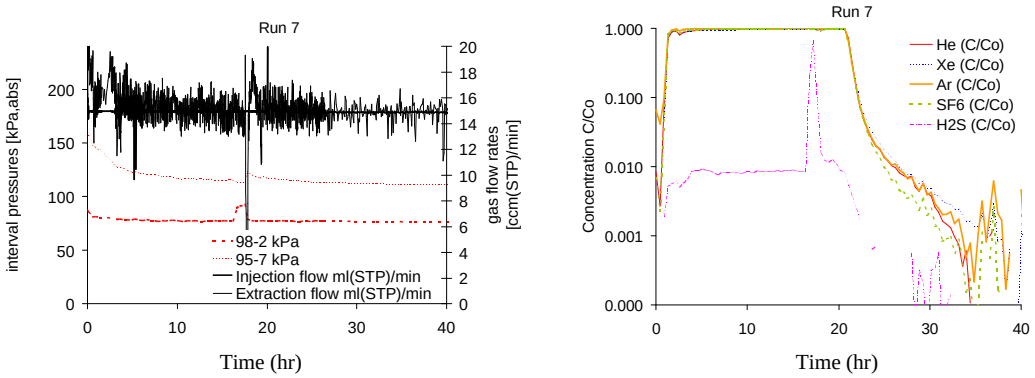

Figure 6.9: Run 7. Left: Injection and extraction interval pressures (bold and thin dashed lines respectively), and injection and extraction dipole gas flow rates (bold and thin continuous lines respectively). Right: Tracer gas breakthrough curves, semi log scale.

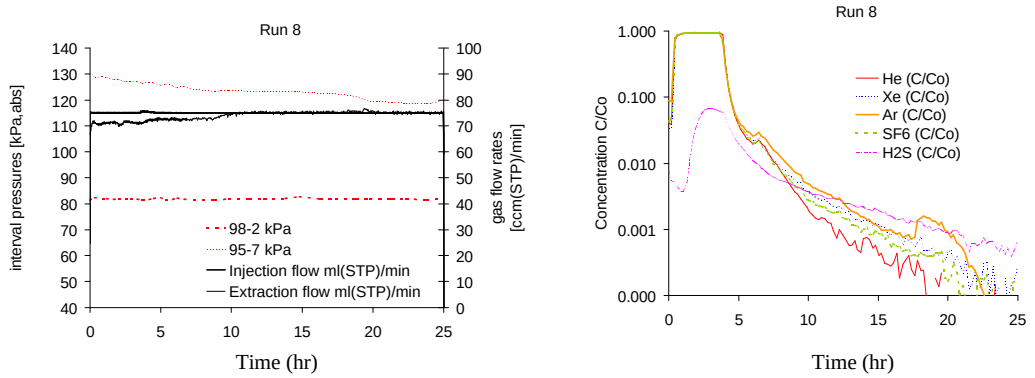

Figure 6.10: Run 8. Left: Injection and extraction interval pressures (bold and thin dashed lines respectively), and injection and extraction dipole gas flow rates (bold and thin continuous lines respectively). Right: Tracer gas breakthrough curves, semi log scale.

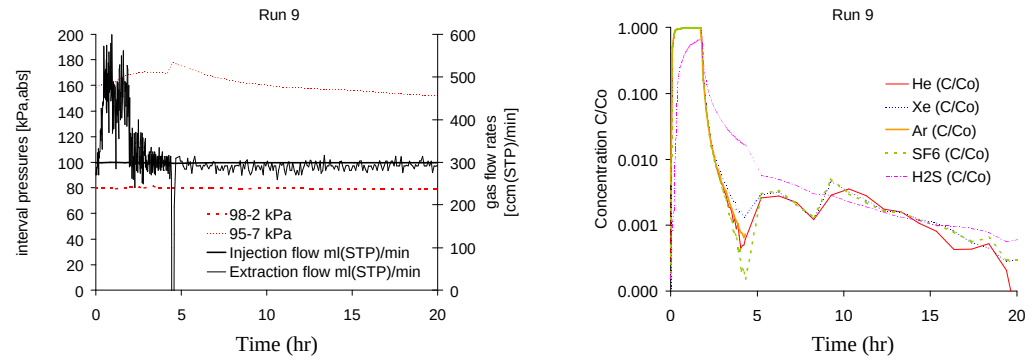

Figure 6.11: Run 9. Left: Injection and extraction interval pressures (bold and thin dashed lines respectively), and injection and extraction dipole gas flow rates (bold and thin continuous lines respectively). Right: Tracer gas breakthrough curves, semi log scale.

In Run10, the flow field was started with an injection rate of 300ml(STP)/min, being the tracer gas mixture rates of 100ml(STP)/min for the gas mixture-1, and 200ml(STP)/min for the gas mixture-2. The flow field was stable during the tracer experiment, showing slight variations in the extraction flow rate (Fig.6.12).

The flow field in Run11 started with an injection rate of 600ml(STP)/min, being the tracer gas mixture rates of 100ml(STP)/min for the gas mixture-1, and 500ml(STP)/min for the gas mixture-2. The pressures within the shear zone were at the beginning of the test not perfectly stable. Injection flow rate was stable during the entire test. The extraction flow rate was slightly fluctuating, and in average about equal to the gas injection rate (Fig.6.13).

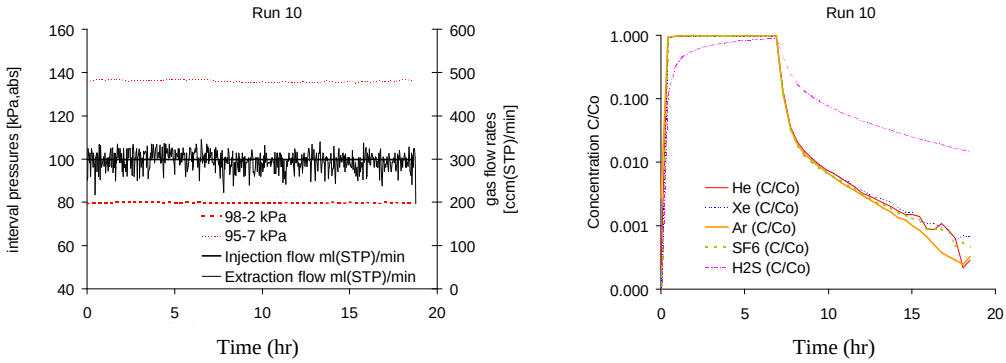

Figure 6.12: Run 10. Left: Injection and extraction interval pressures (bold and thin dashed lines respectively), and injection and extraction dipole gas flow rates (bold and thin continuous lines respectively). Right: Tracer gas breakthrough curves, semi log scale.

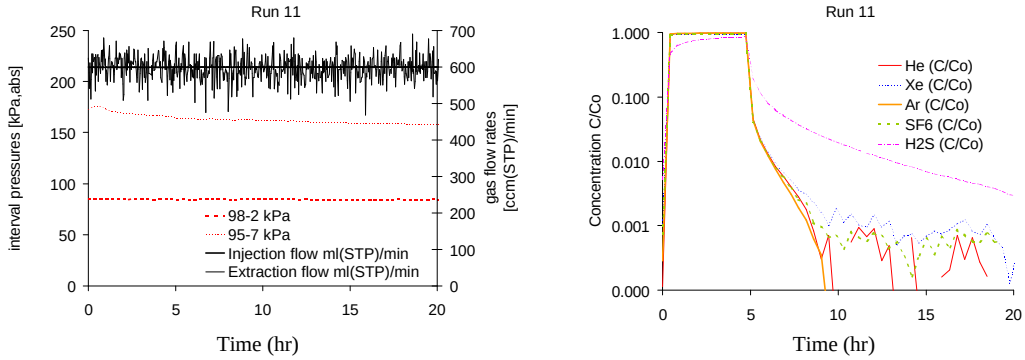

Figure 6.13: Run 11. Left: Injection and extraction interval pressures (bold and thin dashed lines respectively), and injection and extraction dipole gas flow rates (bold and thin continuous lines respectively). Right: Tracer gas breakthrough curves, semi log scale.

All the tests performed during the third testing campaign GT3 were a success from the experimental point of view. As in the case of the GT2 campaign (Run4, Run5 and Run6) all the noble gases (i.e. He, Xe, Ar and SF_6) have similar curves with minor separations (Fig.6.9 and 6.10, right side). This is not true with the reactive tracer H2S which is poorly recovered (Table 6.3). In Run7, the small gas injection rate would explain the almost absence of H2S: big water volumes inside the fracture and small gas fluxes through the fracture are enough to dissolve most H2S. Though H2S breakthrough is very small it appears during Run8. However, it is in the subsequents Run9 to Run11 that enhanced H2S recoveries are found (Table 6.3) (Fig.6.11 to 6.13, right side). Unfortunately, H2S exhibits a non conservative behaviour since it reacts with the injection/extraction metallic pipelines.

6.3 Modelling gas tracer tests.

The methodology consists of two main steps: First to simulate the two phase flow conditions inside the fracture prior to the tracer injection, generating a gas bubble between injection and extraction boreholes, achieving steady state bubble at the two phase flow conditions (i.e. steady gas and liquid pressures and also steady injection and extraction gas flow rates). Once the gas bubble is simulated, the second step becomes to simulate the gas tracer migration through the generated gas bubble.

6.3.1 Generation of the gas bubble

To simulate the generation of the gas bubble it is necessary to compute all the parameters needed to solve the multiphase flow equations, such as transmissivities, porosities, retention curve coefficients, etc. For modelling purposes the fracture conceptualisation for gas migration requires the consideration of two different scenarios, open fracture zones fully saturated with gas (mobile zone), where advection and dispersion are the dominant gas transport mechanisms, and fault gauge filled zones, partially or fully saturated with water, where the capillary pressure is too high to allow the gas to penetrate and water is not displaced (immobile zone). Here the gas tracers dissolve in water and diffuse away from the liquid-gas interface.

The fracture is modelled as a rectangular domain of 18*18 m^2, centred on the access gallery. Transmissivity (Fig.6.2) and aperture field values are the ones obtained through the hydraulic characterisation of the GAM fracture (Chapter 3). Relative permeability curve is a linear relationship with the degree of saturation (Eq. 6.1), based upon the idea that parallel plates that represent the domain are in practice either full or empty of water (similar to the concept of two states in percolation theory). This is accomplished by setting a sufficiently small value of b [$ML^{-1}T^{-2}$] in equation (6.1).

$$P_c = -b\,S_w + (b + P_b) \qquad 0 \leq S_w \leq 1 \tag{6.1}$$

where P_c [$ML^{-1}T^{-2}$] is capillary pressure, P_b [$ML^{-1}T^{-2}$] is the entry pressure, and S_w [-] is the water saturation degree. As the slope of the retention curve, b, varies varies spatially in a fracture aperture field, we vary b as a function of the fracture aperture (desaturation begins in the widest zones and ends in the narrowest zones). On the other hand, the entry pressure P_b is a function of the maximum aperture (desaturation begins in the widest zones). Following the same methodology presented in chapter 5, one can assume that every value of the transmissivity field is the result of an upscaling process inside each transmissivity zone, so, at the end, one can think in terms of a field of geometric mean transmissivities instead of only transmissivities. The same can be said about the aperture field, obtaining a field of geometric mean apertures instead of a field of fracture apertures. This allows us to write down a formal relationship between b, P_b and the geometric mean aperture:

$$b = \frac{4s\,\sinh(a)}{b_g} \tag{6.2}$$

$$P_b = \frac{2s}{b_g\left(\sinh(a) + \cosh(a)\right)} \tag{6.3}$$

where b_g [L] is the geometric mean aperture, a is a parameter related to the aperture standard deviation, and s [MT^{-2}] is the water surface tension.

To simulate the existing steady state gas flow field inside the fracture, a gas injection test (dipole configuration) in an initially water saturated fracture is modeled. We inject gas (nitrogen) through the injection borehole at a constant mass rate, until steady state is achieved, that is, until the gas extraction flow rate through the extraction borehole is constant, and both the gas and liquid pressures inside the fracture become stationary. To simulate the open valve at the extraction interval (withdrawal against atmospheric pressure) a constant pressure (0.1 MPa) boundary condition is applied to the extraction borehole for both gas and liquid phase. No flow boundary condition (for both gas and liquid phase) is imposed in the intersection between the fracture plane and the gallery, whereas constant hydrostatic pressure is imposed at the external boundary of the domain. The multiphase flow finite element simulator CODE-BRIGHT (Olivella et al. 1996) is used to simulate the gas dipole injection test in two phase flow conditions.

Due to the fact that sensitivity analysis presented in the previous chapter was performed using the GT2 dipole configuration Run4 is the first gas tracer test selected to be simulated. The dipole flow field (Fig.6.14) is formed by injecting N_2 at a constant rate of 10ml(STP)/min in the injection borehole (GAM98.04), and imposing a constant pressure (gas and liquid) of 0.1MPa at the extraction borehole (TPF95.04). Once the steady state is achieved the gas tracer injection test is simulated.

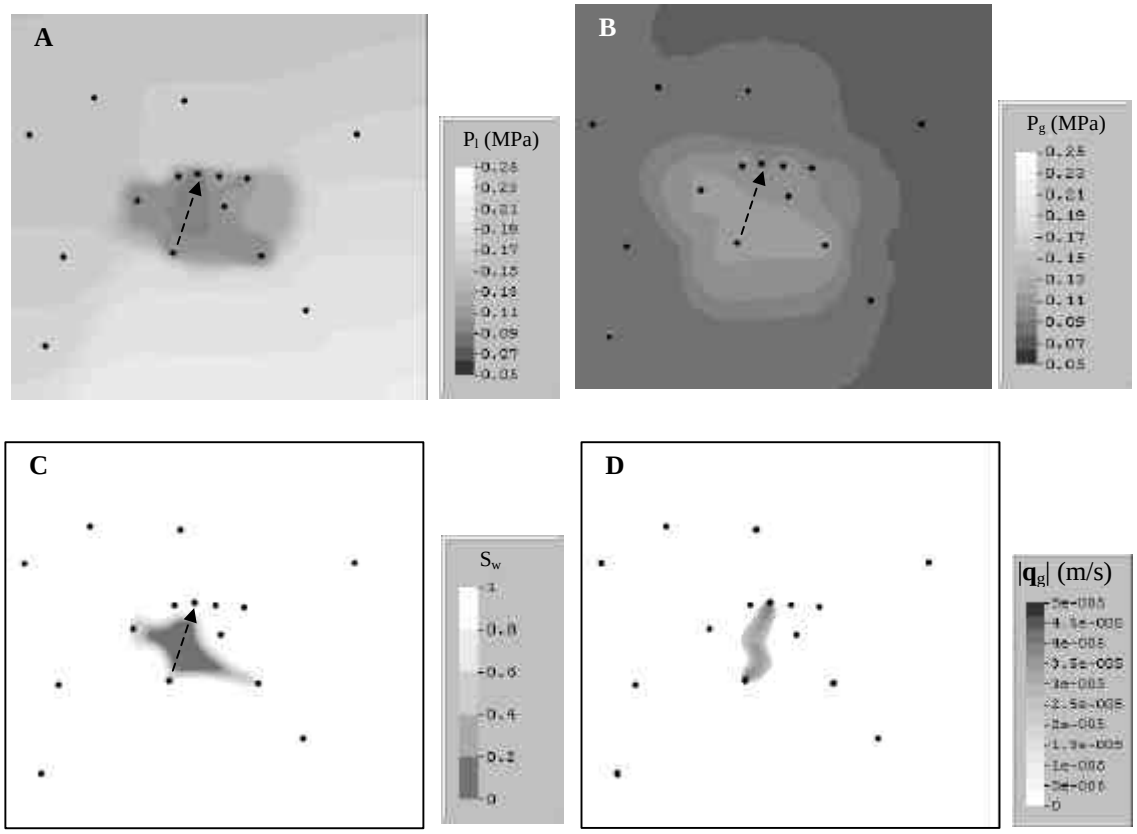

Figure 6.14: A) Liquid pressure, B) gas pressure, C) water saturation degree, and D) gas fluxes in the most discretized zone of the fracture, obtained trough a simulation of a gas injection test (dipole configuration) once the steady state is reached. Black points are the intersection of the boreholes with the GAM shear zone. The dipole is marked by the black arrow between the injection and extraction boreholes (GAM98.04 and TPF95.04 respectively). The length of the dipole is 1.14 m.

6.3.2 Gas tracer transport simulation

The gas tracer injection test consist in injecting gas tracer at a constant mass rate, obtaining different breakthrough curves in terms of the injected gas tracer.

To simulate the gas migration through a partially saturated heterogeneous fracture we apply the same gas transport analogy presented in chapter 5. The objective of the simulations is to reproduce the experimental breakthrough curves, obtaining a common set of gas transport parameters for all species of each gas tracer test. Transport simulations are performed using the finite element code TRANSIN IV (Medina et al., 2000).

Four gas transport simulations have been conducted (one for each gas tracer used in Run4) using the transport parameters directly obtained through the analogy presented in chapter 5. As shown in Figure 6.15, none of the predicted breakthrough curves (dashed lines) fit reasonably well the observed breakthrough curves. The model fails to fit both the peak concentration and the slope of the tail of the breakthrough curves in all the four gas tracers. In order to obtain a good agreement between observed and computed concentrations, a calibration of the transport parameters is done. In all the cases it is necessary to reduce fracture apertures by a factor of 0.33 to match correctly the observed breakthrough times, but the slope of the tails for late times is not fitted for any of the four gas tracers (Fig 15-right). To do so, it is necessary to vary the matrix volume by different factors depending on the gas tracer. The need to use different transport parameters for each gas tracer indicates that something fails in the applied analogy. This may be related with the two phase flow conditions inside the fracture and the total water content available for gas tracer dissolution/diffusion.

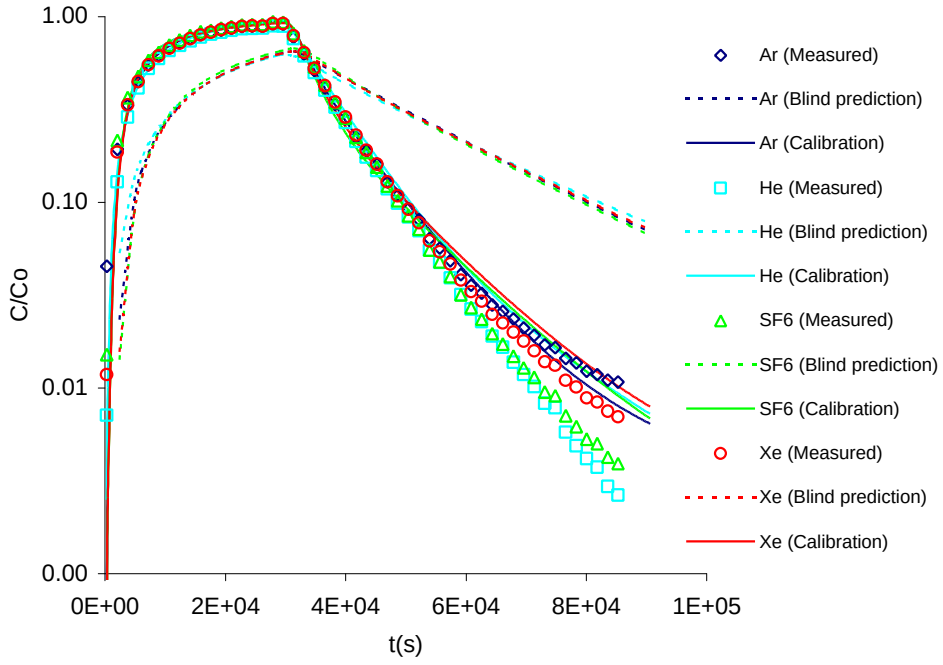

Figure 6.15: Measured breakthrough curves, blind prediction and calibrated (fitting the tracer pick concentration) breakthrough curves for the four gas tracers used in Run4 (Ar, He, Xe and SF_6 respectively)

One of the outcomes of the sensitivity analysis performed in the previous chapter is that the importance of the chromatographic effect (separation of the BTC's for each tracer) depends on the gas tracer properties such as solubility, but it also depends on the gas bubble and fracture geometry, that is gas/water interface area, and also on the total amount of water available for dissolution/diffusion processes. Looking at the experimental breakthrough curves, a very clear chromatographic effect is not observed, nevertheless we have simulated the gas tracer transport, assuming that the different tailing for each gas tracer was due to dissolution/diffusion mechanisms (Chapter 5). The minor gas tracer species separation may be explained in terms of gas tracer diffusion in gas dead volumes, such as those borehole intervals intersecting the fracture plane dewatered through the different gas pressure threshold/injection tests performed in the fracture before conducting the gas tracer test itself.

6.3.3 Modelling gas tracer tests through breakthrough curve analysis

To study in detail the hypothesis that the small chromatographic separation may be explained in terms of gas tracer diffusion in gas dead volumes instead of dissolution/diffusion mechanisms, we have developed a simple transport model which allows us to distinguish between the two transport hypothesis. That is, whether tracer separation is mainly due to dissolution/diffusion in water saturated fault gouge or due to gas diffusion in dead gas volumes.

Looking at the experimental breakthrough curves (Fig.6.4 to 6.13) one can realise that there are two different responses in terms of gas tracer recovery rate. On the one hand all the breakthrough curves belonging to the GT2 campaign (i.e. Run4, Run5 and Run6) display a unique linear relationship between $Log(C/C_0)$ and time through all the recovery period. On the other hand, breakthrough curves belonging to GT1 and GT2 display different linear relationship between $Log(C/C_0)$ and time for early and late recovery times. These types of behaviour are typical of predator-prey systems, in which two variables grow, but one grows at the expense of the other (Fig.6.16).

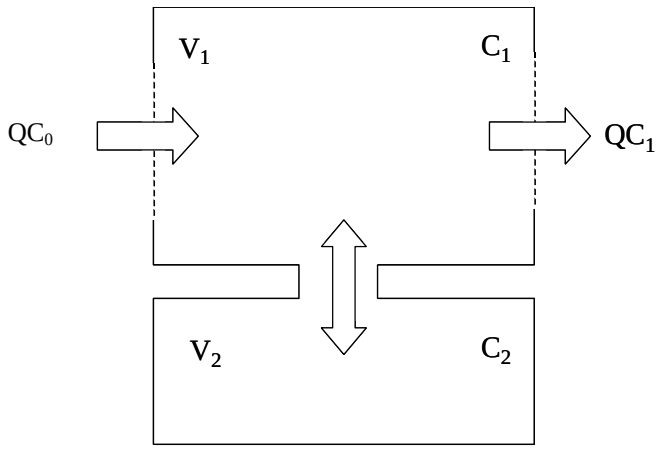

Figure 6.16: Simplified conceptualization of the gas tracer test system, where gas tracer (He, Xe, Ar and SF_6) is being injected with C_0 concentration into the gas bubble (N_2) generated between injection and extraction boreholes. Q is the N_2 injection flow rate. Once the gas tracer injection is finished, the injection-extracion gas dipole is mainteined to recover the main quantity of gas tracer which still explores the gas bubble. V1 and C1 are the volume and the tracer concentration in the bubble (i.e. gas mobile zone), and V2 and C2 are the volume and the tracer concentration in the gas inmobile zone.

The case presented in Figure 6.16, is typically represented as a set of two differential equations:

$$\frac{\partial}{\partial t} C_1 = \frac{Q}{V_1} C_0 - \frac{Q}{V_1} C_1 - \frac{DS}{V_1 L} \left(C_1 - C_2 \right) \tag{6.4}$$

$$\frac{\partial}{\partial t} C_2 = \frac{DS}{V_2 L} \left(C_1 - C_2 \right) \tag{6.5}$$

Where $Q[L^3T^{-1}]$ is the gas injection flow rate, $C_0[ML^{-3}]$ is the gas tracer injection concentration, $V_1[L^3]$ and $C_1[ML^{-3}]$ are the volume and the tracer concentration in the bubble (i.e. gas mobile zone), $L[L]$ is the immobile zone diffusion length, and finally $V_2[L^3]$, $C_2[ML^{-3}]$ and $D[L^2T^{-1}]$ are the volume, the tracer concentration and the gas diffusion coefficient in the gas immobile zone.

To define the gas immobile zones two different scenarios are possible:

- Dead gas volumes belonging to dewatered interval fracture boreholes, situated inside or in the vicinity of the generated gas bubble. In this case D is the gas diffusion coefficient in gas, and V_2 and C_2 are the volume and the gas concentration in the dewatered volume respectively.

- Fault gouge fracture filling material fully water saturated, where the dissolution/diffusion is the main tracer transport mechanism. In this case D stands for gas diffusion coefficient in water, C_2 stands for gas tracer concentration dissolved in water, in equilibrium with the gas tracer partial pressure in the gas bubble, and V_2 is the named Henry's volume, defined as:

$$V_2 = \frac{V_2^* P_g}{K_H} \tag{6.6}$$

  Where $V_2^*[L^3]$ is the fault gouge volume accessible by dissolution/diffusion, $P_g[ML^{-1}T^{-2}]$ is the gas bubble pressure, and K_H $[ML^{-1}T^{-2}]$ is the gas tracer Henry's constant.

The transient differential equation system given by (6.4) and (6.5) represent the gas tracer injection phase, where gas tracer is injected with C_0 concentration and flow rate Q into the existing nitrogen gas bubble between injection and extraction boreholes.

Once the gas tracer injection is finished, the gas tracer recovery phase begins, where the gas bubble structure is maintained to allow the gas tracer to reach the extraction borehole. This gas tracer recovery phase is also represented by equations (6.4) and (6.5), but neglecting the first term on the right hand side of equation (6.4) which represents the gas tracer injection into the gas bubble. This transforms the transient differential equation system described by (6.4) and (6.5) into a homogeneous differential equation system:

Rewriting equations (6.4) and (6.5) in terms of the unknowns C_1 and C_2 we obtain a differential equation system which can be written in matrix form as:

$$\dot{\mathbf{C}} = \mathbf{AC} + \mathbf{F} \tag{6.7}$$

where the matrix **A** contains only constants and **F** is a function of time. The general solution of this system (Eq. 6.7) is given by:

$$\mathbf{C} = e^{\mathbf{A}t}\mathbf{C}_{t_0} + e^{\mathbf{A}t}\int_{t_0}^{t} e^{-\mathbf{A}s}\mathbf{F}(s)ds \tag{6.8}$$

Where $\mathbf{C}_{t_0}$ [ML^{-3}] is a vector containing initial concentration of the gas tracer system (gas mobile and gas immobile zones).

Let **A** be a $n \times n$-matrix with eigenvalues given by l_i and corresponding eigenvectors $\mathbf{u_i}$, (i = 1, 2, ...n), i.e.,

$$\mathbf{Au_i} = l_i\mathbf{u_i} \tag{6.9}$$

We may create a matrix **B** with vectors $\mathbf{u_1}$, $\mathbf{u_2}$ …$\mathbf{u_n}$ set in columns:

$$\mathbf{B} = \begin{pmatrix} \mathbf{u}_1 & \mathbf{u}_2 & \dots & \mathbf{u}_n \end{pmatrix} \tag{6.10}$$

Then the **A** matrix can be expressed as

$$\mathbf{A}=\mathbf{BJB}^{-1} \tag{6.11}$$

Being **J** a diagonal matrix containing the eigenvalues in the main diagonal, that is:

$$\mathbf{J} = \begin{pmatrix} l_1 & 0 & \cdots & 0 \\ 0 & l_2 & \cdots & 0 \\ \vdots & \vdots & \ddots & \vdots \\ 0 & 0 & \cdots & l_n \end{pmatrix} \tag{6.12}$$

The matrix **J** is also known as the Jordan canonical expression of matrix **A.** Taking into account equation (6.11) **J** can be written as:

$$\mathbf{J}=\mathbf{B}^{-1}\mathbf{AB} \tag{6.13}$$

Now the exponential term of equation (6.8) can be calculated as:

$$e^{\mathbf{A}t} = \mathbf{B}e^{\mathbf{J}t}\mathbf{B}^{-1} \tag{6.14}$$

Taking into account equation (6.14), now equation (6.8) can be rewritten as:

$$\mathbf{C} = \mathbf{B}e^{\mathbf{J}t}\mathbf{B}^{-1}\mathbf{C}_{t_0} + \mathbf{B}e^{\mathbf{J}t}\int_{t_0}^{t} e^{-\mathbf{J}s}\mathbf{B}^{-1}\mathbf{F}(s)ds \tag{6.15}$$

In our case, and as we have outlined before, the gas tracer test consists of two different phases:

- The period from t=0 to $t = t_{inj}$ corresponds to the gas tracer injection phase. Gas tracer is injected in an initially gas tracer empty system ($\mathbf{C}_{t_0} = \mathbf{0}$), with constant inflow rate Q and concentration C_0. The latter implies that **F** can be expressed as follows:

$$\mathbf{F} = \begin{pmatrix} \frac{Q}{V_1} C_0 \\ \\ 0 \end{pmatrix} \tag{6.16}$$

  Operating and simplifying, equation (6.15) can be expressed explicitly in terms of the eigenvalues l_1 and l_2 and their corresponding eigenvectors $\mathbf{u}_1(u_{11},u_{12})$ and $\mathbf{u_2}(u_{21},u_{22})$ respectively,

$$\mathbf{C}_{\text{injection}} = \begin{pmatrix} C_{\text{inj}_1}(t) \\ \\ C_{\text{inj}_2}(t) \end{pmatrix} = \begin{pmatrix} \frac{u_{11}u_{22}}{l_1 b}\frac{Q}{V_1}C_0 e^{l_1 t} - \frac{u_{12}u_{21}}{l_2 b}\frac{Q}{V_1}C_0 e^{l_2 t} + \frac{1}{b}\frac{Q}{V_1}C_0\left(\frac{u_{12}u_{21}}{l_2} - \frac{u_{11}u_{22}}{l_1}\right) \\ \\ \frac{u_{12}u_{22}}{l_1 b}\frac{Q}{V_1}C_0 e^{l_1 t} - \frac{u_{22}u_{12}}{l_2 b}\frac{Q}{V_1}C_0 e^{l_2 t} + \frac{u_{22}u_{12}}{b}\frac{Q}{V_1}C_0\left(\frac{1}{l_2} - \frac{1}{l_1}\right) \end{pmatrix} \tag{6.17}$$

  Where C_{inj_1} and C_{inj_2} stand for the gas mobile and immobile zones respectively, and b=det(**B**)

- From $t= t_{inj}$ to $t = t_{end}$ corresponds to the gas tracer recovery phase. In this test phase there is no gas tracer injection, so **F=0.** Now the initial gas tracer system concentration $\mathbf{C}_{t_0}$ is given by the solution of the system of equations (6.17) for $t= t_{inj}$, that is:

$$C_{t_0} = \begin{pmatrix} C_{inj_1}(t_{inj}) \\ \\ C_{inj_2}(t_{inj}) \end{pmatrix} \tag{6.18}$$

  As in the previous case equation (6.15) can be expressed explicitly in terms of the eigenvalues l_1 and l_2 and their corresponding eigenvectors $\mathbf{u}_1$ and $\mathbf{u_2}$ respectively, that is:

$$\mathbf{C}_{\text{recovery}} = \begin{pmatrix} C_{\text{rec}_1}(t) \\ \\ C_{\text{rec}_2}(t) \end{pmatrix} = \begin{pmatrix} \frac{u_{11}}{b}\left(C_{1,0}u_{22} - C_{2,0}u_{21}\right)e^{l_1 t} + \frac{u_{21}}{b}\left(C_{2,0}u_{11} - C_{1,0}u_{12}\right)e^{l_2 t} \\ \\ \frac{u_{12}}{b}\left(C_{1,0}u_{22} - C_{2,0}u_{21}\right)e^{l_1 t} + \frac{u_{22}}{b}\left(C_{2,0}u_{11} - C_{1,0}u_{12}\right)e^{l_2 t} \end{pmatrix} \tag{6.19}$$

Equations (6.17) and (6.19) provide analytical expressions for the temporal dependence of the gas tracer concentration in both mobile and immobile zones, depending on the

geometry of the system, the gas injection and extraction flow rates, and taking into account the different tracer injection and recovery periods. In this sense, and following the analogy presented in Figure 6.16, the measured breakthrough curves from the different tracer tests campaigns (Run-2 to Run11) may be represented with the first component of equations (6.19) and (6.21), that is:

$$\mathbf{C}_{\text{measured}} = \begin{cases} C_{\text{inj}_1}(t) & t \le t_{inj} \\ C_{\text{rec}_1}(t) & t > t_{inj} \end{cases} \tag{6.20}$$

Table 6.5 present the used parameters (V_1, V_2) to fit all the measured breakthrough curves from Run2 to Run11. Figure 6.17 shows the fits obtained for Run11. In general a good agreement between measurements and computed concentration is obtained. All the fits obtained for gas tracer test are presented in Annex-IX.

Table 6.5: Volumes obtained to fit the experimental breakthrough curves using analytical solutions provided by equation (6.20)

	V_1 (l)				V_2 (l)				V_2^* (m^3)			
	He	Ar	Xe	SF6	He	Ar	Xe	SF6	He	Ar	Xe	SF6
Run-02	1.500	1.500	1.500	1.500	0.350		0.410		61.447		4.881	
Run-03	0.750	0.750	0.750	0.750	0.370		0.420		74.238		5.714	
Run-04	1.315	1.315	1.315	1.315	0.030	0.700	0.700	0.300	3.830	21.072	6.061	0.055
Run-05	0.509	0.509	0.509	0.509	0.800	0.700	0.400	0.750	28.090	5.795	0.952	0.038
Run-06	0.500	0.500	0.500	0.500	2.900	3.400	3.200	2.800	407.303	112.583	30.476	0.568
Run-07	0.520	0.520	0.520	0.520	0.073	0.075	0.082	0.049	8.544	2.070	0.651	0.008
Run-08	0.891	0.891	0.891	0.891	0.363	0.520	0.450	0.400	39.164	13.245	3.297	0.062
Run-09	1.067	1.067	1.067	1.067	0.315	0.280	0.347	0.250	8.692	32.772	2.751	0.042
Run-10	2.263	2.263	2.263	2.263	0.870	0.830	0.890	0.860	101.826	22.903	7.063	0.145
Run-11	0.750	0.750	0.750	0.750	0.315	0.260	0.345	0.280	18.434	3.587	1.369	0.024

The volume V_1 associated to the generated gas bubble between injection and extraction boreholes is consistent with the idea of how does the gas bubble grows inside the fracture when the gas bubble is being generated. Gas phase only grow through the larger pores which present the lower capillary entry barrier. Thus, the gas bubble results in a small dewatered fracture volume between injection and extraction boreholes. The bubble volume will remain dewatered while the gas injection flow rate flow do not diminish or stop. In that case gas bubble will collapse, disappearing the direct gas phase connection between injection and extraction boreholes.

The volume V_2 associated to dead gas volumes are very similar for all tracers belonging to the same tracer test. These values are compatible with the volume associated to some observation borehole intervals which intersect the fracture plane.

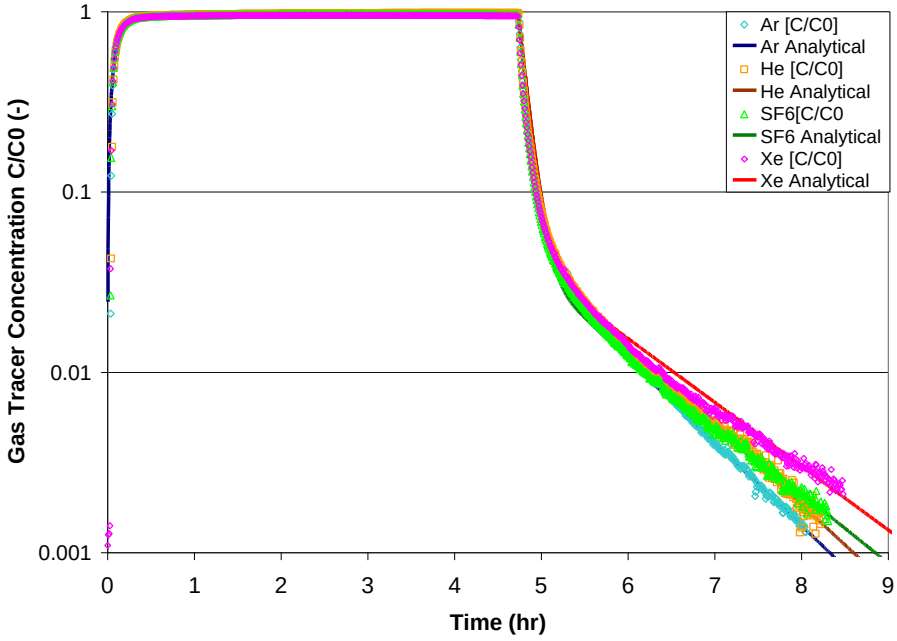

Figure 6.17: Mesured breaktrough curves (symbol) and analytical fit (bold lines) for Run 11

Finally, assuming that the different tailing for each gas tracer is due to dissolution/diffusion mechanisms, the corresponding volume of fault gouge fully water saturated, needed to dissolve the necessary gas to obtain the measured breakthrough curves is given by V_2^*. As it can be seen (tables 4 and 5) , the necessary volume to dissolve the different gas tracers depends on the gas tracer solubility; the larger V_2^* the smaller gas tracer solubility. The obtained value of V_2^* for the different gas tracers are very different in the same run test, varying in general more than four orders of magnitude between the largest and the smallest values. The largest computed value of V_2^* is 407 m^3 for He in Run6, and the smallest is 24 litres belonging to SF_6 in Run11. In both cases, V_2^* is anomalously large. The needed volume of fully water saturated fracture filling material accessible for gas tracer dissolution/diffusion is unrealistic.

The breakthrough curve analysis indicates that the volume associated to the immobile fracture zone, where the gas tracer dissolution/diffusion processes could be important is very small. In our case, gas tracer dissolution in the liquid phase does not govern the small gas tracer separation in the tailing obtained during the gas tracer test campaigns performed in the framework of the GAM project.

6.4 Conclusions

The gas tracer tests carried out at the Grimsel Test Site are complex. The fracture has low transmissivity and exhibits a complex internal heterogeneous structure. The experimental data comes from in situ gas challenging tracer tests: pressures, gas and water flow rates, and tracer concentrations in gas are all small and difficult to measure. The control of tests conditions is another tough task (initial pressure and saturation conditions, stabilised flows). The boundary conditions are poorly known. For instance,

does the gallery drain the shear zone or it is an impervious boundary? can the observation boreholes affect the observed breakthrough curves? Carrying out a gas injection tracer test under these conditions, and obtaining gas mass recoveries larger than 90% is a success from the experimental point of view.

The main objective of the gas tracer testing activities was to investigate realistic mass exchange coefficients in two phase flow through fractures, determining the role played by the different gas tracers solubility and diffusion coefficients. Unfortunately, minor breakthrough differences between the different gas tracers were observed.

The initial gas transport hypothesis taken into account to simulate the gas tracer tests considered that dissolution/diffusion of gas tracers in the liquid phase was the main transport mechanisms to explain the different tailing obtained for each gas tracer. Gas tracer test interpretation was performed following the analogy presented in chapter 5, where different scenarios for gas transport through partially saturated heterogeneous fractures can be considered. The analogy assumes that dissolution/diffusion controls the tailing of the breakthrough curves. Nevertheless, the inconsistency between the obtained transport parameters for different gas tracers indicates that the initial hypothesis was erroneous.

A simpler analysis of the experimental gas tracer breakthrough curves shows that, the minor gas tracer species differences can be explained in terms of gas tracer diffusion in dead gas volumes. Another gas transport model was made to fit the experimental breakthrough curves, taking into account the new gas transport hypothesis. The model yields reasonable volumes for the gas bubble, and dead gas volumes compatible with the volume associated to some dewatered observation borehole intervals, which intersect the fracture plane. The model indicates that volume of fault gouge fully water saturated needed to dissolve the necessary gas tracer to fit the measured breakthrough curves is unrealistic and different for each gas tracer. This means that gas tracer dissolution in the liquid phase does not govern the gas small tracer separation in the breakthrough tailing obtained during the gas tracer test campaigns performed in the framework of the GAM project.

The obtained results indicate that the objective of the experimental testing activities have not been accomplished, because the obtained results do not agree with the target processes under investigation. In this sense, in order to design a new gas tracer test campaign addressed to investigate the same original GAM questions, it is necessary to study under which conditions (gas injection/extraction flow rates, gas back formation pressures, gas solubility, etc) the dissolution/diffusion transport mechanisms should be the most relevant to produce a clear tailing chromatographic separation.

Yet, the experience has been positive for the design of future gas tracer tests.

6.5 References

Bossart, P. and M. Mazurek. Structural geology and water flow-paths in the migrati0on shear-zone. NAGRA (Nationale Genossenschaft für die Lagerung radioaktiver Abfälle) Technical Report 91-12. Wettingen, Switzerland. 1991.

Cooper, H. and C. Jacob. A generalised graphical method for evaluating formation constants and summarising well-field history. AGU, 27(4), 526-534, 1946.

Fierz, T., and M. Piedevache. GTS/GAM: Results of hydraulic tests and gas threshold pressure tests in GAM 98-002 (January/February 2000). NAGRA (Nationale Genossenschaft für die Lagerung radioaktiver Abfälle) Internal Report 00-14, Wettingen, Switzerland, 2000.

Fierz, T., E. Proust., M. Combarieu and P. Meier. GTS/GAM: Gas tracer test series GT1 in the GAM shear zone (February 2000). Dipole flow field GAM98-002/TPF95-007. NAGRA (Nationale Genossenschaft für die Lagerung radioaktiver Abfälle) Internal Report 99-30, Wettingen, Switzerland, 2000.

Gascoyne, M. and D.M. Wuschke. Gas migration through water-saturated, fractured rock: results of a gas injection test. J. Hydrol.,196, 76-98, 1997.

Gemperle,R., GTS/GAM: Hydraulic testing in GAM 98.002 and GAM 98.004. NAGRA (Nationale Genossenschaft für die Lagerung radioaktiver Abfälle) Internal Report 99-02, Wettingen, Switzerland, 1999.

Kennedy, K., (1999): Solute and particle tracer tests PILOT and PT1 in the GAM shear zone (Dec, 1998 to April, 1999). NAGRA Internal Report IB 99-49, Wettingen, Switzerland.

Kennedy, K., (2000a): Solute and particle tracer test PT2 in the GAM shear zone (May, 1999). NAGRA Internal Report IB 00-07, Wettingen, Switzerland.

Kennedy, K., (2000b): Solute and particle tracer test PT3 in the GAM shear zone (August, 1999). NAGRA Internal Report IB 00-08, Wettingen, Switzerland.

Kennedy, K. and Kleiner, A., (2000): Tracer tests PT4 and PT5 in the GAM shear zone (August, September 1999). NAGRA Internal Report IB 00-41, Wettingen, Switzerland.

Lineham, T.R., P.J. Nash, W.R. Rodwell, J. Bolt, V.M.B. Watkins, P. Grainger, M.J. Heath and J.R. Merefield. Gas migration in fractured rock: results and modelling of a helium gas injection experiment at the Reskajeage Farm Test Site, SW England, United Kingdom. J. Contam Hydrol, 21, pp. 101-113. 1996.

Marshall, P., W. Albert, R. Carbonell, J. Carrera, P.B. Davies, W. Kinzelbach, J.C. Mayor and S. Niehren. GTS/GAM: Investigation programme fot thr GTS Phase V experiment "Gas migration in shear zones" (1998-2000). NAGRA (Nationale Genossenschaft für die Lagerung radioaktiver Abfälle) Internal Report 98-12. Wettingen, Switzerland, 1998.

Marschall, P., E. Fein, H. Kull, W. Lanyon, L. Liedtke, I. Müller-Lyda and H. Shao. Conclusions of the tunnel near field programme (CTN). NAGRA (Nationale Genossenschaft für die Lagerung radioaktiver Abfälle)Technical Report 99-07, Wettingen, Switzerland, 1999.

Medina A, Alcolea A, Carrera J, Castro LF., (2000) Modelos de flujo y transporte en la geosfera: Código Transin IV. [Flow and transport modelling in the geosphere: the code TRANSIN IV], in: IV Jornadas de Investigación y Desarrollo Tecnológico de Gestión de Residuos Radiactivo de ENRESA. Technical publication 9/2000: 195-200

Meier, P., M.,Medina, A., Carrera, J., Geostatistical inversion of cross-hole pumping test for identifying preferential flow channels within a shear zone. Ground Water, 39(1), 10-17, 2001.

Olivella, S., J. Carrera, J. Gens, and E. Alonso. Numerical formulation for a simulator (CODE-BRIGHT) for the coupled analysis of saline media, Engineering Computations, Vol 13, Number 7, pp 87-112, 1996.

Ramajo, H., J. Jódar, J. Carrera, and S. Olivella. Progress report on modelling of gas migration processes. NAGRA (Nationale Genossenschaft für die Lagerung radioaktiver Abfälle) Internal Report 99-61, Wettingen, Switzerland, 1999.

Sander, R., (1999). Compilation of Henry's Law Constants for Inorganic and Organic Species of Potential Importance in Environmental Chemistry (Version 3) http://www.henrys-law.org

Thunvik, R. and C. Braester. Calculation of gas migration in fractured rock. Swedish Nuclear Fuel Waste Management Company, KBS Technical Report KBS-TR-87-18, 1987.

Trick, T., T. Fierz, E. Proust, P. Meier and M. Combarieu. GTS/GAM: Gas tracer test series GT2 in the GAM shear zone (August 2000). Dipole flow field GAM98-004/TPF95-004. NAGRA (Nationale Genossenschaft für die Lagerung radioaktiver Abfälle) Internal Report 00-49, Wettingen, Switzerland, 2000.

Trick, T., M. Piedevache, E. Proust, P. Meier and M. Combarieu. GTS/GAM: Gas tracer test series GT3 in the GAM shear zone (December 2000). Dipole flow field GAM98-002/TPF95-007. NAGRA (Nationale Genossenschaft für die Lagerung radioaktiver Abfälle) Internal Report 01-02, Wettingen, Switzerland, 2001.

Wyss, E. GTS/TPF: Site preparation, borehole installation, hydraulic characterisation and gas threshold-pressure tests at the Grimsel Test Site. (July, 1996). NAGRA (Nationale Genossenschaft für die Lagerung radioaktiver Abfälle) Internal Report 96-34, Wettingen, Switzerland, 1996.

Chapter 7: Conclusions

The work presented in this thesis is addressed to improve the understanding into the physics of single and multiphase transport phenomena. Taking into account the applied methodology, results and discussion presented in this document, the following conclusions can be drawn:

The transmissivity fields derived from the inversion reveal a strong heterogeneity and suggest the existence of channels. Nevertheless, all the inverted transmissivity fields show the same transmissivity structure, displaying slight differences in terms of their different anisotropy ratio.

The tracer test model results show that the concentration objective function does not coincide with the Kashyap's criterion in order to select the most suitable T field for flow and transport modelling. To overcome this problem and establish a common selection criterion for flow and transport, a new function named Global Praising Function "G" has been defined. The out come of transport predictions reveal the T field selected by the G criterion as the most suitable for both flow and transport modelling.

The simulated breakthrough curves obtained using the transmissivity field selected by the G selection criterion are very similar. In practice, is difficult to establish an adequate model for the spatial variability of flow porosity and its correlation with transmissivity.

During the simulation of the gas bubble generation, the numerical results show that the system behaviour is very sensitive to way in which we are simulating the gas injection procedure, as well as to the fracture geometry itself. In this sense, it is necessary to include into the model the gas/water exchange in the injection borehole, and also to represent physically the fracture observation boreholes Regarding the internal fracture porosity structure, computed gas pressure in both, injection borehole and inside the fracture grow at different velocity considering an empty fracture or a fault gouge filled fracture. These differences can help to select the most adequate model for the spatial variability of flow porosity.

A numerical model developed to take into account several hypothesis about gas transport through partially saturated heterogeneous fractures. A sensitivity analysis have been carried out, paying special attention to those variables which govern the dissolution/diffusion processes is shear zones.

In general, gas tracer migration is very sensitive to the solubility, affecting to the gas tracer transport in both, mobile and immobile zones. As can be seen in the breakthrough curves, the larger the gas solubility value the most delayed the breakthrough takes place.

Effective gas diffusion coefficients depend among others on temperature. In the transport simulations a isothermal condition is assumed. Nevertheless the model can account with non-isothermal scenarios.

In order to investigate the effect of the heterogeneity on the breakthrough curves, different equally probably transmissivity realisations have been considered. The results show that different breakthrough curves are obtained depending on the water content of

the fracture. A bigger surface of water in contact with the gas tracer implies a larger delay in the breakthrough.

Gas migration shows a great sensitivity respect to the formation pressure. The higher the gas pressure larger the mean residence time and also the surface available for dissolution/diffusion.

The effect of the injection/extraction boreholes (injection interval volume and water saturation) is very important to take into account in the design and performance of future gas tracer injection tests in fractures, due to the fact that the injection interval behaves as a storage for dissolved gas.

The model is potentially useful for predicting gas tracer migration, site characterisation, and also for experimental gas tracer tests design.

This methodology has been applied to simulate the gas tracer tests performed in the framework of the GAM Project. The inconsistency between the obtained transport parameters, and also the small gas tracer separation in the breakthrough tailing indicates that dissolution/diffusion in the liquid phase did not control the gas tracer behaviour during the experimental GAM gas testing campaigns. The observed responses are the result of gas tracer diffusion in dead gas volumes compatible with the volume associated to some dewatered observation borehole intervals.

Annex A1

Interpretation of Cros-Hole Injection Tests
Sinthetic Case Study

INTERPRETATION OF HYDRAULIC TESTS IN THE FRAMEWORK OF THE INVERSE PROBLEM

OBJECTIVE: Verify that the field obtained with the proposed methodology for inverting the hydraulic test bears any resemblence with the true fields.

METHODOLOGY

1: Start from the official T field generated

2: Derivation of a simple T field

3: Simulation of two pumping cross-hole tests

4: Geostatistical interpretation of those tests:

- Assuming the “true” variogram
- Assuming an isotropic variogram
- Using only one pumping test
- Using only two pumping tests

1: START FROM THE OFFICIAL T FIELD GENERATED

OFFICIAL FIELD (600 X 600)

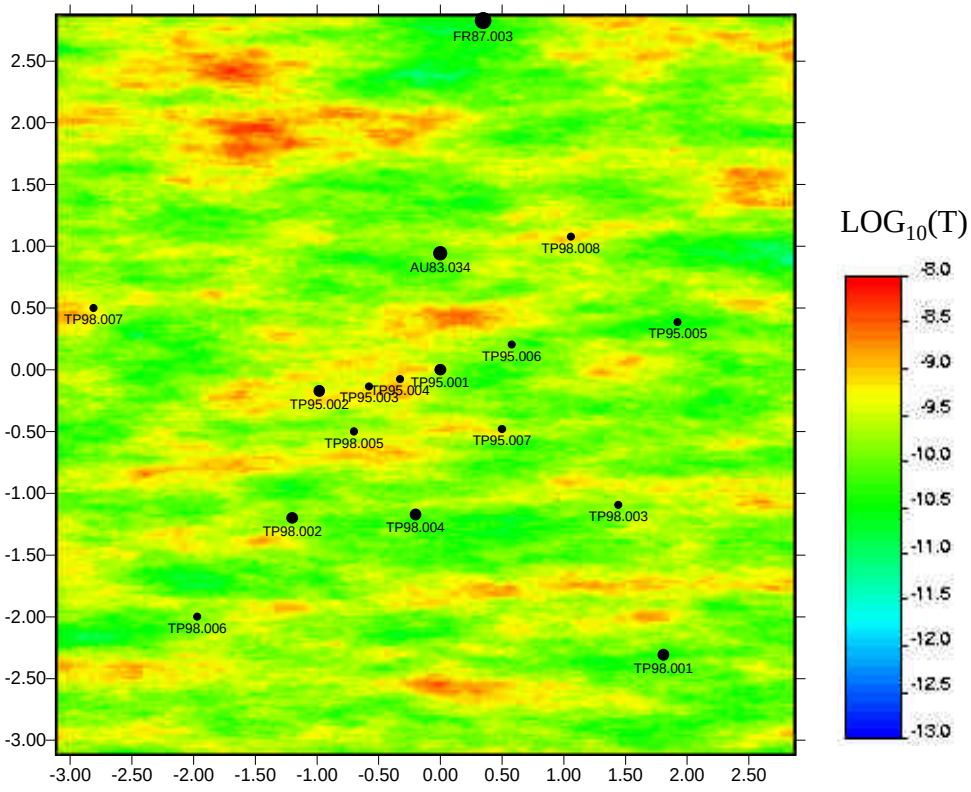

DIMENSIONS: 6 m X 6 m

DISCRETIZATION: 600 X 600

VARIOGRAM:

- SPHERICAL MODEL
- Mean = -10
- Variance = 1
- Range(x) = 1.44
- Range(y) = 0.36

Code : GCOSIM3D (Gomez-Hernandez , 1992)

2: DERIVATION OF A SIMPLE T FIELD

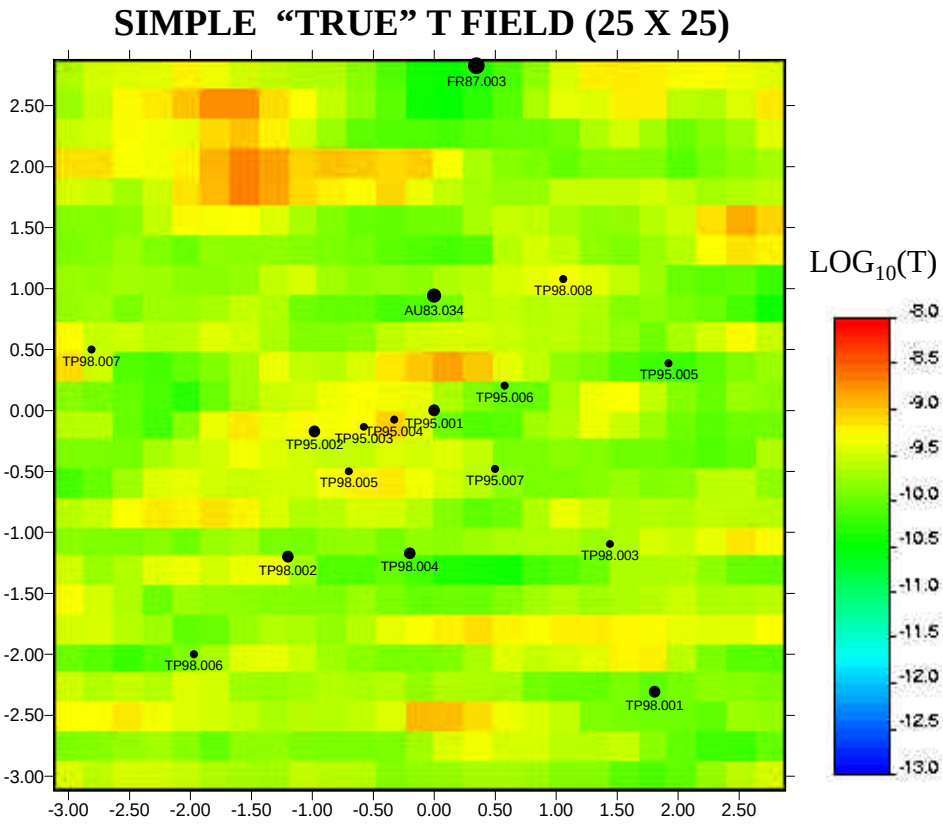

DIMENSIONS: 6 m X 6 m

DISCRETIZATION: 25 X 25

T_{cell} Value: GEOMETRIC MEAN (T)

3: SIMULATION OF TWO PUMPING CROSS-HOLE TESTS INTERPRETATION METHODOLOGY

3.1 ASSUME THE GEOSTATISTICAL MODEL

VGM-TRUE	VGM-ISO
Spherical model	Spherical model
Mean = 0	Mean = 0
Range(x) = 1.44	Range(x) = 0.7
Range (y) = 0.36	Range (y) = 0.7

3.2 KRIGING THE POINT T DATA AT THE OBSERVATION POINTS OF THE HYDRO TEST

VGM-TRUE

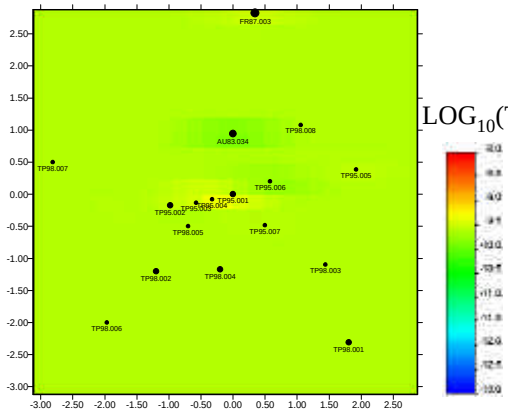

VGM-ISO

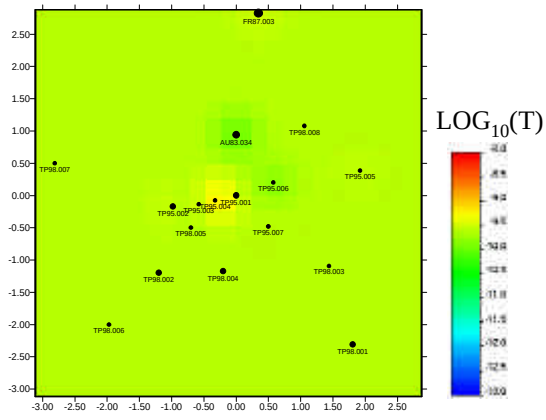

3.3 USING THESE LOGT VALUES AS OUR PRIOR INFORMATION IN EVERY TEST AND TAKING THE HEAD DATA WE HAVE COMPUTED BEFORE, WE HAVE MINIMIZE THE J FOR CONVERGENCE:

$$J = J_h + l J_Y$$

3.2 SIMULATE CROSS-HOLE TEST

MODEL STRUCTURE: Using true 25x25 T field

TEST 1 Q= 2.4 ml/min

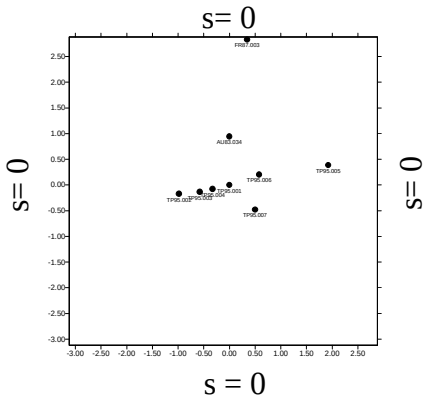

SIMULATED DRAWDOWNS
8 OBSERVATION BOREHOLES

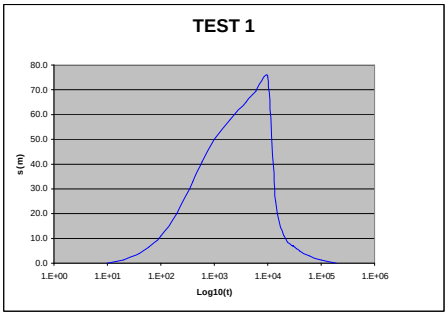

TEST 2 Q= 1.8 ml/min

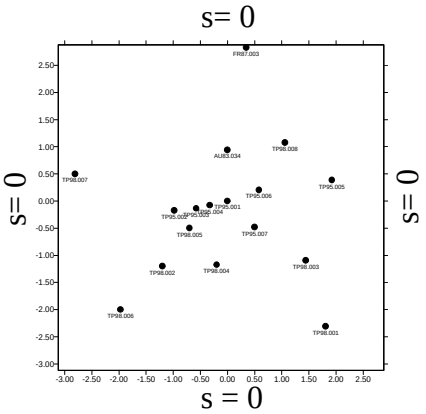

SIMULATED DRAWDOWNS
16 OBSERVATION BOREHOLES

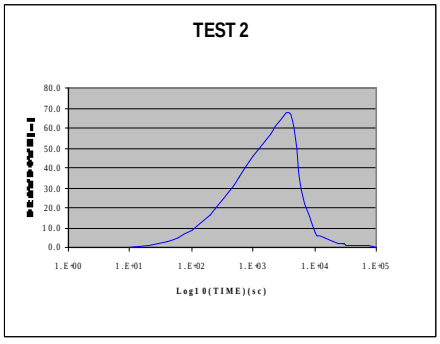

The calculated heads taken from these simulations are going to be the "true" head data for the following interpretations.

4. GEOSTATISTICAL INTERPRETATION

4.1 Single interpretation of Test-1

Initial hypothesis:

- **Varying initial transmissivity**
- **Assuming the true variogram: vgm_true**

Results in terms of Convergence:

l=10

INITIAL VALUE	OBJ. FUNCTION	OBJ. HEAD FUN.	OBJ. PARAMETER FUNC.
Tkriging	12.30	3.87	8.41
T=1E-9	37.40	3.88	33.50
T=1E-11	18.60	5.79	12.80
Ttrue	18.50	5.68	12.80

l=1

INITIAL VALUE	OBJ. FUNCTION	OBJ. HEAD FUN.	OBJ. PARAMETER FUNC.
Tkriging	2.34	0.57	1.77
T=1E-9	27.40	0.54	26.90
T=1E-11	3.19	0.64	2.56
Ttrue	3.19	0.64	2.56

l=0.1

INITIAL VALUE	OBJ. FUNCTION	OBJ. HEAD FUN.	OBJ. PARAMETER FUNC.
Tkriging	0.37	0.06	0.31
T=1E-9	25.40	0.06	25.30
T=1E-11	0.49	0.08	0.41
Ttrue	0.49	0.08	0.41

4.2 Joint interpretation of Test-1 and Test-2

Initial hypothesis:

- **Varying initial transmissivity**
- **Assuming the true variogram: vgm_true**

Results in terms of Convergence:

l=10

INITIAL VALUE	OBJ. FUNCTION	OBJ. HEAD FUN.	OBJ. PARAMETER FUNC.
Tkriging	15.50	5.95	9.50
T=1E-9	15.50	5.95	9.50
T=1E-11	15.50	5.95	9.50
Ttrue	16.00	6.26	9.72

l=1

INITIAL VALUE	OBJ. FUNCTION	OBJ. HEAD FUN.	OBJ. PARAMETER FUNC.
Tkriging	3.32	0.89	2.43
T=1E-9	3.32	0.89	2.43
T=1E-11	3.32	0.93	2.43
Ttrue	3.37	0.88	2.49

l=0.1

INITIAL VALUE	OBJ. FUNCTION	OBJ. HEAD FUN.	OBJ. PARAMETER FUNC.
Tkriging	0.56	0.11	0.45
T=1E-9	0.56	0.11	0.45
T=1E-11	0.55	0.11	0.45
Ttrue	0.56	0.11	0.45

Preliminary conclusions in terms of concergence:

1. Slight difference between values in the single test (“poor convergence”)

2. Convergence less sensitive to initial transmissivity value in the double test case

5. RESULTS

5.1 EFFECT OF INVERTING

(Joint interpretation of the two tests assuming vgm_true)

TRUE T FIELD

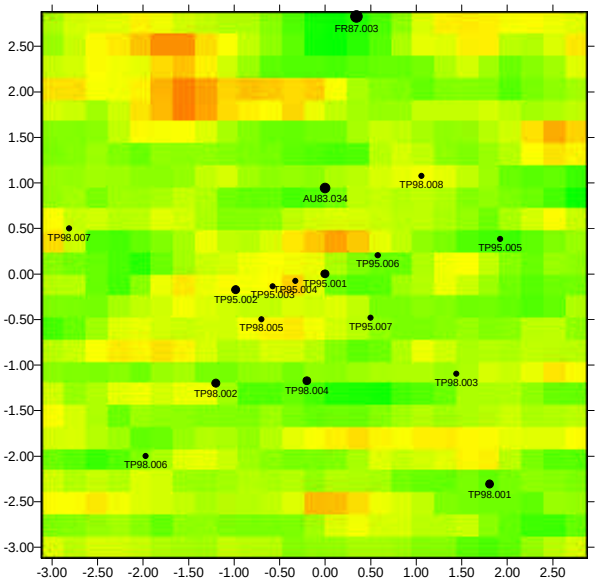

KRIGING T FIELD

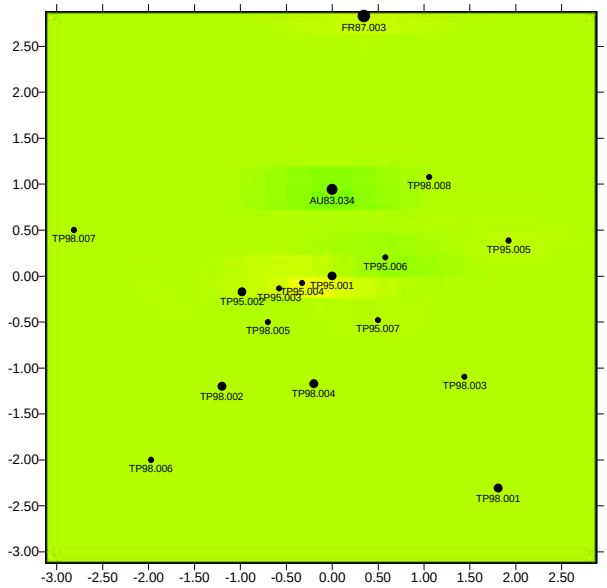

ESTIMATED T FIELD (l=0.10)

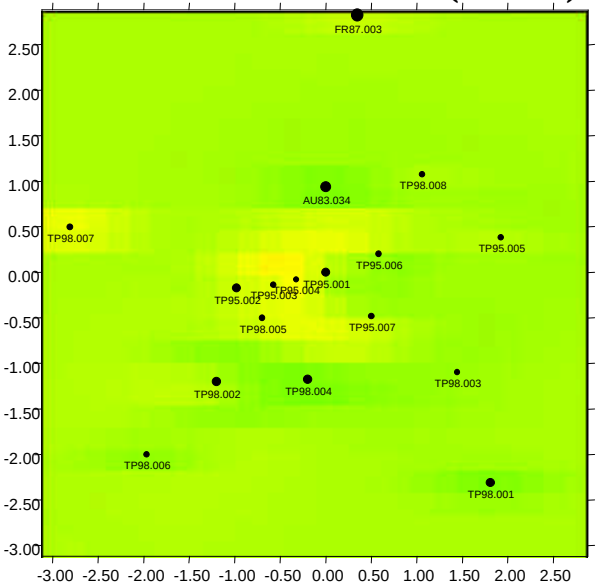

ESTIMATED T FIELD (l=0.1)

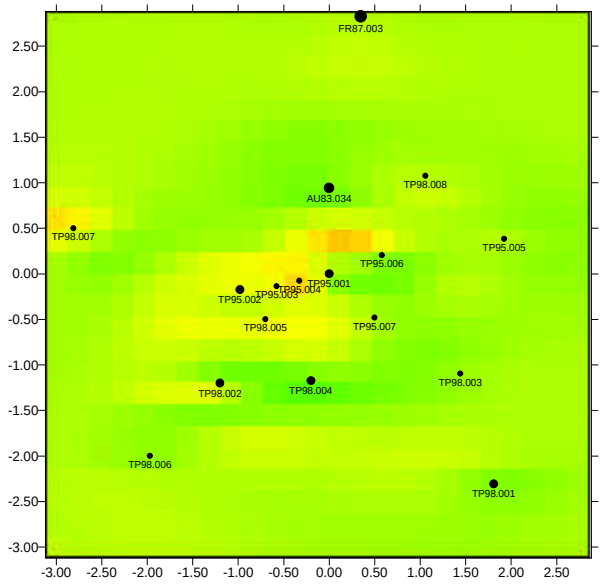

5.2 EFFECT OF GEOSTATISTICAL MODEL ASSUMPTION

Joint interpretation of the two tests

TRUE FIELD(25X25)

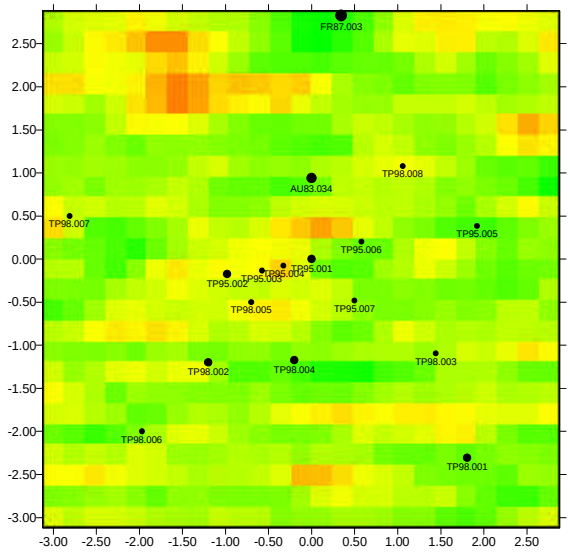

VGM_TRUE

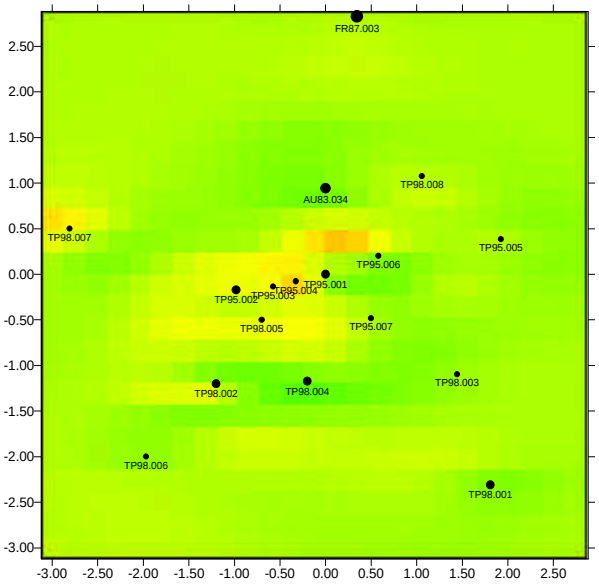

VGM_ISO

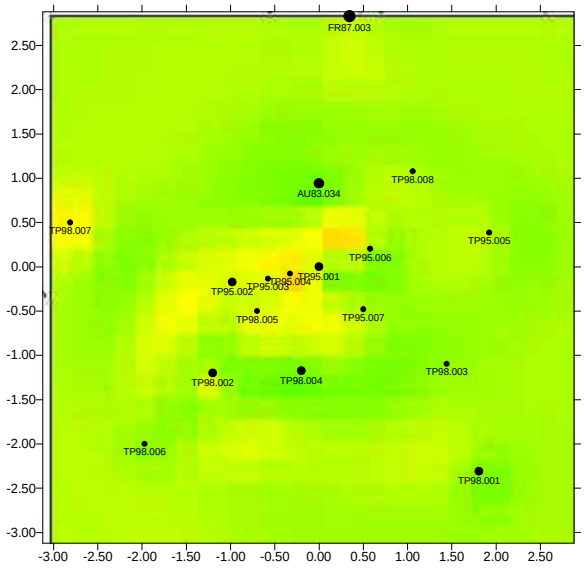

5.2 EFFECT OF NUMBER OF DATA

Sinle (Test-1) and joint (Tests 1 & 2) interpretation assuming vgm_true

TRUE FIELD(25X25)

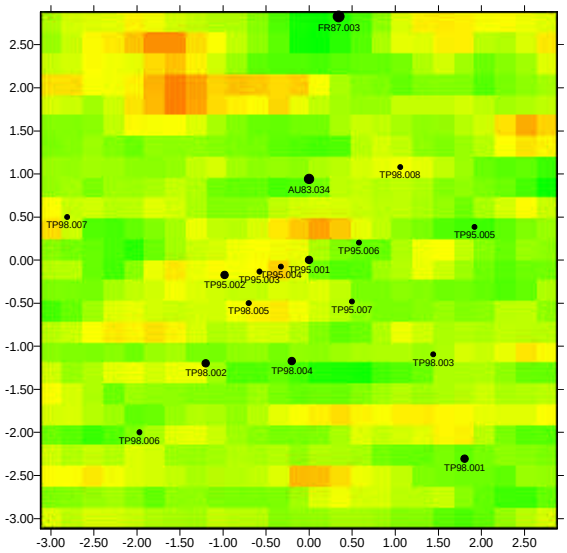

SINGLE TEST INTERPRETATION (TEST 1)

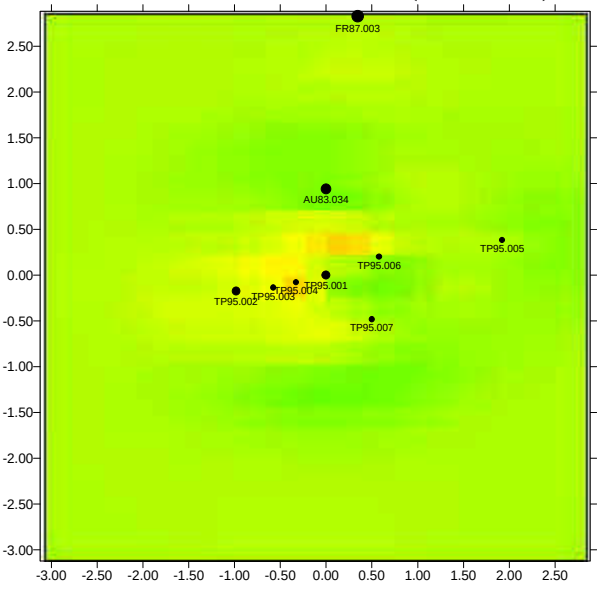

JOINT INTERPRETATION OF TESTS 1 AND 2

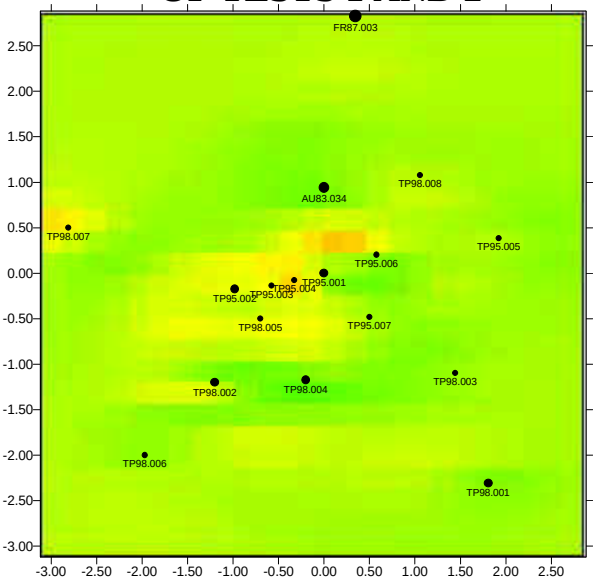

5.3 EFFECT OF SPATIAL DISCRETIZATION

Sinle (Test-1) interpretation assuming vgm_true

TRUE FIELD(50X50)

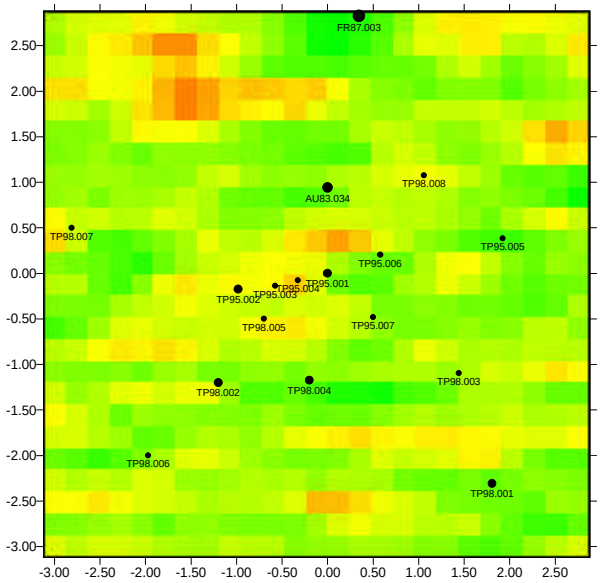

ESTIMATED T FIELD (25 X 25) (l =0.1)

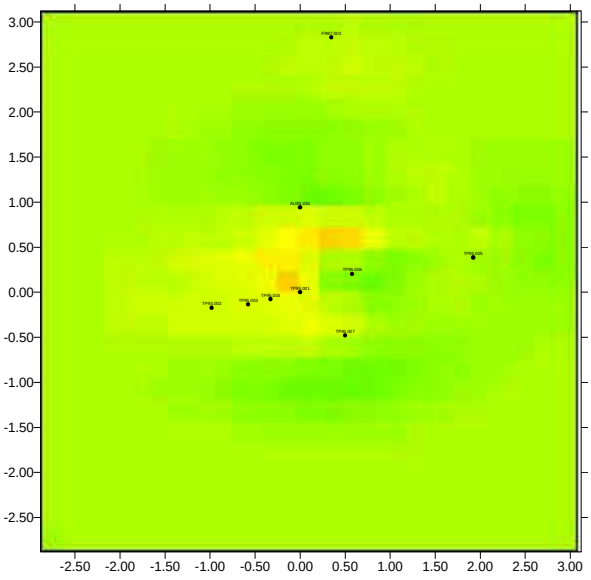

ESTIMATED T FIELD (50 X 50) (l =0.1)

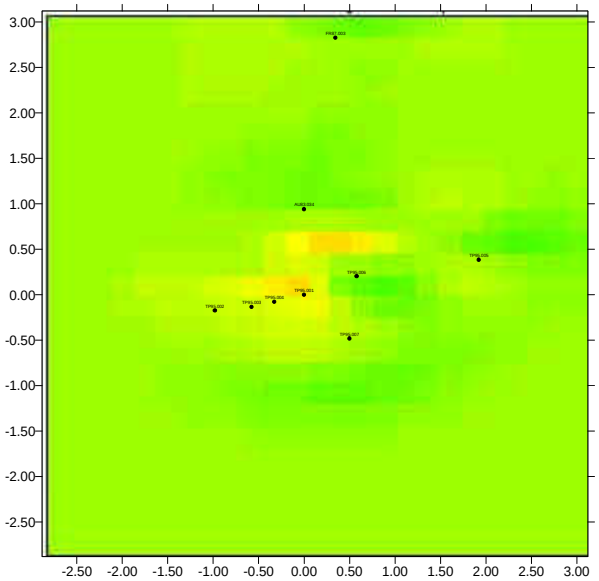

6. CONCLUSIONS

- Good head fits possible with all the models

- The more data we have , the more similar the hypothetical and the estimated field.

- Head data do not suffice to identify which geostatistical model represents best our hypothetical field.

Annex A2

Two Phase Flow Simulations
Sinthetic Case Study

SIMULATION OF AIR INJECTION TESTS THROUGHT 2D FIELDS

OBJECTIVE: Preliminary numerical simulations of gas flow tests. Sensitivity study respect to heterogeneity, grid size, and also gas flow parameters scale changes.

METHODOLOGY

1: Start from official field generated

2: Transform official field to soil texture field (% sand)

3: Change to grid scale

4: Derive fields of model parameter (λ, P_0)

5: Simulate Gas Injection Test

1: START FROM THE OFFICIAL T FIELD GENERATED

OFFICIAL FIELD (600 X 600)

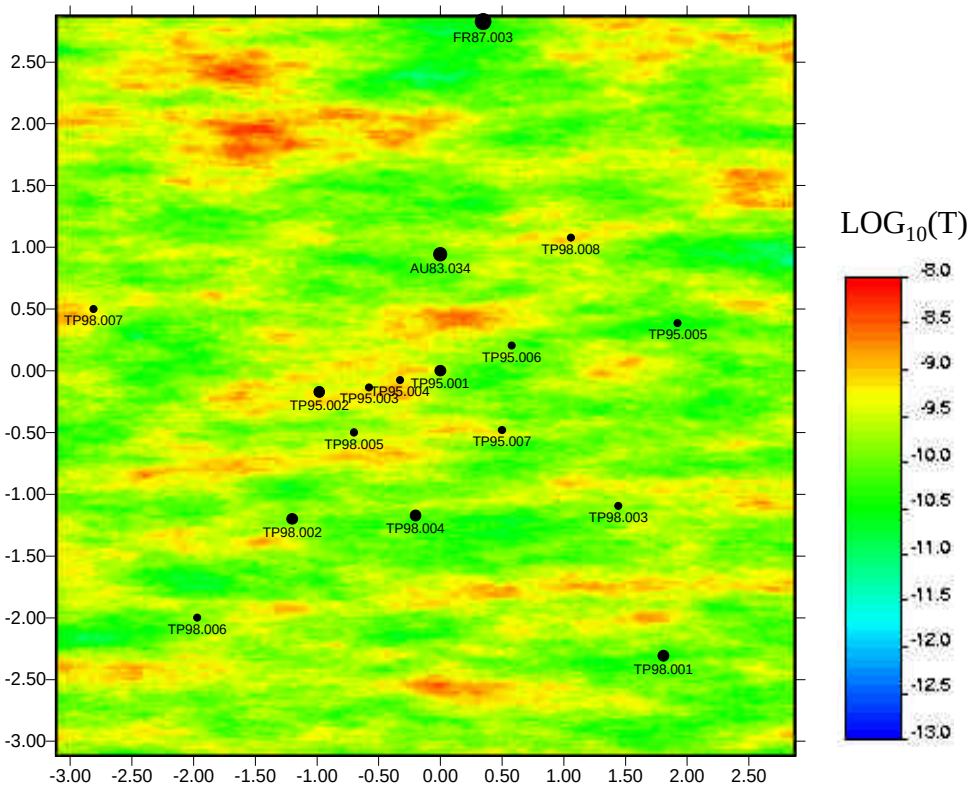

DISCRETIZATION: 600*600 zones
FIELD DIMENSIONS: 6m*6m = 36m^2
(Zone Area= 1cm^2)

VARIOGRAM:

- SPHERICAL MODEL
- Mean = -10
- Variance = 1
- Range(x) = 1.44
- Range(y) = 0.36

Code : GCOSIM3D (Gomez-Hernandez , 1992)

2: TRANSFORM OFICIAL FIELD TO SOIL TEXTURE FIELD (%SAND)

Equal the point distribution function of the standard field to that of a sand field, such that the variability of soil properties is equal to that measured by Fisher et al (1996)

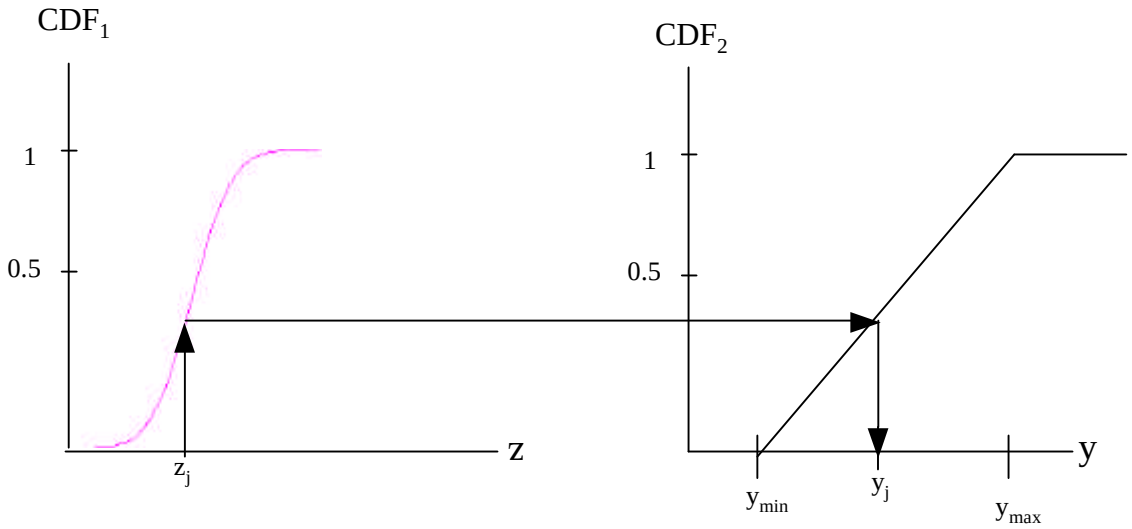

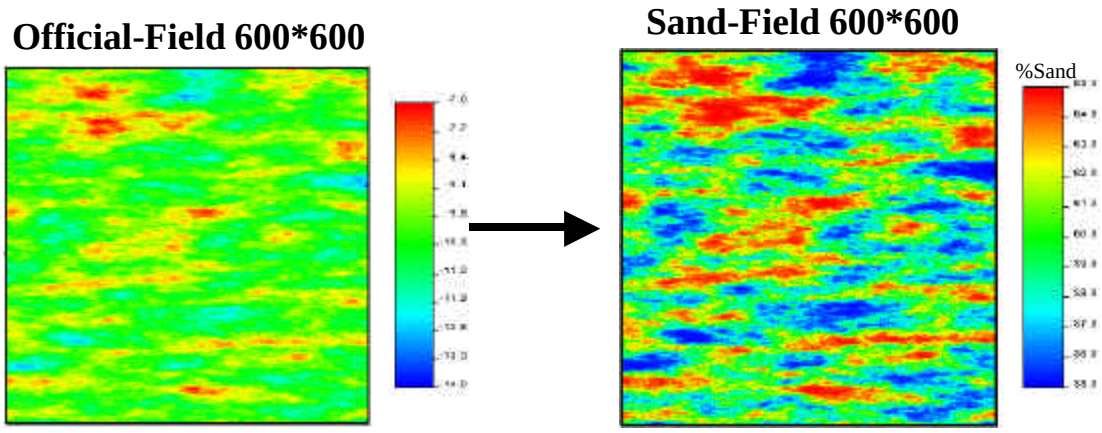

3: CHANGE TO GRID SCALE

3.1 Selection of the "Gas Injection Test Area" (GITA) from the Sand Field

- Interest area ? Left-Down corner, containing (100*100) zones
- Total Area ? $1m^2$

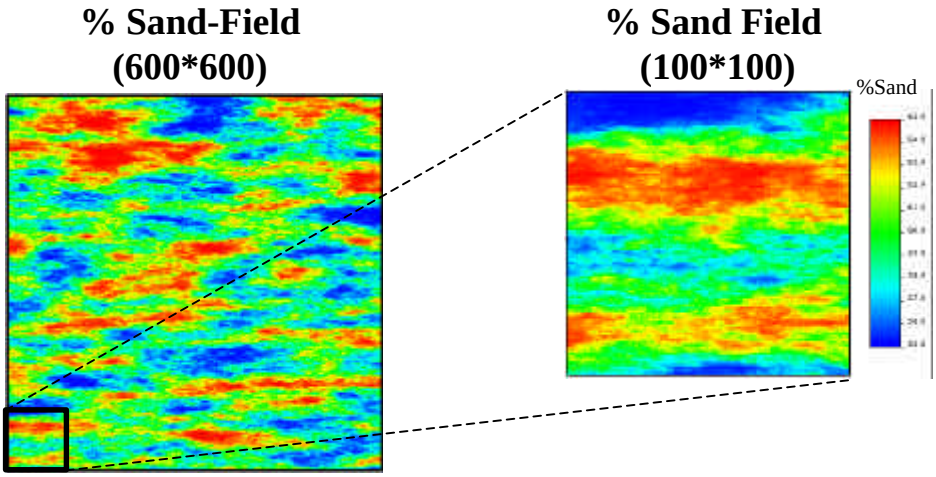

3.2 Redefine the number of elements per unit of area in the GITA

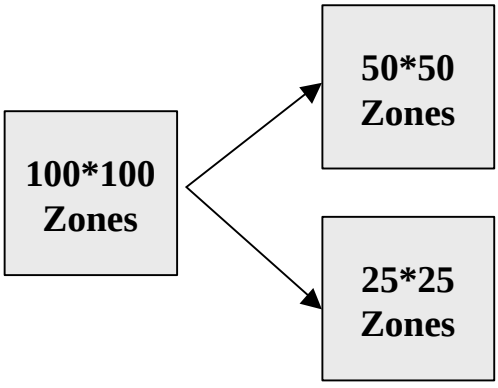

3.3 Asign (% Sand) to the new generated elements in the GITA

•Point Model

Value from the left-down zone to block

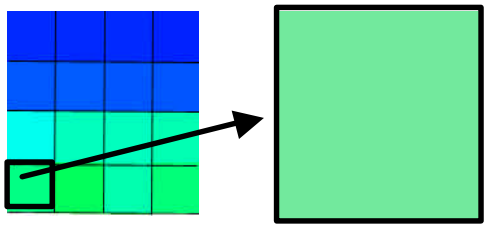

(100*100) **(50*50)** **(25*25)**

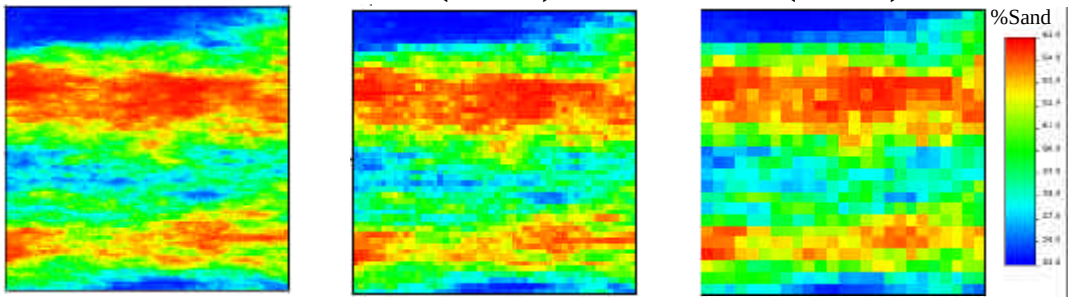

•Averaged Model

Block value obtained through value zones averaging

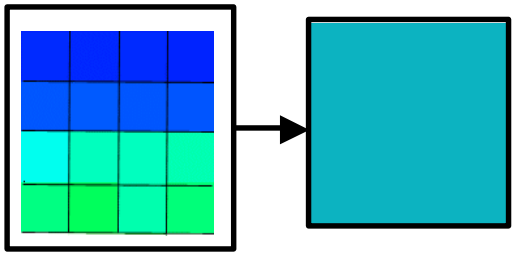

(100*100) **(50*50)** **(25*25)**

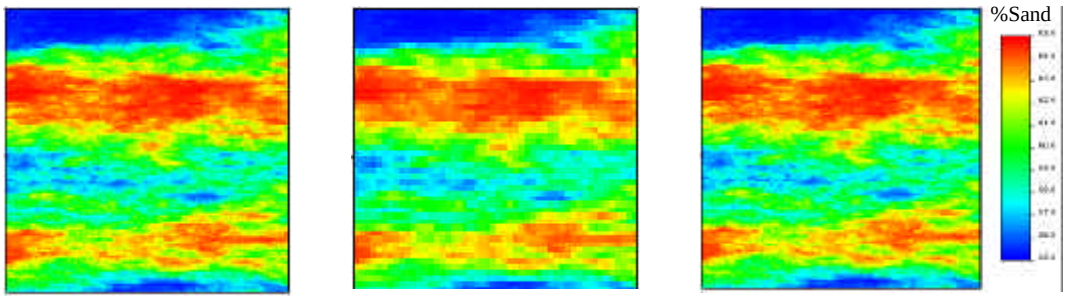

4: DERIVE FIELDS OF MODEL PARAMETERS (l, P_0)

Use equations of Rawls and Brakensiek (1988), derived from many soil samples, and transform %Sand fields in hydraulic parameter fields.

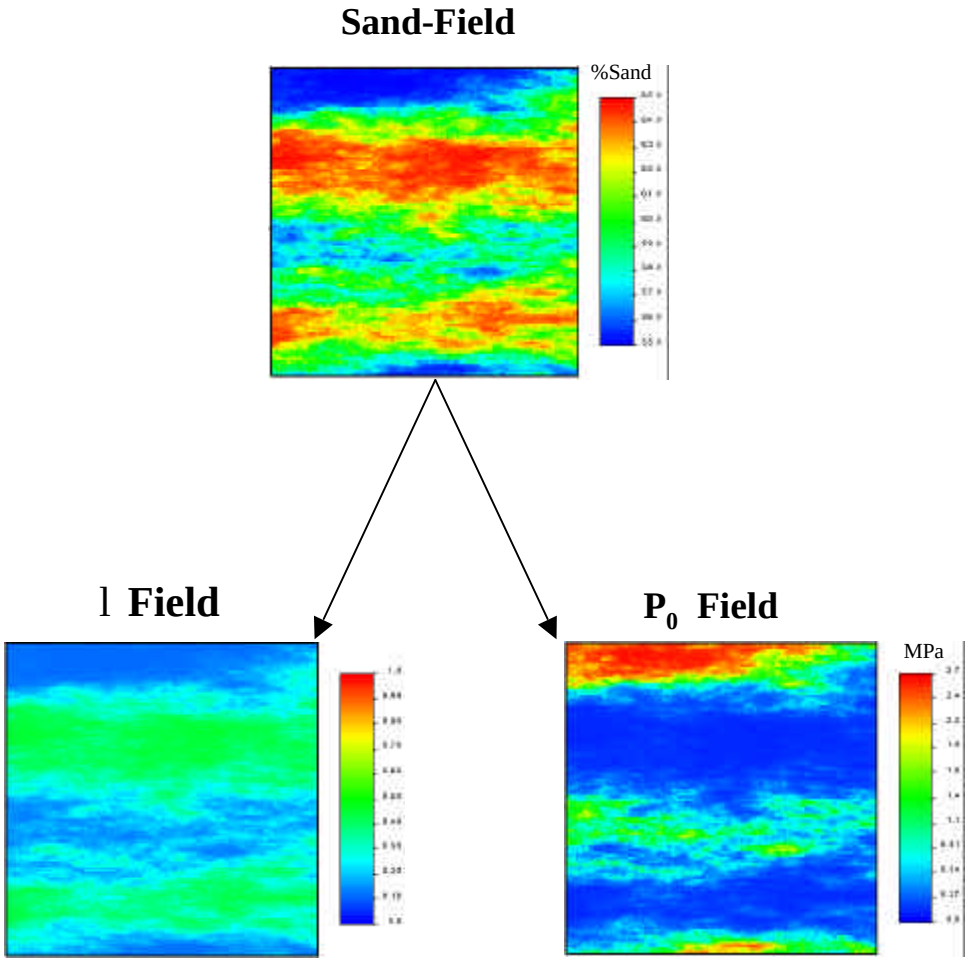

5: GAS INJECTION TEST SIMULATION

4.1 Basic Equations

Simulations are performed using the Finite Element program **CODE-BRIGHT**

• Water mass balance

$$\frac{\partial}{\partial t}(q_s^w(1-f)+q_l^w S_l f+q_g^w S_g f)+\nabla(j_s^w+j_l^w+j_g^w)=f^w$$

• Air mass balance

$$\frac{\partial}{\partial t}(q_l^a S_l f+q_g^a S_g f)+\nabla(j_l^w+j_g^w)=f^a$$

• Capilary Pressure (Van Genuchten model)

$$P = P_0(S_e^{-\frac{1}{l}}-1)^{1-l}$$

• Relative Permeability (Van Genuchten model)

$$k_{rl} = \sqrt{S_e}(1-(1-S_e^{\frac{1}{l}})^l)^2$$

4.2 Conceptual Model

Objective: Air injection in a horizontal, initially saturated fracture of an area of $1m^2$

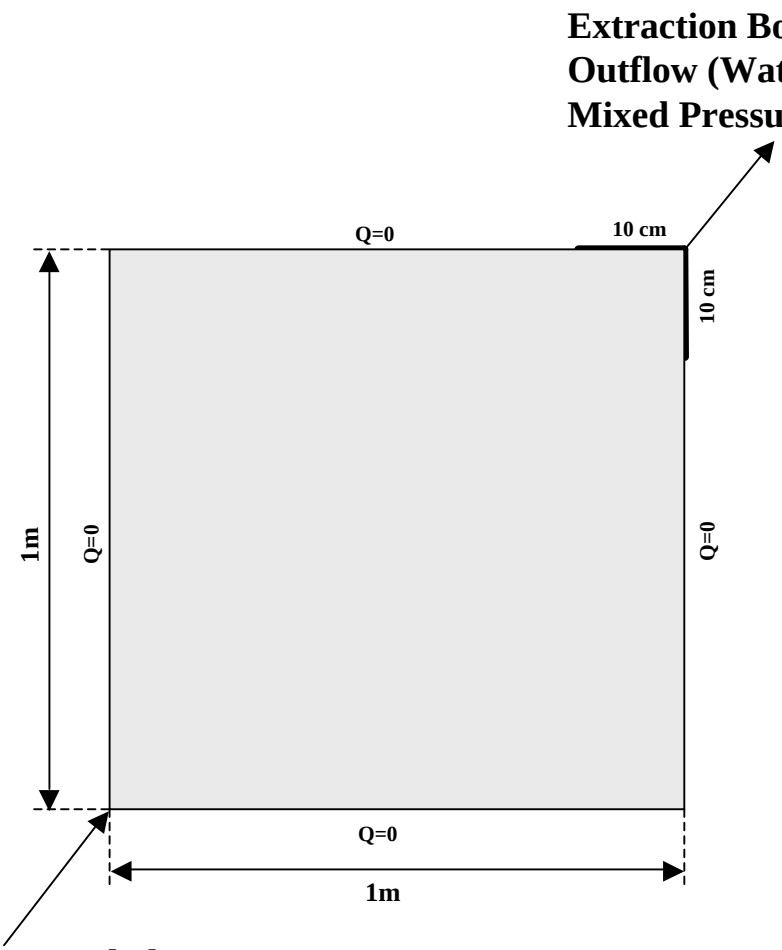

5: SENSITIVITY ANALYSIS

- **Homogeneous Fields**: (25*25) Vs (50*50) zone grids
  Recovery mass flux at the extraction borehole

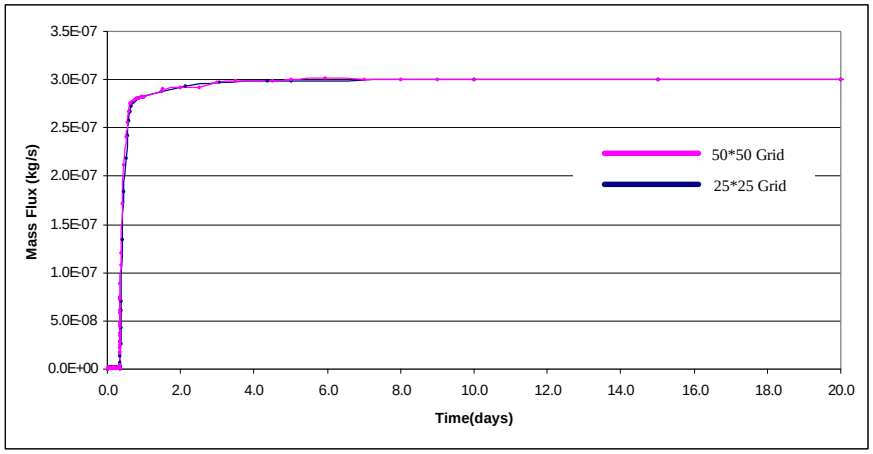

- l **Parameter**: (25*25) Vs (50*50) zone grids - Point Model
  Recovery mass flux at the extraction borehole

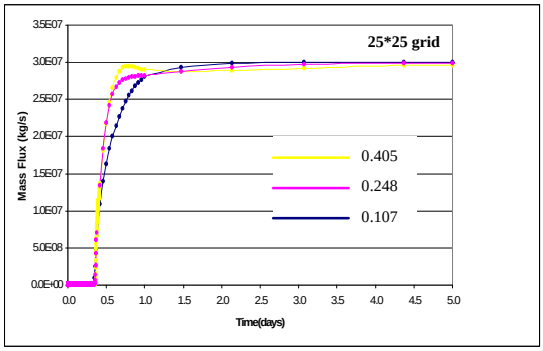

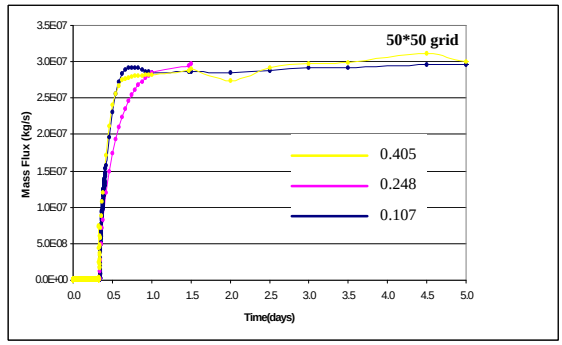

- **P_0 Parameter**: (25*25) Vs (50*50) zone grids – Point Model
  Recovery mass flux at the extraction borehole

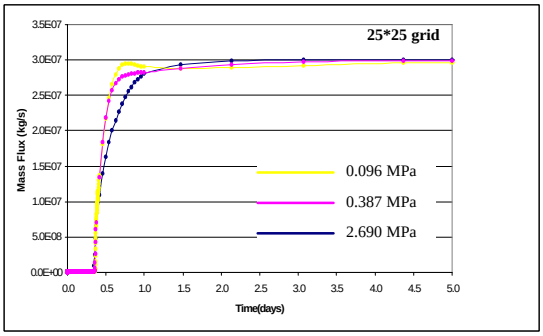

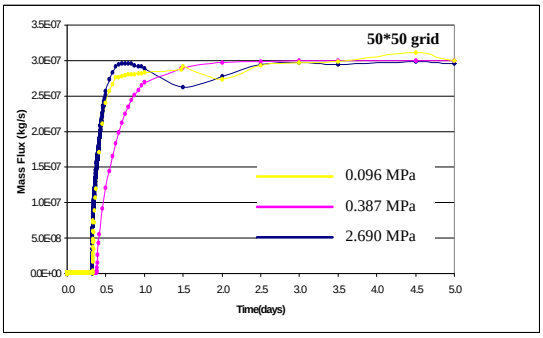

- **Grid size and zone parameter assignment**
  Air & water pumping flow rates

Point Model

Air out-flow rate

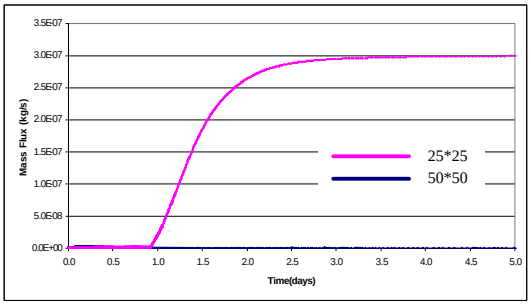

Water out-flow rate

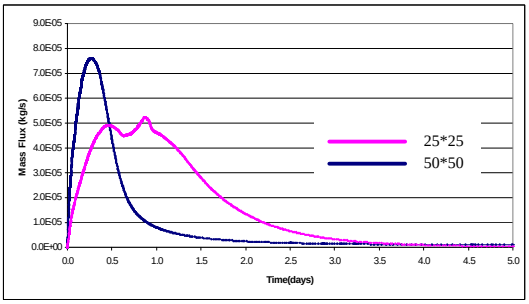

Averaged Model

Air out-flow rate

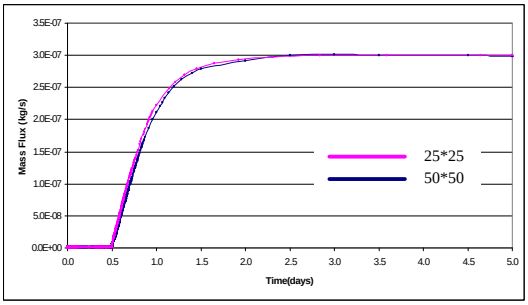

Water out-flow rate

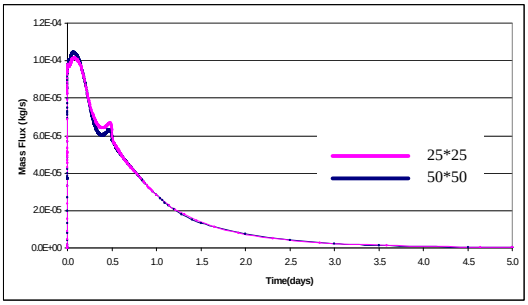

•Grid size and zone parameter assignment

Spacial distribution of total mass out_flow

Upper Boundary

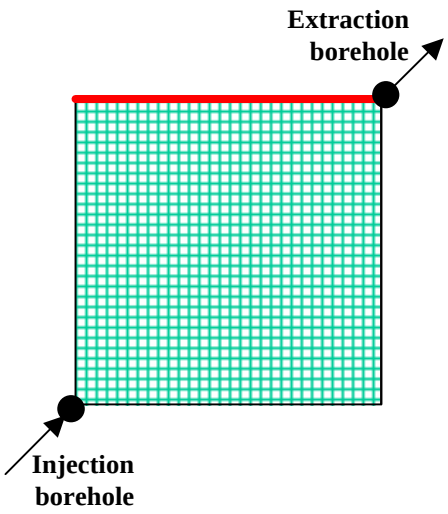

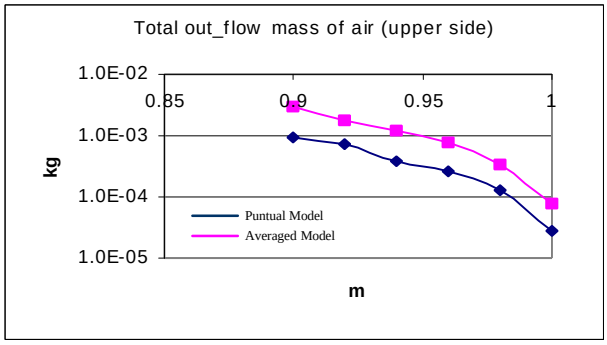

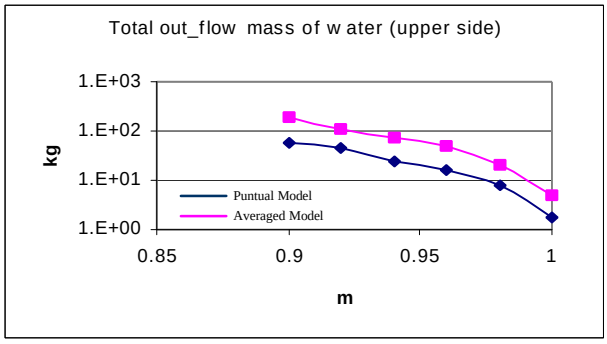

Right Boundary

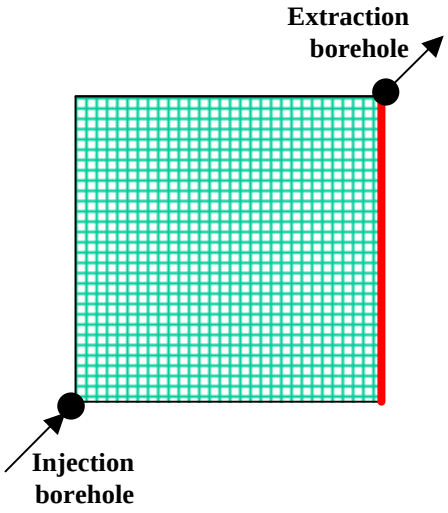

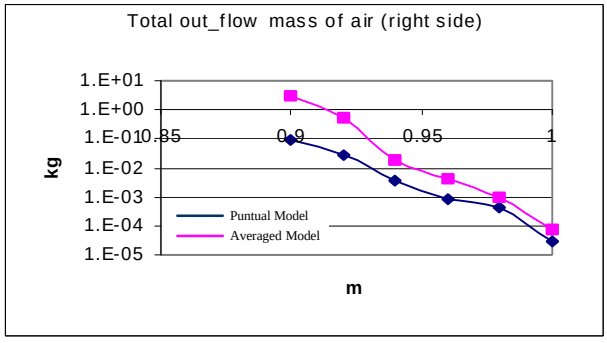

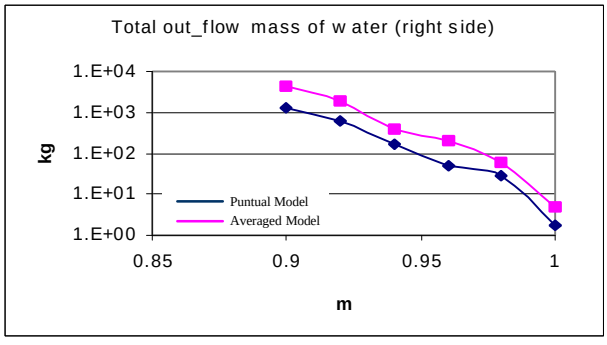

•**P_0 Parameter**: (50*50) – Point Model

Saturation degree section (y_1? y_2)

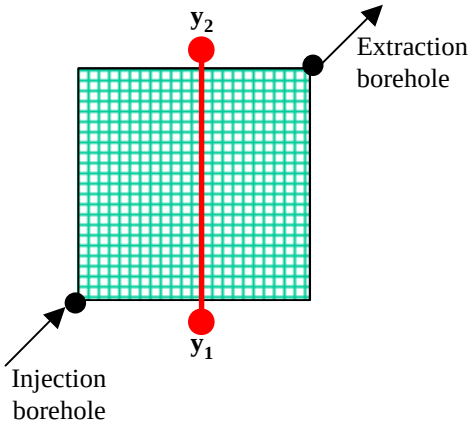

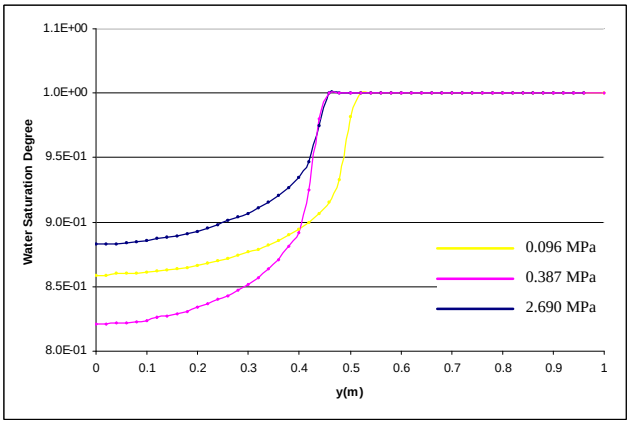

6: CONCLUSIONS

• Grid size does not affect results significantly

• Dependence of results on grid size is sensitive to the way in which upscaling is performed.

• The air (and water) out_flow tends to concentrate on only one bondary node (the one closest to the injection). This reflects both the spatial variability of the rock properties and our uncertainties about how to write the boundary conditions.

Annex A3

Gas Tracer Test Simulations. Sinthetic Case Study

Analitical Gas Tracer Test Simulation Numerical (1D) Gas Tracer Test Simulation

MODELLING GAS TRACER TESTS.

In order to better understand the gas transport mechanisms and properties in shear zones and to determine realistic mass exchange coefficients in a two-phase flow (gas and water) system it is necessary to obtain a good estimation of the contact area between gas and liquid. One of the processes that provide us with this information is the comparison of the transport behaviour of gas tracers with different solubilities.

Gas transport is controlled by advection, dispersion and dissolution in the liquid phase. In a fractured medium, the rock matrix (and small aperture fractures) remains filled with virtually immobile water. Therefore, dissolved gasses reach the interior of the matrix by molecular diffusion. The overall process is similar to matrix diffusion. Hence, it is very sensitive to gas solubility, diffusion coefficient and to the surface and volume available for dissolution/diffusion. Another important goal is to choose suitable gas tracers cannot be address without an a priori estimation of the water content in the medium (Nelson et al., 1999). We focus on the design of tracer tests aimed at characterizing these parameters. The main target is to investigate whether under the conditions of the experiment the separation is possible or not.

1. Analitical solution for gas transport

Gas tracers are injected inside the fracture once a stable gas bubble has been created between the injection and the extraction boreholes. The dissolution-diffusion mechanism is expected to be an important factor in the gas mass balance inside the fracture. Presumably, concentration in the liquid at the interface is equal to the solubility of the gas (actually, the solubility times partial pressure, according to Henry's Law). Then diffusion mass flux into a semi-infinite porous medium is given by:

$$J_m = C_0 f \left(\frac{D_m}{p\, t} \right)^{\frac{1}{2}}$$

$$M_m = \int J_m dt = 2 C_0 f \left(\frac{D_m\, t}{p} \right)^{\frac{1}{2}}$$

where J_m[$ML^{-2}T^{-1}$] is mass flux at time t[T] and M_m[ML^{-2}] is accumulated mass, D_m[L^2T^{-1}] is the molecular diffusion coefficient, f[-] is the porosity and C_0[ML^{-3}] is the dissolved concentration at the interface (solubility for the given partial pressure).

The above equations make it apparent that tracer exchange between liquid and gas phases is a function of solubility (the higher, the better) and diffusion coefficient. Mass dissolves and diffused into the water saturated portion of the medium also grows with residence time, surface area (we assume that diffusion takes place from a fissure, so that the exchange surface area is equal to twice the planar area of the fissure), temperature (it affects solubility, but we take it as constant; besides, temperature increases cause solubility to go down).

In this section we express the analytical solution for diffusion within a semi-infinite medium. The characteristics of the model are: a porosity of 0.1, the molecular diffusion coefficient in water of gas He divided by 10, which is $6.28 \cdot 10^{-10}$ m^2/s, and considering a semi-infinite diffusion distance. This calculation is carried out for two pulses. On one hand, a pulse of 1 hour is assumed. On the other hand, the pulse lasts 1 day is considered.

Figure A1 exhibits the mass flux in the origin point for the two pulses of concentrations. Figure A2 shows the injected mass to this region of the medium. And finally, the Figure A3 presents the cumulative mass coming to fracture since the beginning of the test.

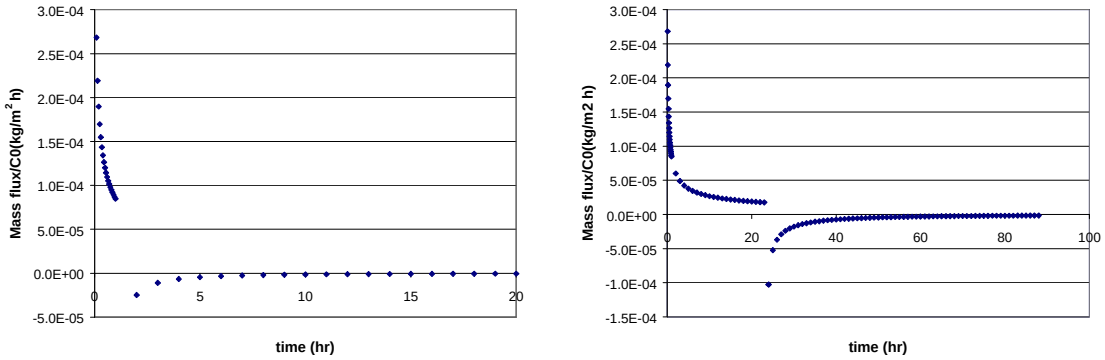

(a) (b)

Figure A.1: Mass flux passing through the origin point when diffusion is produced from a unit concentration boundary. (a) Mass flux when the pulse last 1 h. (b) Mass flux when the pulse last 1 day.

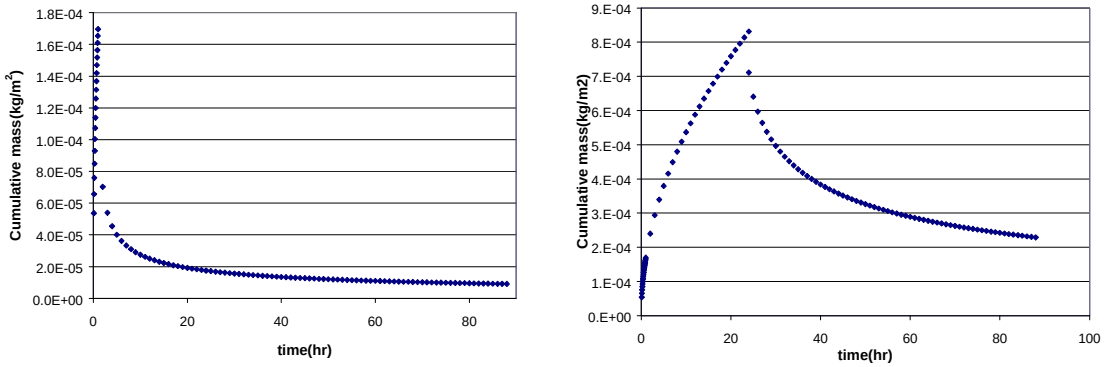

(a) (b)

Figure A2: Total mass accounted in these two cases. (a) Cumulative mass when the pulse last 1 h. (b) Cumulative mass when the pulse last 1 day.

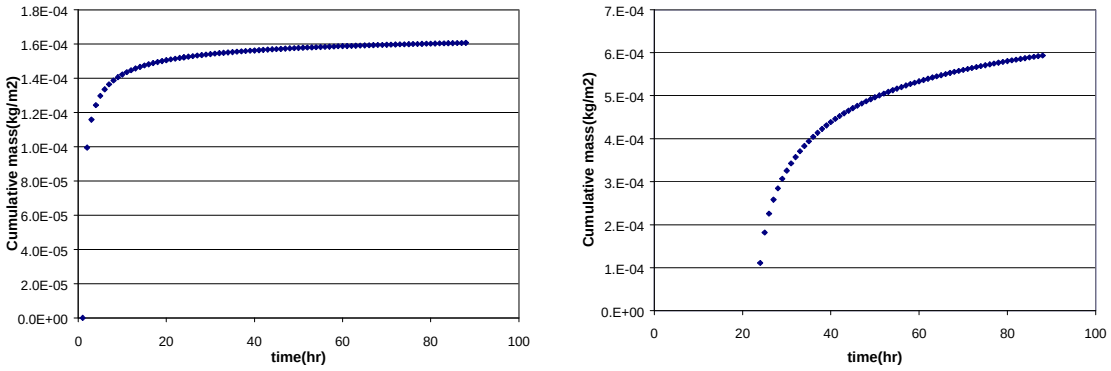

(a) (b)

Figure A.3: This plot represents the mass coming to fracture since the beginning of the pulse.(a) Cumulative mass coming to fracture when the pulse last 1 h. (b) Cumulative mass coming to fracture when the pulse last 1 day.

2. Numerical (1D) Gas Transport Simulation

2.1 Model development

The main objective of this work is the characterisation of the transport processes at two phase flow conditions in a fracture.

The dual continuum model (DCM) represents a fractured porous medium as two interacting continuums, with one corresponding to the fracture and the other to the matrix. A coupling term provides mass transfer between the two continuums.

The fracture is characterized by high permeability and low porosity compared to the matrix. In our conceptual model we have the fracture, which is the advective gas phase domain (i.e. $q_l \cong 0$; $S_l << S_g$ being q_l[LT^{-1}] the water flux through the fracture and S_l[-] and S_g[-] the water and gas saturation degree respectively), and the matrix, which contains the immobile water domain (i.e. $q_l \cong 0$; $S_l \cong 1$) (see Fig.A1). The latter is not the granodiorite rock, but the fault gouge material, which is the filling material present in the shear zone

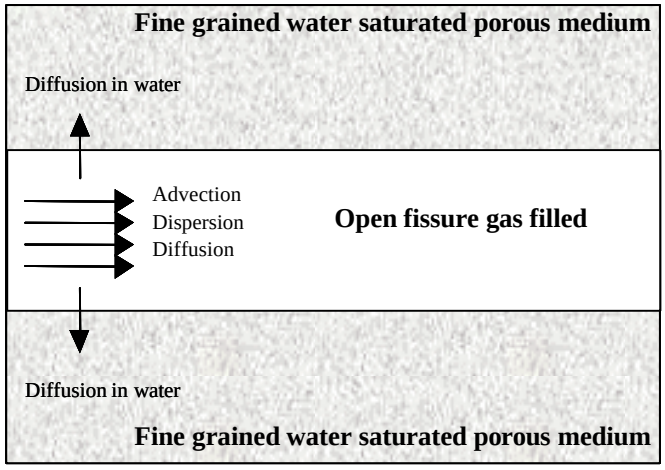

Fig. A1: Scheme of the dissolution-diffusion mechanism

The test to be studied is a gas tracer test, which consists on an instantaneous pulse of a determinate in situ gas tracer test injected at the injection well keeping the extraction well opened. These tests are something that is recently appearing. Consequently, there are no codes specially programmed for them. One possible solution might be to interpret them by means of the analogy presented in Chapter 5.

The fracture is conceptualised as an open fracture with flow porosity bf, being f the porosity, and b the local aperture fracture.

The length of the fracture is 0.9 m represented with a 1-D grid containing 15 elements. The reason for such a small domain is that this is the representative distance for a dipole test carried out at the Grimsel Site fracture. The matrix is modelled using vertical lines (composed of a number of nodes) from every node of the horizontal grid (fracture) (see Fig. 4.8). The number of elements growing up from every node of the fracture is 4, separated one from the next with a progressing increasing length (up to 0.0025 m).

The different parameter chosen to do the sensitivity analysis are summarized in Table A1

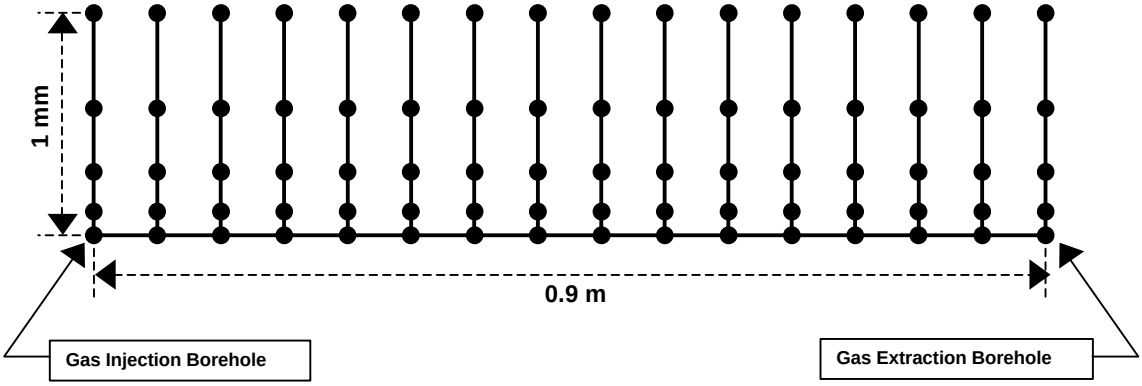

Figure A2: Scheme of the conceptual model to simulate the gas tracer tests.

Table. A1: Summary of the different cases performed

Model	Focused Parameter	Matrix thickness porosity $L_m f$	Facture thickness-porosity $b_m f$	Matrix Length L_m	Diffusion Area	Injection Rate	Injection Time
		(m)	(m)	(mm)	(m^2)	(moles/s)	(hr)
Base Case	Base Case	0.025	10^{-3}	2.5	0.9	1.8	10^{-4}
Low Flow Rate	Flow Rate	0.025	10^{-3}	2.5	0.9	1.8	10^{-5}
Thin Fracture	Fracture thickness	0.025	10^{-4}	2.5	0.9	1.8	10^{-4}
Thin Matrix	Matrix thickness	0.025	10^{-3}	2.5	0.9	9.0	10^{-4}
Thick Matrix	Matrix thickness	0.025	10^{-3}	5.0	0.9	9.0	10^{-4}
Long Duration Tracer Injection	Injection Time	0.025	10^{-3}	2.5	0.9	1.8	10^{-4}

2.2 Results

The gases accounted in the simulations have been (from the less to the most soluble gas tracer): He, Xe, H2S; SO2, NH3 (Table A2).

From the theoretical modelling the first conclusion attained when assuming the above mentioned base case is the retardation of the gas tracers; i.e. the chromatographic effect we talked about in chapter 5. As it was expected the noble gases are the one which exhibit less retardation due to their low solubility factor (Henry's constant). To be more precise, for for values of Henry's constant higher than 10^{-3} matrix diffusion (matrix only contains liquid phase) has a stronger effect, then breakthrough curves show retardation and the advancing front becomes smoother.

When comparing the base case with the case that assumed a smaller porosity for the fracture the retardation effect is higher. Consequently, the matrix dissolves more gas tracer.

Another case where the retardation effect is greater is when the thickness of the matrix is greater. In this case the matrix diffusion effect plays a more important role. This retardation effect has not been noticed in situ during the 1st and 2on campaign (see Chapter 6). One explanation should be the intrinsic heterogeneity. For example, gas may flow primarily around zones of higher water content because of the reduced K_{rg} associated to these zones. Such bypass flow may limit the contact of the gas tracer to the periphery of the higher saturated zone. This is the reason why the heterogeneity must be taken into account into the gas transport modeling, because it constraint the effectiveness of partitioning tracer test.

Base Case

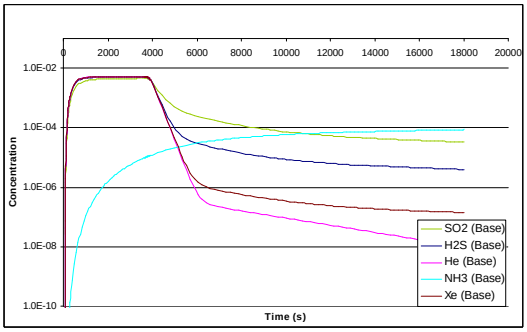

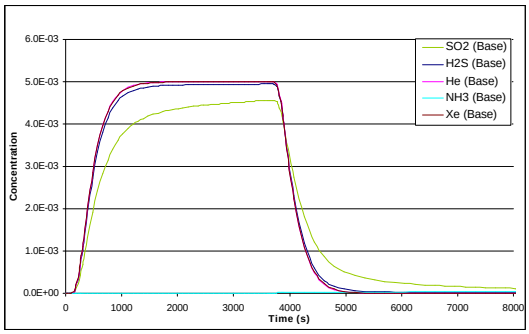

Thin Matrix

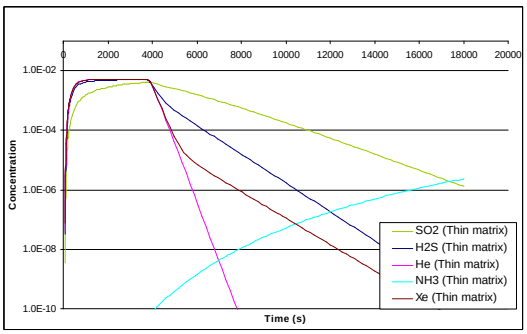

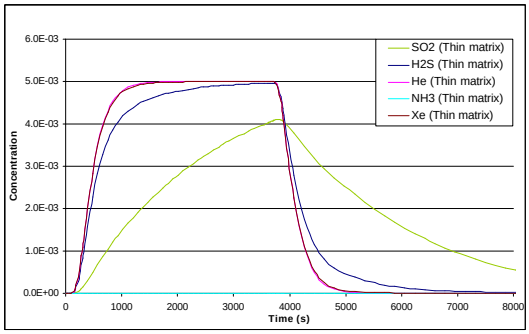

Thick Fracture

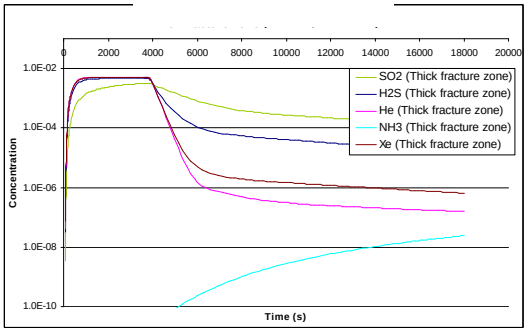

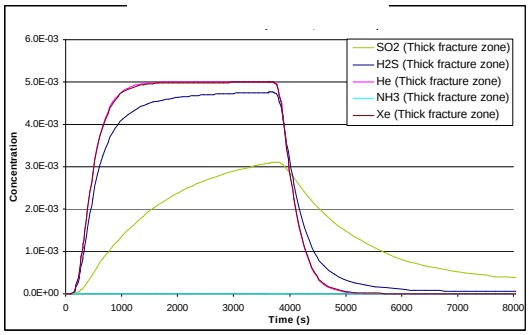

Thin Fracture

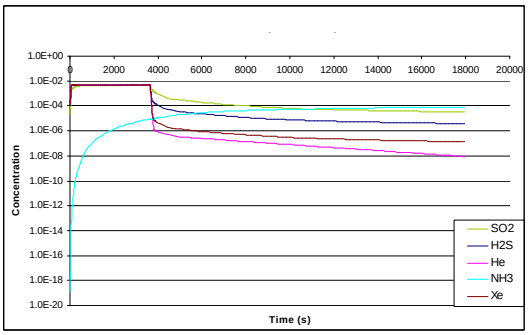

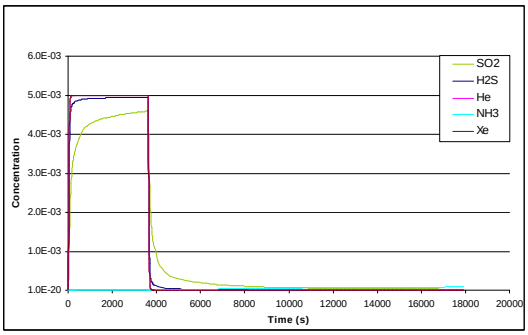

Low Flow Rate

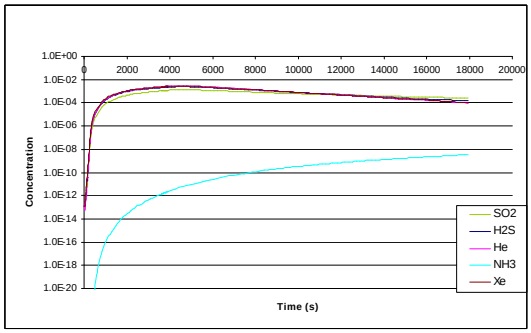

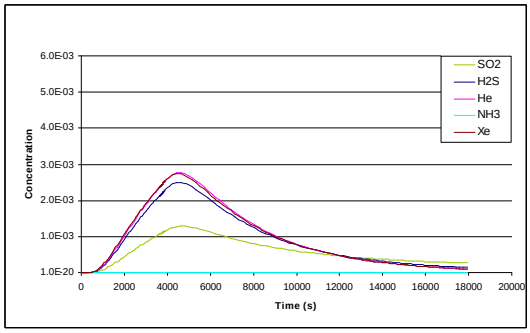

Long Duration Tracer Injection

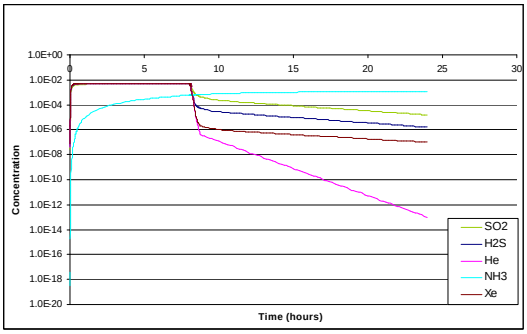

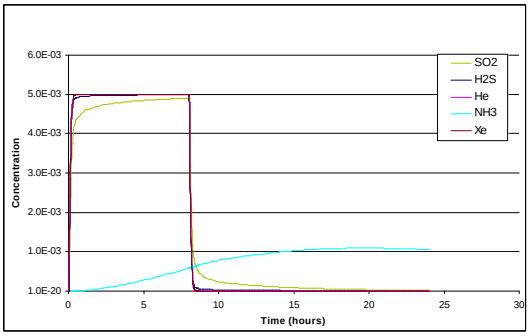

Figure A3: This figure exhibits the breakthrough curves for several gas tracer, for the different cases performed (i.e. Base Case, Thin Matrix, Thick Fracture, Thin Fracture, low Flow Rate and ong Duration Tracer Injection).

Annex A4

Pulse Test Interpretation

In this Annex the analisys of the pressure recovery curve obtained through the different pulse tests performed in the GAM fracture is presented. On the left hand column the automatic calibration based on Barker Solution taking into acccount two different hypothesys: fixing (thin line) or estimating (bold line) $S_{W.}$. On the right hand side the manual calibration match reported by Wyss (1996) using Cooper's type curves.

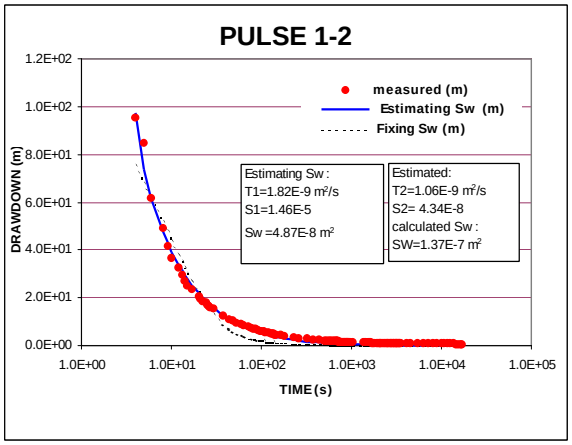

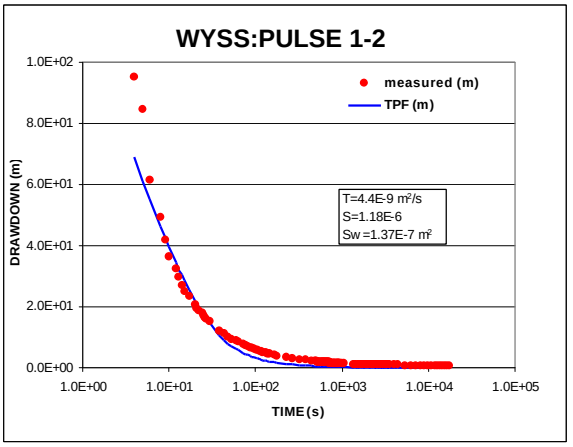

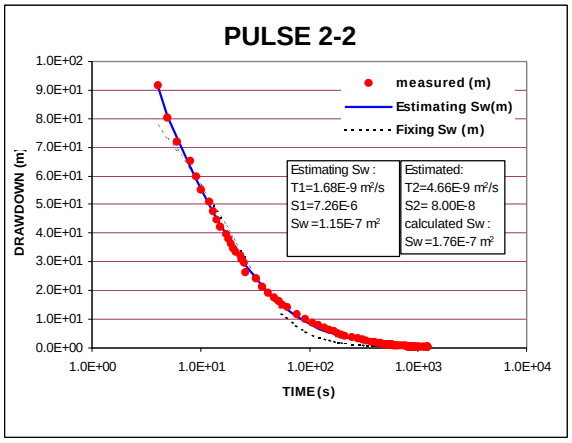

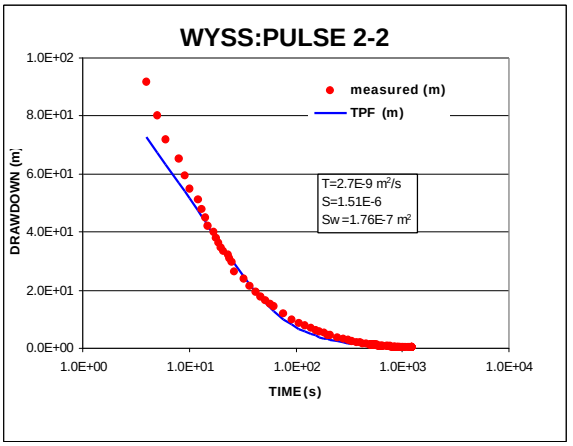

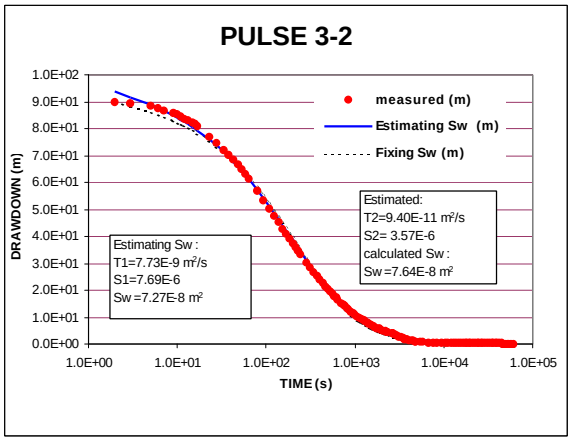

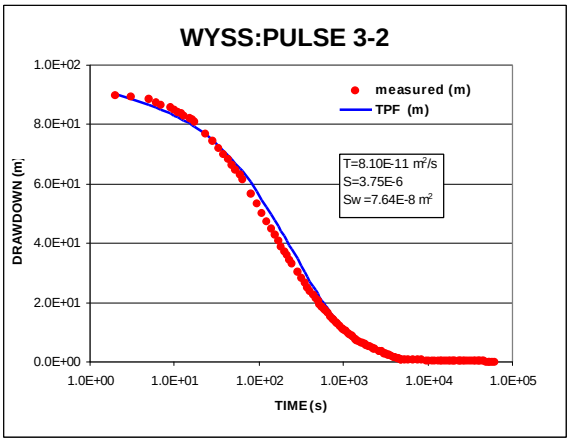

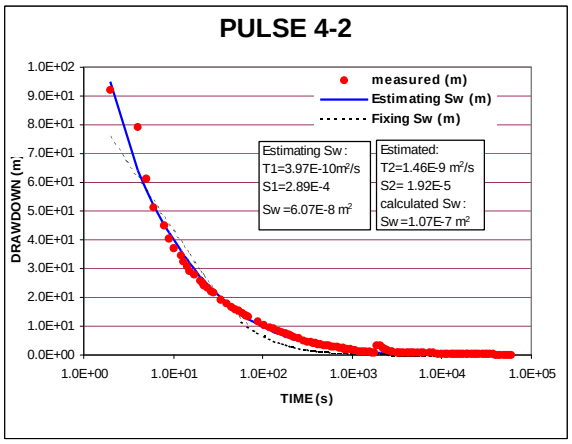
PULSE 4-2
measured (m)
Estimating Sw (m)
Fixing Sw (m)
Estimating Sw :
T1=3.97E-10m²/s
S1=2.89E-4
Sw =6.07E-8 m²
Estimated:
T2=1.46E-9 m²/s
S2= 1.92E-5
calculated Sw :
Sw =1.07E-7 m²
DRAWDOWN (m)
TIME (s)

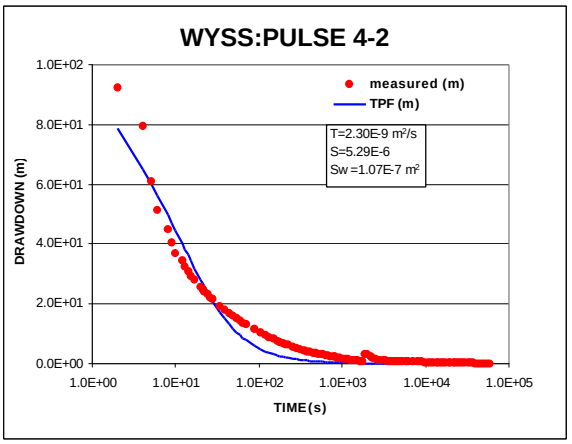
WYSS:PULSE 4-2
measured (m)
TPF (m)
T=2.30E-9 m²/s
S=5.29E-6
Sw =1.07E-7 m²
DRAWDOWN (m)
TIME (s)

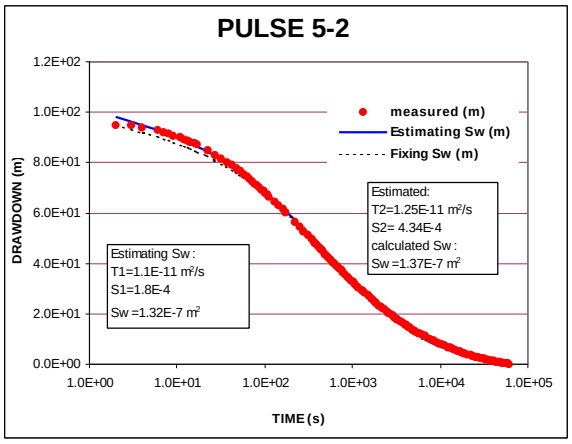
PULSE 5-2
measured (m)
Estimating Sw (m)
Fixing Sw (m)
Estimated:
T2=1.25E-11 m²/s
S2= 4.34E-4
calculated Sw :
Sw =1.37E-7 m²
Estimating Sw :
T1=1.1E-11 m²/s
S1=1.8E-4
Sw =1.32E-7 m²
DRAWDOWN (m)
TIME (s)

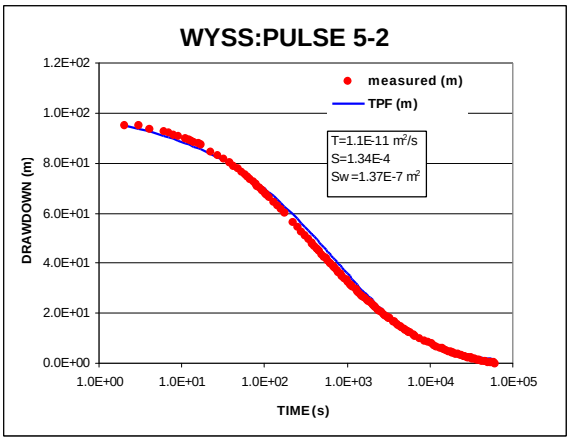
WYSS:PULSE 5-2
measured (m)
TPF (m)
T=1.1E-11 m²/s
S=1.34E-4
Sw =1.37E-7 m²
DRAWDOWN (m)
TIME (s)

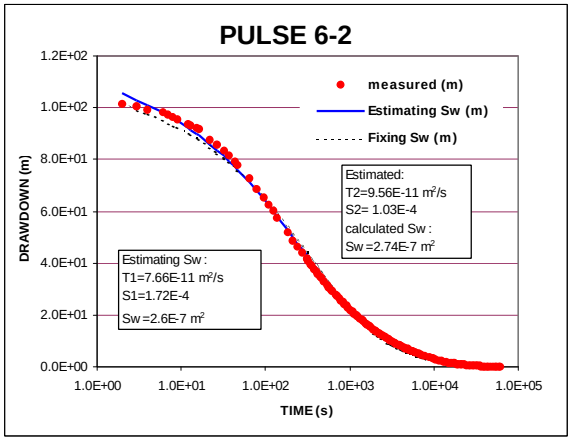
PULSE 6-2
measured (m)
Estimating Sw (m)
Fixing Sw (m)
Estimated:
T2=9.56E-11 m²/s
S2= 1.03E-4
calculated Sw :
Sw =2.74E-7 m²
Estimating Sw :
T1=7.66E-11 m²/s
S1=1.72E-4
Sw =2.6E-7 m²
DRAWDOWN (m)
TIME (s)

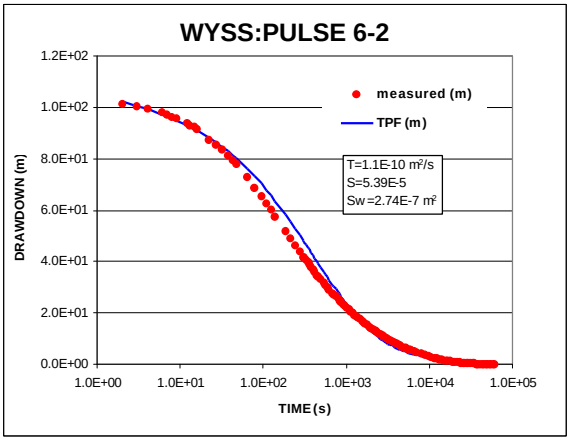
WYSS:PULSE 6-2
measured (m)
TPF (m)
T=1.1E-10 m²/s
S=5.39E-5
Sw =2.74E-7 m²
DRAWDOWN (m)
TIME (s)

Annex A5

Constant Rate Injection Test Interpretation
Jacob's semi-logarithmic approximation

Semi-log plot of the computed drawdown (red line) through the conventional interpretation (automatic calibration adjusting the parameters corresponding to Theis solution, using MARIAJ code) of the drawdown measured data (blue dots), obtained for every observation point used in each hydraulic (constant **R**ate **I**njection) test performed in the framework of the GAM project (**RI1**, **RI2**, **RI3**, **RI4**).

RI1

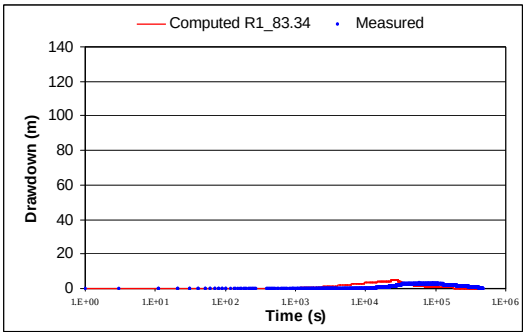

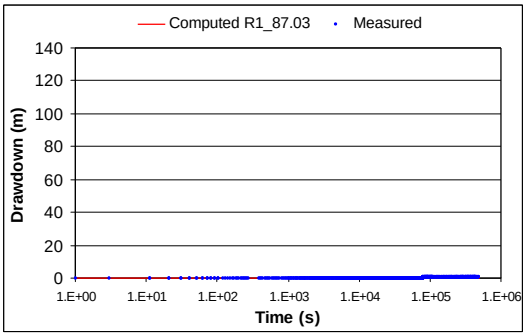

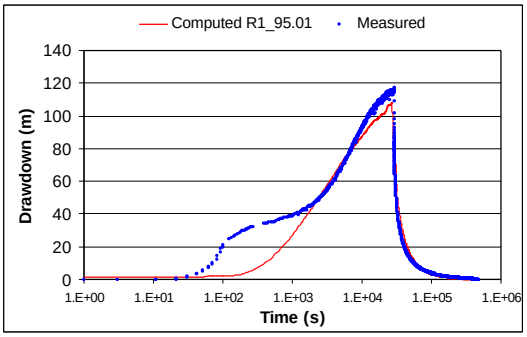

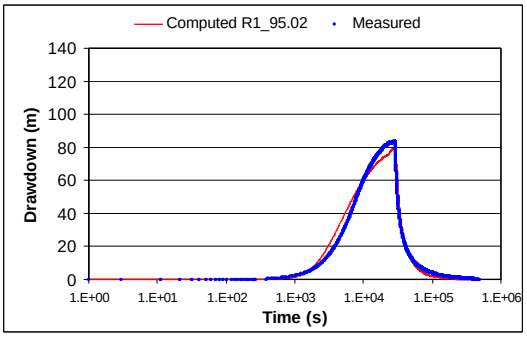

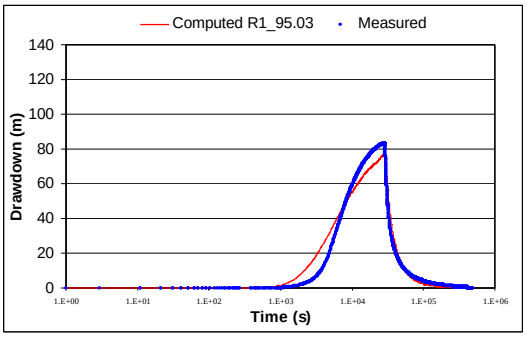

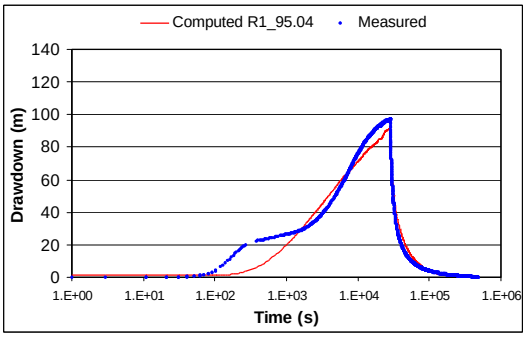

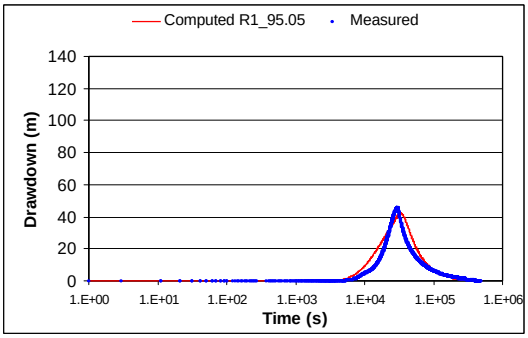
Computed R1_95.05
Measured
Drawdown (m)
140
120
100
80
60
40
20
0
1.E+00
1.E+01
1.E+02
1.E+03
1.E+04
1.E+05
1.E+06
Time (s)

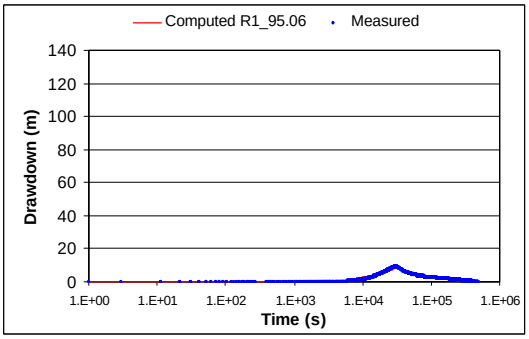
Computed R1_95.06
Measured
Drawdown (m)
140
120
100
80
60
40
20
0
1.E+00
1.E+01
1.E+02
1.E+03
1.E+04
1.E+05
1.E+06
Time (s)

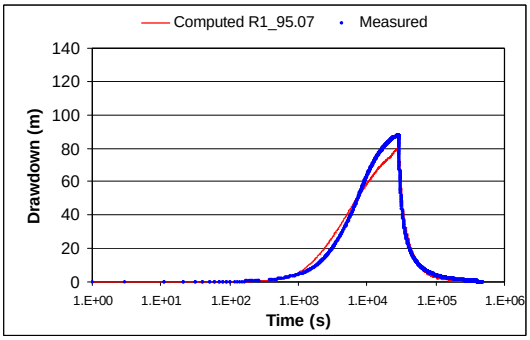
Computed R1_95.07
Measured
Drawdown (m)
140
120
100
80
60
40
20
0
1.E+00
1.E+01
1.E+02
1.E+03
1.E+04
1.E+05
1.E+06
Time (s)

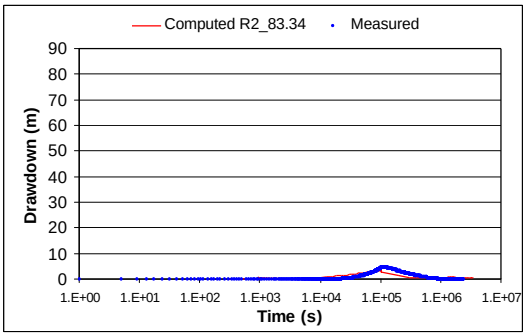
Computed R2_83.34
Measured
Drawdown (m)
Time (s)

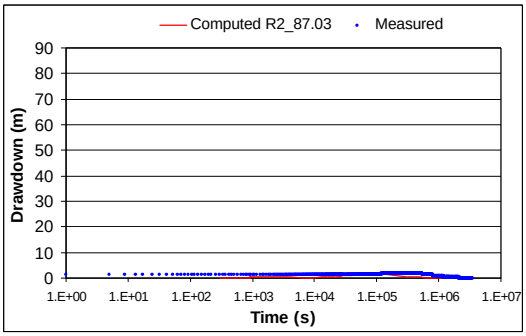
Computed R2_87.03
Measured
Drawdown (m)
Time (s)

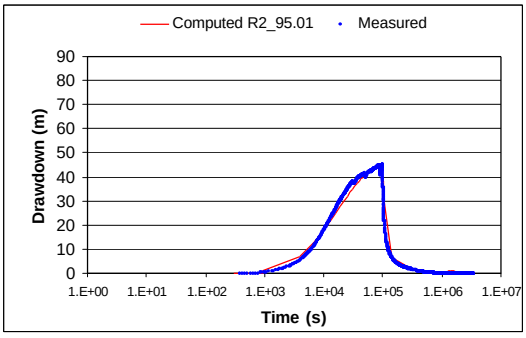
Computed R2_95.01
Measured
Drawdown (m)
Time (s)

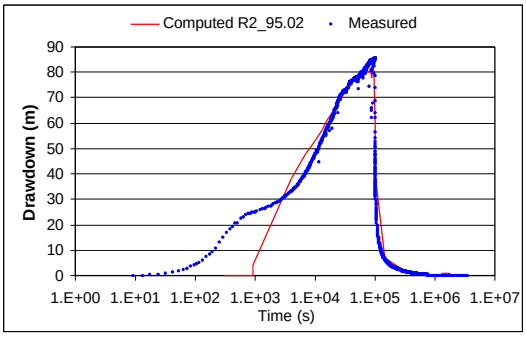
Computed R2_95.02
Measured
Drawdown (m)
Time (s)

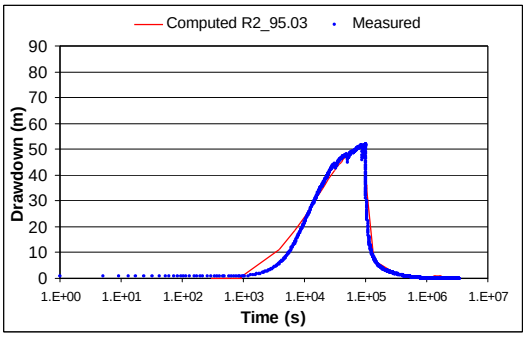
Computed R2_95.03
Measured
Drawdown (m)
Time (s)

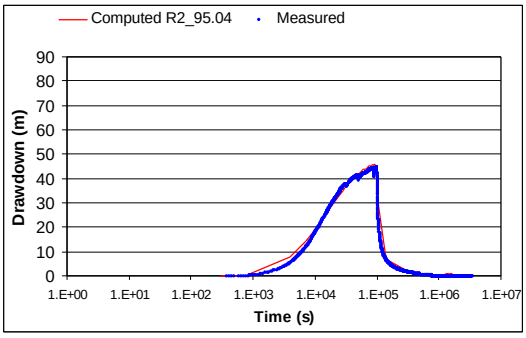
Computed R2_95.04
Measured
Drawdown (m)
Time (s)

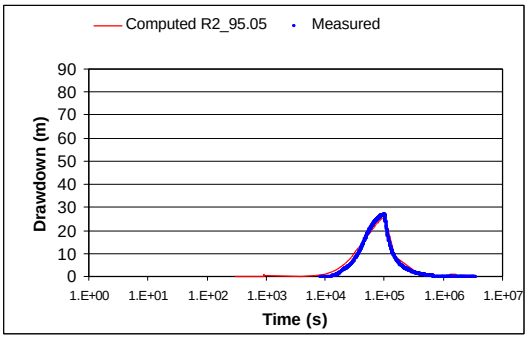
Computed R2_95.05
Measured
Drawdown (m)
Time (s)

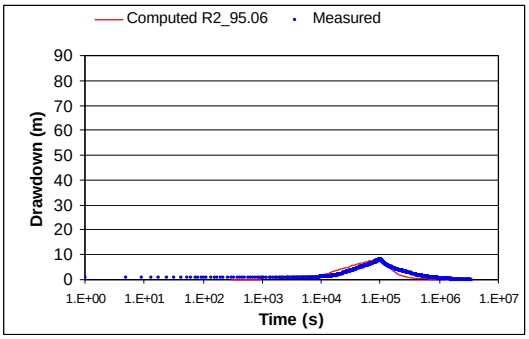
Computed R2_95.06
Measured
Drawdown (m)
Time (s)

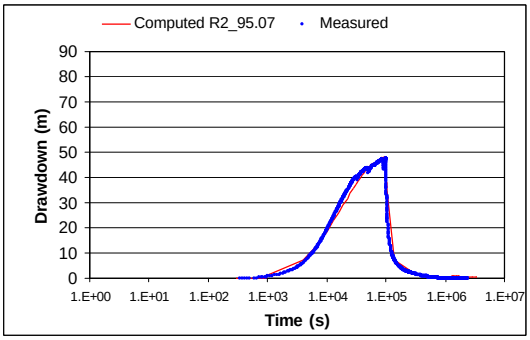
Computed R2_95.07
Measured
Drawdown (m)
90
80
70
60
50
40
30
20
10
0
1.E+00
1.E+01
1.E+02
1.E+03
1.E+04
1.E+05
1.E+06
1.E+07
Time (s)

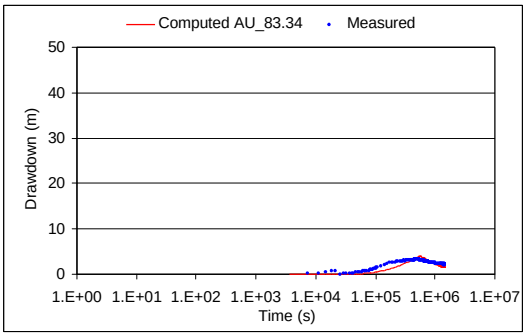
Computed AU_83.34
Measured
Drawdown (m)
0
10
20
30
40
50
1.E+00 1.E+01 1.E+02 1.E+03 1.E+04 1.E+05 1.E+06 1.E+07
Time (s)

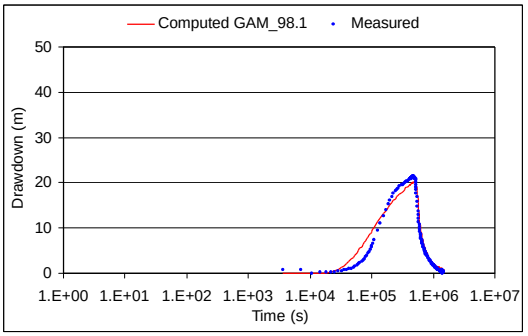
Computed GAM_98.1
Measured
Drawdown (m)
0
10
20
30
40
50
1.E+00 1.E+01 1.E+02 1.E+03 1.E+04 1.E+05 1.E+06 1.E+07
Time (s)

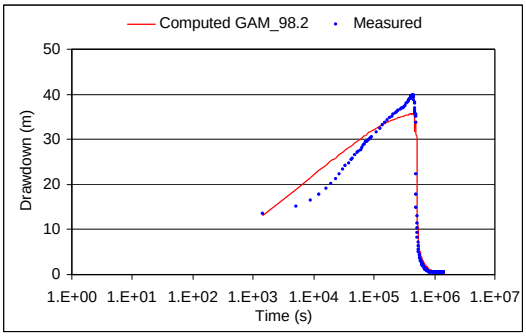
Computed GAM_98.2
Measured
Drawdown (m)
0
10
20
30
40
50
1.E+00 1.E+01 1.E+02 1.E+03 1.E+04 1.E+05 1.E+06 1.E+07
Time (s)

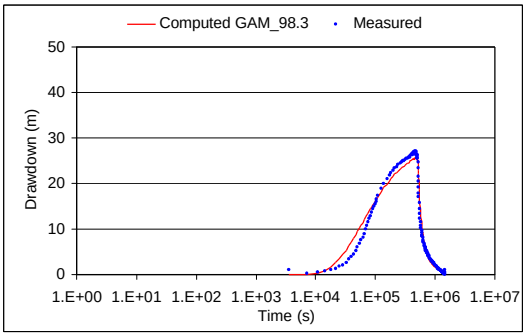
Computed GAM_98.3
Measured
Drawdown (m)
0
10
20
30
40
50
1.E+00 1.E+01 1.E+02 1.E+03 1.E+04 1.E+05 1.E+06 1.E+07
Time (s)

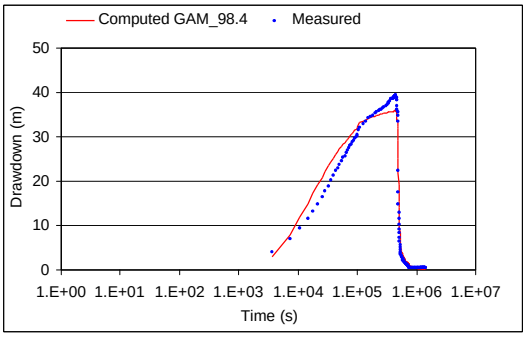
Computed GAM_98.4
Measured
Drawdown (m)
0
10
20
30
40
50
1.E+00 1.E+01 1.E+02 1.E+03 1.E+04 1.E+05 1.E+06 1.E+07
Time (s)

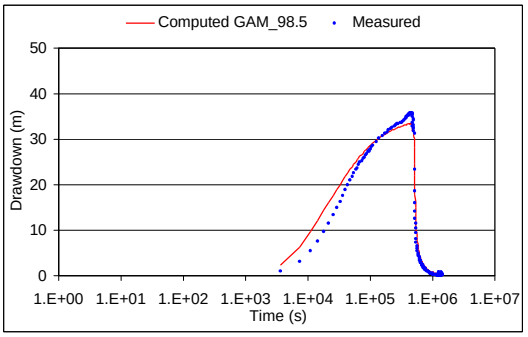
Computed GAM_98.5
Measured
Drawdown (m)
0
10
20
30
40
50
1.E+00 1.E+01 1.E+02 1.E+03 1.E+04 1.E+05 1.E+06 1.E+07
Time (s)

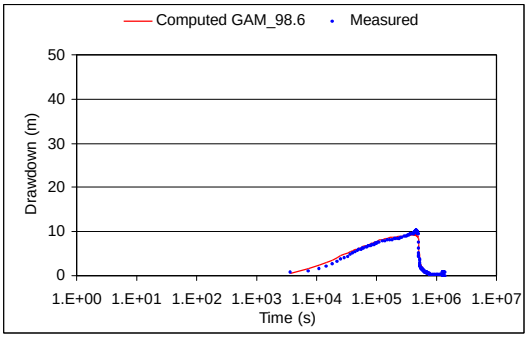
Computed GAM_98.6
Measured
Drawdown (m)
0
10
20
30
40
50
1.E+00 1.E+01 1.E+02 1.E+03 1.E+04 1.E+05 1.E+06 1.E+07
Time (s)

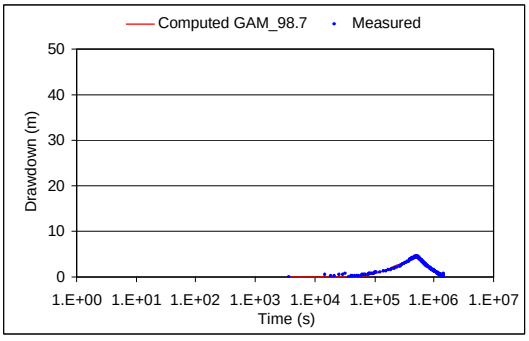
Computed GAM_98.7
Measured
Drawdown (m)
0
10
20
30
40
50
1.E+00 1.E+01 1.E+02 1.E+03 1.E+04 1.E+05 1.E+06 1.E+07
Time (s)

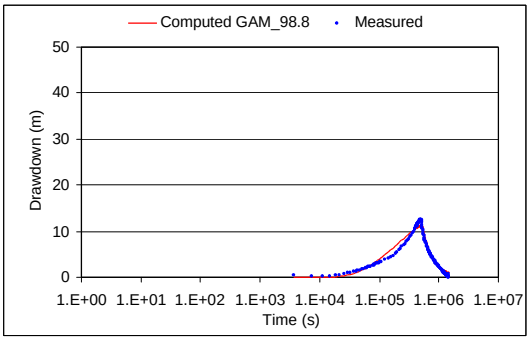
Computed GAM_98.8
Measured
Drawdown (m)
0
10
20
30
40
50
1.E+00 1.E+01 1.E+02 1.E+03 1.E+04 1.E+05 1.E+06 1.E+07
Time (s)

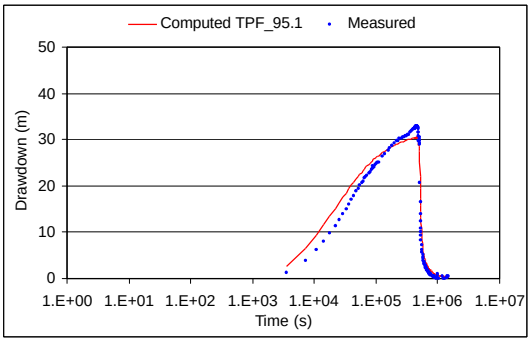
Computed TPF_95.1
Measured
Drawdown (m)
0
10
20
30
40
50
1.E+00 1.E+01 1.E+02 1.E+03 1.E+04 1.E+05 1.E+06 1.E+07
Time (s)

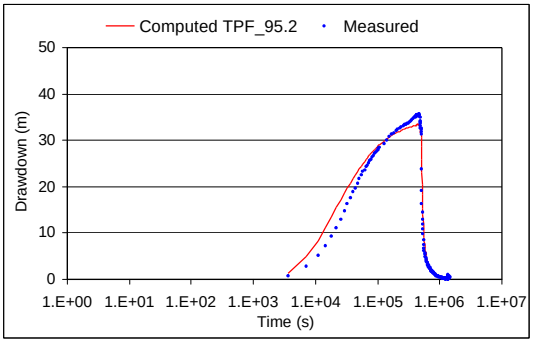
Computed TPF_95.2
Measured
Drawdown (m)
0
10
20
30
40
50
1.E+00 1.E+01 1.E+02 1.E+03 1.E+04 1.E+05 1.E+06 1.E+07
Time (s)

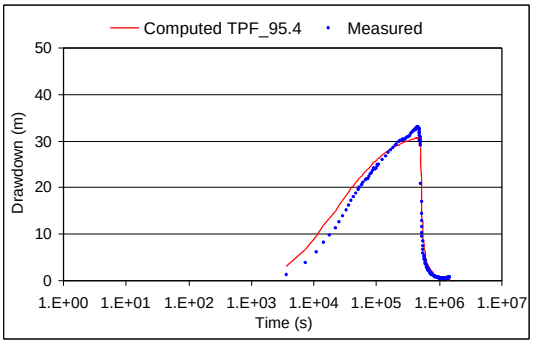
Computed TPF_95.4
Measured
Drawdown (m)
0
10
20
30
40
50
1.E+00 1.E+01 1.E+02 1.E+03 1.E+04 1.E+05 1.E+06 1.E+07
Time (s)

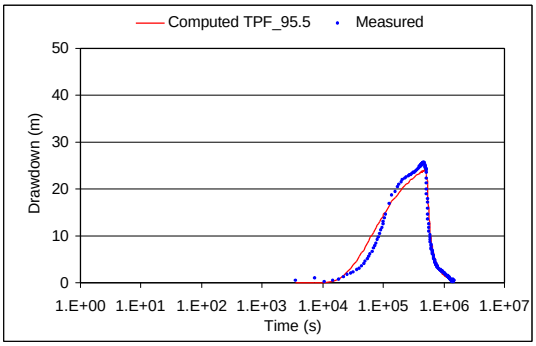
Computed TPF_95.5
Measured
Drawdown (m)
0
10
20
30
40
50
1.E+00 1.E+01 1.E+02 1.E+03 1.E+04 1.E+05 1.E+06 1.E+07
Time (s)

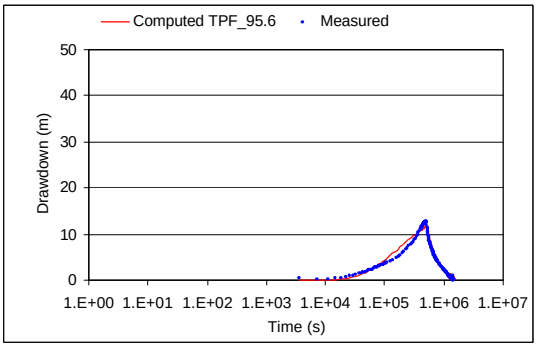
Computed TPF_95.6
Measured
Drawdown (m)
0
10
20
30
40
50
1.E+00 1.E+01 1.E+02 1.E+03 1.E+04 1.E+05 1.E+06 1.E+07
Time (s)

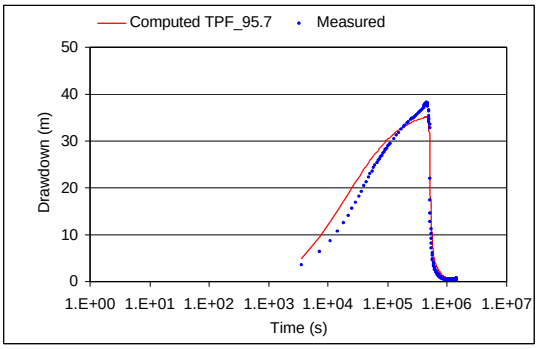
Computed TPF_95.7
Measured
Drawdown (m)
0
10
20
30
40
50
1.E+00 1.E+01 1.E+02 1.E+03 1.E+04 1.E+05 1.E+06 1.E+07
Time (s)

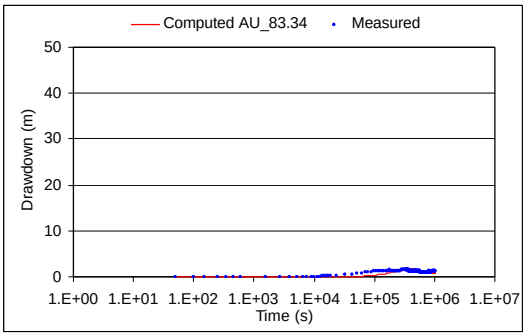
Computed AU_83.34
Measured
Drawdown (m)
0
10
20
30
40
50
1.E+00 1.E+01 1.E+02 1.E+03 1.E+04 1.E+05 1.E+06 1.E+07
Time (s)

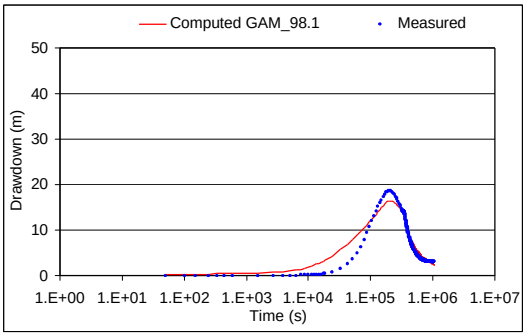
Computed GAM_98.1
Measured
Drawdown (m)
0
10
20
30
40
50
1.E+00 1.E+01 1.E+02 1.E+03 1.E+04 1.E+05 1.E+06 1.E+07
Time (s)

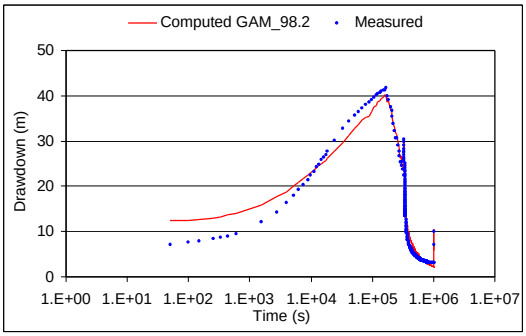
Computed GAM_98.2
Measured
Drawdown (m)
0
10
20
30
40
50
1.E+00 1.E+01 1.E+02 1.E+03 1.E+04 1.E+05 1.E+06 1.E+07
Time (s)

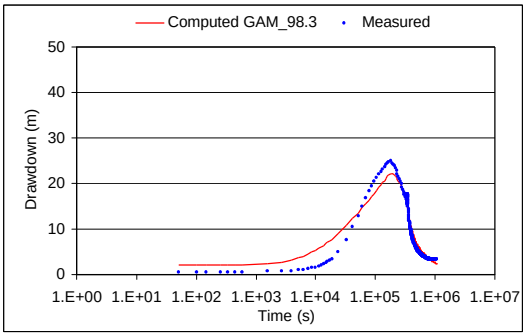
Computed GAM_98.3
Measured
Drawdown (m)
0
10
20
30
40
50
1.E+00 1.E+01 1.E+02 1.E+03 1.E+04 1.E+05 1.E+06 1.E+07
Time (s)

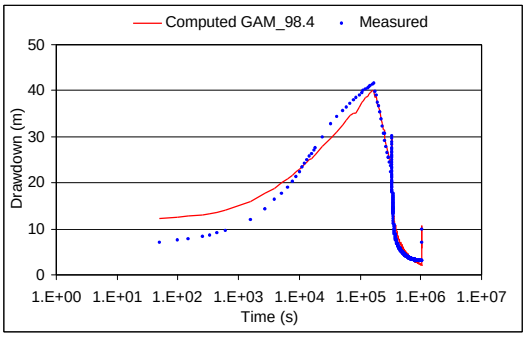
Computed GAM_98.4
Measured
Drawdown (m)
0
10
20
30
40
50
1.E+00 1.E+01 1.E+02 1.E+03 1.E+04 1.E+05 1.E+06 1.E+07
Time (s)

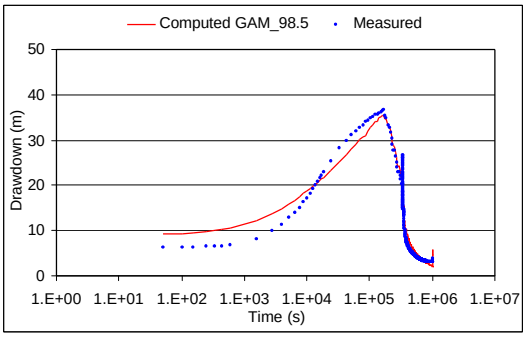
Computed GAM_98.5
Measured
Drawdown (m)
0
10
20
30
40
50
1.E+00 1.E+01 1.E+02 1.E+03 1.E+04 1.E+05 1.E+06 1.E+07
Time (s)

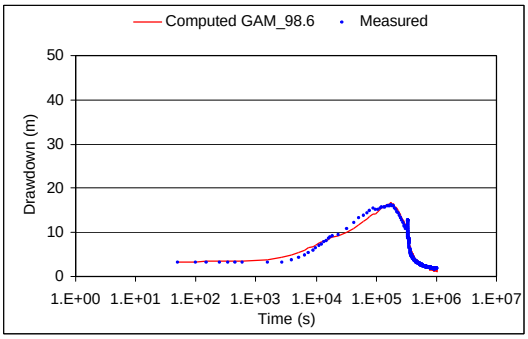
Computed GAM_98.6
Measured
Drawdown (m)
0
10
20
30
40
50
1.E+00 1.E+01 1.E+02 1.E+03 1.E+04 1.E+05 1.E+06 1.E+07
Time (s)

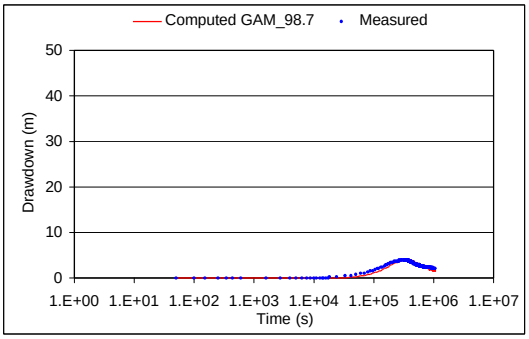
Computed GAM_98.7
Measured
Drawdown (m)
0
10
20
30
40
50
1.E+00 1.E+01 1.E+02 1.E+03 1.E+04 1.E+05 1.E+06 1.E+07
Time (s)

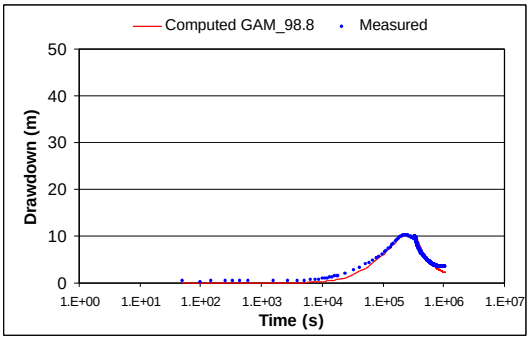
Computed GAM_98.8
Measured
Drawdown (m)
0
10
20
30
40
50
1.E+00
1.E+01
1.E+02
1.E+03
1.E+04
1.E+05
1.E+06
1.E+07
Time (s)

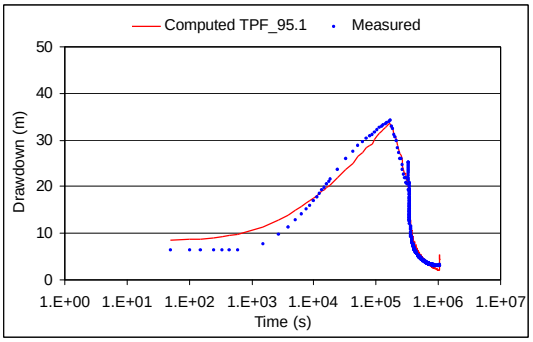
Computed TPF_95.1
Measured
Drawdown (m)
0
10
20
30
40
50
1.E+00
1.E+01
1.E+02
1.E+03
1.E+04
1.E+05
1.E+06
1.E+07
Time (s)

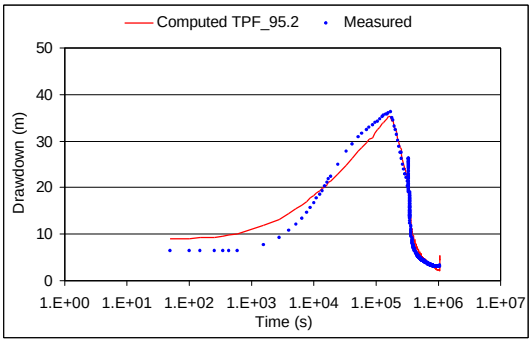
Computed TPF_95.2
Measured
Drawdown (m)
0
10
20
30
40
50
1.E+00
1.E+01
1.E+02
1.E+03
1.E+04
1.E+05
1.E+06
1.E+07
Time (s)

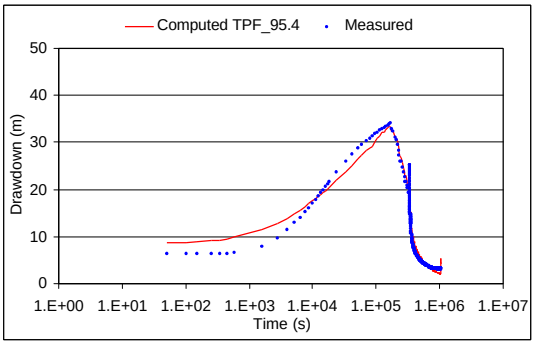
Computed TPF_95.4
Measured
Drawdown (m)
0
10
20
30
40
50
1.E+00
1.E+01
1.E+02
1.E+03
1.E+04
1.E+05
1.E+06
1.E+07
Time (s)

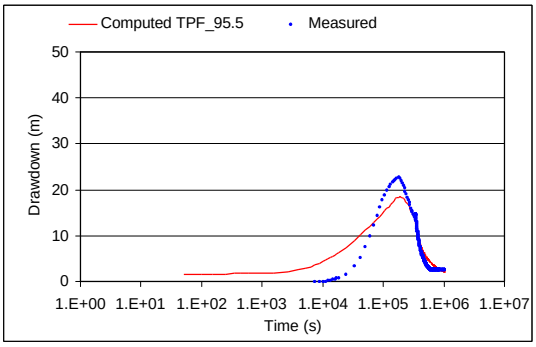
Computed TPF_95.5
Measured
Drawdown (m)
0
10
20
30
40
50
1.E+00
1.E+01
1.E+02
1.E+03
1.E+04
1.E+05
1.E+06
1.E+07
Time (s)

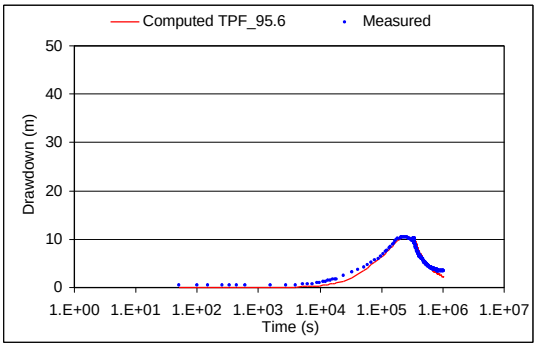
Computed TPF_95.6
Measured
Drawdown (m)
0
10
20
30
40
50
1.E+00
1.E+01
1.E+02
1.E+03
1.E+04
1.E+05
1.E+06
1.E+07
Time (s)

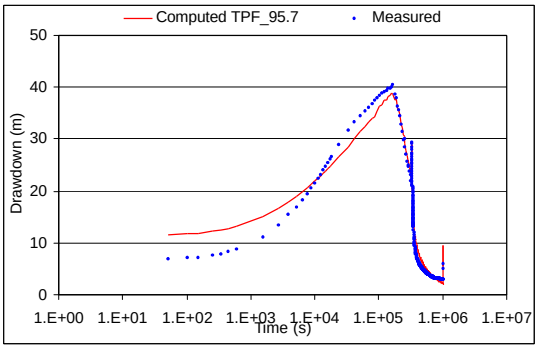
Computed TPF_95.7
Measured
Drawdown (m)
0
10
20
30
40
50
1.E+00
1.E+01
1.E+02
1.E+03
1.E+04
1.E+05
1.E+06
1.E+07
Time (s)

Annex A6

Geostatistical Inversion
Joint Cros-hole Interpretation of Ri1-RI2-RI3-RI4

In this annex measured (red dots) and computed (blue line) cross-hole drawdown data for the different pumping tests considered in the joint geostatistical inversion performed for different geostatistical hypothesis on the T field structure are depicted. Four different hydraulic tests (RI1 to RI4) are jointly considered. The geostatistical inversion was performed using TRANSIN-II code.

The results are presented in terms of the accounted T field. In all cases an exponential variogram was considered, with the same sill but different T correlation lengths R_x and R_y (i.e. correlation length in X and Y directions respectively), pointed in the upper right corner of every sheet, and expressed in terms of the correlation ratios R_x/R_y, that is: [0.4m/0.4m], [0.8m/0.4m], [0.8m/0.8m], [1.6m/0.4m], [1.6m/0.8m], [1.6m/1.6m], [3.2m/0.4m], [3.2m/0.8m], [3.2m/1.6m] and [3.2m/3.2m].

The obtained fits are presented in Lineal-Lineal and Semi-Log plot scales (left hand side and right hand side respectively).

RI1

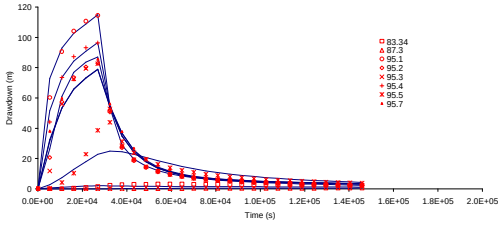

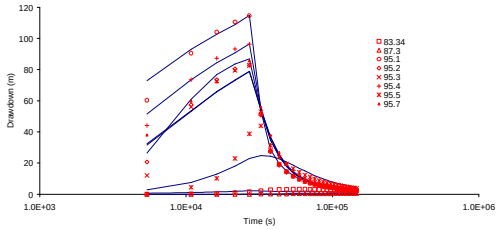

RI2

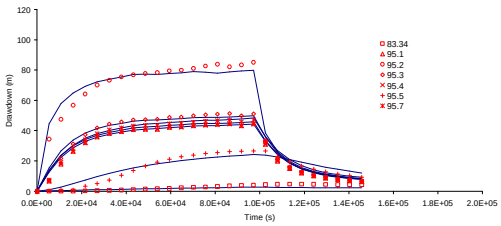

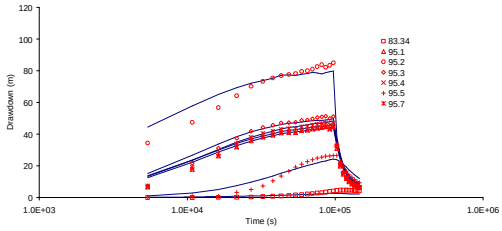

RI3

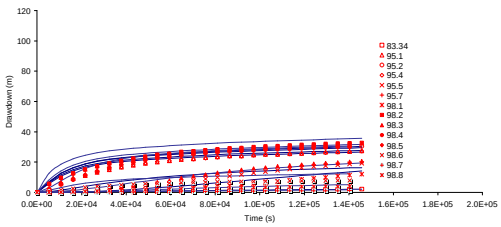

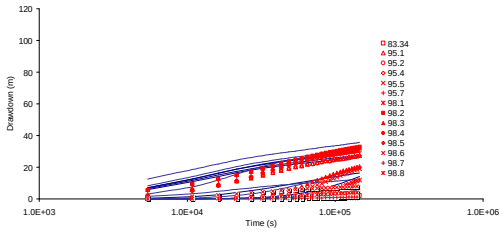

RI4

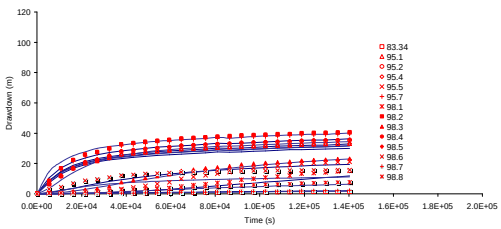

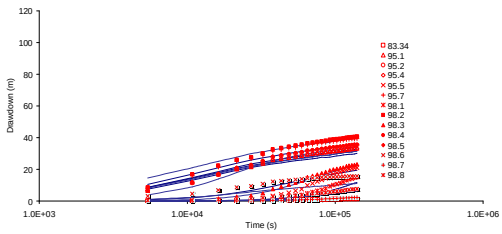

RI1

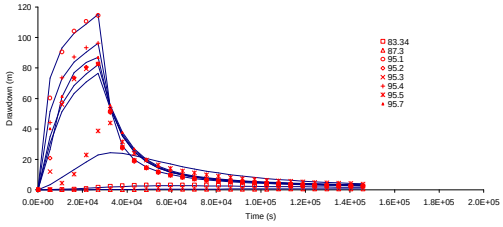

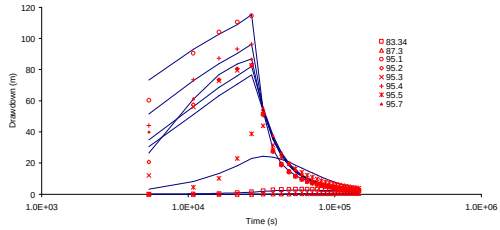

RI2

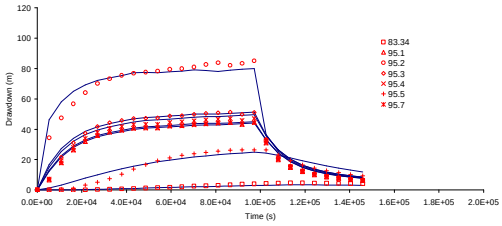

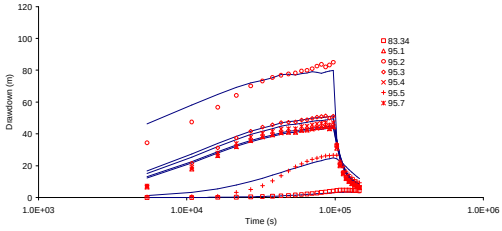

RI3

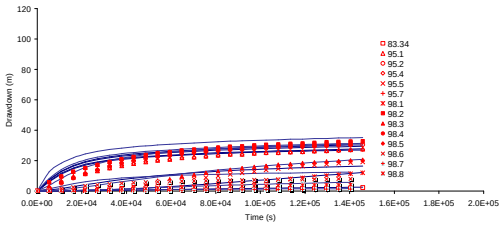

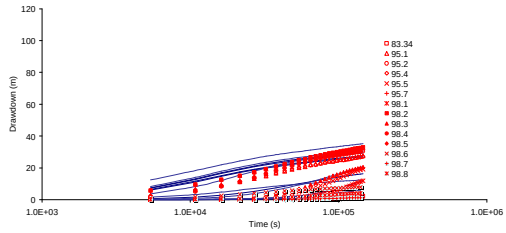

RI4

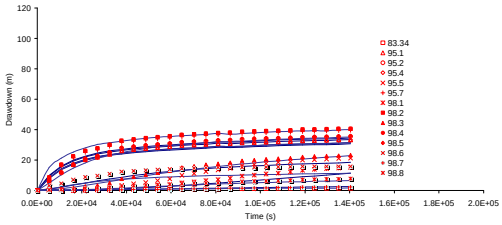

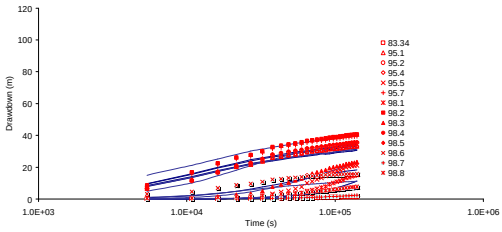

RI1

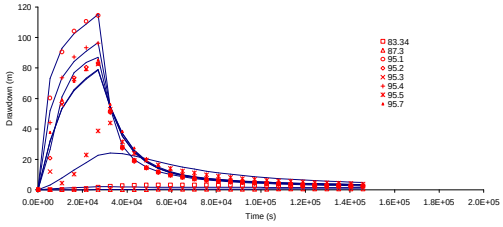

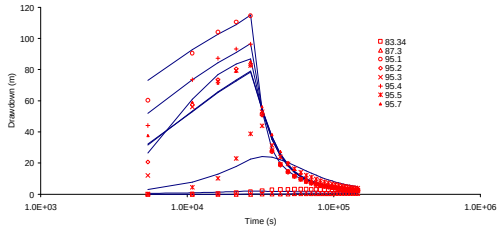

RI2

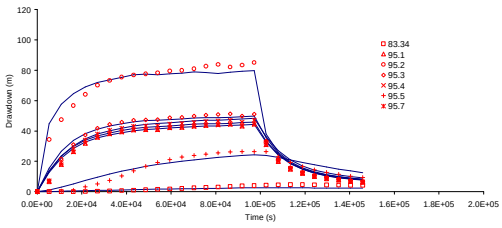

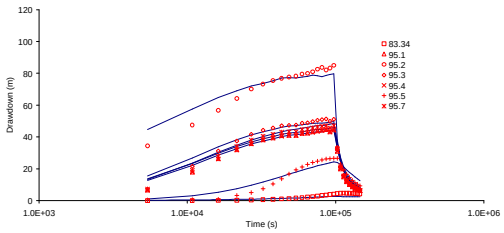

RI3

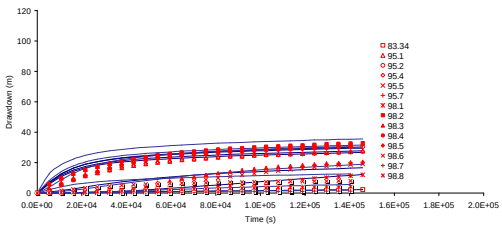

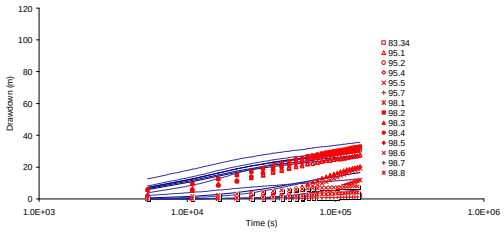

RI4

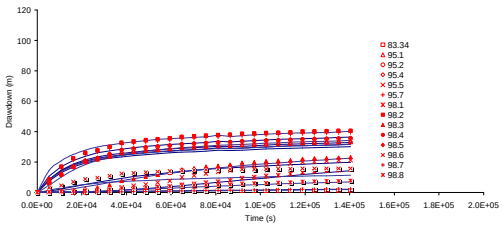

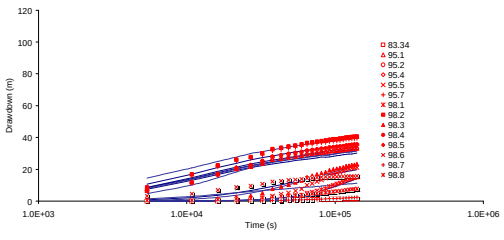

RI1

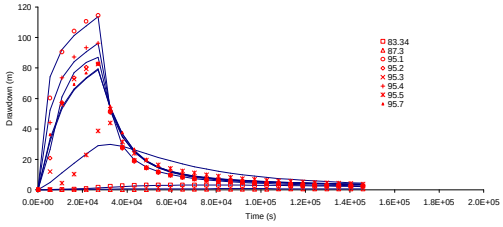

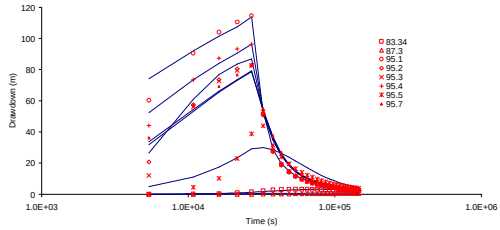

RI2

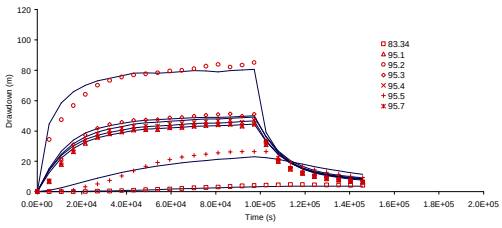

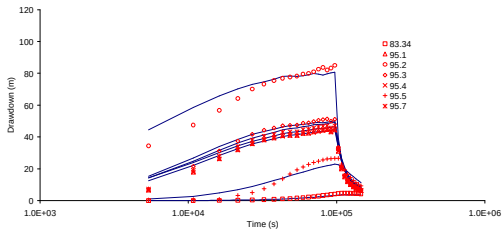

RI3

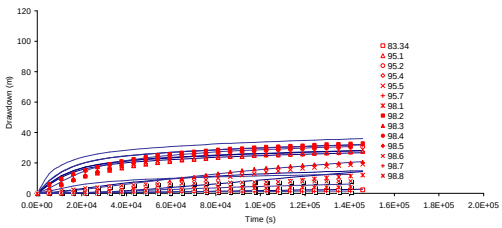

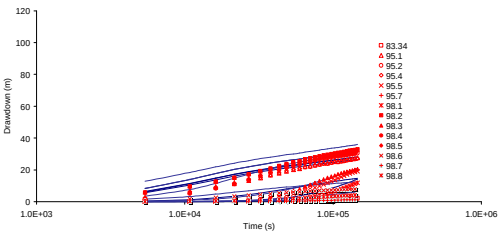

RI4

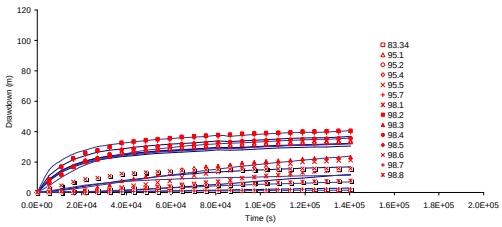

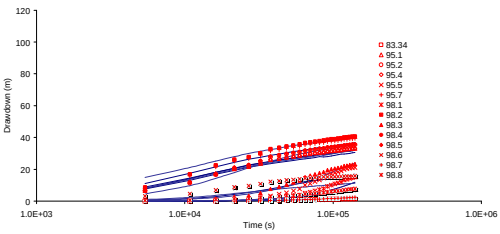

RI1

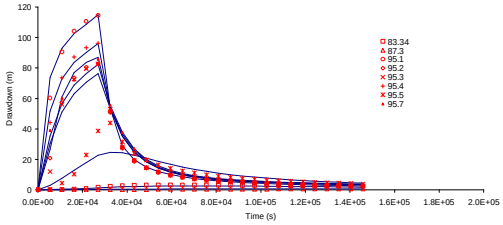

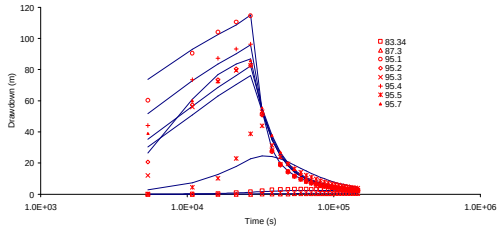

RI2

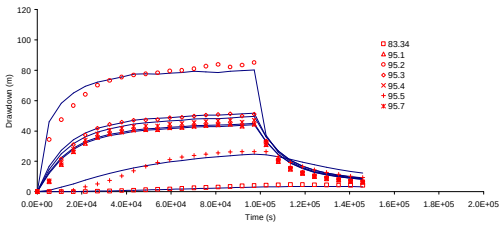

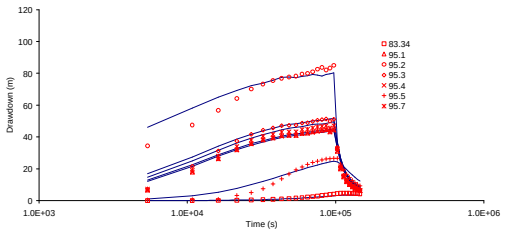

RI3

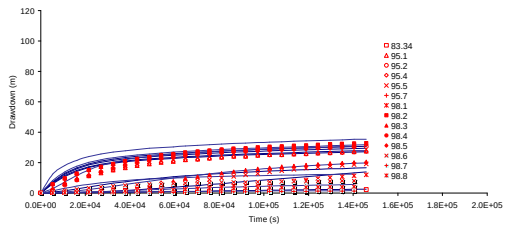

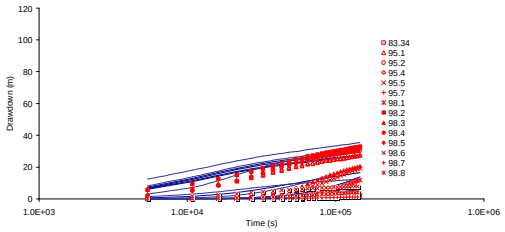

RI4

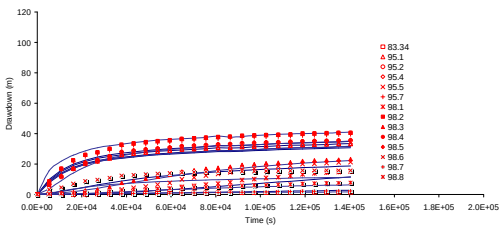

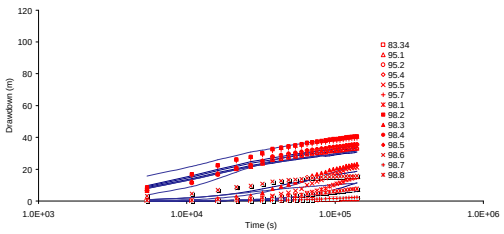

RI1

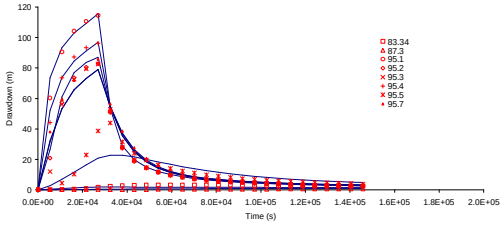

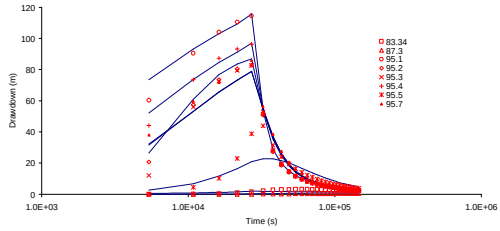

RI2

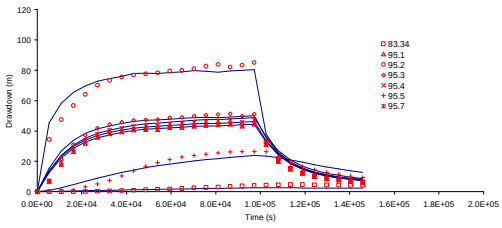

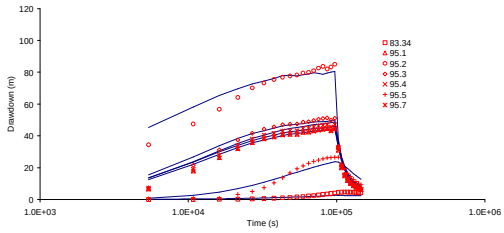

RI3

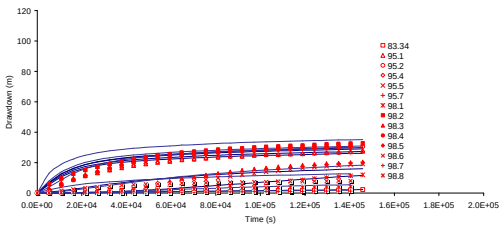

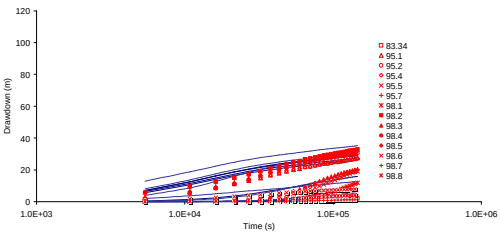

RI4

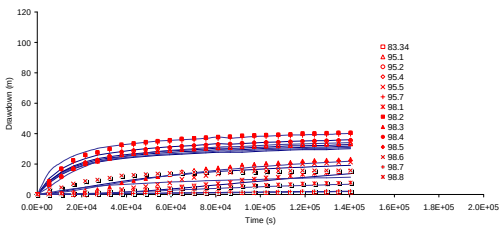

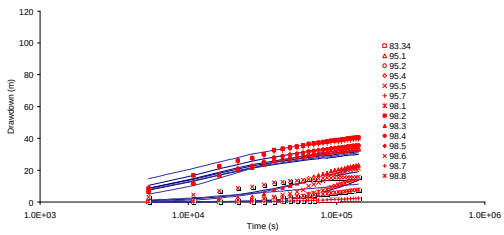

RI1

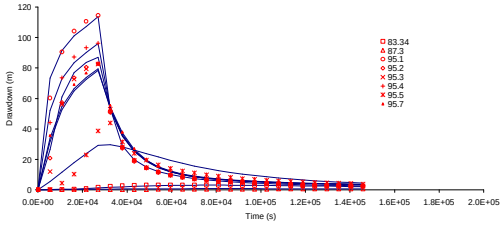

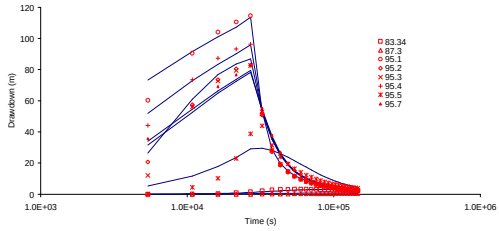

RI2

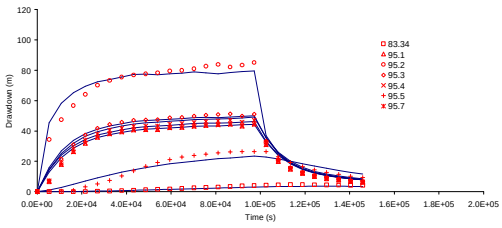

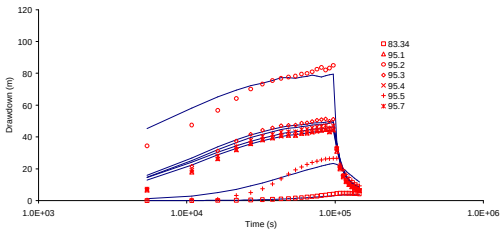

RI3

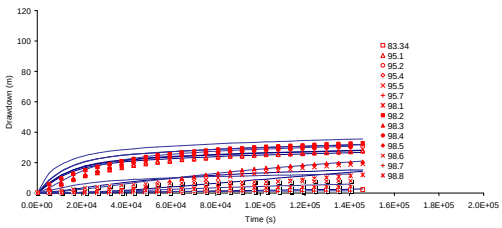

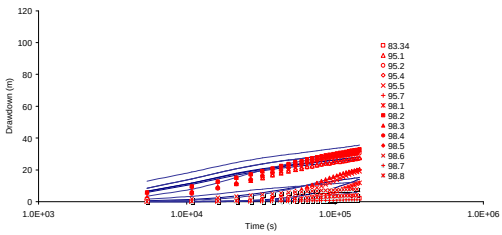

RI4

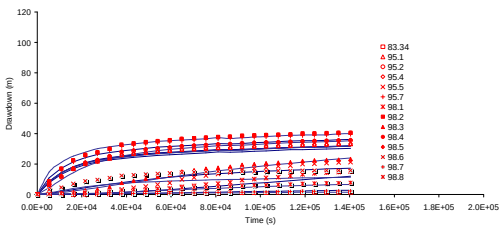

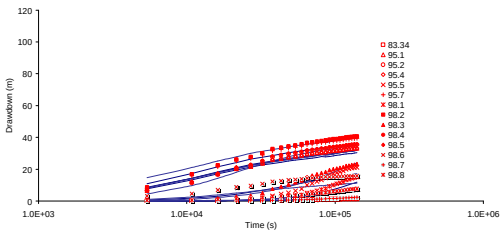

RI1

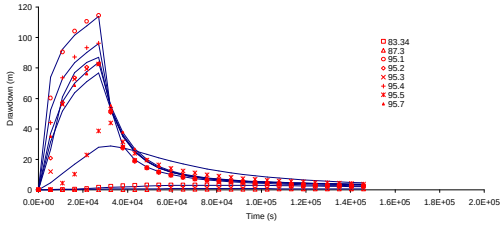

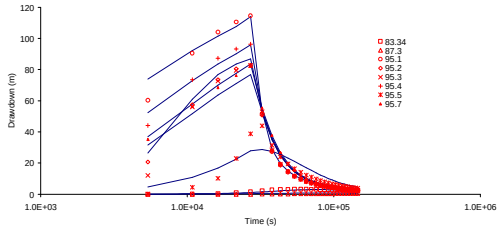

RI2

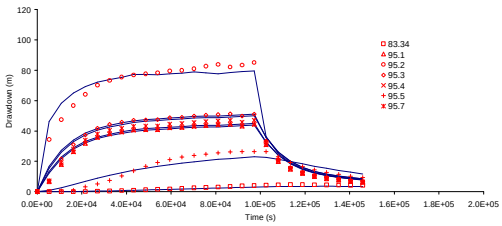

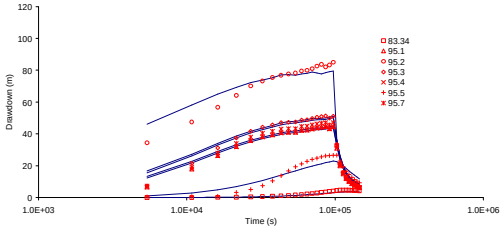

RI3

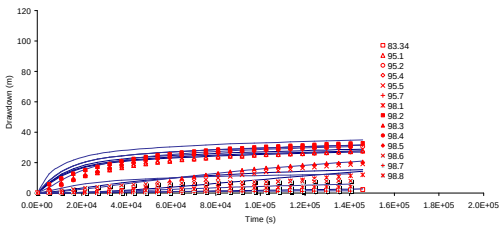

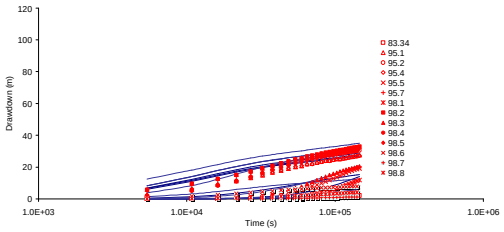

RI4

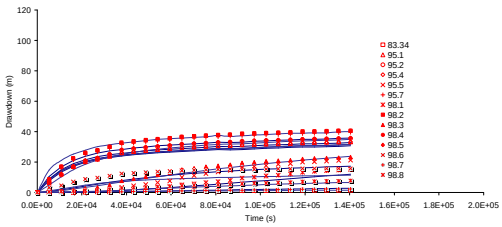

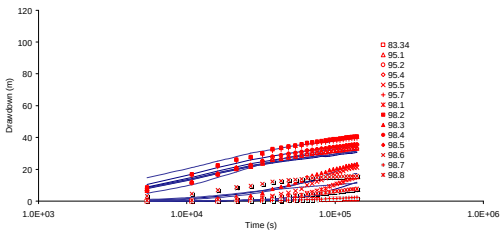

RI1

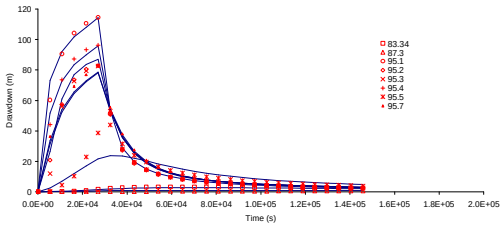

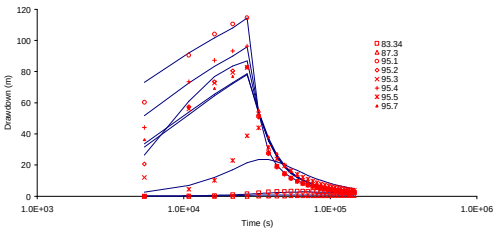

RI2

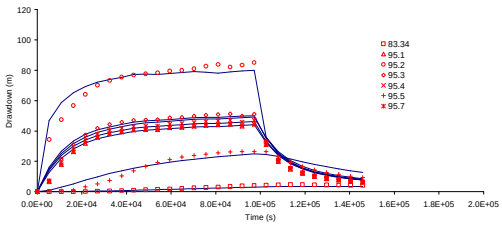

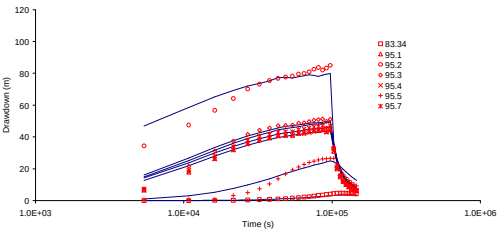

RI3

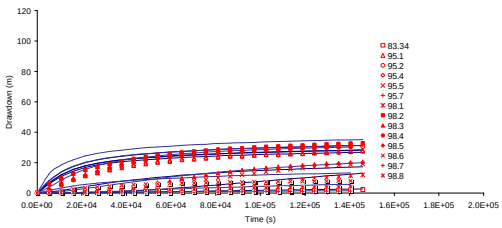

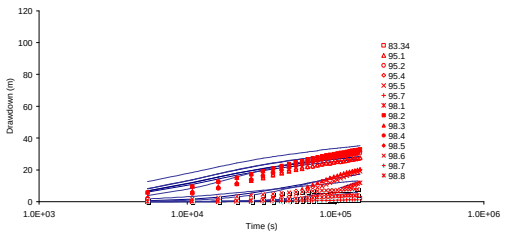

RI4

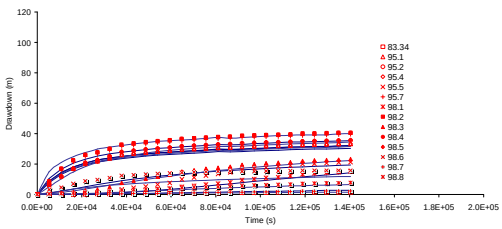

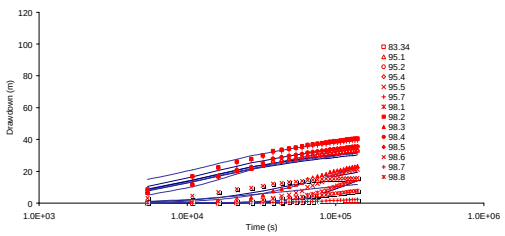

RI1

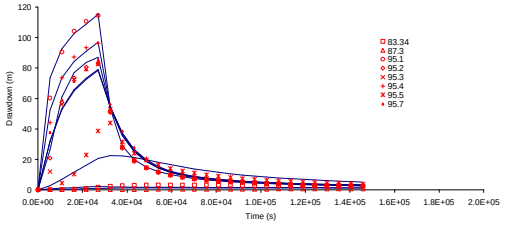

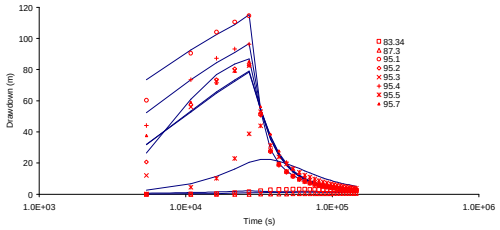

RI2

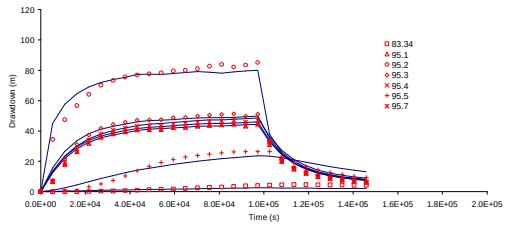

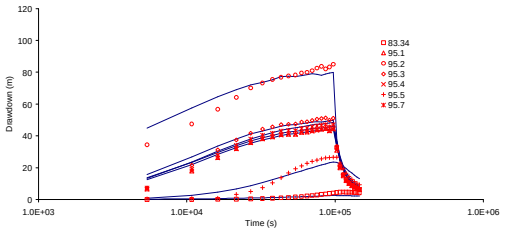

RI3

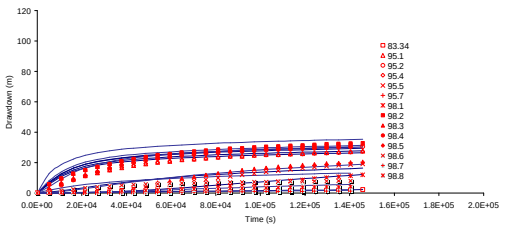

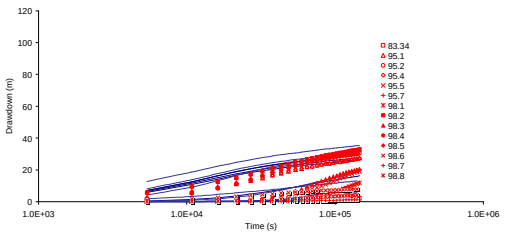

RI4

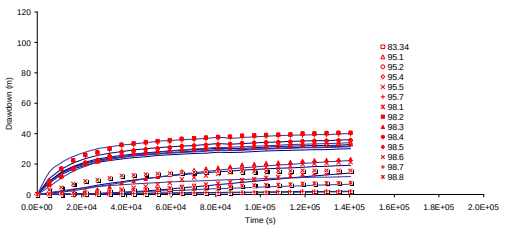

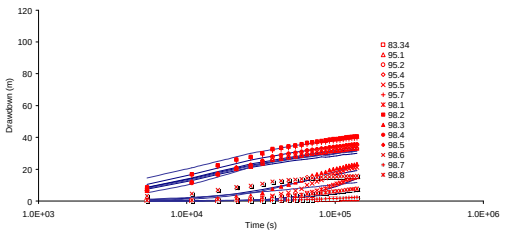

Annex A7

Tracer Test Calibration
Joint Interpretation of PT1-PT2-PT3-PT4

In this annex measured (red dots) and computed breakthrough curves coming from the **joint interpretation** of the four tracer test **PT1**, **PT2**, **PT3**, **PT4** are depicted. The results are presented in terms of the accounted T field (expressed in terms of the correlation ratios R_x/R_y and pointed in the upper right corner of every sheet). For the same T field there are two sets of computed breakthrough curves, depending if the transport model accounts (MD) or not (NMD) for matrix diffusion.

For every breakthrough curve set (i.e. selected T field and selected or not matrix diffusion) three different fracture models are considered: FFC (red line), FFNC (blue dashed line), OF (green dashed line). The obtained fits are presented in Lineal-Lineal and Log-Log plot scales (left hand side and right hand side respectively).

0.4 / 0.4 NMD

PT1

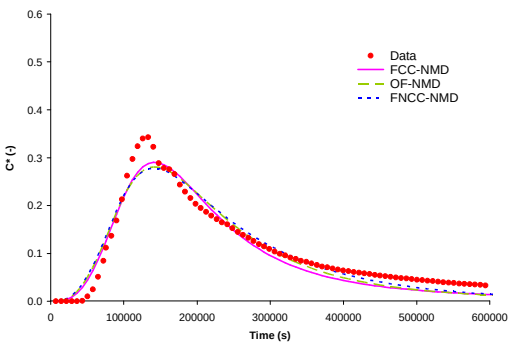

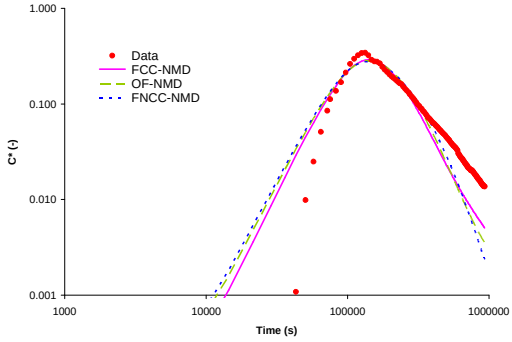

PT2

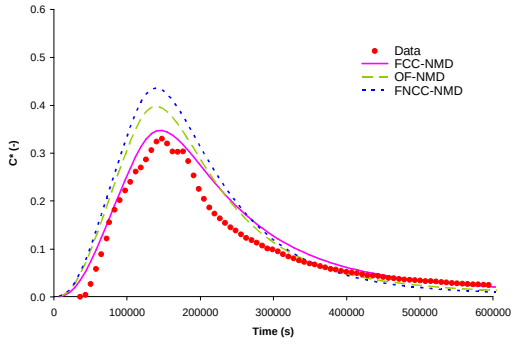

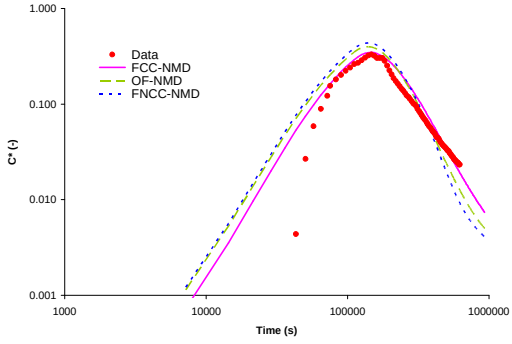

PT3

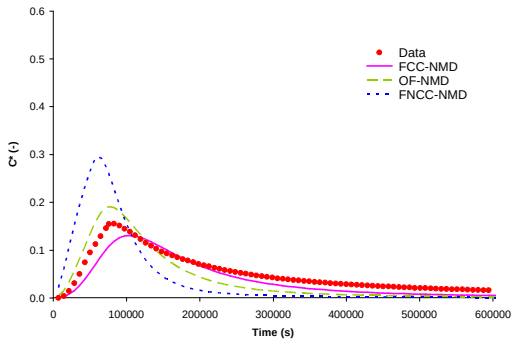

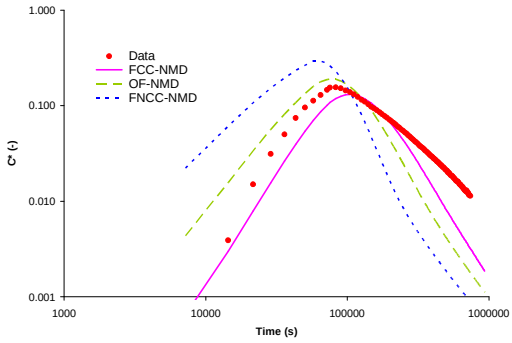

PT4

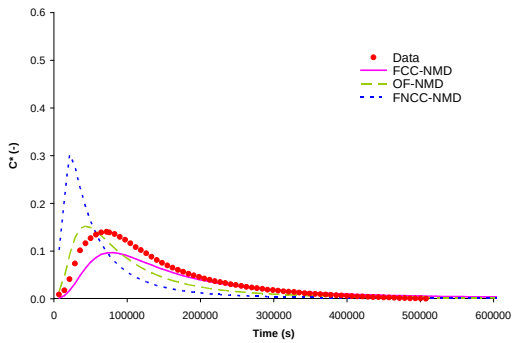

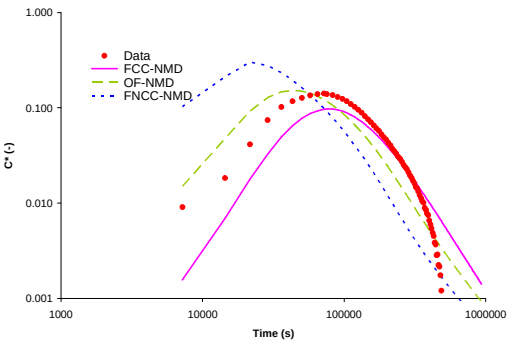

0.4 / 0.4 MD

PT1

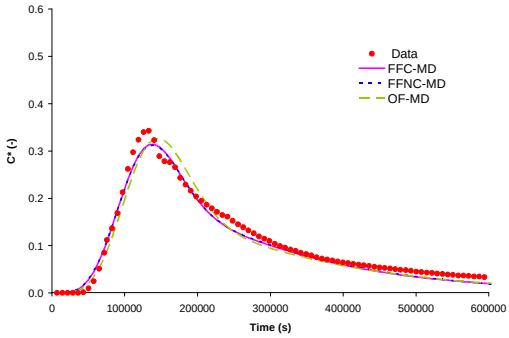

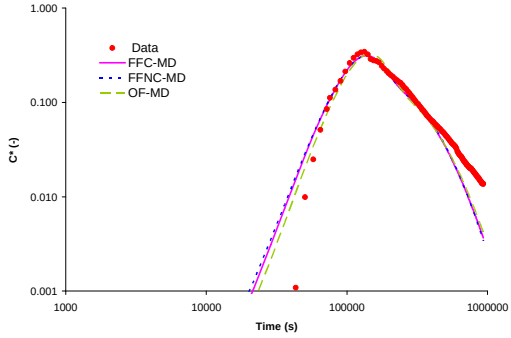

PT2

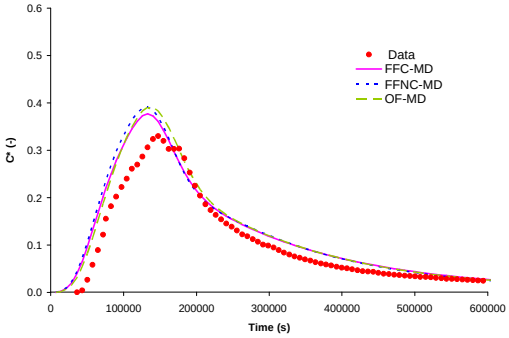

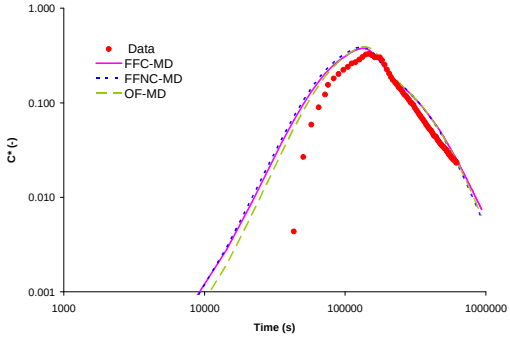

PT3

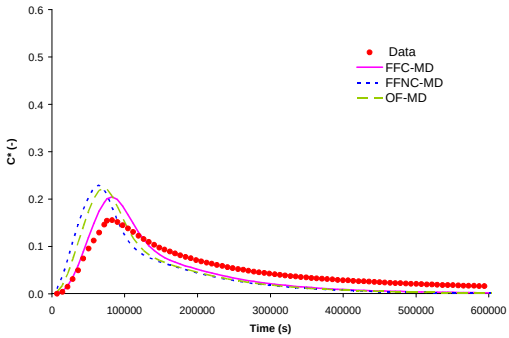

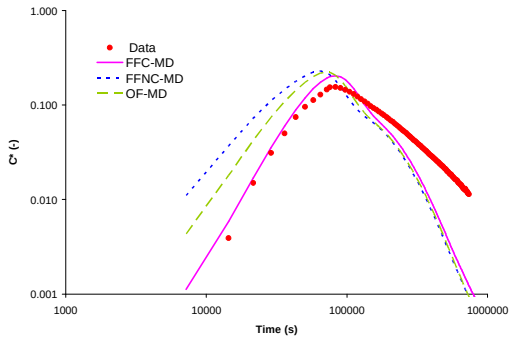

PT4

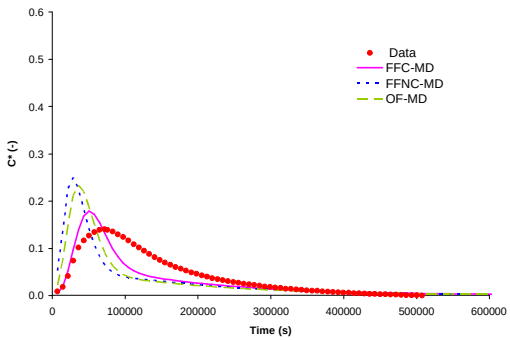

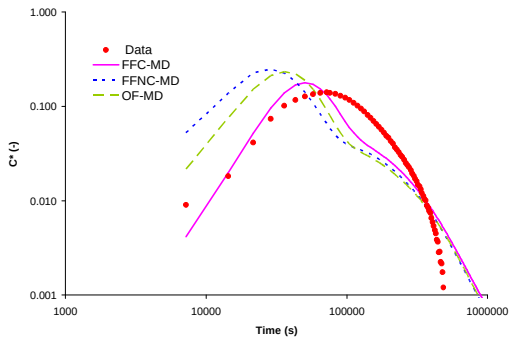

0.8 / 0.4 NMD

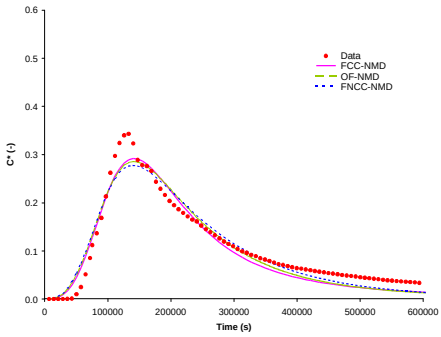

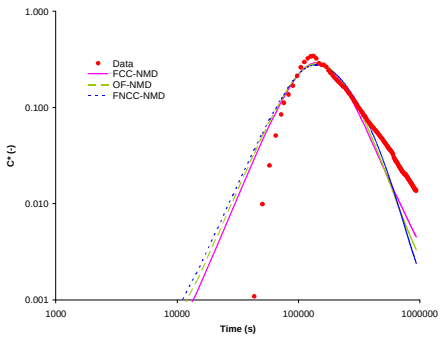

PT1

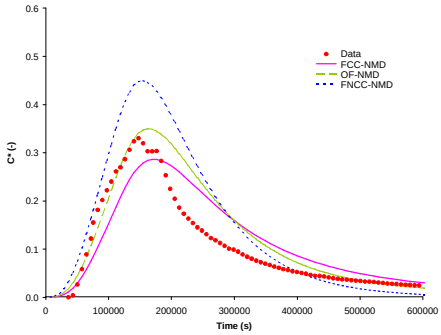

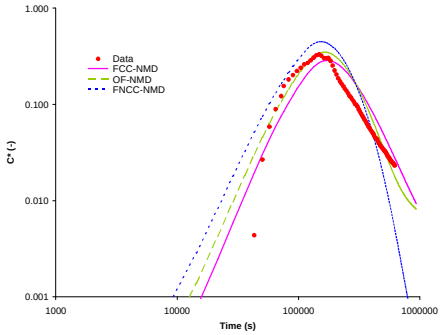

PT2

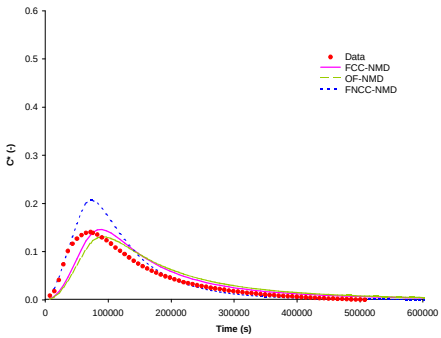

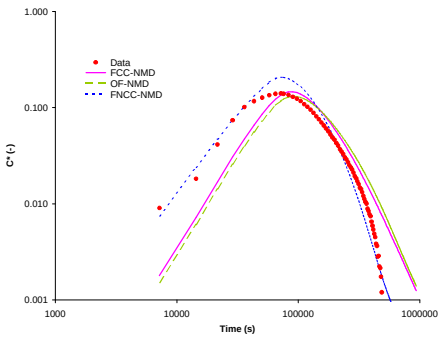

PT3

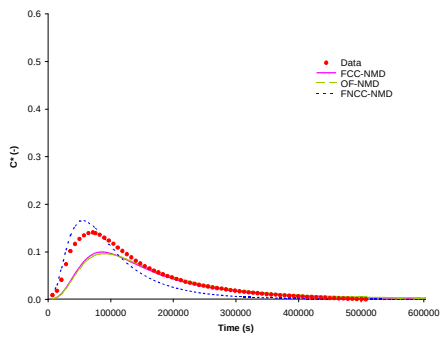

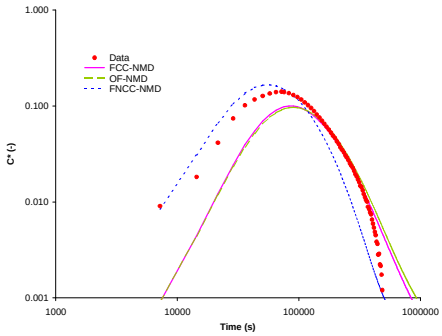

PT4

0.8 / 0.4 MD

PT1

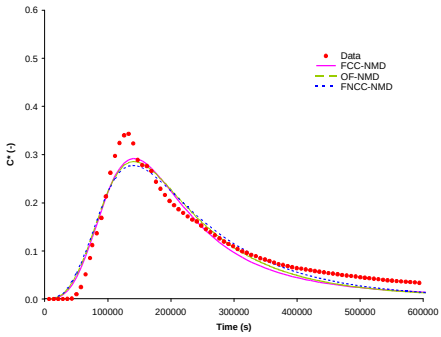

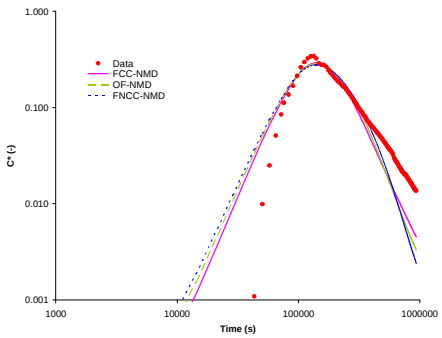

PT2

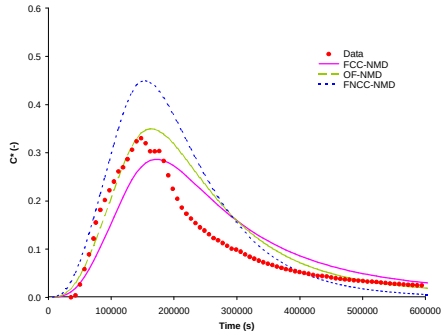

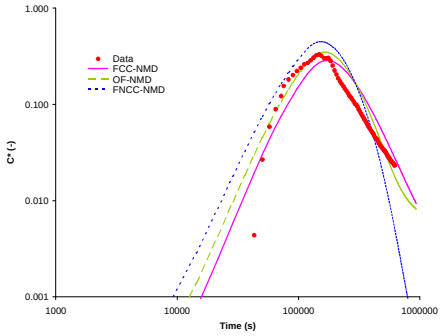

PT3

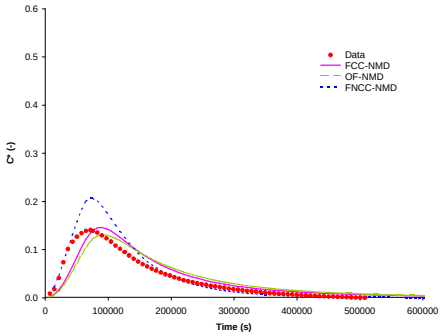

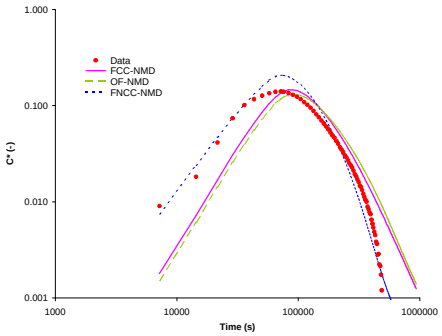

PT4

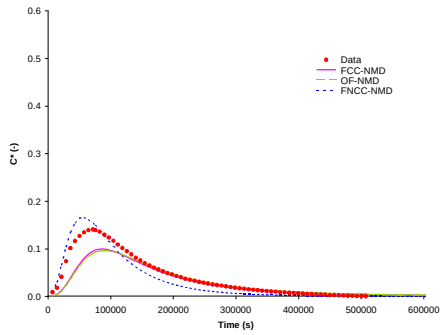

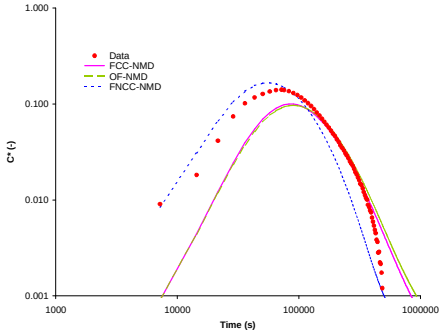

0.8 / 0.8 NMD

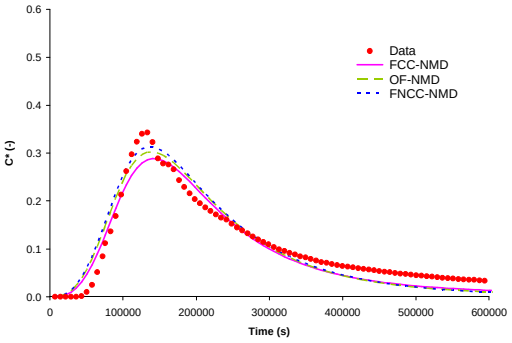

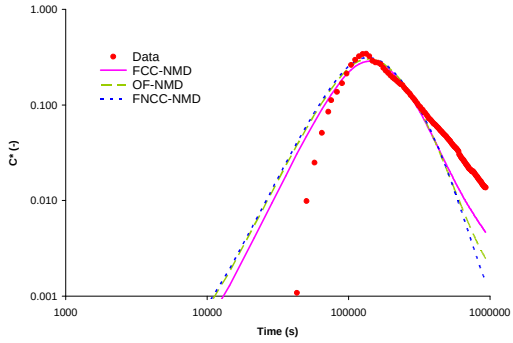

PT1

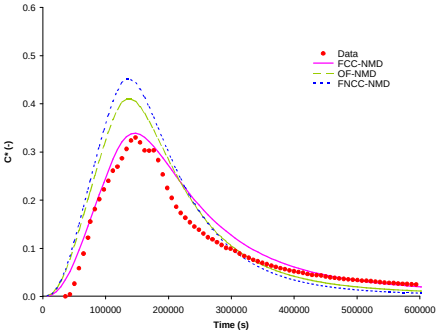

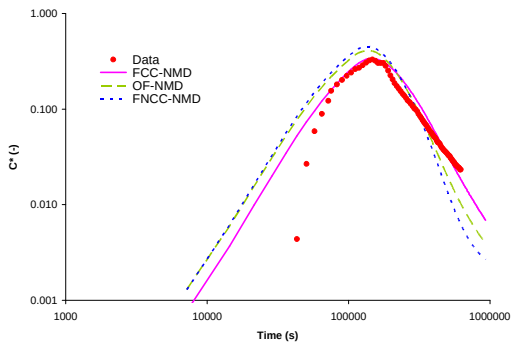

PT2

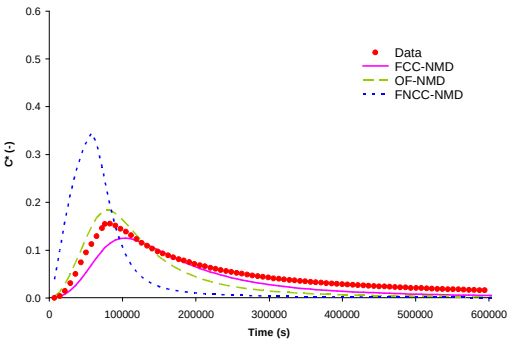

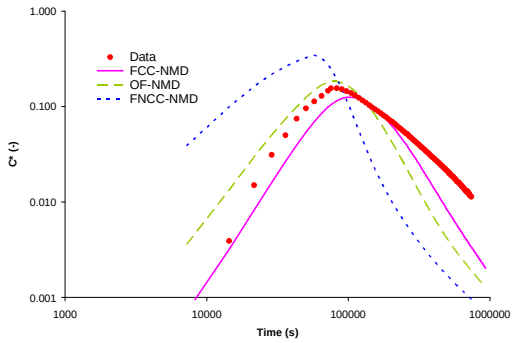

PT3

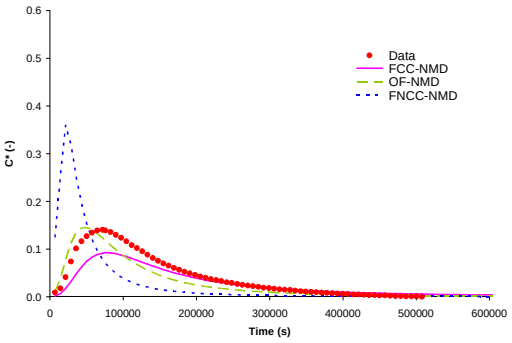

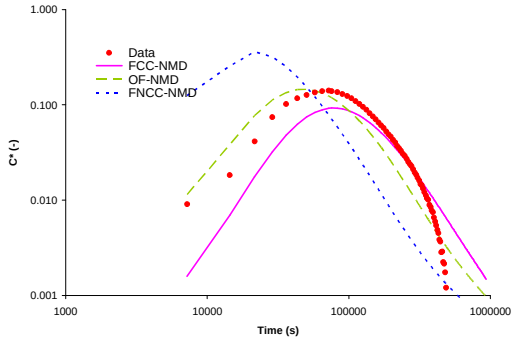

PT4

0.8 / 0.8 MD

PT1

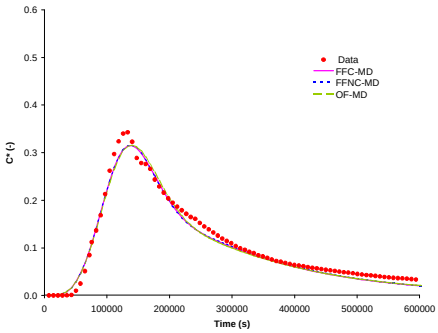

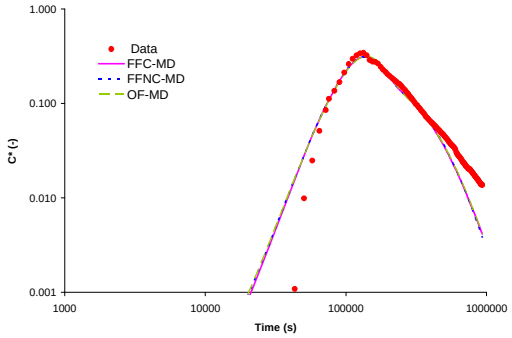

PT2

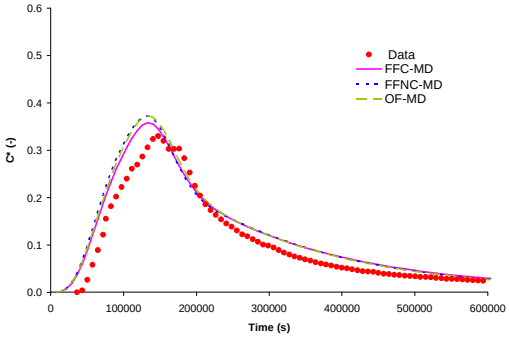

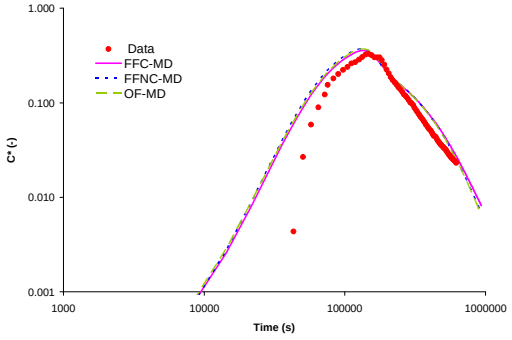

PT3

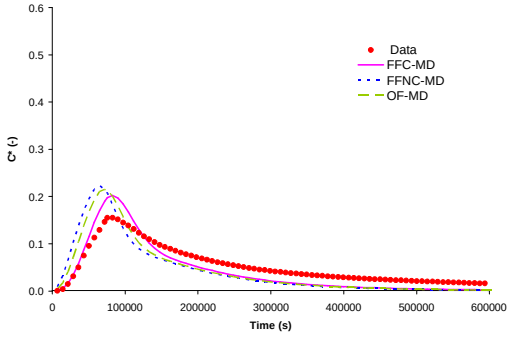

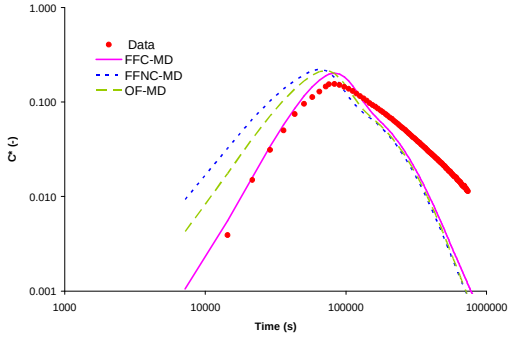

PT4

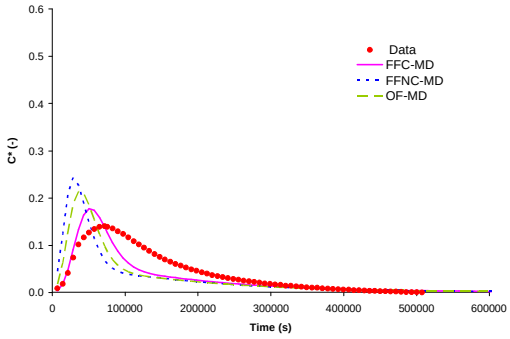

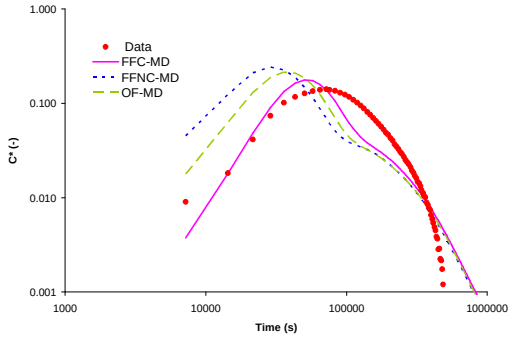

1.6 / 0.4 NMD

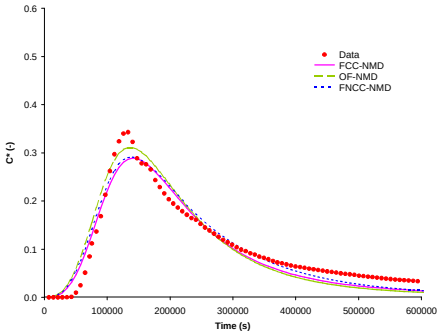

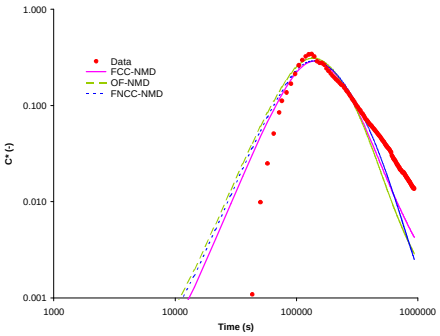

PT1

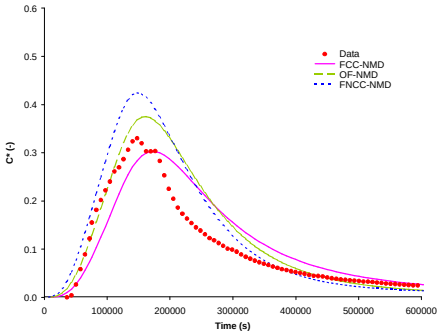

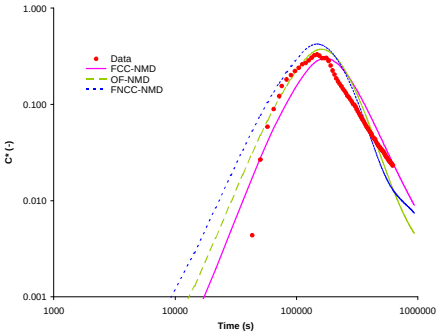

PT2

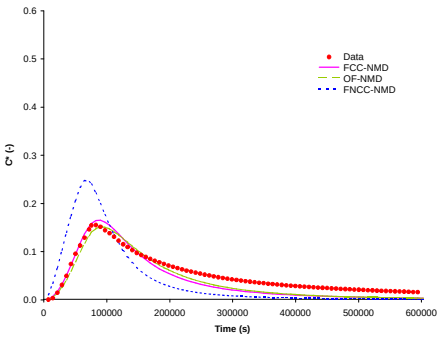

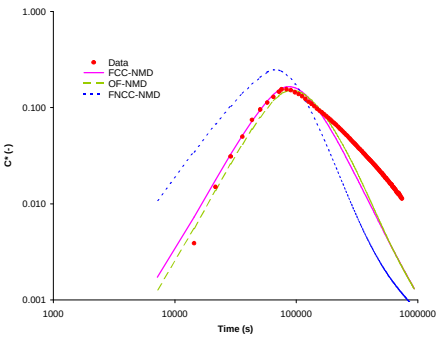

PT3

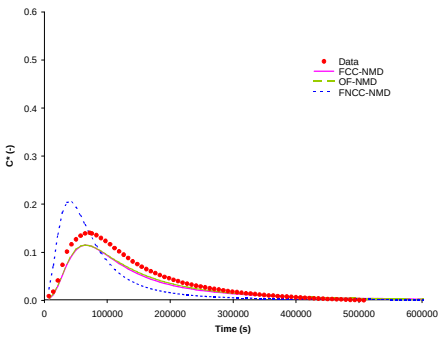

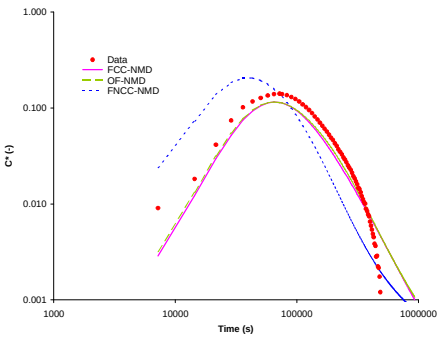

PT4

1.6 / 0.4 MD

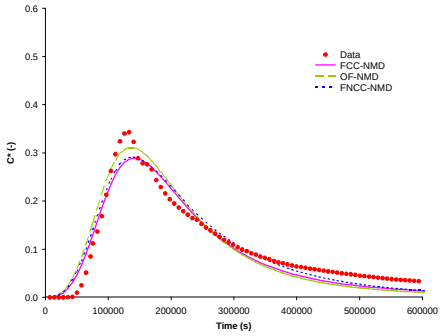

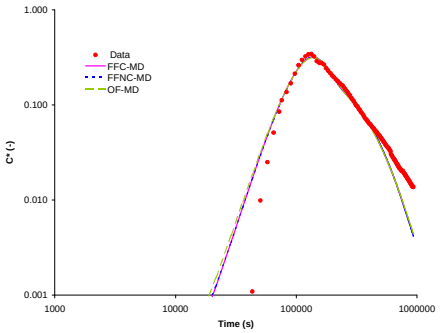

PT1

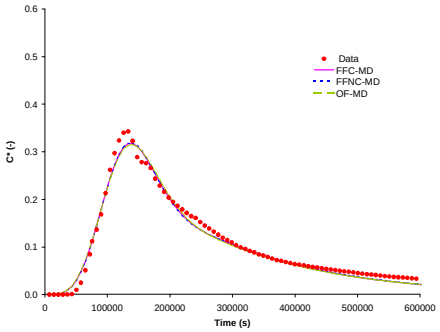

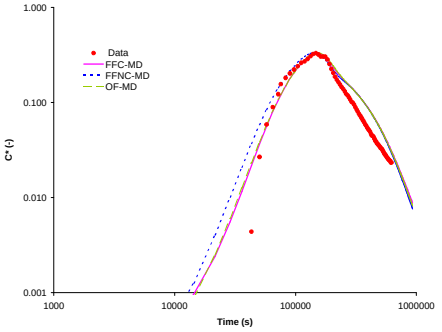

PT2

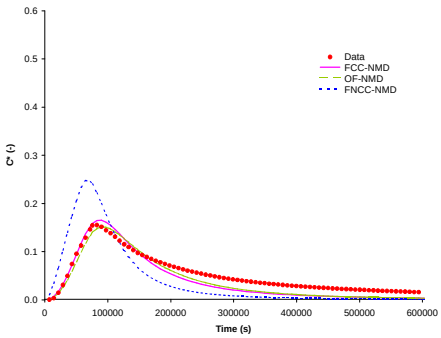

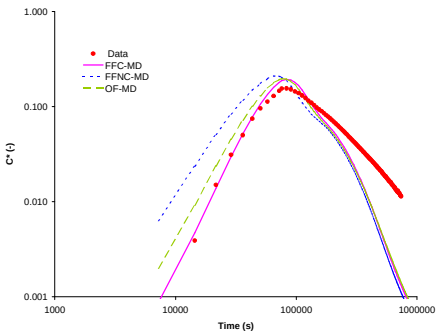

PT3

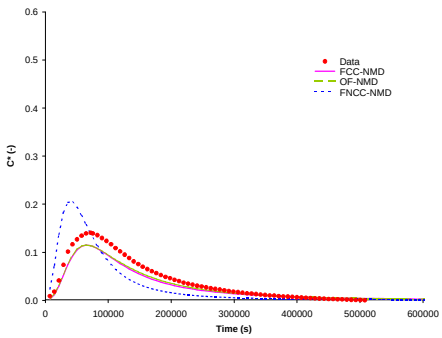

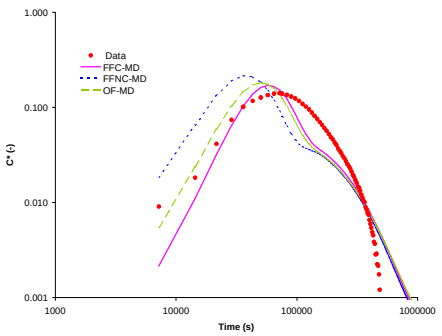

PT4

1.6 / 0.8 NMD

PT1

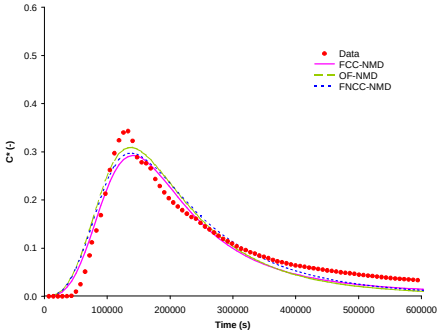

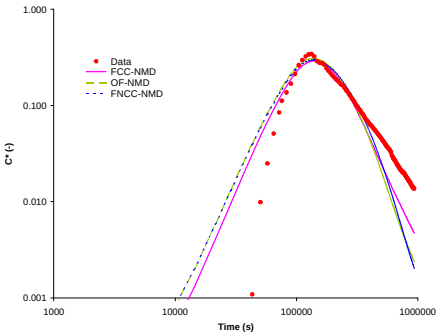

PT2

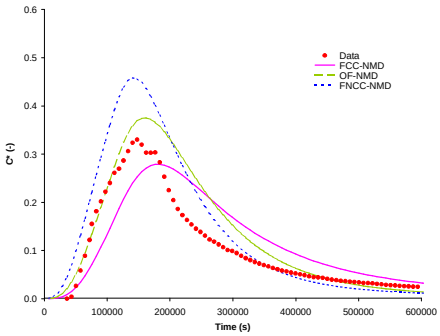

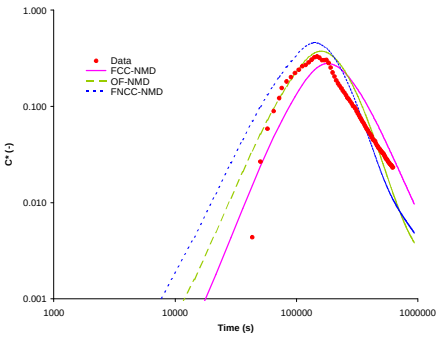

PT3

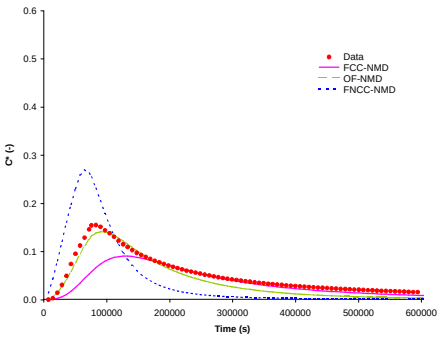

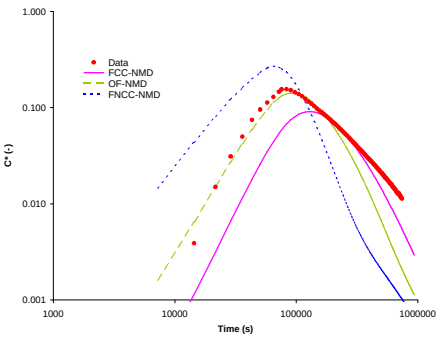

PT4

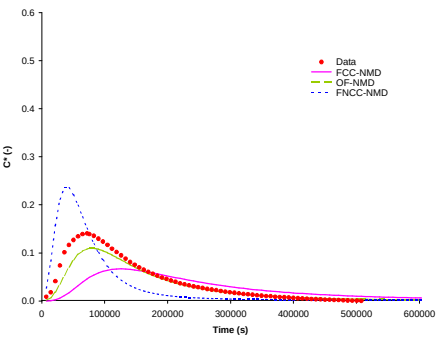

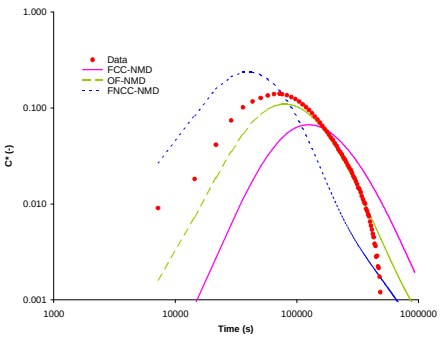

1.6 / 0.8 MD

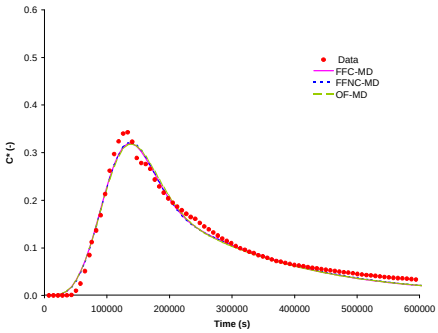

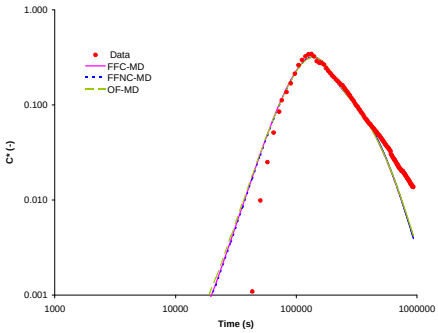

PT1

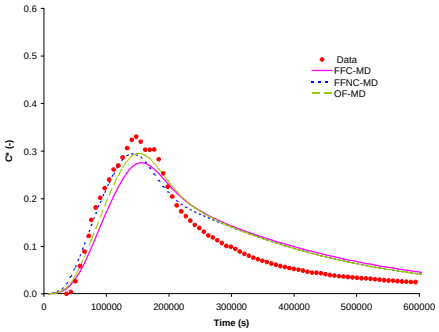

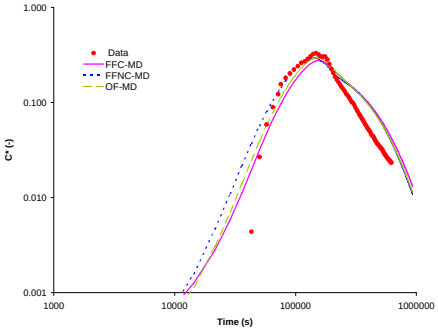

PT2

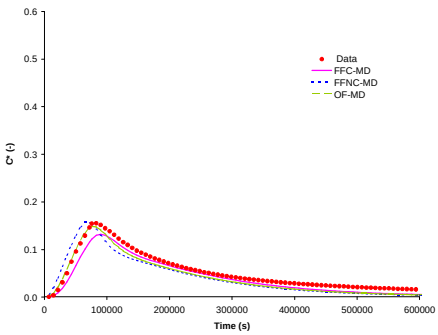

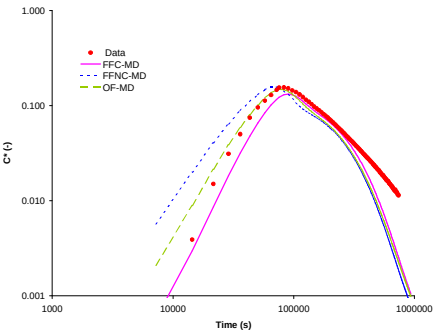

PT3

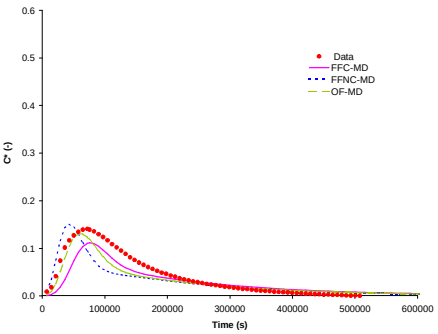

PT4

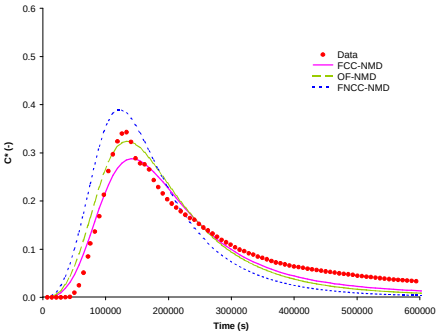

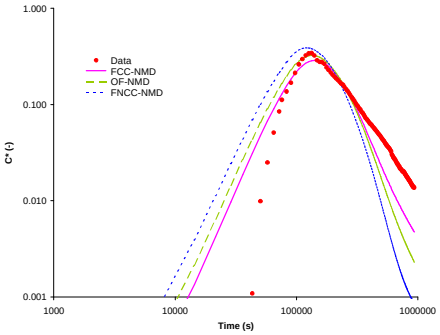

PT1

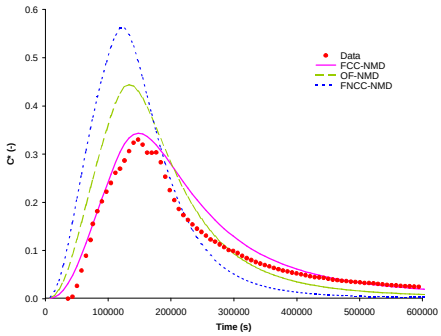

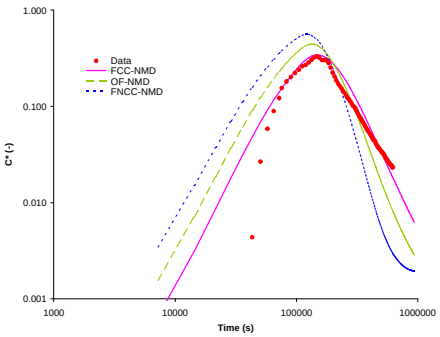

PT2

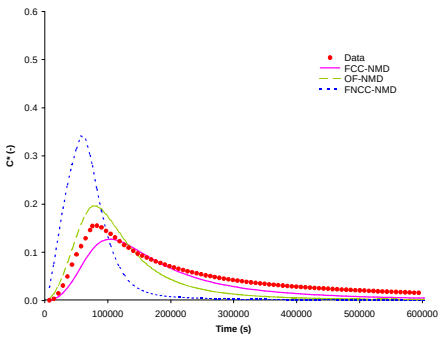

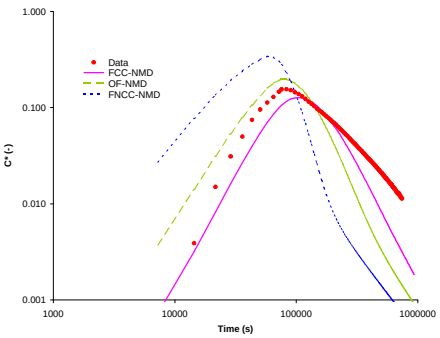

PT3

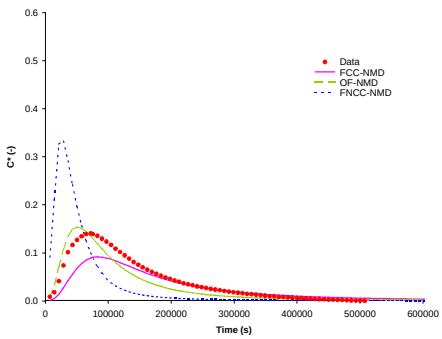

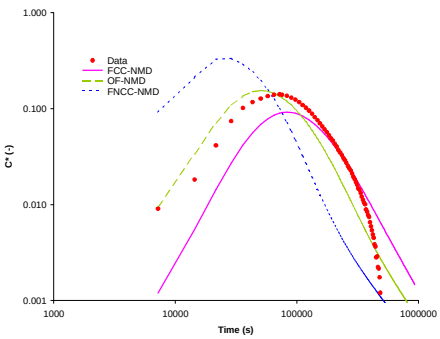

PT4

PT1

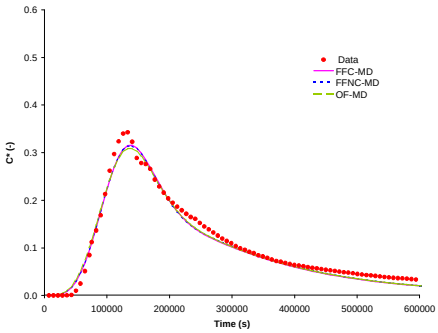

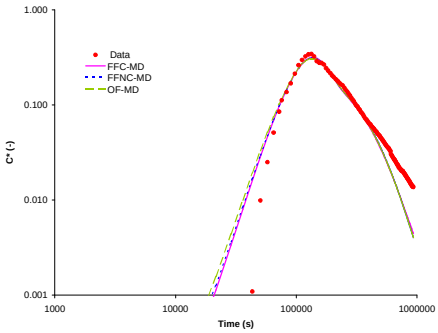

PT2

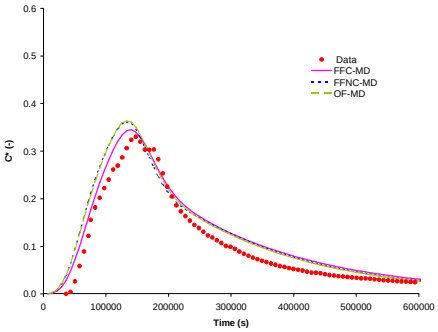

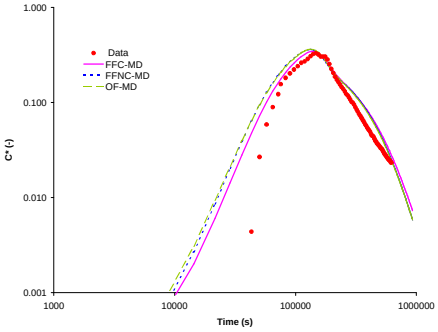

PT3

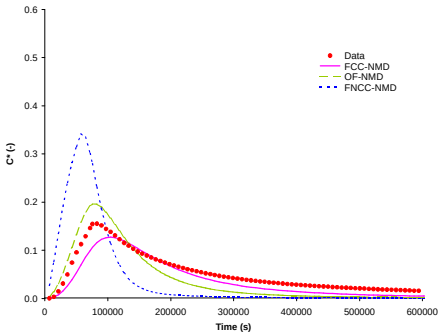

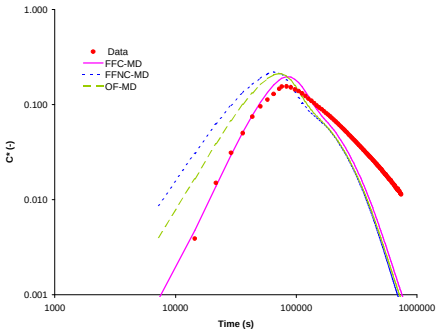

PT4

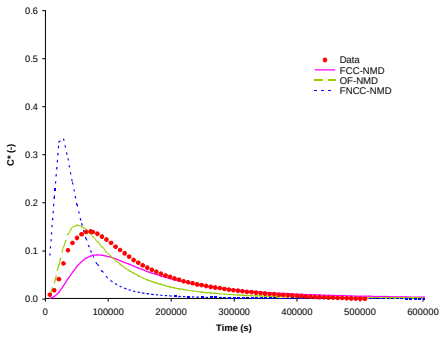

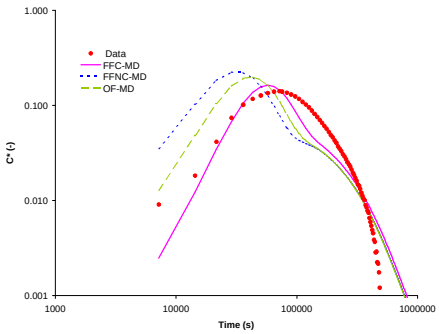

PT1

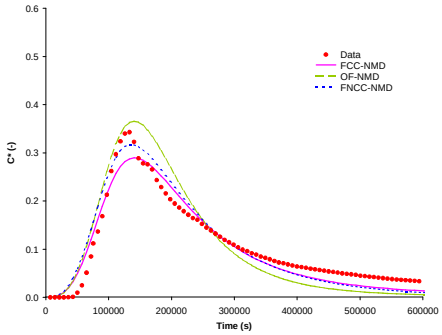

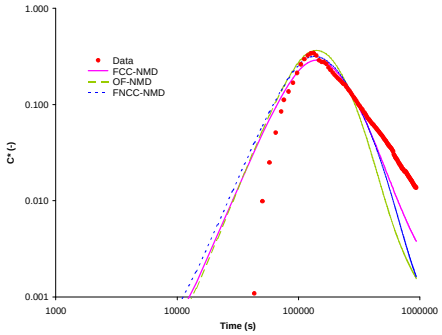

PT2

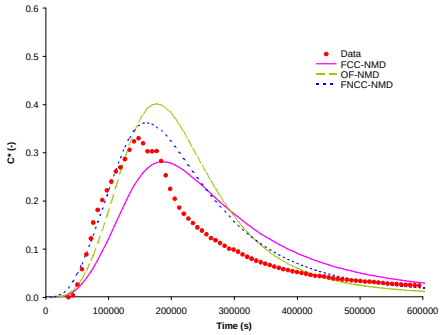

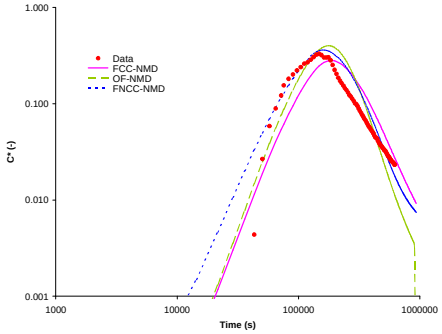

PT3

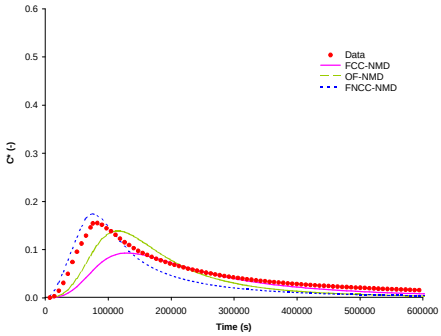

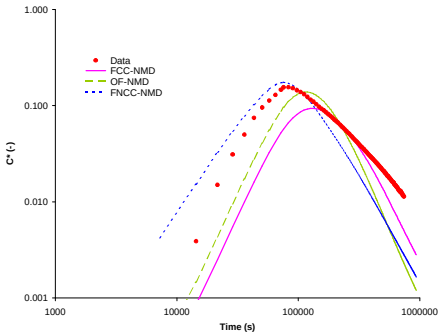

PT4

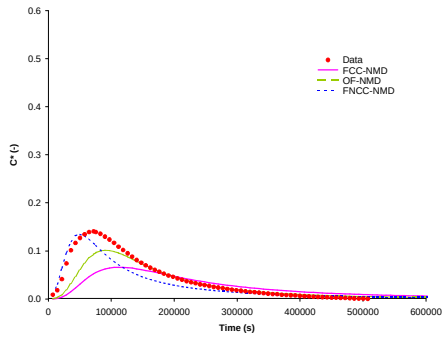

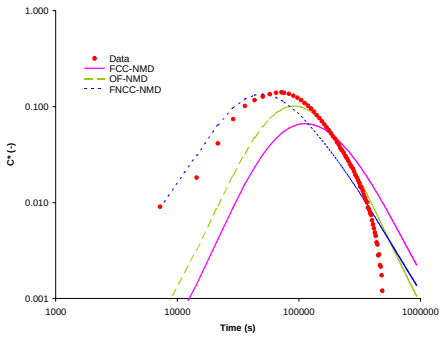

3.2 / 0.4 MD

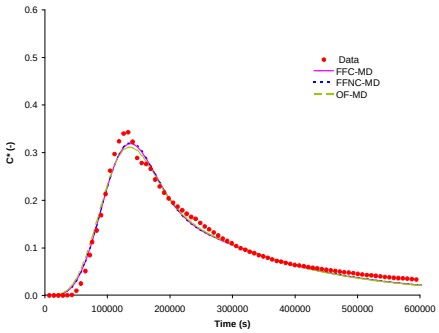

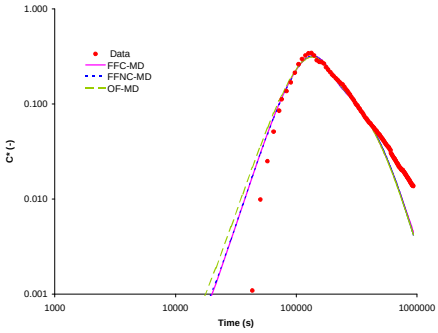

PT1

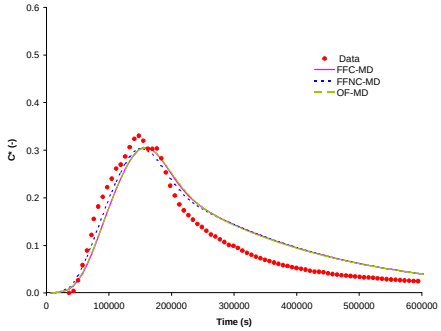

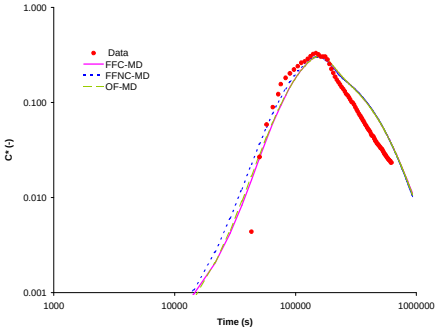

PT2

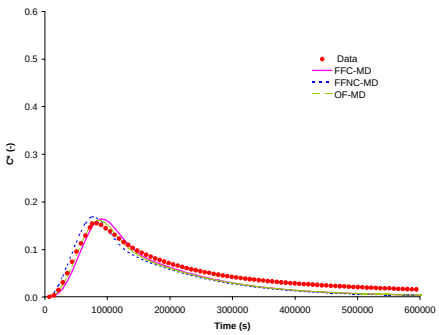

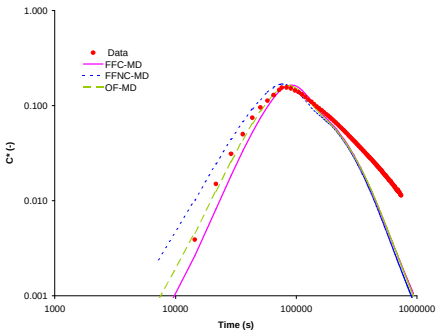

PT3

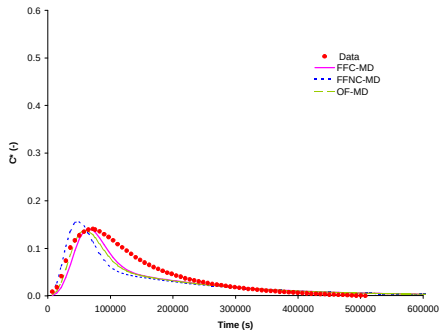

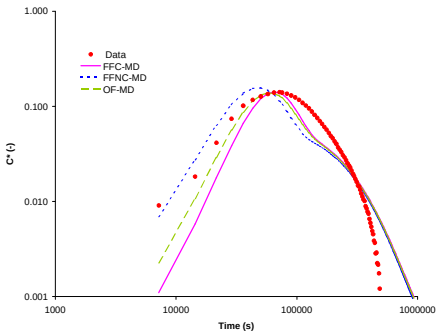

PT4

3.2 / 0.8 NMD

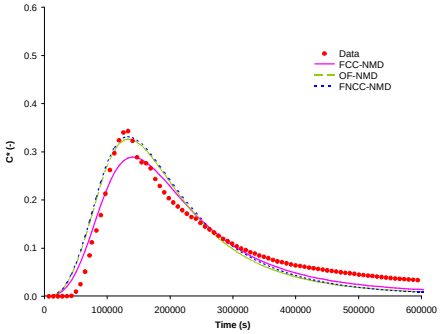

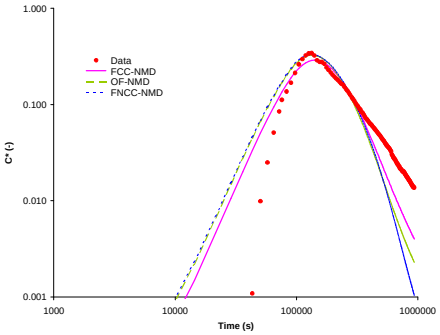

PT1

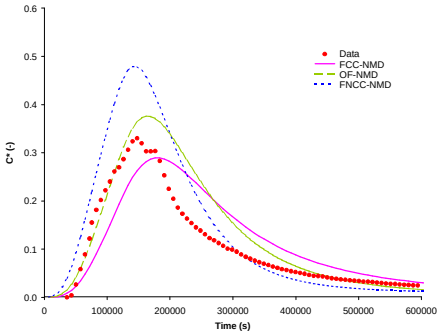

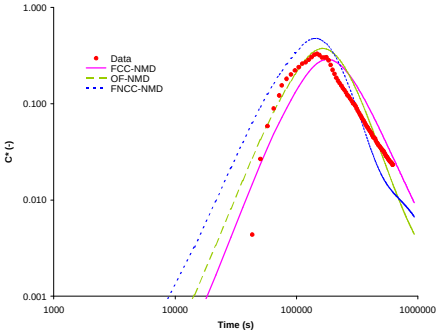

PT2

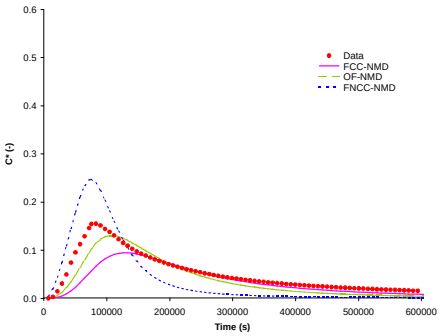

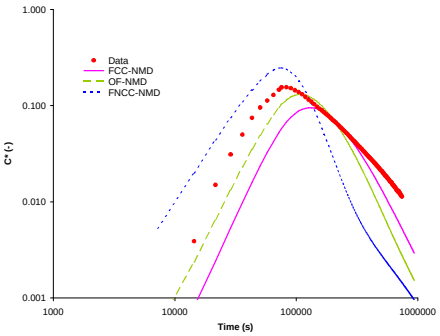

PT3

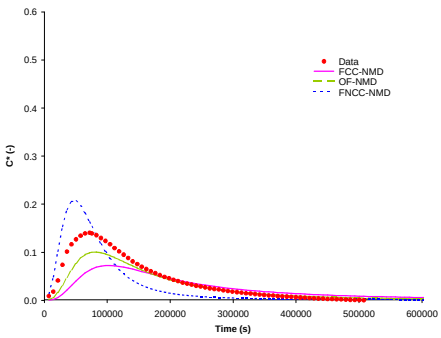

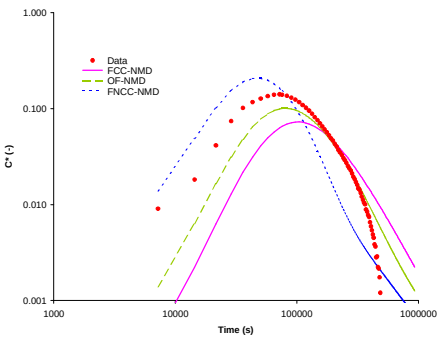

PT4

3.2 / 0.8 MD

PT1

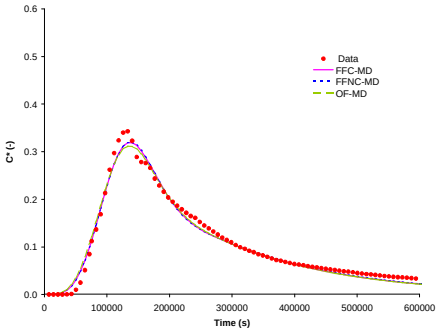

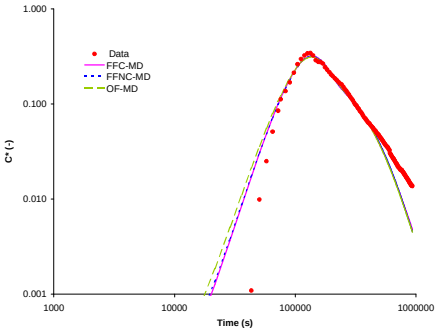

PT2

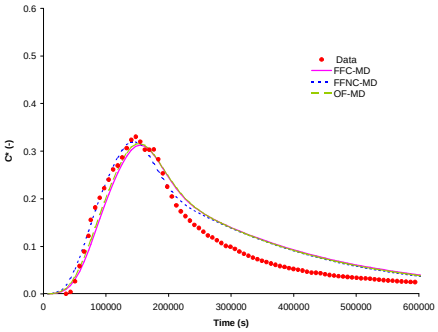

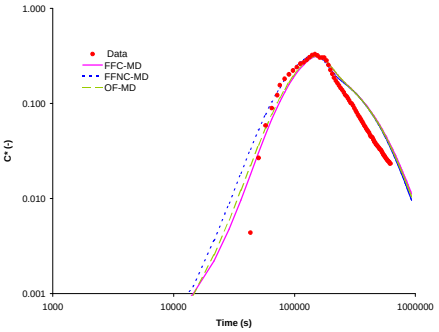

PT3

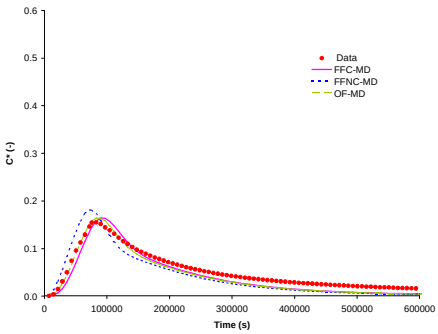

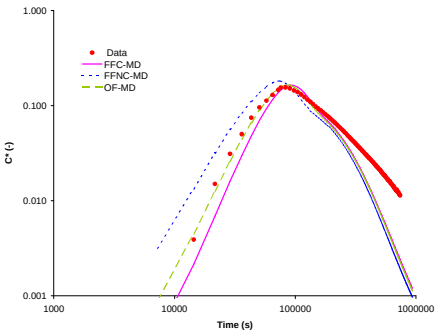

PT4

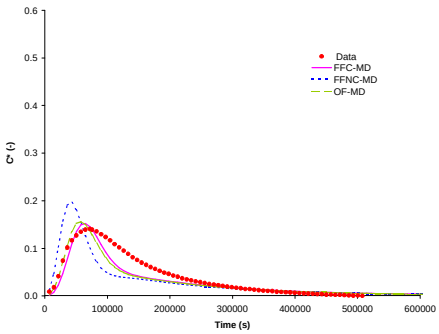

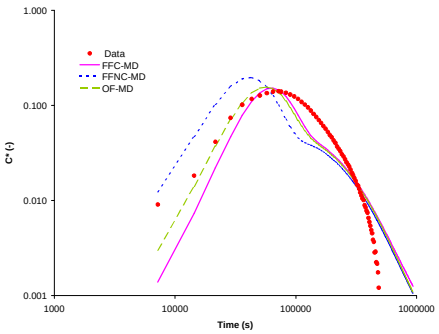

3.2 / 1.6 NMD

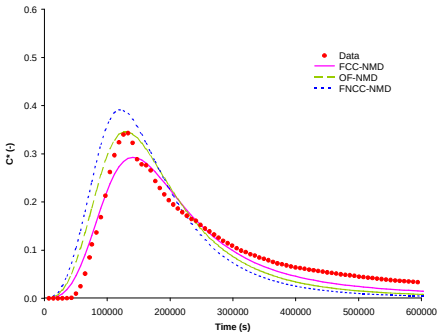

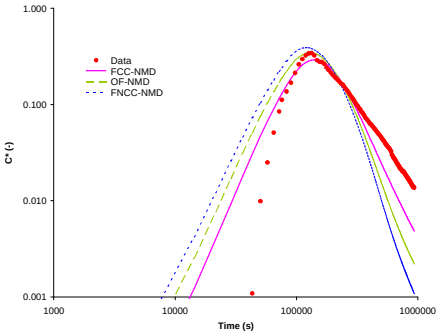

PT1

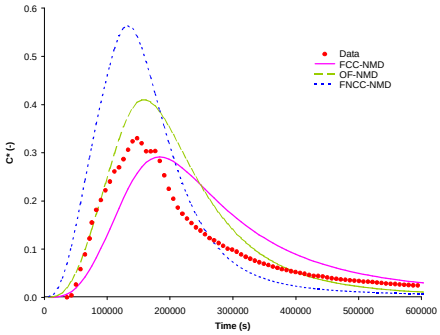

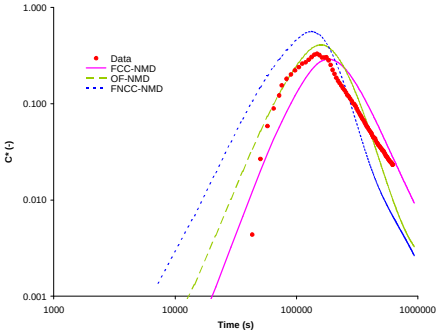

PT2

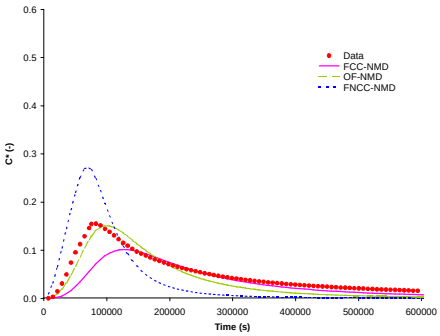

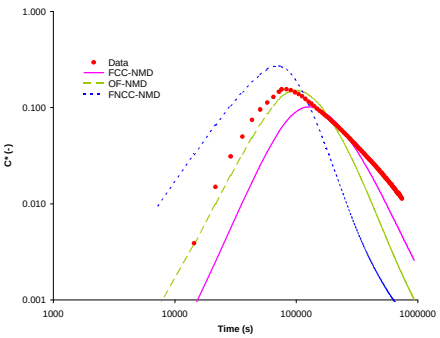

PT3

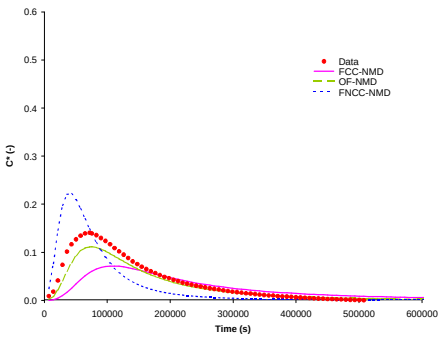

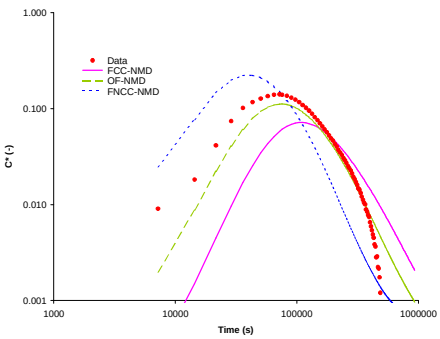

PT4

3.2 / 1.6 MD

PT1

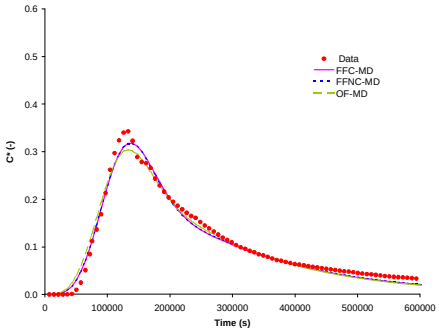

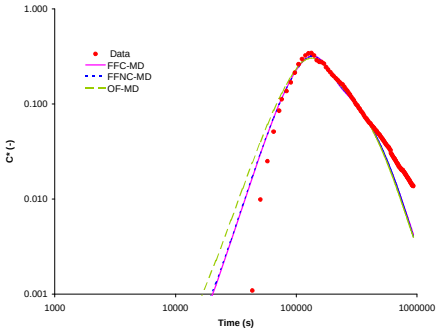

PT2

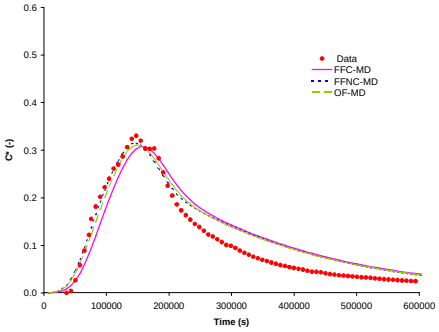

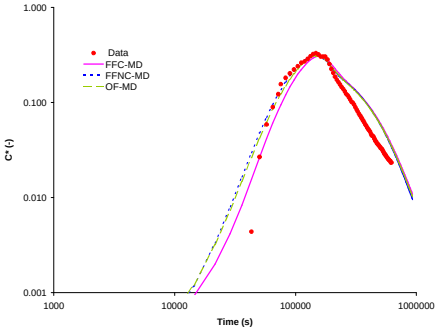

PT3

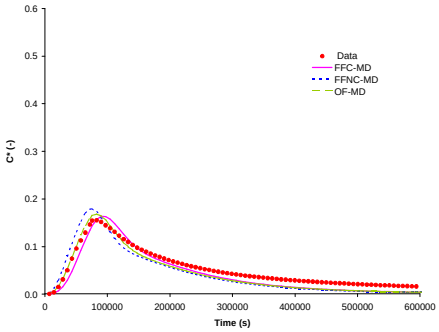

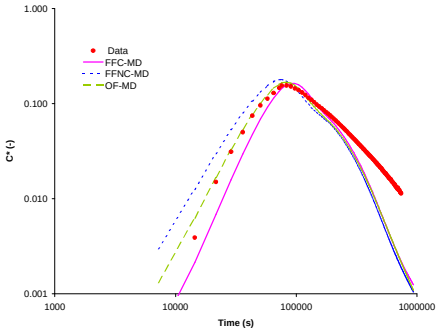

PT4

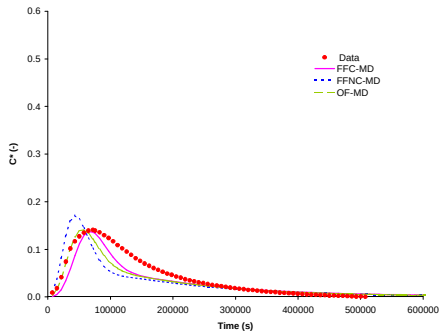

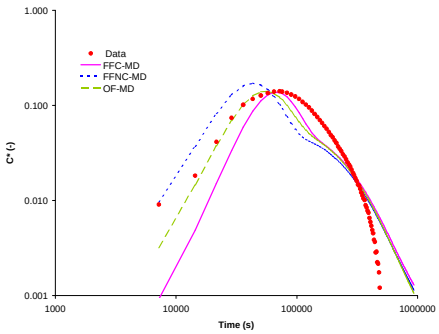

PT1

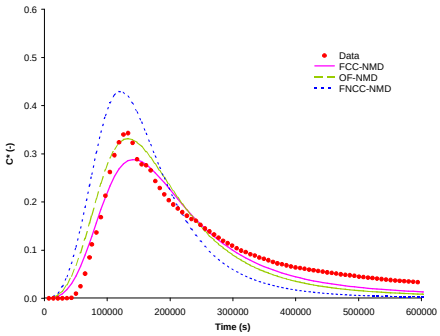

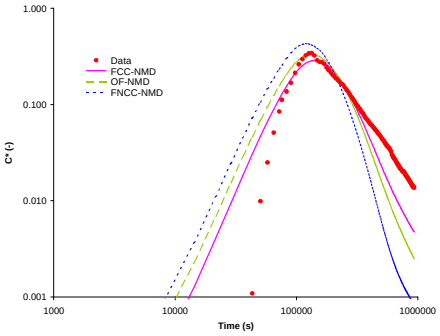

PT2

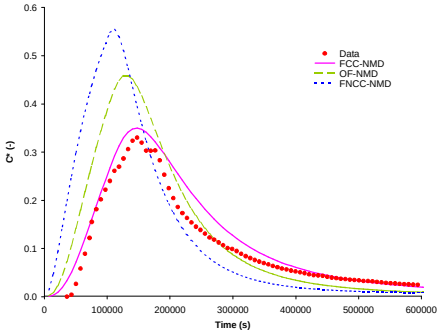

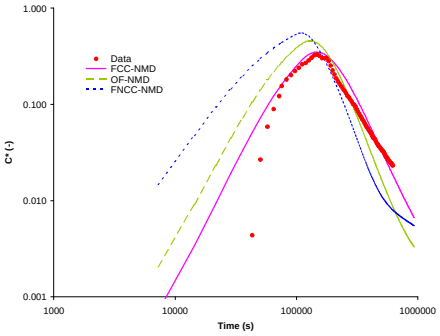

PT3

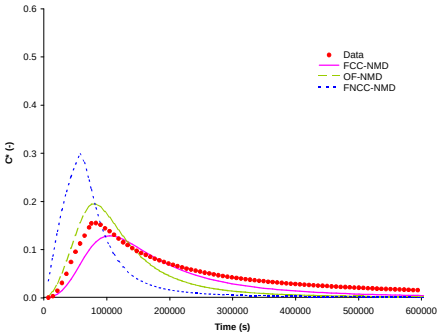

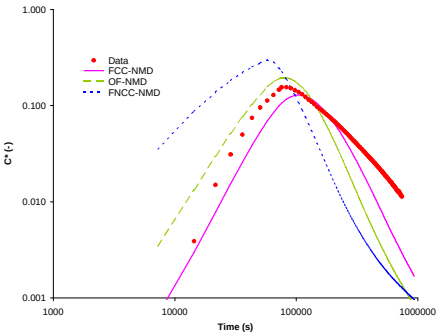

PT4

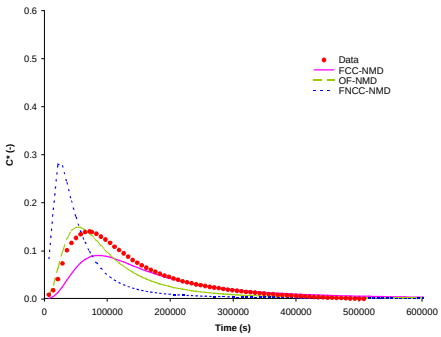

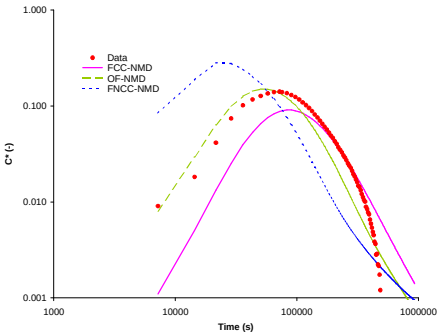

PT1

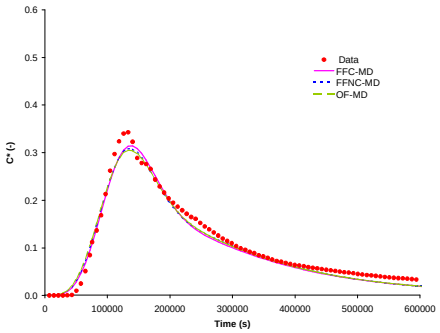

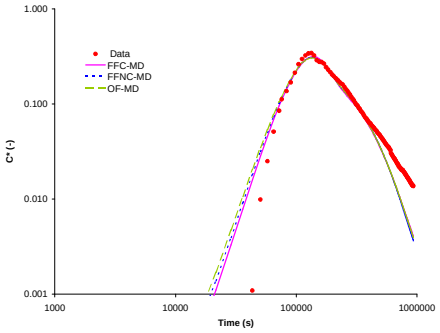

PT2

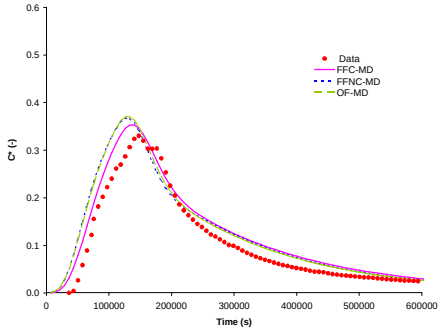

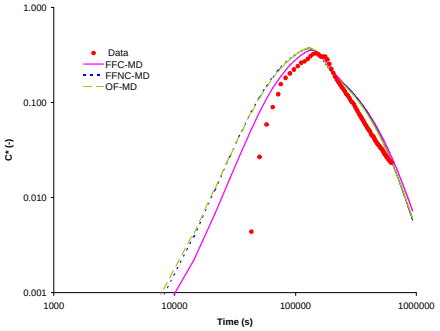

PT3

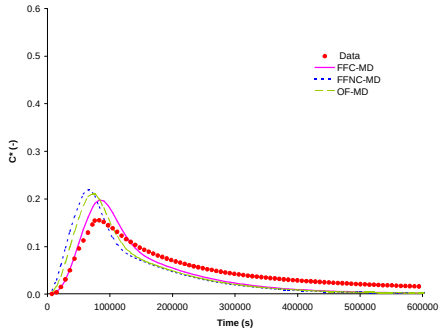

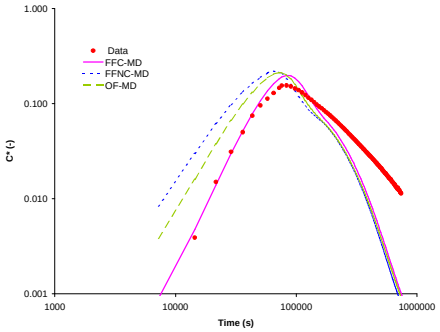

PT4

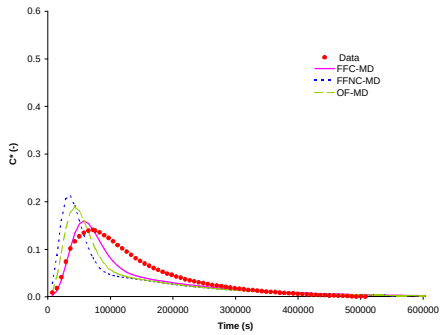

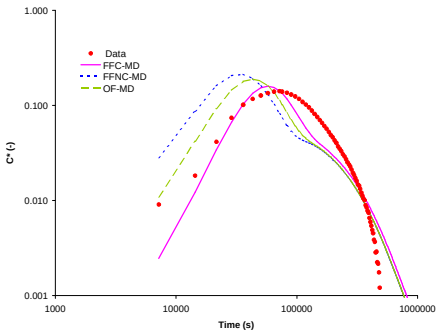

Annex A8

Tracer Test Simulation
Blind Prediction of PT5

In this annex measured (red dots) and computed breakthrough curves coming from the **blind prediction** of the **PT5** tracer test are depicted. The results are presented in terms of the accounted T field (expressed in terms of the correlation ratios R_x/R_y and pointed in the upper right corner of every sheet). For the same T field there are two sets of computed breakthrough curves, depending if the transport model accounts (MD) or not (NMD) for matrix diffusion.

For every breakthrough curve set (i.e. selected T field and selected or not matrix diffusion) three different fracture models are considered: FFC (red line), FFNC (blue dashed line), OF (green dashed line). The obtained fits are presented in Lineal-Lineal and Log-Log plot scales (left hand side and right hand side respectively).

PT5-NMD

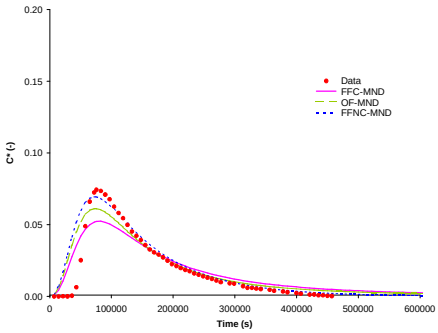

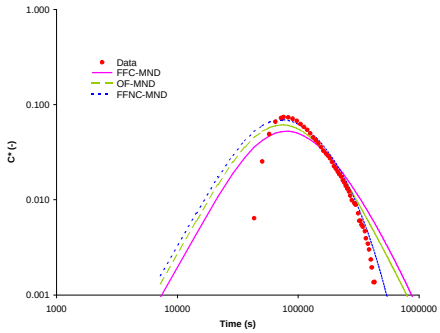

0.4/0.4

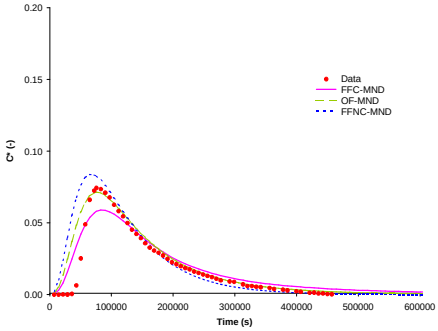

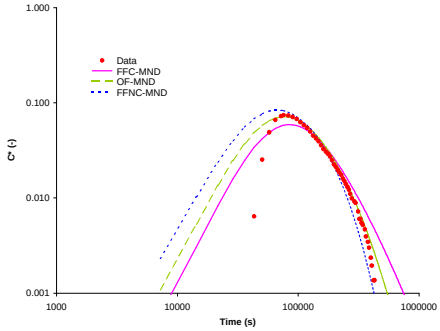

0.8/0.4

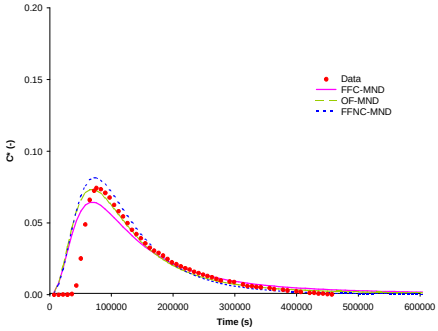

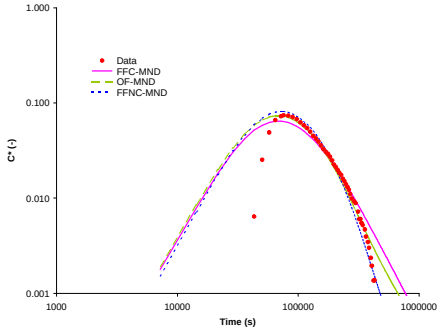

0.8/0.8

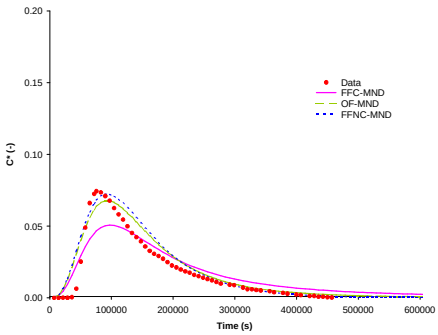

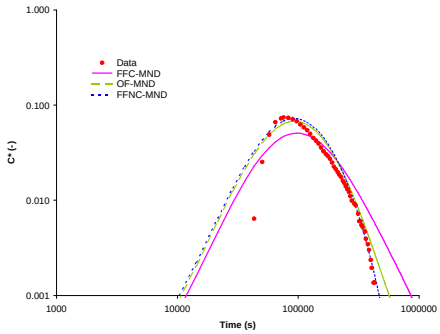

1.6/0.4

PT5-NMD

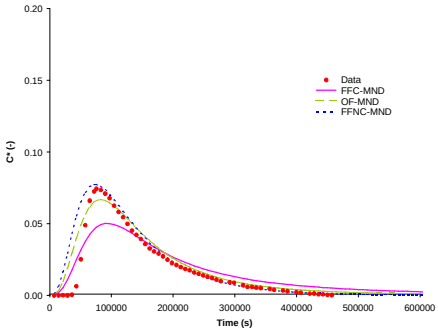

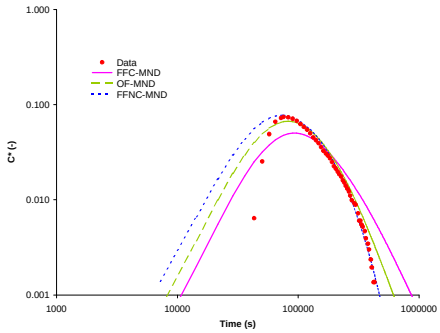

1.6/0.8

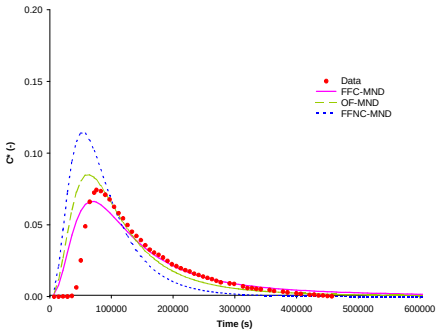

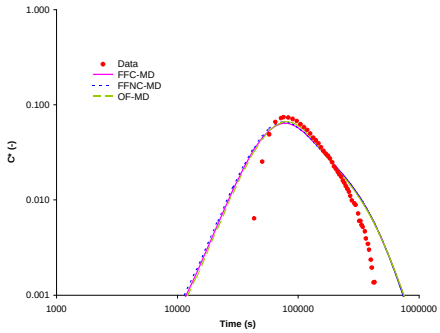

1.6/1.6

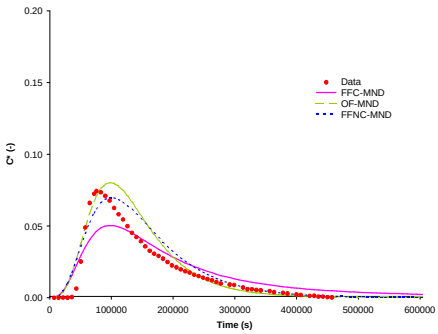

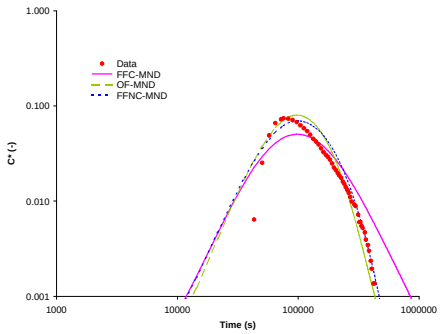

3.2/0.4

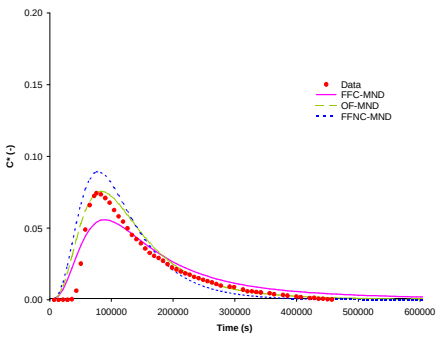

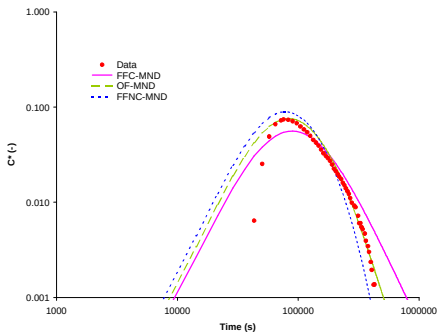

3.8/0.8

PT5-NMD

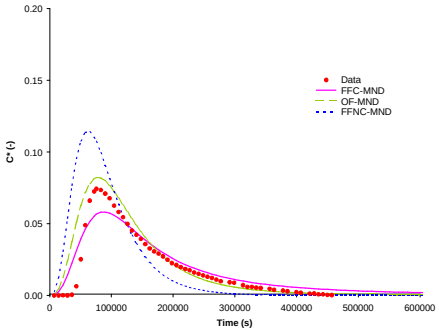

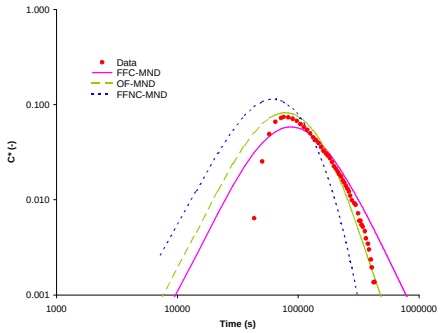

3.2/1.6

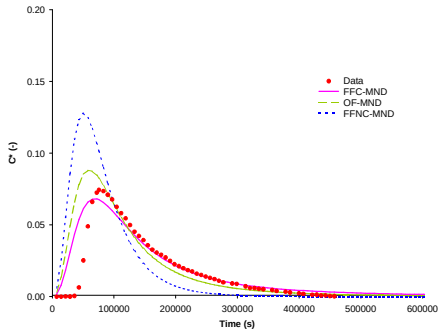

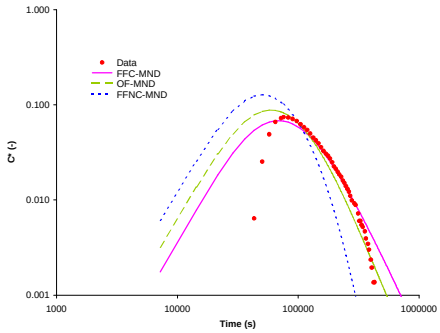

3.2/3.2

PT5-MD

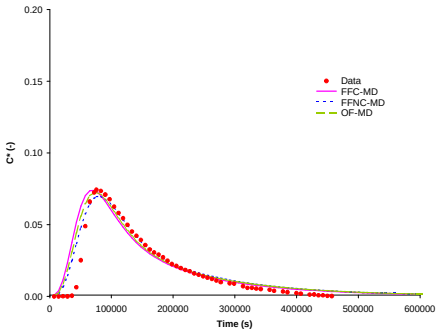

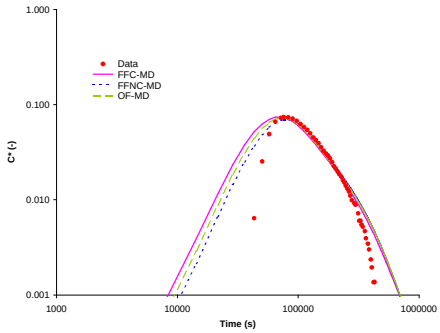

0.4/0.4

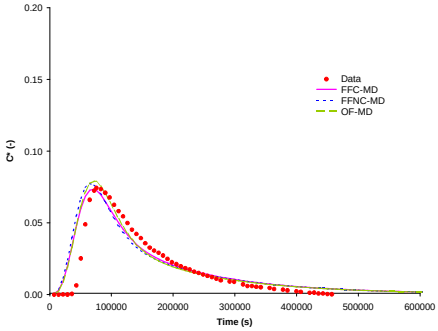

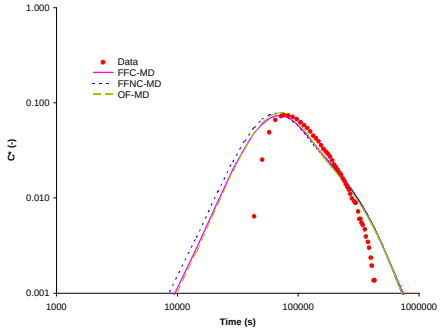

0.8/0.4

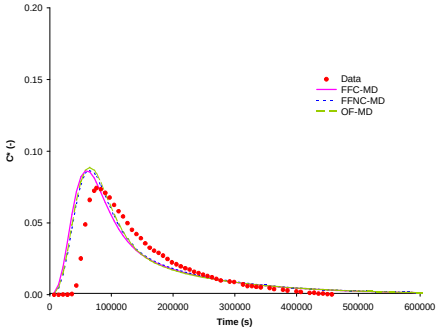

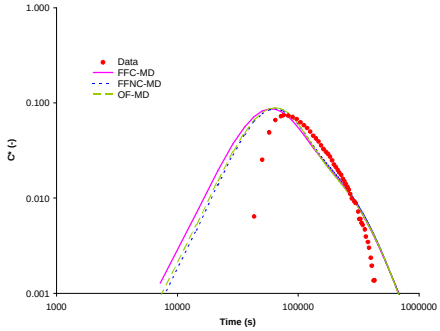

0.8/0.8

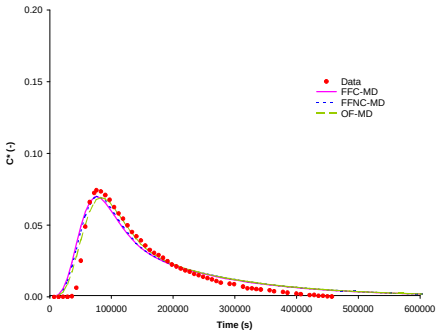

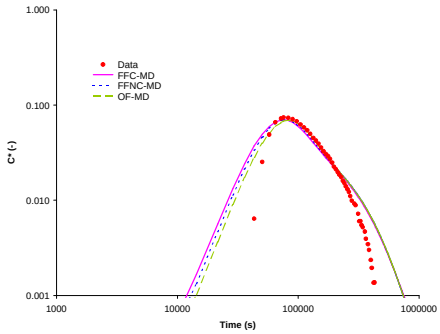

1.6/0.4

PT5-MD

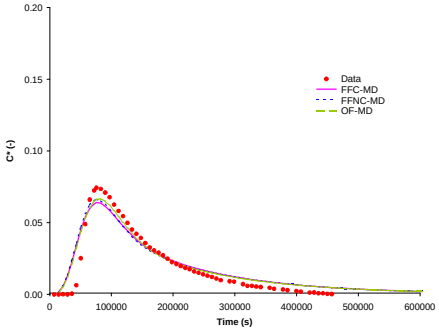

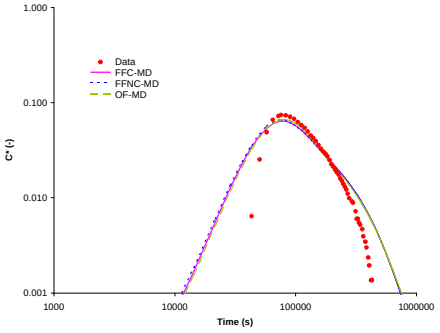

1.6/0.8

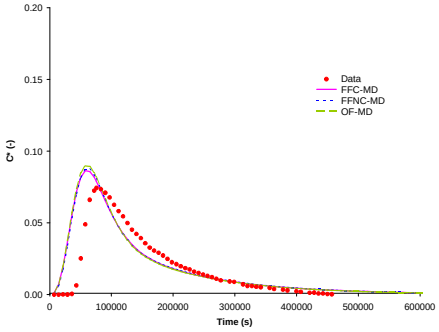

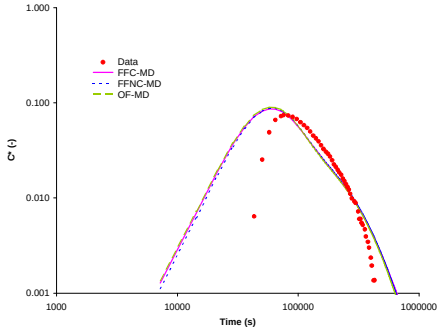

1.6/1.6

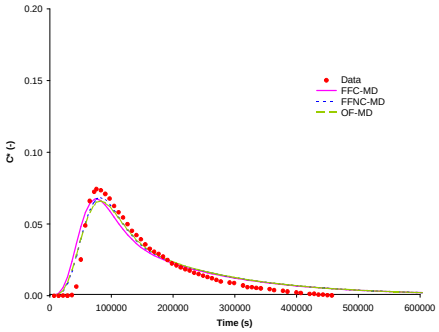

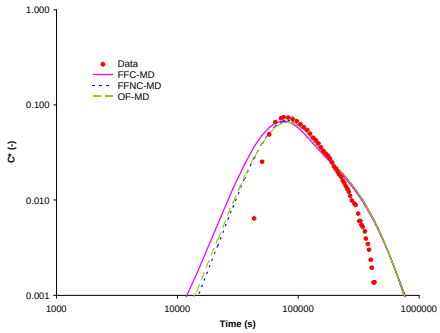

3.2/0.4

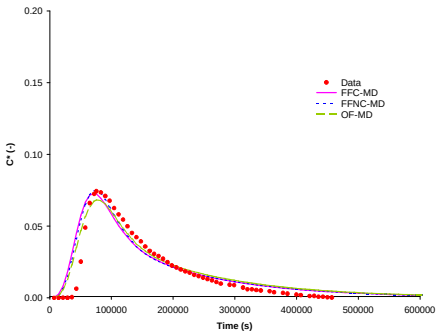

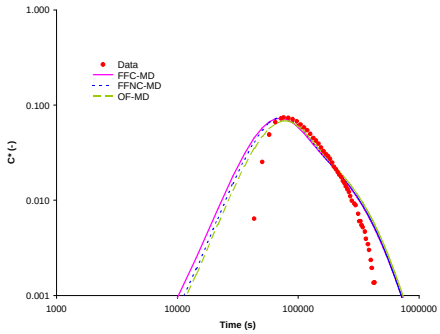

3.8/0.8

PT5-MD

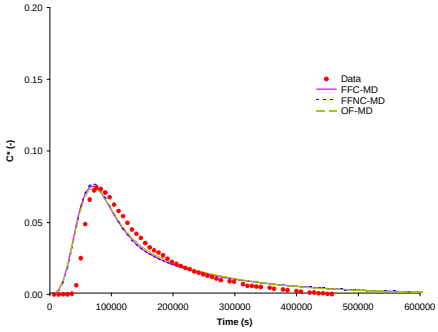

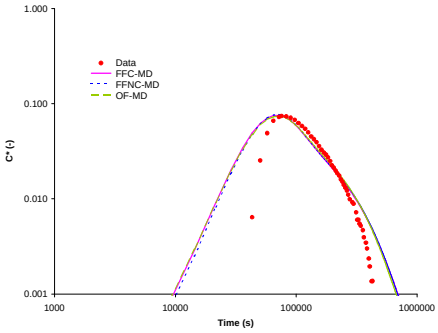

3.2/1.6

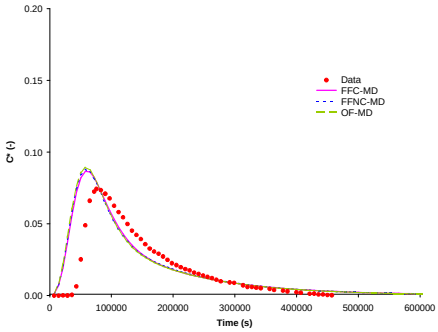

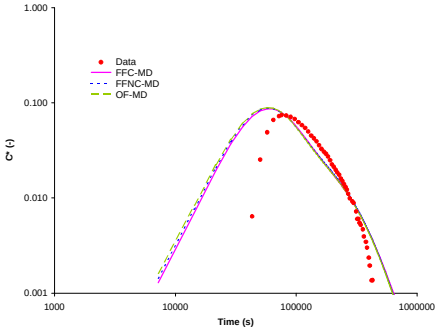

3.2/3.2

Annex A9

Gas Tracer Test Calibration

In this annex measured and computed gas tracer breakthrough curves coming from the calibration of the gas transport parameters of the analytical solution of the gas migration governing equation are depicted. The results are presented for every “Run” (gas tracer test) performed in the framework of the GAM project (Run-2 to Run-11).

Concentration measurements are drawn using different symbol and also different light color for every gas tracer. Computed concentration are depicted using lines, colored with the dark color corresponding to the selected gas tracer.

GT1- Run2

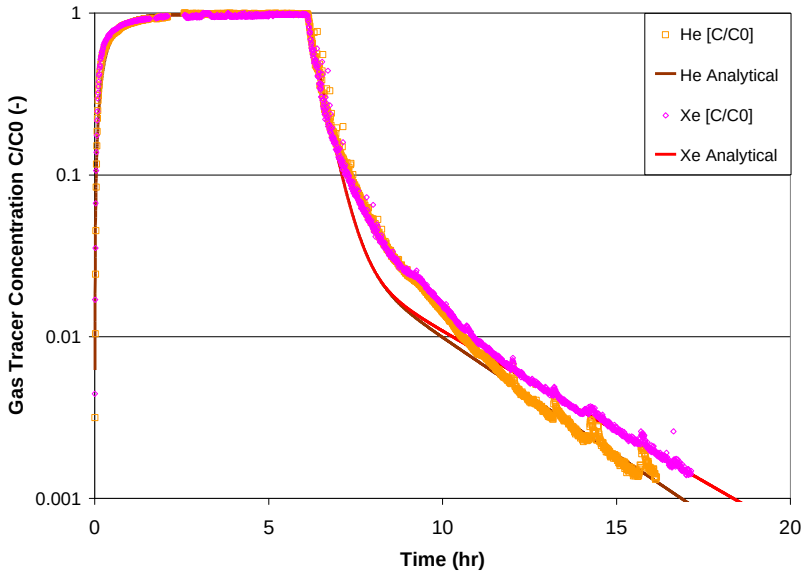

GT1- Run3

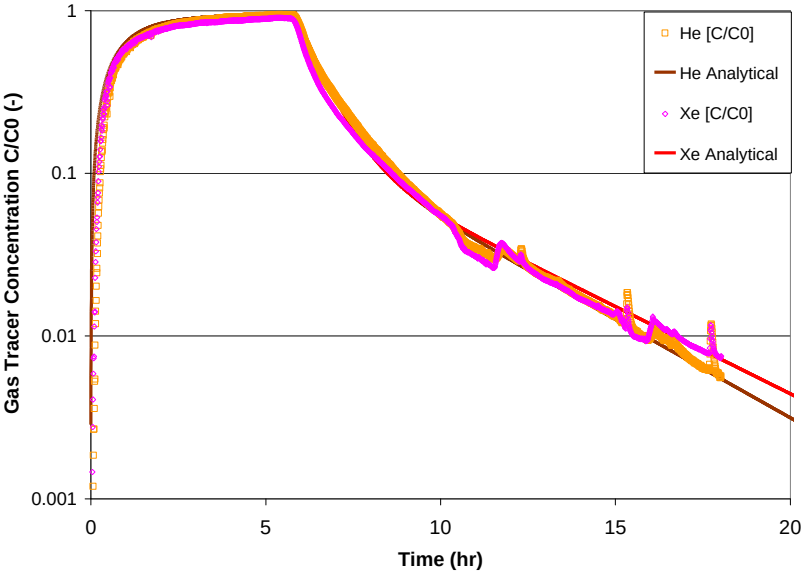

GT2- Run4

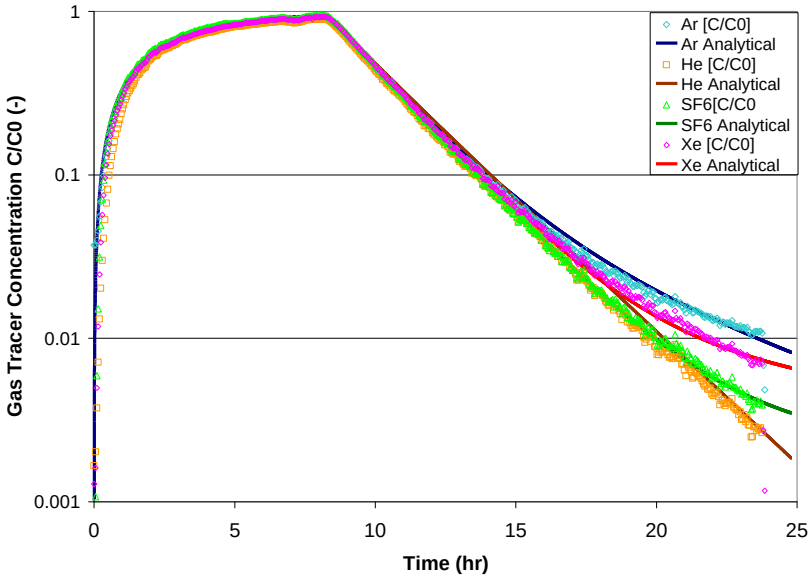

GT2- Run5

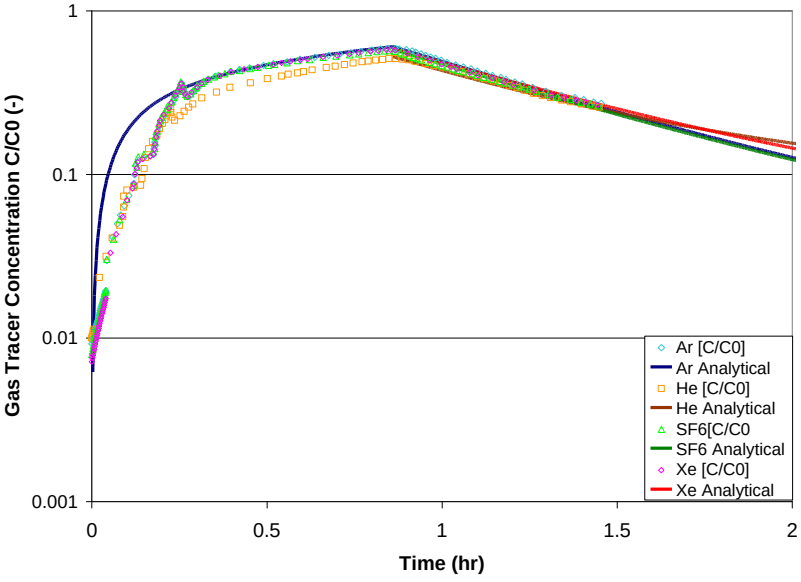

GT2- Run6

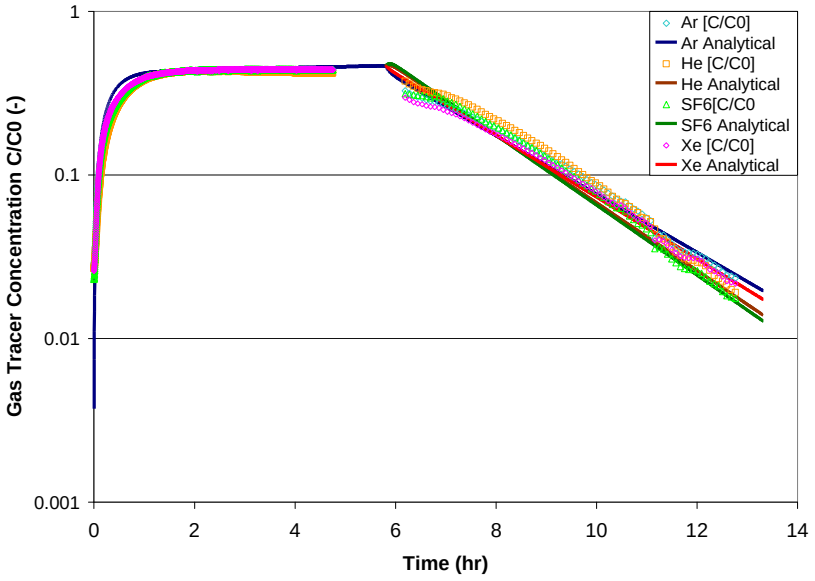

GT3- Run7

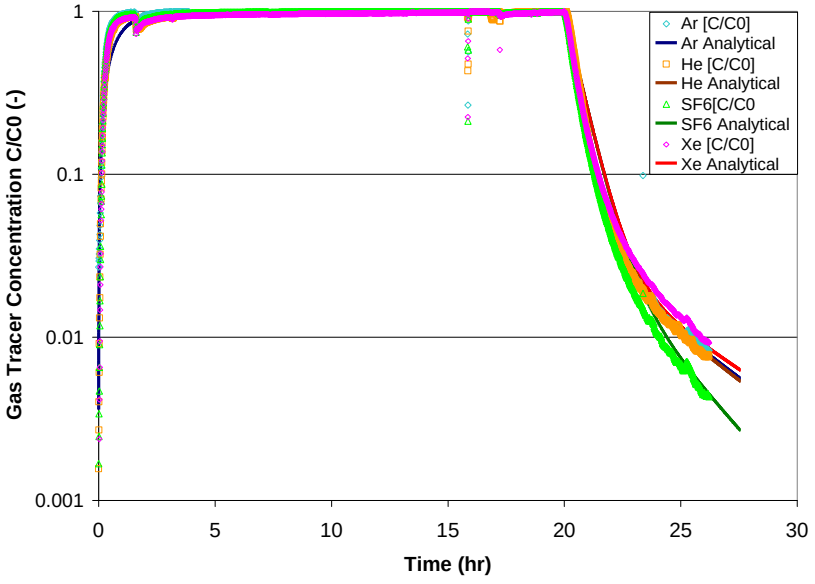

GT2- Run8

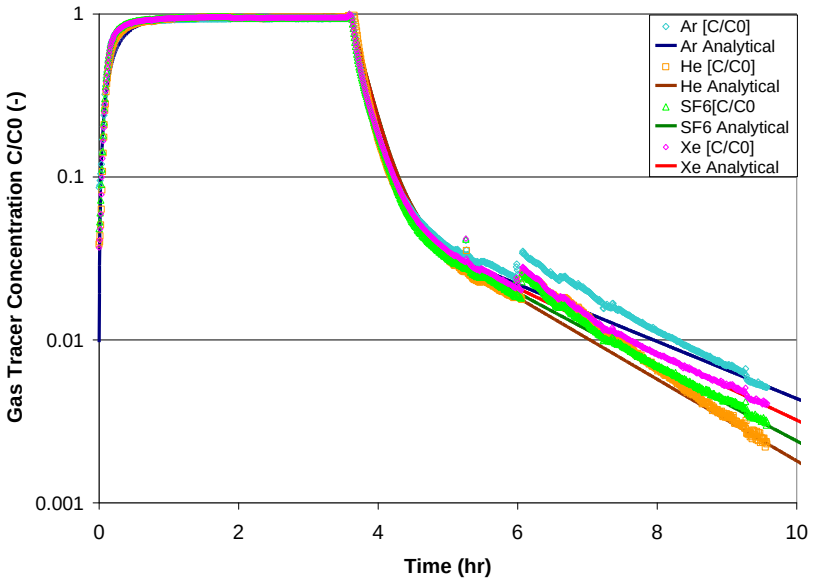

GT3- Run9

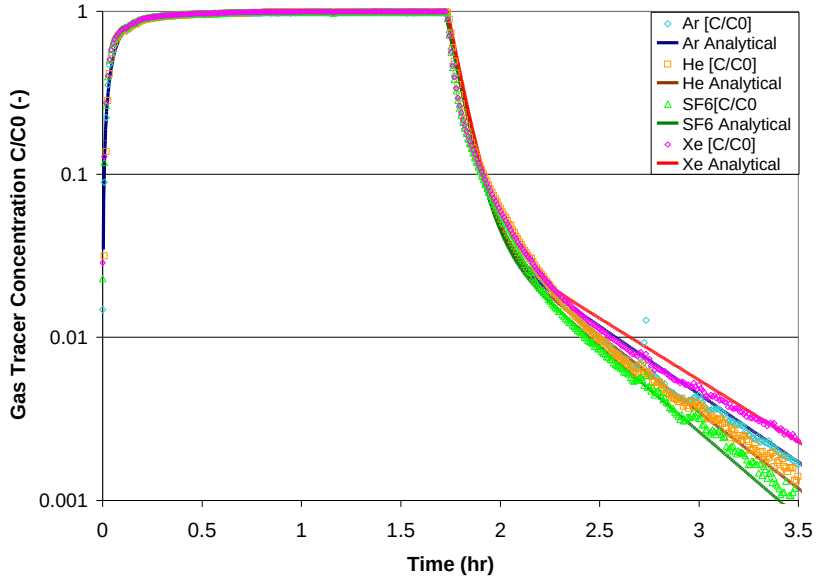

GT2- Run10

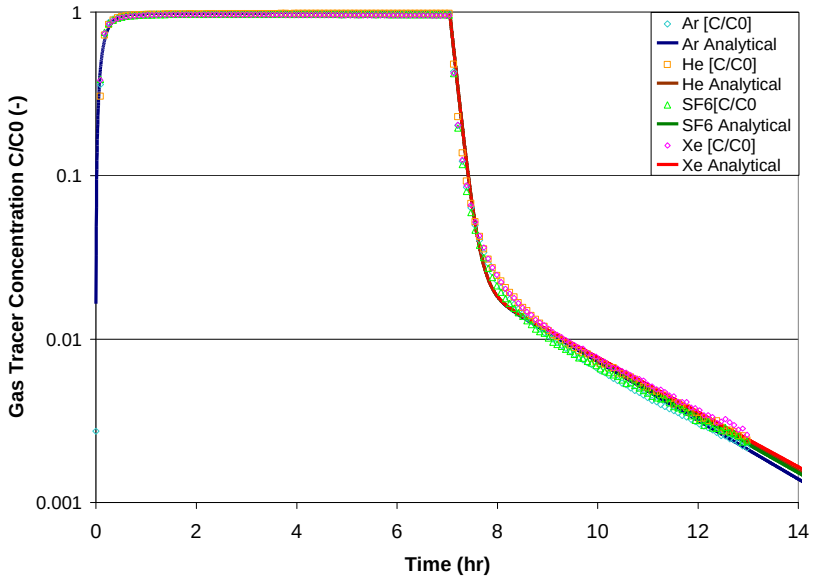

GT3- Run11